

CHARLES UNIVERSITY

Faculty of Science

Department of Physical and Macromolecular Chemistry



Study of protein-protein interactions of human E3 ubiquitin
ligase Nedd4-2

Studium protein-proteinových interakcí lidské E3 ubikvitin
ligázy Nedd4-2

M.Sc. Rohit Ashok Joshi

Doctoral thesis
of study program Physical Chemistry

Supervisor: RNDr. Veronika Obšilová, Ph.D.

Consultant: prof. RNDr. Tomáš Obšil, Ph.D.

Prague 2024

Declaration

I declare that I prepared the final thesis independently and that I have listed all the information sources and literature used. This work, or a substantial part of it, has not been submitted for the award of another or the same academic degree.

.....

In Prague, Date:

Rohit Ashok Joshi

Acknowledgement

If this were a separate chapter, it would have been the longest one. Even after writing all the thesis, I find writing acknowledgments very difficult, so many people to thank in such a little space. All of them have transformed my PhD into a wonderful experience.

Firstly, I would like to express my sincere gratitude to my supervisor RNDr. Veronika Obsilova, Ph.D., who has been the greatest support system of my PhD life. She showed an incredible amount of patience and trust in me. Most importantly, she gave me the time and space while working. Her advice on both research as well as on my career have been invaluable. Her mentorship was paramount in providing a well-rounded experience consistent with my long-term career goals. Her truly scientist intuition has made her a constant oasis of ideas and passions in science, which exceptionally inspire and enrich my growth. Thank you very much.

As well as, I am very thankful to my consultant prof. RNDr. Tomas Obsil, Ph.D. for his excellent advice and suggestions during my work as well as study, which were valuable for me. I am grateful to him for giving me the opportunity to work in his laboratory.

I am grateful to the entire team of the Laboratory of Structural Biology of Signaling Proteins, Institute of Physiology, Czech Academy of Sciences, detached BIOCEV and Laboratory of Biophysical Chemistry of Protein Complexes at the Faculty of Science of Charles University, Czech Republic. I am thankful to my colleagues Mgr. Pavel Pohl Ph.D., Mgr. Dana Kalábová Ph.D., for helping me in cloning, protein purification and data analysis work. I also thank Bc. Gabriela Kočárová and all the team members of prof. RNDr. Tomáš Obšil, Ph.D., and RNDr. Veronika Obšilová, Ph.D. for their help and support during my Ph.D. study.

I would like to express my sincere gratitude to prof. RNDr. Petr Herman, CSc. and RNDr. Dita Strachotova, Ph.D. from Institute of Physics, Faculty of Mathematics and Physics, Charles University for their immense help and support in conducting fluorescence spectroscopy and data analysis.

In addition, I would like to thank several people from the Centre of Molecular Structure, Institute of Biotechnology, Czech Academy of Sciences, BIOCEV for invaluable help and support in conducting X-ray crystallography experiments. I would like to express my special gratitude to RNDr. Petr Pompach, Ph.D., and Mgr. Pavla Vaňková, Ph.D. for their help in measuring, evaluating data of chemical crosslinking coupled to mass spectrometry.

Last but not the least, I express my deep gratitude toward my sole inspiration and strength, my beloved mother Mrs. Jayshri Joshi, my fiancé Shweta, my family and friends for their unflagging love, sacrifice and unconditional support throughout my life and my studies. Thank you very much.

This dissertation was realized thanks to the financial support of:

Czech Science Foundation (Projects No. 20-00058S and 23-04686S)

Grant Agency of the Charles University (Project No. 348421)

Abstract

Post-translational modifications through ubiquitination play a crucial role in the regulation of membrane proteins. Nedd4-2, a human HECT E3 ubiquitin ligase is the last component of the ubiquitination cascade that transfers the ubiquitin molecules and triggers the endocytosis of its downstream target molecules. Dysregulation of Nedd4-2 can cause various disorders, including epilepsy, respiratory distress, and Liddle syndrome. Despite the involvement of different adaptor proteins in the regulation of Nedd4-2, our focus in this research was on the conserved 14-3-3 proteins, well-known negative regulators of Nedd4-2. In this study, we performed biophysical characterization of Nedd4-2¹⁹⁰⁻⁵⁸¹ and Nedd4-2¹⁸⁶⁻⁹⁷⁵ constructs while in complex with 14-3-3 to get further insight into the dynamics of this interaction. Our results from time-resolved fluorescence spectroscopy revealed that 14-3-3 binding impacts the emission properties and mobility of specific WW domains (WW3 and WW4) of Nedd4-2, while sparing others (WW1). Intriguingly, the catalytic HECT domain undergoes conformational changes and increased solvent exposure upon complex formation. We propose that steric hindrance of WW3 and WW4 domains, combined conformational alterations in the catalytic HECT domain, may underlie the regulatory mechanism mediated by 14-3-3 binding. Chemical cross-linking coupled with mass spectrometry and limited proteolysis experiments further elucidate extensive structural changes in Nedd4-2 domains in the presence of 14-3-3 proteins, highlighting the protective role of 14-3-3 against proteolytic degradation. Overall, our comprehensive findings shed light on the intricate molecular mechanisms governing the 14-3-3 binding-mediated regulation of Nedd4-2, offering valuable insights into the better understanding of ubiquitin-mediated regulation of membrane protein functions and its possible role in various pathological conditions.

Abstrakt

Posttranslační modifikace prostřednictvím ubikvitinace hrají klíčovou roli v regulaci membránových proteinů. Nedd4-2, lidská HECT E3 ubikvitin ligáza, je poslední komponentou ubikvitinační kaskády, která přenáší molekuly ubikvitinu a spouští endocytózu svých následných cílových molekul. Dysregulace Nedd4-2 může způsobovat různé poruchy, včetně epilepsie, respirační úzkosti a Liddleova syndromu. Přestože se na regulaci Nedd4-2 podílejí různé adaptorové proteiny, v tomto výzkumu jsme se zaměřili na konzervované proteiny 14-3-3, známé negativní regulátory Nedd4-2. V této studii jsme provedli biofyzikální charakterizaci konstruktů Nedd4-2¹⁹⁰⁻⁵⁸¹ a Nedd4-2¹⁸⁶⁻⁹⁷⁵ v komplexu s 14-3-3, abychom získali další náhled do dynamiky této interakce. Naše výsledky časově rozlišené fluorescenční spektroskopie odhalily, že vazba 14-3-3 ovlivňuje emisní vlastnosti a pohyblivost specifických WW domén (WW3 a WW4) Nedd4-2, zatímco ostatní (WW1) šetří. Zajímavé je, že katalytická doména HECT prochází při tvorbě komplexu konformačními změnami a zvýšenou exponovaností rozpouštědla. Předpokládáme, že sterická inhibice domén WW3 a WW4 v kombinaci s konformačními změnami v katalytické doméně může být základem regulačního mechanismu zprostředkovaného vazbou proteinem 14-3-3. Chemické zesílení spolu s hmotnostní spektrometrií a experimenty s limitovanou proteolýzou dále objasňují rozsáhlé strukturní změny v doménách Nedd4-2 v přítomnosti proteinů 14-3-3, což podtrhuje ochrannou roli 14-3-3 proti proteolytické degradaci. Naše komplexní zjištění tedy celkově vrhají světlo na složité molekulární mechanismy řídící regulaci Nedd4-2 zprostředkovanou vazbou 14-3-3 a nabízejí cenné poznatky pro lepší pochopení regulace funkcí membránových proteinů zprostředkované ubikvitinem a její možné úlohy u různých patologických stavů.

Abbreviations

AMP	Adenosine monophosphate
APS	Ammonium persulphate
ATP	Adenosine Triphosphate
BS3	Bis (sulfosuccinimidyl) suberate
BRCA1	Breast Cancer 1
C2	Calcium binding domain
C209	Cysteine at position 209 (all nedd4-2 variants written same way)
Cbl	Casitas B-lineage lymphoma
CKIP-1	Casein Kinase 2-interacting protein 1
CFTR	Cystic fibrosis transmembrane conductance regulator
DVL1	dishelved-1
DNA	Deoxyribose nucleic acid
DSA	Disuccinimidyl adipate
DSG	Disuccinimidyl glutarate
DSS	Disuccinimidyl suberate
DUB	deubiquitinases
E1	Ubiquitin-activating enzyme
E2	Ubiquitin-conjugating enzyme
E3	Ubiquitin ligase
E6-AP	E6-associated protein
EDTA	Ethylenediaminetetraacetic acid
EGFR	Epidermal Growth Factor Receptor
ENaC	Epithelial sodium channel
ExoS/T	Exotoxin S/T
HECT	Homologous to E6-associated protein Carboxyl Terminus
HHARI	human homolog of Ariadne
HOIP	HOIL-1L Interacting protein
HPV	Human papillomavirus
His-Tag	Histidine affinity tag
IBR	In-between-RING
IC	Internal conversion
IGF-1	Insulin-like growth factor-1
IPTG	Isopropyl β -d-1 thiogalactopyranoside
ITCH	itchy E3 ubiquitin protein ligase
ISC	Intersystem crossing

K _D	Dissociation constant
MDM2	Mouse double minute 2
MEM	Maximum Entropy Method
MS	Mass spectrometry
M _w	Molecular weight
Navs	Voltage gated sodium channel
Ndfip1	Nedd4 family interacting protein 1
Nedd4	Neural precursor cell expressed developmentally downregulating protein 4
Nedd4-2	Neural precursor cell expressed developmentally downregulating protein 4-like
NEDD8	Neuronal precursor cell-expressed, developmentally downregulated protein 8
NedL1	HECT-type ubiquitin-protein isopeptide ligase 1
o-GlcNAc	O-linked β-N-acetylglucosamine
PBS	Phosphate-buffered saline
PCR	Polymerase chain reaction
PDB	Protein data bank
PKA	cAMP dependent protein kinase A
PMSF	Phenylmethylsulphonyl fluoride
pNedd4-2	Phosphorylated Nedd4-2 protein
pS342	phosphorylated residue Ser ³⁴² of Nedd4-2 protein
pS448	phosphorylated residue Ser ⁴⁴⁸ of Nedd4-2 protein
polyUb	Polyubiquitin chain
PTM	Post translational modification
RBR	Ring between ring
RING	Really interesting new gene
RNA	Ribonucleic acid
rpm	Revolutions per minute
S342	Serine at position 342
S448	Serine at position 448
SDS PAGE	Sodium dodecyl sulphate polyacrylamide gel
SGK1	Serum and glucocorticoid-regulated kinase 1
Smurf	Smad ubiquitin regulatory factor
SUMO	small ubiquitin-like modifier
SV	Stern-Volmer
TBE PAGE	Tris-borate-EDTA polyacrylamide gel electrophoresis

TCEP	Tris (2-carboxyethyl) phosphine
TEMED	Tetramethylethylenediamine
TEV	Tobacco etch virus protease
Tris-HCl	Tris-(hydroxymethyl)-aminomethane and hydrochloric acid
Ub	Ubiquitin
UBB/UBC	Polyubiquitin B/C
UBD	Ubiquitin binding domain
UBL	Ubiquitin like proteins
v/v	Volume by volume
VR	vibrational relaxation
w/v	Weight by volume
w/w	Weight by weight
WW	Domain of Nedd4-2, named after two conserved tryptophan
WWP1	WW domain-containing E3 ubiquitin protein ligase 1
XL-MS	Chemical crosslinking coupled mass spectrometry

List of publications

1. **Joshi, R.**, Pohl, P., Strachotova, D., Herman, P., Obsil, T., Obsilova, V. Nedd4-2 binding to 14-3-3 modulates the accessibility of its catalytic site and WW domains. *Biophys. J.* **121**, 1299–1311 (2022).
2. Pohl, P., **Joshi, R.**, Petrvalska, O., Obsil, T., Obsilova, V. 14-3-3-protein regulates Nedd4-2 by modulating interactions between HECT and WW domains. *Commun. Biol.* **4**, 899 (2021).

Table of Content

Acknowledgement	3
Abstract	5
Abstrakt	6
Abbreviations	7
List of publications	10
Table of Content	11
1. Introduction	14
2. Theoretical Background	15
2.1 Post translational modifications	15
2.2 Ubiquitination	16
2.2.1 Ubiquitination cascade	19
2.2.2 E1 - Ubiquitin-activating enzyme	20
2.2.3 E2 - Ubiquitin-conjugating enzyme	20
2.2.4 E3 - Ubiquitin ligase	21
2.3 Nedd4 family	23
2.3.1 Domain Architecture	24
2.3.2 Function and regulation	25
2.4 Nedd4-2 or Nedd4L	27
2.4.1 Regulations	29
2.4.2 Disorders	30
2.5 14-3-3 family	31
2.5.1 Isoforms	31
2.5.2 Structure	32
2.5.3 Motifs	33
2.5.4 Non-phosphorylated motifs	34
2.5.5 Regulation	35
2.5.6 Associated disorders	36
2.6 Nedd4-2 and 14-3-3 Interaction	38
3. Aims	39
4. Methods and material	40
4.1 Material	40
4.1.1 Biological material	40

4.1.2	Chemicals	40
4.1.3	Laboratory material	41
4.1.4	Instruments	42
4.2	Experimental methods	43
4.2.1	Expression and purification of 14-3-3 protein	43
4.2.2	Site directed mutagenesis of Nedd4-2	46
4.2.3	Expression and purification of Nedd4-2 protein variants	48
4.2.4	Mass spectrometry (MS)	50
4.2.5	Differential scanning fluorimetry (DSF)	51
4.2.6	Fluorescence Spectroscopy	52
4.2.7	Limited proteolysis	60
4.2.8	Chemical crosslinking coupled with mass spectrometry	61
4.2.9	Protein crystallography	63
5.	Results	66
5.1	Mutagenesis, expression, purification and labelling of recombinant proteins.	66
5.1.1	Site directed mutagenesis of Nedd4-2 protein	66
5.1.2	Expression and purification of Nedd4-2 ¹⁹⁰⁻⁵⁸¹ variant	68
5.1.3	Expression and purification of Nedd4-2 ¹⁸⁶⁻⁹⁷⁵ variants	69
5.1.4	Expression and purification of 14-3-3 protein	70
5.2	Assessing the protein stability by DSF	71
5.3	Labelling of recombinant proteins by 1,5-IAEDANS	72
5.4	Time-resolved fluorescence intensity and anisotropy decay measurements	73
5.4.1	Time-resolved emission polarization anisotropy measurements	75
5.4.2	Time-resolved fluorescence quenching experiments	77
5.5	Structural characterization of Nedd4-2 ¹⁸⁶⁻⁹⁷⁵ :14-3-3 η complex by chemical crosslinking coupled mass spectrometry (XL-MS)	79
5.6	Limited proteolysis - protection against proteolytic cleavage	81
5.7	Protein structure determination.	82
6.	Discussion	85
7.	Conclusion	89
8.	Literature	90
9.	Internet sources	107
10.	Published articles	108

10.1 Publication I	108
10.2 Publication II	151

1. Introduction

The presented research was carried out as a part of my PhD studies and was mostly conducted in the Laboratory of Structural Biology of Signaling Proteins of the Institute of Physiology, CAS (the detached workplace BIOCEV) under the supervision of RNDr. Veronika Obšilová, Ph.D. The laboratory has extensive experience in the study of interaction, regulation and function of signalling proteins, e.g. 14-3-3, Nedd4-2, etc. The present work focuses on the structural characterization of Nedd4-2 and its known partner 14-3-3 protein, thereby providing a mechanistic explanation of their function and regulation.

This dissertation aims to study the structural protein-protein interactions of human E3 ubiquitin ligase Nedd4-2 and 14-3-3 proteins. Nedd4-2 belongs to the family of Nedd4 HECT E3 ubiquitin ligases and is responsible for ubiquitylating its substrates (most of them membrane-related, in the form of ion channels or transporters). Because of an array of targets, the dysfunctionality of this ubiquitin ligase leads to the development of many pathological disorders. The role of Nedd4-2 in controlling/regulating the Na⁺ homeostasis by ubiquitylating the epithelial sodium channel (ENaC), and the development of Liddle syndrome in case of its impairment is well known. Moreover, previous studies have shown that the 14-3-3 dimer negatively regulates Nedd4-2 activity by binding to its phosphorylated serine residues, preventing it from interacting with its targets. However, the molecular mechanism behind this regulation remains largely elusive and is the subject of scientific scrutiny.

The understanding of Nedd4-2 interactions and its regulation within the ubiquitination system could serve as a basis for the development of novel therapeutic approaches. Our recent work has highlighted structural insights into the 14-3-3-dependent regulation of Nedd4-2, most likely by direct interaction and consequential conformational changes of this enzyme. Therefore, the objective of our work is to structurally characterize this interaction by using structural biology and biophysical techniques including fluorescence spectroscopy, protein crystallography, and structural mass spectrometry.

2. Theoretical Background

2.1 Post translational modifications

Proteins represent the most versatile building blocks available to living organisms and perform the reactions that allow the cell to carry out its function. Protein abundance is mainly regulated by gene transcription to mRNA and translation on ribosomes into proteins. Once the mRNA is translated into a protein, the cell utilizes posttranslational modifications (PTM) to diversify them by altering their activity and function. This generates an additional layer of protein complexity (see Fig. 2.1), which was necessary for the evolution of eukaryotic cells. This complexity allows the cells to go through a number of phases of the cell cycle, adapt to cellular changes, and collaborate to function. In general, protein behaviour and fate are modulated by post-translational modifications (PTM) (see Fig. 2.2)¹⁻⁵.

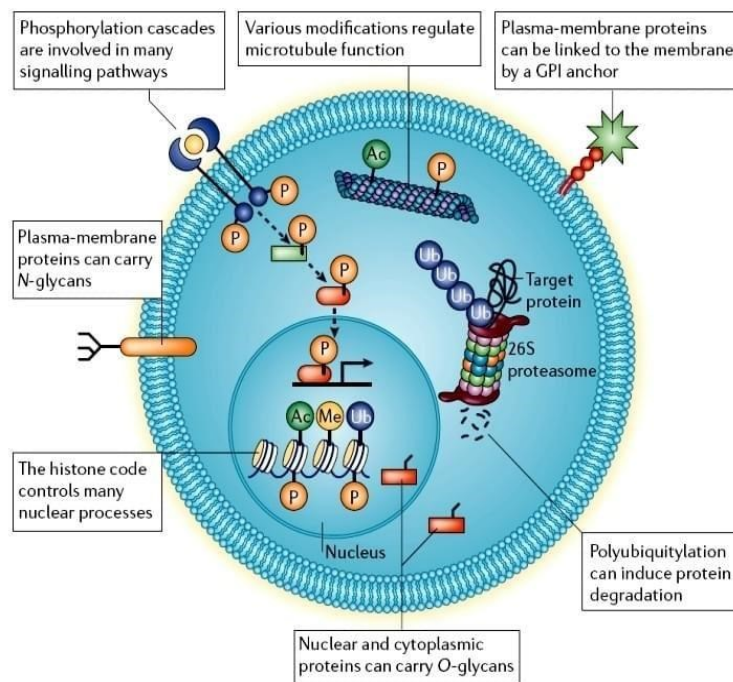


Figure 2.1: Types of post-translational modifications. Location and role of some of the most important post-translational modifications. Post-translational modifications are required for all types of proteins, altering the physicochemical properties of the proteins (Figure is taken from Jensen O. N, 2006)⁶.

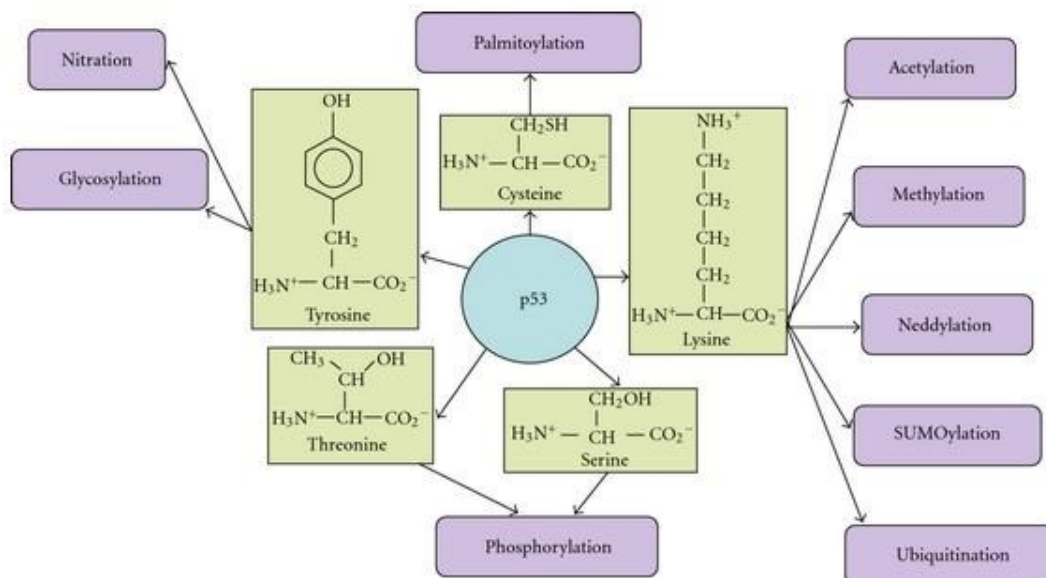


Figure 2.2: Post-translational modifications of p53, a tumour suppressor protein. The figure shows several posttranslational modifications that are commonly seen in p53 and have different functional consequences in both healthy and diseased conditions (Figure is taken from Karve TM, 2011)⁷.

2.2 Ubiquitination

Among all posttranslational modifications, ubiquitination is the most conserved, easily inducible and reversible modification, involved in cell signaling and cellular homeostasis^{8,9,22}. It is a widespread mechanism, regulating the functions of eukaryotic proteins by covalently attaching a small protein called ubiquitin (Ub) to a target protein¹⁰.

Ubiquitin was first discovered in 1977 as a small polypeptide bound to lysine residue of the histone protein¹¹. It is a highly conserved 8 kDa protein, named for its ubiquitous localization in all living cells, both prokaryotic and eukaryotic^{12,13}. In humans, RPS27A and UBA52 genes encode one molecule of ubiquitin attached with the ribosomal proteins S27a and L40, respectively. The UBB and UBC genes code for a polyubiquitin cassette. A number of ubiquitin conjugations with different structures and functions are produced by cells¹⁴.

During the ubiquitylation reaction, the Ub molecule is bind to its target by an amide bond between the C-terminal glycine residue's free carboxyl group of Ub and in the side-chain of a lysine residue's ϵ amino group in the target protein.¹⁵. This is a hierarchical enzymatic cascade

reaction which involves E1 (ubiquitin-activating), E2 (ubiquitin-conjugating), and E3 (ubiquitin ligase) enzymes¹⁶. Most of the time this designates the Ub-tagged protein for degradation by the proteasome, a large multi-subunit complex. Covalent attachment of Ub can lead to rapid changes: in a protein's half-life, in subcellular location, in assemblies to complexes, conformation, enzyme activity or other properties¹⁷. The way to reverse this attachment is done by deubiquitinating enzymes (DUBs), a group of enzymes connected to this process since they are responsible for removing Ub from its target proteins¹⁸.

Ubiquitin has seven lysine residues (namely K6, K11, K27, K29, K33, K48 and K63) and the backbone amino group of the N-terminal methionine (M) residues which can serve as ubiquitination sites, with the best characterized chains being K48 and K63 (Fig. 2.3A)¹⁹. Using the side-chains of these residues, several ubiquitin moieties are attached to each other and form polyubiquitin chains²⁰⁻²². Therefore, the target protein can be mono-, multi-, or poly-ubiquitinated. The number and pattern of ubiquitin molecules attached to the target protein may vary, and different patterns of ubiquitination may have different effects on the function of the target protein. For example, monoubiquitination of a protein can regulate its subcellular localization or interaction with other proteins, monoubiquitination at multiple sites is usually related to endocytosis, whereas the result of polyubiquitination depends on the lysine residue responsible for forming a chain (see Fig. 2.3B)^{23,24}.

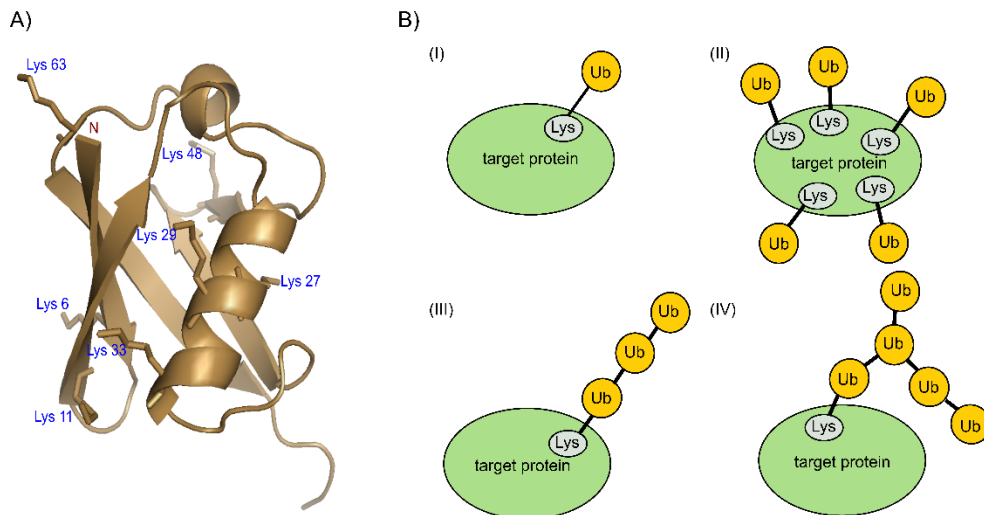


Figure 2.3: Ubiquitin structure and modes of protein ubiquitination. (A) The structure of ubiquitin proteins and the positions of their lysine residues (PDB: 1UBQ). (B) Protein fate is determined by the various types of ubiquitin labelling in ubiquitination (Figure is inspired from Ries, L, 2020)^{25,26}.

The difference in substrate fate is a consequence of distinct conformations, the relative arrangements the polymeric ubiquitin chains adopt and the specific effector proteins that recognise them. Particularly chains that leads to proteasomal degradation are linked via K11 or K48. However, the regulation of signalling complex assembly and protein sorting during autophagy and endocytosis is carried out by chains that are linked via M1 or K63^{27–30}.

The ubiquitin-binding domains (UBDs) of various ubiquitin-binding partners can discern the spatial relationships between ubiquitin subunits by varying the lengths of the gaps between ubiquitin-interacting motifs. In its entirety, the fate of the protein just depends on a specific lysine residue targeted for ubiquitination. Alternatively, the covalent attachment of lysine residues by Ub-like modifiers like neuronal precursor cell-expressed developmentally downregulated protein 8 (NEDD8) or small ubiquitin-like modifier (SUMO). These modifiers are structurally and biochemically very similar to Ub and rely on the sequential action of specific activating, conjugating, and ligating enzymes, just as Ub does (Fig. 2.4)^{31–34}.

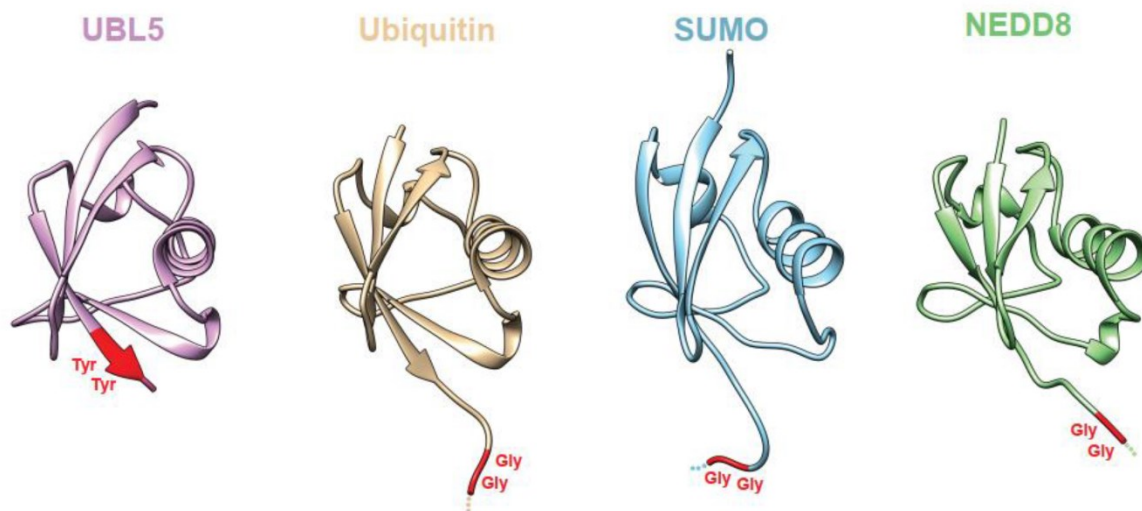


Figure 2.4: Structures of UBL5 (ubiquitin like protein 5) with other ubiquitin family members. The available structure of UBL5 (PDB ID: 4PYU), ubiquitin structure (PDB ID: 1UBQ), SUMO-3 structure (PDB ID: 1U4A), and NEDD8 structure (PDB ID: 2N7K) (Figure is taken from Chanarat S. 2021)³⁴.

In summary, ubiquitination regulates protein activity by promoting protein-protein interactions and altering protein conformation. Defects in ubiquitin pathways are associated with numerous diseases, including cancer, neurodegenerative disorders, and viral infections³⁵.

2.2.1 Ubiquitination cascade

Ubiquitination is the coordinated action of three distinct enzymes: E1 (activating), E2 (conjugating) and E3 (ligase) acting in a sequential manner. The E1 enzyme adenylylates the C-terminus of ubiquitin using ATP in order to activate it. Once activated, the Ub molecule covalently attaches to the side chain of a cysteine residue in the E1 enzyme via thioester bond¹⁶ (Fig. 2.5). Following its transfer to the E2 enzyme, Ub is subsequently attached to intended target substrate by the E3 enzyme³⁶⁻³⁸.

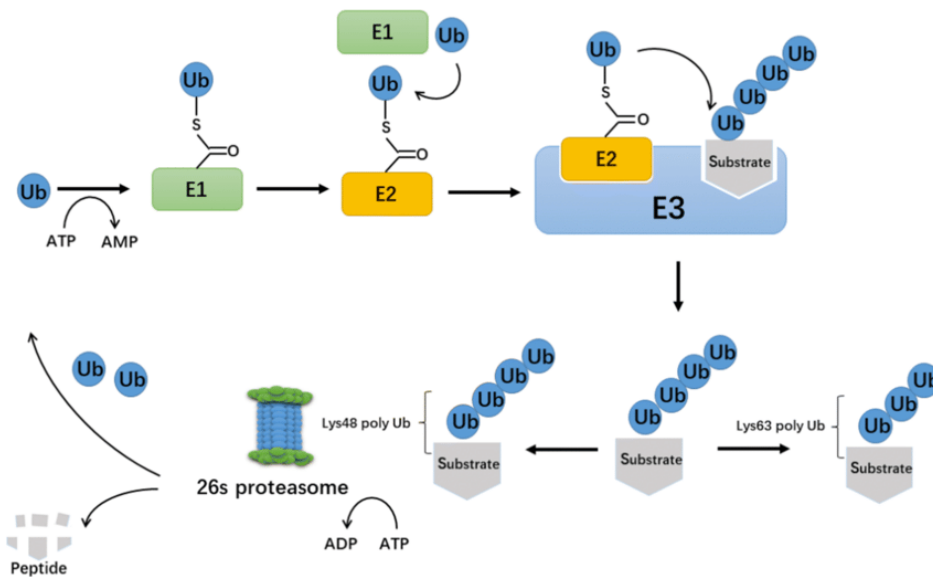


Figure 2.5: Schematic diagram of ubiquitination cascade. Ubiquitin molecule is activated and bound to the E1 enzyme and subsequently transferred to the E2 enzyme. Last step is the E3 ubiquitin ligase which catalyses the covalent attachment of the ubiquitin to the target protein and often generates a polyubiquitin chain (Figure is taken from Gong, X. *et al*, 2020)³⁸.

Some of the ubiquitin labelled substrates are recognized and broken down by the 26S proteasomes³⁹ (Fig. 2.5). This approximately 2.5 MDa in size, macromolecular complex is ubiquitous in all eukaryotes, archaea, and bacteria. It consists of one 20S subunit and two 19S subunits. The 19S subunits are located on both sides of the 20S subunit and with their ubiquitin-binding motifs are able to identify the tagged substrate and, in an ATP-dependent process, unfold it⁴⁰. The unfolded substrate proteins enter the hollow 20S subunit. Inside, there are protease active sites, responsible for breaking down the substrate first into small peptides and later into individual amino acids, which are recycled during new protein synthesis.

Deubiquitinating enzymes (DUBs) are also a part of this ubiquitination cascade. They are substrate-specific enzymes that regulate the activity of E3 ligases by cleaving ubiquitin chains attached to substrates and decomposing them into individual ubiquitin moieties, which can be recycled and reused in another ubiquitination cycles⁴¹.

2.2.2 E1 - Ubiquitin-activating enzyme

E1 is the first enzyme of the ubiquitination cascade. There are eight different activation enzymes identified in humans, and each of these enzymes has unique preferences within different UBLs⁴². For example, the human E1 enzyme known as Uba1 is a monomeric, multidomain protein that is about 110 kDa and associated with the NEDD8 pathway⁴³⁻⁴⁵.

The first step in the ATP-dependent activation of ubiquitin is the cleavage of ATP to create a covalent bond between AMP and the C-terminal glycine of ubiquitin (adenylation), which requires the presence of Mg²⁺ ions. The second step involves the transfer and binding of the C-terminus of the adenylated ubiquitin to the conserved catalytic cysteine of Uba1, which then forms a thioester bond and leads to the release AMP. Subsequently, the second ubiquitin is adenylated and the first ubiquitin is transferred from the catalytic Cys to the E2 enzyme^{16, 46}.

2.2.3 E2 - Ubiquitin-conjugating enzyme

E2 conjugation enzymes play the role between the activating enzyme E1 and the ubiquitin ligase E3. The human genome encodes approximately 40 E2 enzymes, which are divided into 17 different subfamilies based on genetic analysis⁴⁷. All of them display a significant amount of conservation, specifically regarding the 3D structure of the central catalytic domain.

The central catalytic domain of the E2 enzyme contains a catalytic Cys that accepts activated ubiquitin from the catalytic Cys of the E1 enzyme. Next step is related to the binding of E2 to E3 via the E3 binding domain, during which the activated ubiquitin is transferred from E2 to the substrate or to the E3 catalytic Cys in the case of HECT E3 ligases⁴⁸.

Structural difference determines the overall function of E2s as well as the specificity for different E1, UBL and E3⁴⁹. Some E2s are only involved in monoubiquitination, whilst others can be also in polyubiquitination⁵⁰⁻⁵².

2.2.4 E3 - Ubiquitin ligase

The E3 ubiquitin ligases are highly abundant and diverse as they are responsible for providing specificity in the ubiquitination cascade by targeting certain proteins^{53–55}. As a consequence, numerous physiological functions (to name a few: immunological responses, cell division, apoptosis, cell cycles) are affected by their activity and any irregularity can cause the development of pathological conditions. Therefore, it is a good strategy to try to develop novel therapeutic discoveries, which could regulate the activity of these enzymes^{56,57}.

Depending on the process through, they transfer ubiquitin molecules, E3 ubiquitin ligases are classified in three groups: RING, HECT and RBR (Fig. 2.6).

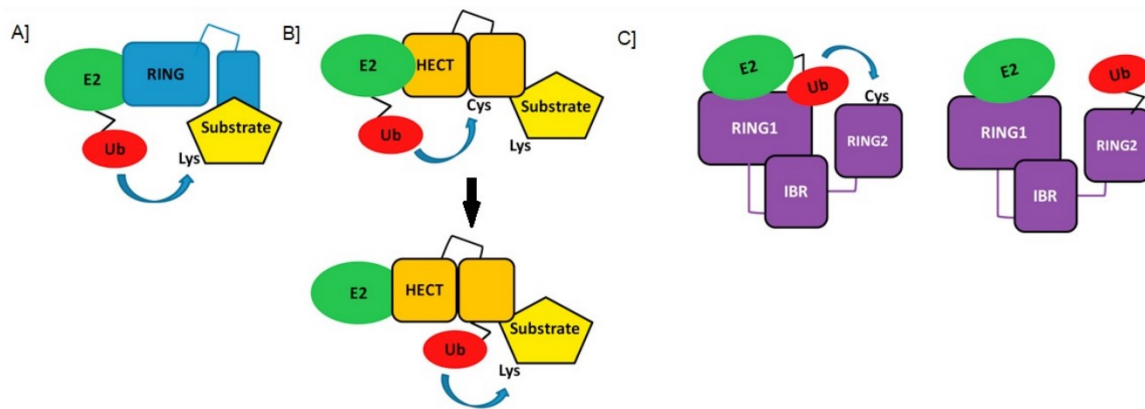


Figure 2.6: Scheme of the mechanism of activity of different E3 ubiquitin ligases. (A) RING E3 ligase acts as a scaffold for the ubiquitin-conjugating enzyme and the substrate, thereby allowing the indirect transfer of ubiquitin. (B) The HECT E3 ligase first accept the ubiquitin on their catalytic Cysteine from the E2 enzyme and then they transfer it to the bound substrate. (C) RBR ubiquitin ligases are a mixture of the previous two groups – RING1 domain binds E2, but the ubiquitin molecule is only transferred to the RING2 domain and later to the substrate (Figure was taken and modified from Wenzel, D. M. 2012)⁵⁷.

A) The RING (Really Interesting New Gene) ligases

RING ligases, also known as RING-finger ligases, are a class of E3 ubiquitin ligases, which are responsible for transferring ubiquitin from an E2 enzyme to the target protein^{58–60}. RING ligases are characterized by the presence of a specific protein domain known as the RING finger domain, which is essential for their E3 ligase activity. The mechanism of RING ligases involves

bringing the E2 enzyme and the substrate into close proximity, allowing the ubiquitin transfer. Unlike other E3 ligases, RING ligases do not transfer ubiquitin directly to the target protein. Instead, they act as scaffolds or adapters that bring the E2 and the substrate protein into close proximity, facilitating the transfer of ubiquitin from E2 to the substrate. RING ligases are highly specific and determine which target proteins will be tagged by ubiquitin for degradation by recognizing sequence motifs or structural features within them. They can also facilitate the addition of multiple ubiquitin molecules, resulting in the formation of polyubiquitin chains^{36,60,61}.

RING ligases are critical for maintaining cellular homeostasis by regulating the levels of specific proteins involved in cellular processes, including cell cycle regulation, DNA repair, signal transduction, and stress response. Dysregulation of RING ligases has been associated with a variety of diseases, including neurodegenerative disorders and cancer, making them important targets for research and potential therapeutic interventions. Well-known examples are MDM2 (Mouse double minute 2), Cbl (Casitas B-lineage Lymphoma) or BRCA1 (Breast Cancer 1)^{51, 62-64}.

B) HECT (Homologous to E6-associated protein carboxyl terminus) ligases

HECT ligases are an additional family of E3 enzymes involved in the process of ubiquitination. Unlike other classes of E3 ligases, they form a thioester intermediate with ubiquitin before transferring it to the target protein. First step is recruiting ubiquitin from the E2 enzyme with their catalytic cysteine, which causes the formation of the ubiquitin-thioester intermediate followed by the transfers of the ubiquitin molecule from its own cysteine residue to the lysine residue of the target protein, thereby forming an isopeptide bond. HECT ligases play essential roles in regulation of several cellular processes, including protein endocytosis, DNA repair, and cell signaling pathways. Since HECT ligases play a crucial role in maintaining the cellular homeostasis, any mutations or their dysregulation lead to the development of different pathophysiological conditions^{9,63-66}.

The HECT ligase family includes several members, each with its unique substrate specificity and biological functions. Well-known HECT ligases include E6-AP (E6-associated protein) which is best known for its role in the ubiquitination and degradation, as well as its association with human papillomavirus (HPV) E6 protein. Another member of the HECT family, NEDD4

(Neural Precursor Cell Expressed Developmentally Down-regulated 4) regulates a variety of cellular functions, such as cell proliferation, ion channel regulation, and endocytosis. It is known to interact with a wide range of substrates, including membrane proteins like the Epidermal Growth Factor Receptor (EGFR)⁶⁷⁻⁷⁰.

C) RBR (Ring-Between-Ring E3) ubiquitin ligases

RBR E3 ubiquitin ligases are the final subclass of E3 ubiquitin ligases that are mostly known for their crucial role in the ubiquitin-proteasome pathway. RBR E3 ubiquitin ligases are unique because they combine the properties of both RING-type and the HECT-type E3 ligases. RBR has a RING finger domain followed by an in-between-RING (IBR) and a RING2 domain. The RING1 domain in RBR E3 ligases is responsible for binding to the E2 ubiquitin-conjugating enzyme and facilitates the transfer of ubiquitin from the E2 enzyme to the RING2 domain. This step is crucial in the ubiquitination process. The IBR domain acts as a linker between the RING1 and RING2 domains and plays a role in regulating the overall conformation and activity of RBR E3 ligases. The RING2 domain is responsible for the final transfer of ubiquitin from the RBR E3 ligase to the target protein. It functions similarly to the RING domain found in other types of E3 ligases. This combination allows them to function as both a scaffold for the ubiquitin-conjugating enzyme (E2) and as a catalytic domain for the transfer of ubiquitin from the E2 enzyme to the target protein. This arrangement distinguishes them from other types of E3 ligases, such as the RING finger E3 ligases and the HECT E3 ligases^{51,65,71}.

The RBR E3 ubiquitin ligases are also involved in various cellular processes, including regulation of signal transduction pathways, the regulation of protein stability and turnover, and the immune response. Alterations or irregularities in RBR E3 ligases can result in a range of health conditions. Well-known examples of RBR ligases are Parkin, human homolog of Ariadne (HHARI) and HOIL-1L interacting protein (HOIP), which are mostly studied^{72,73}.

2.3 Nedd4 family

Nedd4 (Neuronal precursor cell-expressed developmentally downregulated 4) family of HECT E3 ubiquitin ligases is a large part of this class and plays a crucial role in the ubiquitination of various, mostly membrane, targets⁷⁴. The human genome contains 28 distinct putative HECT domain proteins, and there are nine members of the Nedd4 family in mammals (See Fig.

2.7)^{67,75,76}. By polyubiquitination, they mainly regulate cellular trafficking while monoubiquitination mostly causes endocytosis.

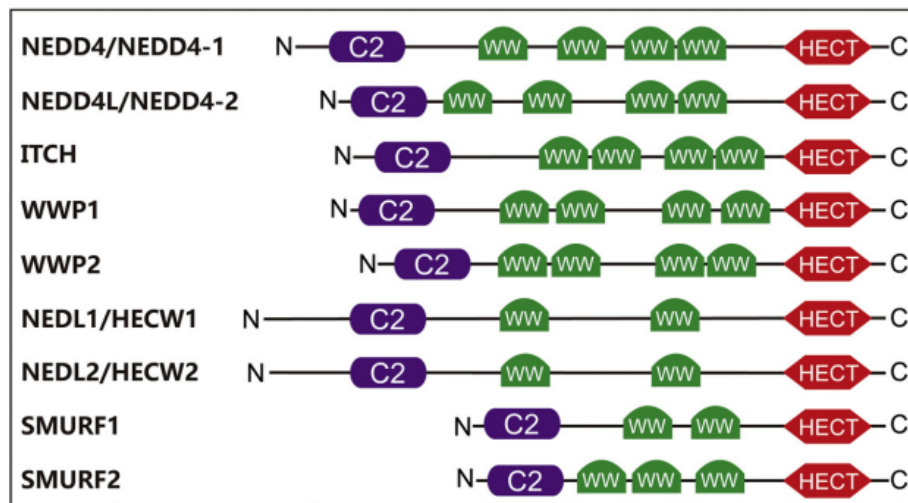


Figure 2.7: Domain architecture of human Nedd4 family ubiquitin ligases. All members contain three distinct domains: membrane binding C2 domain, WW domains (2-4) and the catalytic bilobed HECT domain (Figure is taken from Zou, X. 2015)⁷⁶.

2.3.1 Domain Architecture

The Nedd4 family typically contains one N-terminal Ca^{2+} -dependent C2 domain, two to four WW domains and a C-terminal catalytic HECT domain (Fig. 2.7, Fig. 2.8).

The C2 domain has rod-like, eight-stranded β -sandwich structure. It mainly binds phospholipids such as phosphatidylcholine, phosphatidylserine, and phosphatidylinositol^{77,78}. By interacting with membranes, it controls the intracellular localization of the enzyme and positions it closer to its substrates. This domain can be divided based on its ability to bind calcium ions. Group that doesn't interact with these ions, contains a positively charged patch in their variable loop region.

WW domains, named after their two conserved tryptophan residues, is the smallest known protein domain (only 35 amino acids). It consists of three anti-parallel β -sheets. Conserved phenomenon is that one N-terminal residue forms hydrophobic interactions with a C-terminal proline of their substrates⁷⁹. These domains are further divided by the specific primary sequence of the motif they recognize^{80,81}.

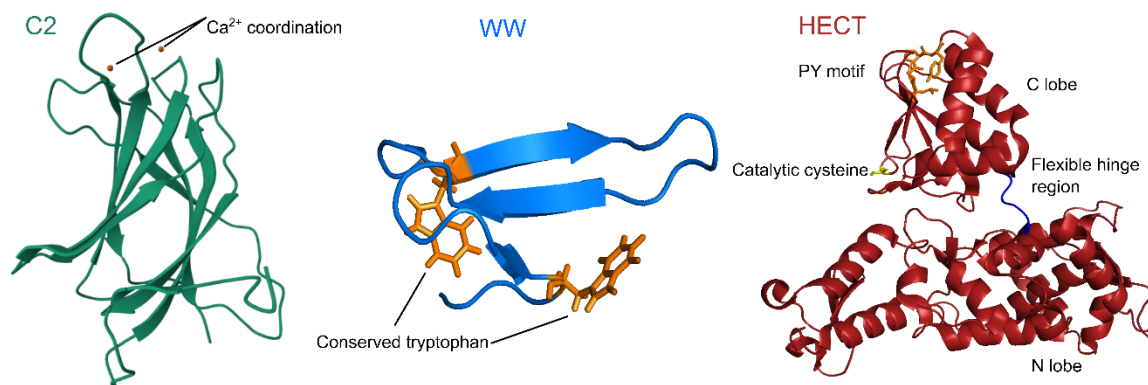


Figure 2.8: Schematic diagram of Nedd4 ubiquitin ligase domains. Three domains typical for Nedd4 family are shown, C2 domain structure (2NSQ) with calcium coordination sites, WW domain structure (2MPT) in blue with side chain of tryptophan and the of HECT domain crystal structure (3JW0) with C-lobe and N-lobe connected by flexible loop, PY motif and position of catalytic cysteine (Pymol was used to create the figure (<https://pymol.org/>)).

HECT is the largest domain responsible for the catalytic transfer of ubiquitin molecule to target substrates. The HECT domain contains two subdomains, the N-lobe and C-lobe, which are interconnected by a flexible loop. The catalytically conserved cysteine residue is found on the C-lobe of the HECT, while the E2 enzymes (with ubiquitin) bind to the N-lobe. Through detailed structural studies, it has been shown that the flexible loop allows structural rearrangements of these subdomains, facilitating the positioning of the catalytic residue closer to the E2 enzyme^{82, 83}. The C-lobe of the HECT domains of this family of ligases contains a conserved I/LPPY motif, which exhibits a slight deviation from the PPxY sequence found in the typical PY motif. Nevertheless, it was found that this modified motif still interacts with WW domains when the ligase is in an inactive state⁸⁴.

2.3.2 Function and regulation

The Nedd4 family targets a variety of tumour suppressors and transmembrane receptors (Fig. 2.9). Human cancers and immunological disorders have been associated with genetic defects and changes in substrate expression levels^{85, 86}. Therefore, maintaining cellular homeostasis requires precise control over these ligases' catalytic activity, substrate selectivity, and cellular localization. The regulations at different levels are executed by PTMs. Moreover, these ligases possess the ability to control their own expression through auto-ubiquitination, enabling them

to adjust their abundance during distinct stages of the cell cycle and differentiation⁸⁷⁻⁸⁹. The nine human members of HECT family (with the exception of Nedd4-2, which would be discussed in detail later) with their substrates, roles and some of their representative mechanisms of regulation are:

- a) ITCH - The main substrates of Itch ubiquitin ligase are T-cell differentiation factors. Malfunctions in Itch regulation causes itchy phenotype in mice that result in persistent skin irritation and multi-system inflammation⁹⁰. Binding of the HECT domain to the central region of this enzyme causes it to be in a closed conformation which can be released either by phosphorylation of the proline-rich region (PRR, near the WW1 domain) by JNK-1 or by binding to adaptor proteins Ndfip1/2 (Nedd4 family-interacting proteins 1 and 2)⁹¹⁻⁹³.
- b) Smurf - Smurf1 and Smurf2 are known for function in tagging R-Smads (1/5/8 and 2/3, respectively) and I-Smads (6/7) with ubiquitin. These proteins play a key role in the BMP and TGF- β signalling pathways.⁹⁴⁻⁹⁵. Smad7 plays a crucial role in assembly of Smurf2, which forms a strong complex with TGF- β receptors before being ubiquitinated in the lysosome⁹⁶. The ability of Smurf1 to recognize substrates is enhanced by the adaptor protein CKIP-1 (Casein Kinase 2-interacting protein 1), while phosphorylation by PKA alters the substrate selections of this ligase⁹⁷⁻⁹⁸.
- c) WWP1 and WWP2 are known regulator of TGF- β signalling. While WWP2 targets Smad2/3 and Smad7, WWP1 targets the TGF- β receptor using Smad7 as a scaffold⁹⁹⁻¹⁰⁰. Furthermore, while WWP2 targets PTEN, a well-known tumour suppressor that is commonly altered in a variety of cancers, WWP1 targets LATS1 in the Hippo/LATS tumour suppressor-signalling pathway, which controls organ growth. There are several isoforms of both ligases, and they all have different substrate specificities¹⁰⁰⁻¹⁰³.
- d) NEDL1 and NEDL2 is responsible for the stability of two tumour suppressors' p53 and p73. In addition, NEDL1 targets DVL1 (Disheveled-1), which is a key regulator of cell proliferation and neuroblast specification^{97, 104-105}.
- e) Nedd4-1, or Nedd4, plays a direct role in regulating the IGF-1 (insulin-like growth factor-1) signaling pathway. Additionally, it is involved in the reduction of PTEN (Phosphatase and tensin homolog deleted on chromosome 10) levels. The closed conformation mediated by

C2-HECT interactions (Inactive state), can be reversed and activated by the binding of Ca^{2+} ions and/or NDFIP1/2¹⁰⁶⁻¹⁰⁹.

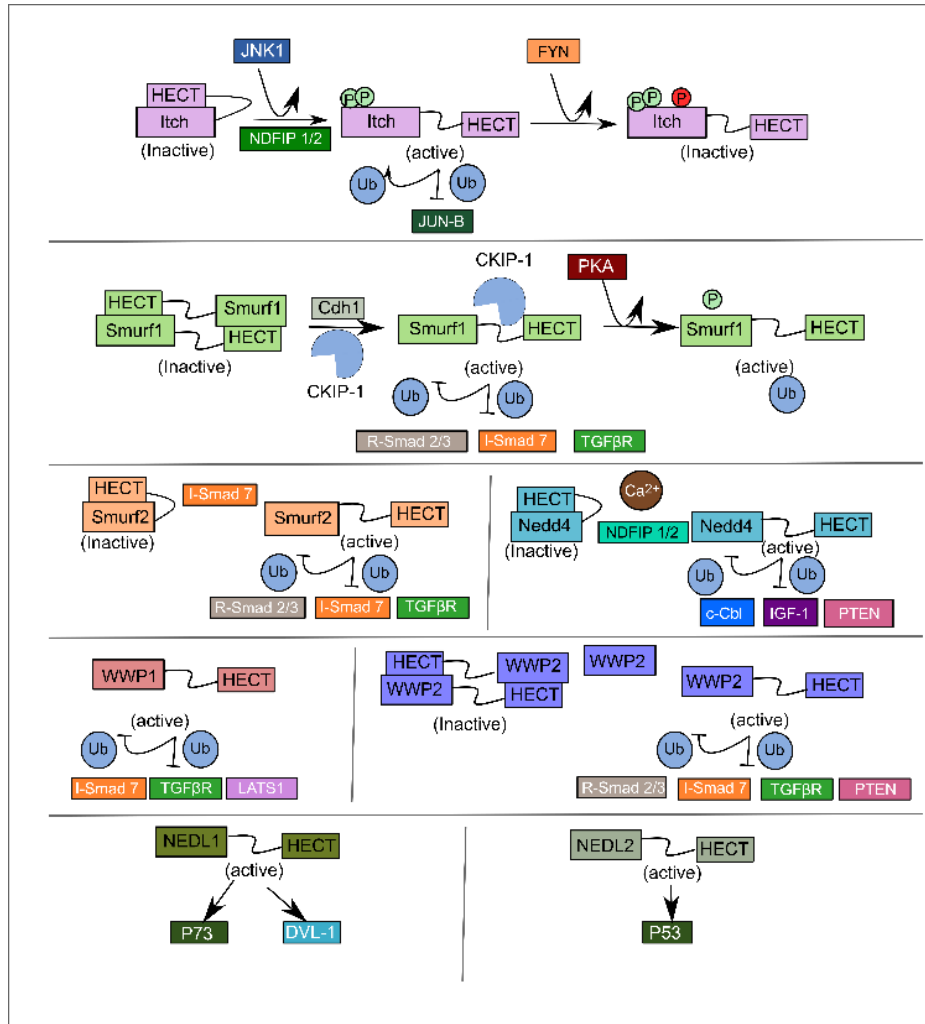


Figure 2.9: The roles and regulatory mechanisms of Nedd4 family of E3 Ubiquitin Ligase
Schematic representations of the principal targets and regulatory mechanisms of each Nedd4 ligase (Figure is inspired from Zou, X, 2015 and Escobedo, 2014)⁷⁶.

2.4 Nedd4-2 or Nedd4L

Nedd4-2 is encoded by, a single gene spanning more than 400 kb and containing over 40 exons. However, only eight different isoforms of Nedd4-2 were detected in cells so far^{110,111}.

Nedd4L (or Nedd4-2) ubiquitinates downstream target molecules such as membrane proteins, transporters, ion channels, including ENaC and hERG^{112, 113}. ENaC is essential for epithelial homeostasis as it maintains sodium ion reabsorption in the kidneys, lungs, and large intestine intact. The cytoplasmic PPxY motif mutations found in ENaC have been shown to cause Liddle syndrome (hypertension)¹¹⁴⁻¹¹⁶. For example, Nedd4L has been associated with cystic fibrosis where it targets the CFTR- Δ F508 variant; its downregulation induces overexpression of ENaC (Fig. 2.10). Treating the CFTR- Δ F508 mutation with the glucocorticoid dexamethasone induces the SGK1 (serum/glucocorticoid-induced kinase 1) activation. This activation leads to the downregulation of Nedd4L, consequently restoring the typical levels of CFTR and ENaC in the plasma membrane¹¹³.

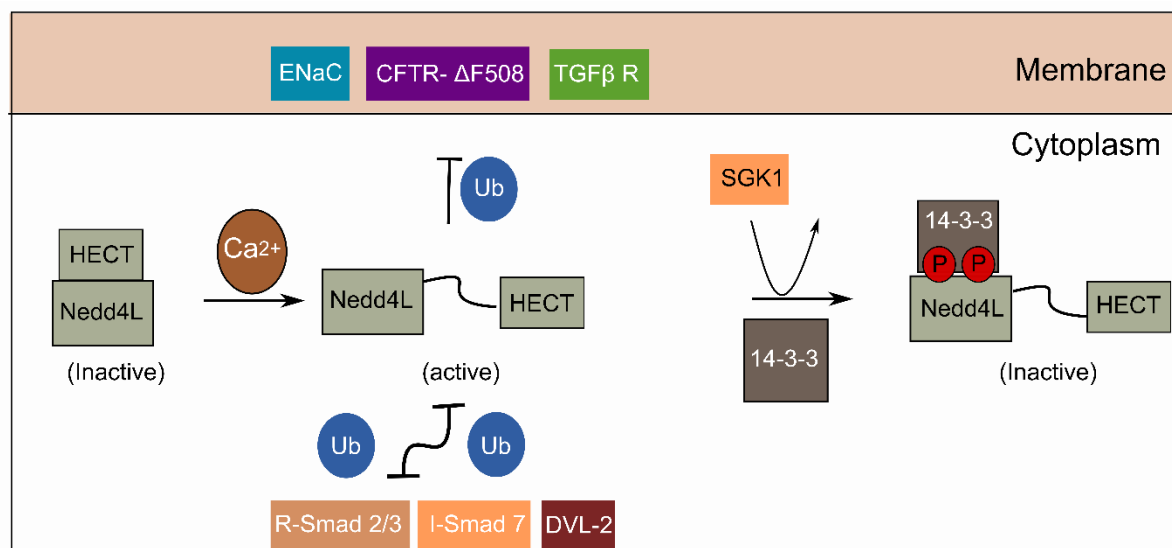


Figure 2.10: Nedd4-2L functions and regulation. In inactive conformation, C2 and HECT domains are associated in contacts. Once calcium ions are detected by C2 domains, the ligase gets activated and moves to target membrane proteins including the TGF- β cytokine receptor). Active ligase targets Smad proteins in the cytoplasm, where it undergoes auto ubiquitination. The Nedd4L ligase is phosphorylated by SGK-1, which causes 14-3-3 binding and ligase inactivation (Figure is adapted from Albesa M. 2011)¹¹².

Nedd4L is regulated at different levels, one of which is phosphorylation by SGK1, PKA and Akt kinases at position S342, T367 and S448 (linker regions surrounding WW domains) which is accompanied by the subsequent binding of the accessory protein, 14-3-3, which downregulates the activity of this ligase^{117,118}. Additional mechanism of regulation, not only specific to this Nedd4 ubiquitin ligase, is a form of auto inhibition caused by the binding of

HECT and C2 domain¹⁰⁹. It is a question whether or not WW domains also partake in this intramolecular binding, as this enzyme contains a partially buried LPxY motif in the HECT C-lobe structures. However, this additional interaction would require prior unfolding of the HECT domain⁸⁴. In total, the autoinhibition state is released by Ca²⁺, which additionally causes translocation of Nedd4L from the cytoplasm to different intracellular membranes (C2 binding to specific phospholipids)¹¹¹. Nedd4L also undergoes auto-ubiquitination, which labels it for proteasomal degradation.

2.4.1 Regulations

Regulation of Nedd4-2 by post-translational modifications has been studied in depth in kidney cells and it was demonstrated that phosphorylation plays a large part in it (Fig. 2.11). The hormone vasopressin triggers adenylate cyclase, whereas aldosterone induces SGK1 transcription; this results in an elevation of cAMP and PKA (protein kinase A) activation¹¹⁹. Both of these kinases phosphorylate and bind to three distinct sites on the consensus sequence RxRxx(S/T) i.e. S348, T367 and S342 of Nedd4-2. This phosphorylation induces subsequent binding of the 14-3-3 protein, which inhibits Nedd4-2 activity and decreases its capacity to bind to and ubiquitinates ENaC^{115,120}. This is proof that this consensus sequence is a convergent point for different regulatory pathways.

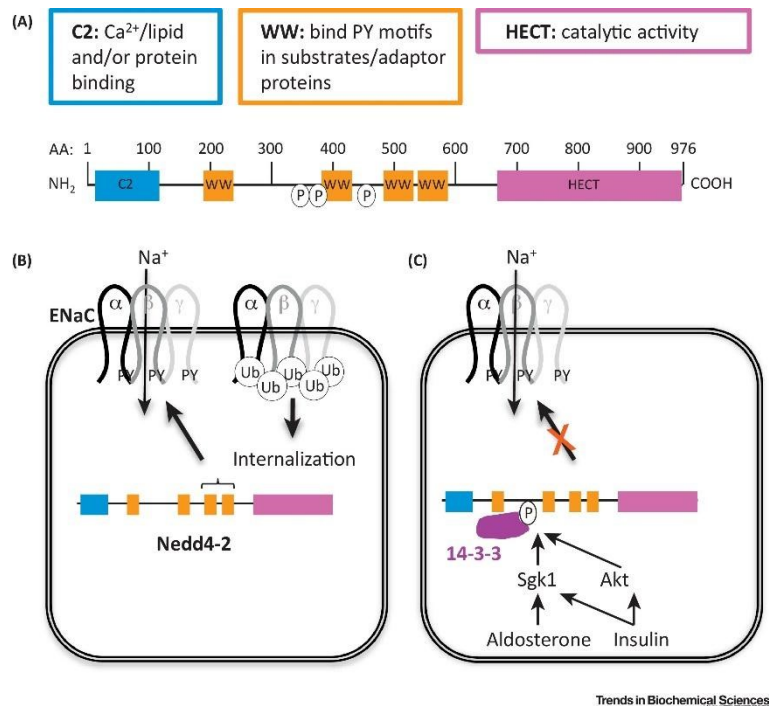


Figure 2.11: Nedd4-2 domains and its regulation in epithelial sodium channel A) Nedd4-2 contained calcium dependent C2 domain, WW domains that helps in interaction with target proteins, and catalytic C terminal HECT domain. B) Sodium channel associated with epithelial cell membrane, ubiquitinated by Nedd4-2. C) The phosphorylation of Nedd4-2 by SGK1 and AKT and subsequent 14-3-3 binding result in its downregulation. (Figure taken from Manning et.al, 2018)¹²⁰.

2.4.2 Disorders

As Nedd4-2 regulates a number ion channels, transporters, and signalling pathways, its dysregulation causes severe diseases.

- Respiratory distress – Nedd4-2 deficiency and disturbance in its ENaC regulation leads respiratory distress and other respiratory diseases¹²¹.
- Hypertension – Nedd4-2 controls blood pressure by maintaining Na⁺ homeostasis. Nedd4-2 cause increased ENaC expression and hypertension^{122,123}.
- Kidney diseases – deficiency of Nedd4-2 cause cystic fibrosis; also affect ENaC activity responsible for kidney diseases.

- Epilepsy - Nedd4-2 controls Na⁺ voltage channels to regulate pain sensitivity and neuronal excitability. Deficiency of Nedd4-2 shows behavioural changes and is associated with disruption of nervous system^{124–126}.

2.5 14-3-3 family

The 14-3-3 protein belongs to a family of conserved regulatory acidic molecules, ubiquitously present in all eukaryotic organisms. It was discovered in 1967 by Moore and Perez in the bovine brain extract. 14-3-3 proteins were found in the 14th fraction of the DEAE-cellulose column and at position 3.3 on a starch electrophoresis gel in samples of bovine brain¹²⁷. This family of proteins is responsible for regulating the activity of many others by acting as a scaffold, providing stability, controlling protein localization, promoting protein-protein interactions and controlling signal transduction. One mechanism of regulation studied in depth is binding to phosphorylated serine/threonine containing motifs, as is the case of human Nedd4-2 (as mentioned before).

Given their involvement in several signalling pathways, any malfunction in their activity leads to several pathological conditions. A better understanding of the mechanism can help in providing therapeutic approaches against a variety of pathological conditions.

2.5.1 Isoforms

There are multiple 14-3-3s isoforms of express in different organisms. Until now, seven of them (β , γ , ϵ , ζ , η , σ , τ) have been identified in mammals, ten in plant cells and two yeast and drosophila cells^{126–130}. They exclusively form dimers (homo- or heterodimers) with each protomers being a ~30 kDa curved L-shaped protein composed of nine α -helices^{131–134}. Specific feature of these dimers is the U-shaped central groove, a consequence of the diagonal symmetry of protomers known to attach to hundreds of intracellular binding partners (enzymes, metabolic intermediates, endosomal trafficking components, regulators of cytoskeletal filaments, membrane receptors, effectors of small GTPase, components necessary for DNA replication, transcription and translation)^{135–143}. All known isoforms show high sequence similarity, but each has different binding specificities and different targets. In contrast to the other areas in 14-3-3, which display more variations, residues surrounding the groove exhibit high conservation across evolution and isoforms^{144–146}.

2.5.2 Structure

All seven human 14-3-3 isoforms crystal structures have already been solved¹⁴⁷⁻¹⁴⁹. It is apparent all of them possess a dimeric nature with a high helical content (Fig. 2.12). As mentioned before, each monomer is a rigid structure of nine α -helices and a single phosphopeptides binding site. The dimer molecule contains a twofold symmetry and by shape resembles a cup. Helices (H3, H5, H7 and H9) form a central channel with highly conserved amino acids responsible for the binding of ligands.

Because of their specific domain structure, 14-3-3 proteins are presumed to have evolved from tetratricopeptide repeat (TPR) proteins^{150,151}. The TPR motif, which consists of 34 amino acids and is found in 3–16 tandem arrays, is recognised for its ability to form scaffolds that promote protein-protein interactions, similar to the function of 14-3-3¹⁵² (Fig. 2.12). However, 14-3-3 protein's scaffolding is highly dependent on their dimeric form stabilized at the interface of protomers by a variety of electrostatic and hydrophobic interactions¹⁵³.

By comparing these isoforms, most structural differences would be linked to the interface of two protomers. First consequence of this are the variations in the ability to form additional weak interactions responsible for stabilizing this region, as was first reported in the case of 14-3-3 ζ ¹⁵⁴. For example, the number of salt bridges differs in stabilizing 14-3-3 homodimers (one in 14-3-3 ϵ , two in 14-3-3 γ and η , and three in 14-3-3 β , ζ , σ and τ)¹³⁴. Second, it causes different monomeric isoforms to show preference for creating homo- or heterodimers¹⁵⁵. 14-3-3 σ forms exclusively homodimers. Along with five other isoforms, 14-3-3 ζ forms both homodimers and heterodimers; however, 14-3-3 ϵ preferentially forms heterodimers stabilised by several salt bridges^{149,156}. Third, all of this creates different binding affinities of specific target molecules towards specific homo- or heterodimer combinations. This is the case for 14-3-3 β/ϵ heterodimer an aldosterone-stimulated regulator of the epithelial sodium channel (ENaC)¹⁵⁷, and also the 14-3-3 ζ/τ heterodimer responsible for regulating the activity of Slingshot phosphatase in keratinocytes¹⁵⁸. It is also necessary to mention that the complexity of the whole system increases with the number of 14-3-3 binding partners and the number of 14-3-3 binding sites in each of them.

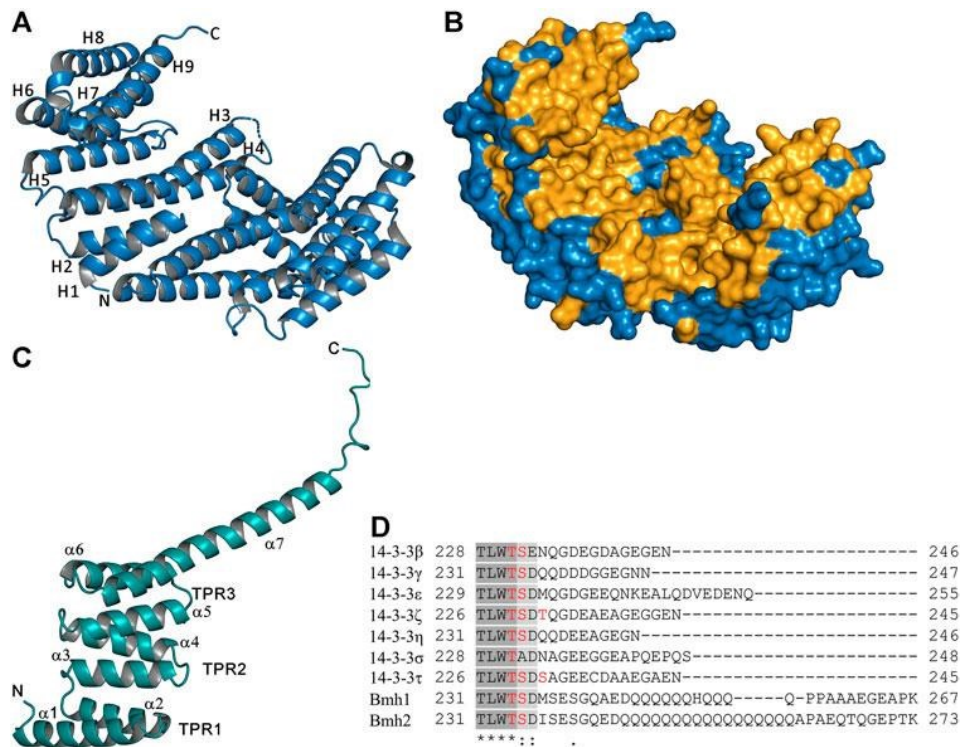


Figure 2.12: Crystal structures and sequence alignment of 14-3-3 proteins. (A) The human 14-3-3 protein isoform ζ (PDB ID: 1QJB)¹⁵⁹, and (B) its surface representation. (C) The TPR domain of PP5 (TPR motifs and α -helices visible, PDB ID: 1A17)¹⁵². (D) Sequence alignment of the C-terminal region (with the marked conserved domain) of different 14-3-3 proteins (seven human: β , γ , ϵ , ζ , η , σ , τ and two yeast: Bmh1 and Bmh2¹⁴⁰). (Figure is taken from Obsilova V. 2022)¹⁷³.

2.5.3 Motifs

The 14-3-3 family of proteins have mostly been described to interact with partners preferentially containing either a phosphoserine or a phosphothreonine amino acid, but the non-phosphorylated motifs have been also described (Fig. 2.13)¹⁴⁴.

The following three phosphorylation motifs recognized by 14-3-3 protein are listed in the order of most to least likely to occur in substrates: R [S/ Φ][+](pS/ pT)XP, RX [Φ /S][+](pS/pT)XP and pS/pTX₁₋₂-COOH (where pS/pT= phosphoserine or phosphothreonine, Φ is an aromatic residue, + is a basic residue, and X is any type of residue)¹⁵⁹⁻¹⁶¹. Conserved 14-3-3 residues responsible for interacting with these motifs are located in helices H3 and H5 (numbering based on the human ζ isoform: Lys49, Arg56, Arg127 and Tyr128). They form a positively charged area within the amphipathic ligand-binding groove. Additionally, conserved residues Asn173 and Asn224 interact with the phosphopeptides backbone and in synergy with the hydrophobic

patch fix these peptides in an extended conformation. Still, in concordance with many crystal structures solved between 14-3-3 proteins and synthetic phosphopeptides, it is known that this binding does not significantly alter the structure of the dimer (Fig. 2.12)^{118,149,159-165}. Taking into account only the sheer variety of 14-3-3 substrates, it would be difficult to assume all of them could contain one of these three phosphorylated binding motifs¹⁶⁶.

2.5.4 Non-phosphorylated motifs

Some of the most notable examples of alternative binding motifs are in the case of *Pseudomonas aeruginosa* exoenzyme S (ExoS) that use their LDLA-box motif to form hydrophobic interactions with the groove^{163,167,168}. Another example is the R18 peptide (derived from the phage display library¹⁶⁹) whose binding is mediated through its WLDLE motif, which recognizes the same conserved basic residues located in the ligand-binding groove as phosphorylated motifs do¹⁷⁰. Finally, proteins that have the O-linked β -N-acetylglucosamine (O-GlcNAc) moiety (Fig. 2.13), a consequence of the common reversible PTM of threonine and serine residues in cytoplasmic and nuclear proteins¹⁷¹. Position of this moiety within the binding domain is same as with the WLDLE motif. However, the nature of this modification suggests an interesting topic of study of the likelihood of crosstalk between the O-phosphate and O-GlcNAc signalling pathways.

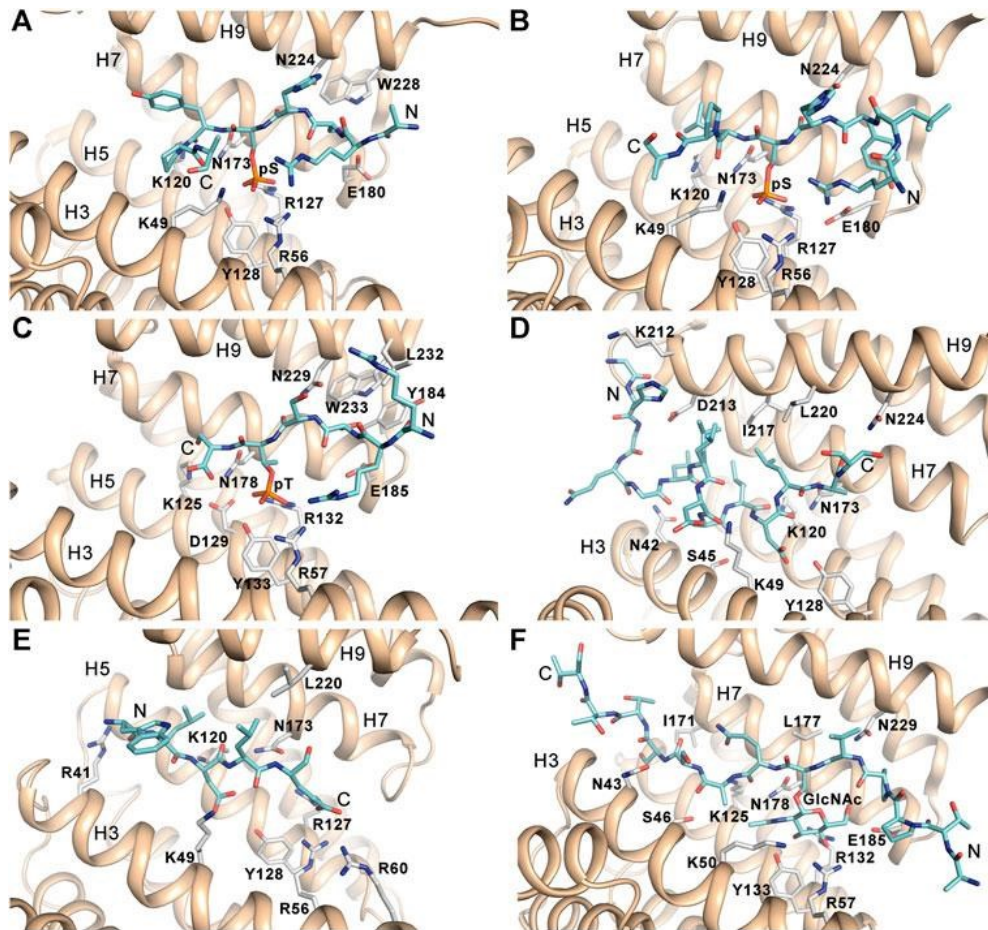


Figure 2.13: 14-3-3 binding motifs. Three canonical phospho-motifs (A-C): (A) R [S/Φ][+](pS/ pT)XP (PDB:1QJB), (B) RX [Φ/S][+](pS/pT)XP (PDB:1QJA) and (C) pS/pTX₁₋₂-COOH (PDB: 7A6R), where pS/pT = phosphoserine/ phosphothreonine, Φ = aromatic residue, + = basic residue, X = any residue^{159, 172}. Non-phosphorylated motifs (D-E): (D) ExoS peptide (PDB: 2O02)¹⁶³, (E) R18 peptide (PDB: 1A38)¹⁷⁰, (F) glycosylated Ser-O-GlcNAc peptide (PDB: 6BYJ)¹⁷¹. (This figure is taken from Obsilova V. 2022)¹⁷³.

2.5.5 Regulation

Numerous 14-3-3 protein-protein interactions (PPIs) can be stabilized or disrupted by short peptides or small molecules^{174, 175}. For example, the previously mentioned short peptide termed R18, which contains a negatively charged phosphorylation-mimicking sequence. Because of that, it acts as a competitor for the positively charged ligand-binding groove and inhibits other 14-3-3 PPIs¹⁶⁹. Inspired by its ability to block PPIs, dimeric form of R18 (known as difopein) was designed and shown to increase the ability of certain chemotherapy medication (specifically cisplatin) to kill cells and trigger tumour cell apoptosis^{168,169,176,177}. Several kinds

of small-molecule that inhibit 14-3-3 have been found, like FOBISIN101 (a radiation-triggered therapeutic drug that prevents binding of 14-3-3 with Raf-1).¹⁷⁸, macrocyclic peptides¹⁷⁹ and rac-UTKO1^{180,181}.

Notably, 14-3-3 PPI inhibitors are lacking selectivity for 14-3-3 isoforms despite being diverse because these compounds typically target the ligand-binding groove, which has the highest similarity in sequence among the isoforms. Nevertheless, because all isoforms have a tendency to compensate one another, this “non-specific” targeting is still functional^{182,183}. On the other hand, there are exceptions in which it would be beneficial to have more specificity, such as 14-3-3 σ , which stands out because it serves as a tumour suppressor by positively regulating p53¹⁸⁴. Furthermore, while 14-3-3 ζ expression decreases in breast cancer, but it is abundant in the majority of cancers¹⁸⁵. Therefore, discovering small-molecule inhibitors of this isoform might help the development of therapies for different cancers.

In contrast, there are numerous situations in which preserving 14-3-3 PPIs might be more favourable. Fusicoccin A (FC-A, which is produced by the phytopathogenic fungus *Phomopsis amygdali* as a diterpene glycoside toxin) was first used by Oecking to target one side of the 14-3-3 ligand-binding groove, hence stabilising 14-3-3 PPIs.^{162,163,186} Conclusion was, FC-A fills a gap in the 14-3-3 ligand-binding groove interface and the phosphopeptides, which enhances their affinity to each other.

Several 14-3-3 PPI stabilisers, such as cotylenin-A, has been discovered until now¹⁸⁷, pyrrolidone 1, epibestatin¹⁸⁸, adenosine monophosphate¹⁸⁹, phosphonate derivatives¹⁹⁰, macrocyclic compounds¹⁹¹. The potential application of 14-3-3 PPI-stabilizers in drug discovery has been emphasised by all of these structural and functional studies.

2.5.6 Associated disorders

14-3-3 plays a crucial role in various cellular processes by interacting with a variety of target proteins. Since 14-3-3 proteins were isolated from brain tissue, they have been directly associated with several neurodegenerative disorders, like Creutzfeldt–Jakob (CJD)¹⁹², Alzheimer¹⁹³, Parkinson¹⁹⁴ and poly-glutamine repeat¹⁹⁵ diseases. More recently, it has found that 14-3-3 proteins have been associated with to foster poorer outcomes and chemo resistance in cancer patients, especially patients with breast, lung, prostate, head and neck cancer, glioblastoma and myeloma^{196–199}. This all leads to the conclusion that the dysfunction or

irregulation of 14-3-3 dimers can cause variety of diseases and disorders. Followings are a few examples:

Neurodegenerative Diseases: 14-3-3 proteins associated with several neurodegenerative diseases (e.g. Alzheimer's disease, Parkinson's disease, prion diseases)²⁰⁰⁻²⁰³. For example, abnormal proteins-protein interactions between tau and 14-3-3 protein were detected in a patients suffering from Alzheimer's disease, which is thought to play a part in neurofibrillary tangles formation, a hallmark of the disease^{204, 205}.

Cancer: 14-3-3 proteins interact with key regulatory proteins that governs the cell cycle control, apoptosis, and DNA repair. Aberrant interactions can lead to uncontrolled cell growth and tumour formation. One example is when these dimers interact with p53 (tumour suppressor protein) and Bcl-2 (proto-oncogene), which influences cell survival and proliferation²⁰⁶⁻²⁰⁹.

Neurological conditions: Mutations in the genes encoding 14-3-3 proteins can cause disruption in normal neurological functioning and cause seizures typically associated with different forms of epilepsy. In addition to epilepsy, 14-3-3 impairments were connected to the development of schizophrenia and bipolar disorder²¹⁰⁻²¹³.

Cardiovascular Disease: 14-3-3 proteins bind to (calcium-interacting) proteins involved in cardiac muscle contraction thereby regulating different cardiovascular signalling pathways. Any disruptions within them are linked to several heart conditions, typically hypertrophy of the myocardium and terminally heart failure²¹⁴⁻²¹⁶.

Infectious Diseases: It is possible for different bacteria (*Helicobacter pylori*)²¹⁷, parasites (*Toxoplasma gondii*)^{218,219} or viruses (hepatitis C virus)²²⁰ to interact with 14-3-3 dimers and initiate their DNA replication, which allows these organisms to survive in their host cell. This is one of the mechanisms for furthering the progression of the disease.

Diabetes: Because of their involvement in the insulin-signalling pathways and the glucose metabolism in general, any dysregulation is described to contribute to the development of insulin resistance or impaired glucose regulation (central features of type 2 diabetes)^{221,222}.

Autoimmune Disorders: A complex mechanisms by which normophysiologic immune system suddenly attack healthy cells often involves faulty regulation of 14-3-3 proteins^{223,224}.

This is just a short summary of 14-3-3 proteins involvement in various pathological conditions. Overall, it suggests significance of these present dimers, both from functional and structural perspectives, highlighting the need for continued research in this domain.

2.6 Nedd4-2 and 14-3-3 Interaction

As described in previous sections, 14-3-3 scaffold protein is known to interact and regulate the activity and substrate specificity of Nedd4-2^{117,225}.

One of the most famous example is the regulation of the epithelial sodium channel (ENaC). In a mouse knockout study¹²⁰, Nedd4-2 was shown to be responsible for regulating the ENaC activity by binding to its PPxY (PY) motif using its WW domains and its subsequent ubiquitination. Thus, it is responsible for balancing the reabsorption Na⁺ ions by the kidney epithelial cells and maintains the same ion level throughout the body. Any dysregulation regarding the Nedd4-2 ubiquitin ligase is known to cause the development of the Liddle syndrome, a rare form of hypertension that stems from the failure to regulate the ENaC and lead to an increased Na⁺ reabsorption^{115,226}. Same effect seen in case of PPxY mutation of the same channel. Various studies have reported that the 14-3-3 protein is a negative regulator of Nedd4-2-dependent ENaC ubiquitination. Recent reports suggest that, by forming a Nedd4-2:14-3-3 protein complex, 14-3-3 inhibit Nedd4-2 ubiquitination by preventing Nedd4-2 from interacting with its downstream target molecules. (e.g. EnaC, SCN2A/Nav1.2, SCN3A/Nav1.3).

This example demonstrates that the exact mechanism and consequences of the binding between a 14-3-3 dimer and Nedd4-2 can vary depending on the specific context, phosphorylation, cellular environment and specific isoforms of both interacting proteins. Additional point is that this interaction can prevent the increased rate of auto-ubiquitination of Nedd4-2 and its subsequent degradation; therefore controlling the abundance of Nedd4-2 present in the cells. Nevertheless, mostly 14-3-3 proteins affect the ubiquitination of specific target proteins of Nedd4-2, which consequently has a downstream effect on their stability, activity and fate. This demonstrates control over protein degradation and influences the direction of various signalling pathways.

3. Aims

The aim of this dissertation was to understand the structural dynamics associated with 14-3-3-mediated Nedd4-2 regulation and to elucidate the impact of this interaction on the structural domains of Nedd4-2 by using various biochemical and biophysical techniques including expression and purification of recombinant protein, site-directed mutagenesis, fluorescence spectroscopy, X-ray crystallography, structural mass spectrometry.

Specific aims:

1. Preparation of single cysteine mutant variants of Nedd4-2¹⁹⁰⁻⁵⁸¹ and Nedd4-2¹⁸⁶⁻⁹⁷⁵ constructs. Mutagenesis, expression, purification and phosphorylation of Nedd4-2 protein variants.
2. Verification of the thermal stability of Nedd4-2 mutants by differential scanning fluorimetry and its ability to form a complex with 14-3-3 protein by native TBE-PAGE.
3. Labelling of the protein with dansyl group (1,5-AEDANS) attached to different cysteine residues in Nedd4-2 and verification of the labelling by mass spectrometry.
4. Monitoring the conformation and flexibility of Nedd4-2 in the presence and absence of 14-3-3 protein using various time-resolved fluorescence spectroscopy techniques.
5. Mapping the structural changes between Nedd4-2 alone and in the complex with 14-3-3 using chemical crosslinking.
6. Perform the limited proteolysis to analyze the comprehensive proteolytic effects on Nedd4-2, both in the presence and absence of 14-3-3 protein.
7. Refining the crystal structure of 14-3-3 γ Δ C with the Nedd4-2 peptide containing the 14-3-3 binding motif pS342.

4. Methods and material

4.1 Material

4.1.1 Biological material

Plasmid pET-15b	Novagen, USA
Plasmid pST39	Novagen, USA
Plasmid pGEX-6P-1	Sigma-Aldrich, USA
<i>Escherichia coli</i> BL21 (DE3) strain	Stratagene, USA

4.1.2 Chemicals

1, 4-dithiothreitol (DTT)	Carl Roth GmbH, Germany
1,5-IAEDANS	Invitrogen by Thermofisher Scientific, USA
2-mercaptoethanol	Sigma-Aldrich, USA
4-(2-hydroxyethyl)-1 piperazineethanesulfonic acid (HEPES)	Sigma-Aldrich, USA
Acrylamide	Carl Roth GmbH, Germany
Agarose GTQ	Carl Roth GmbH, Germany
Ammonium persulfate (APS)	Sigma-Aldrich, USA
Ampicillin	Sigma-Aldrich, USA
Bis-acrylamide	Carl Roth GmbH, Germany
Bromophenol blue	Carl Roth GmbH, Germany
Calcium chloride	PENTA s.r.o., Czech Republic
Chloramphenicol	Sigma-Aldrich, USA
Coomassie Brilliant Blue R 250 LKB	Bromma, Sweden
Disodium (EDTA)	Lachema, s.r.o., Czech Republic
DNA marker (1 kb)	New England BioLabs, USA
DNase	ZellBio GmbH, Germany
Electrophoresis Loading-Dye	New England BioLabs, USA
Ethanol 96% v/v for UV spectroscopy	PENTA s.r.o., Czech Republic
Ethyl alcohol 96% G.R	Lach:NER, s.r.o., Czech Republic
Glycerol	PENTA s.r.o., Czech Republic
Hydrochloric acid	PENTA s.r.o., Czech Republic

Imidazole	Carl Roth GmbH, Germany
Isopropyl β -D-1-thiogalactopyranoside	EMD Biosciences, Inc., Germany
Kanamycin	Sigma-Aldrich, USA
Luria-Bertani (LB) agar	Carl Roth GmbH, Germany
Luria-Bertani (LB) medium	Carl Roth GmbH, Germany
Lysozyme	SERVA Electrophoresis GmbH, Germany
Magnesium sulfate heptahydrate	PENTA s.r.o., Czech Republic
N, N, N', N'-tetraethylenediamine (TEMED)	Carl Roth GmbH, Germany
Nickel sulfate hexahydrate	PENTA s.r.o., Czech Republic
Phenylmethylsulfonyl fluoride (PMSF)	Carl Roth GmbH, Germany
Phusion high fidelity DNA polymerase	New England Biolabs, United Kingdom
PreScission Protease	Prepared in our laboratory
Precision plus protein standard (dual color)	Bio-Rad Laboratory, USA
Restriction endonuclease	Thermofisher Scientific, USA
Roti marker Tricolor protein marker	Carl Roth GmbH, Germany
Sodium chloride	Lach:NER, s.r.o., Czech Republic
Sodium dodecyl sulphate (SDS)	Carl Roth GmbH, Germany
Sodium hydroxide	LACH-NER, s.r.o., Czech Republic
T4 DNA ligase	New England Biolabs, United Kingdom
Tobacco Etch Virus nuclear-inclusion- endopeptidase (TEV protease)	Prepared in our laboratory
Tris (2-carboxyethyl) phosphine (TCEP)	Sigma-Aldrich, USA
Tris (hydroxymethyl) aminomethane (Tris)	Carl Roth GmbH, Germany
Urea	Sigma-Aldrich, USA

4.1.3 Laboratory material

Centricon concentrators	Sartorius, United Kingdom
Chelating Sepharose Fast Flow	GE Healthcare, USA
Dialysis membrane, type 27/32 (cut off 14000)	Carl Roth GmbH, Germany
DNA isolation kit	Thermofisher Scientific, USA
Glutathione Sepharose 4 Fast Flow	GE Healthcare, USA
HiTrap Q sepharose	GE Healthcare, USA

Quick Change™ Mutagenesis kit	Stratagene, USA
Spartan 13/0.45 RC filter unit	GE Healthcare, USA
Superdex 75 HiLoad 26/600 column	GE Healthcare, USA
Superdex 200 HiLoad 26/600 column	GE Healthcare, USA
Vivaspin Turbo centrifugal filter device (cut off 5000, 10000 and 30000 MWC ₀)	Sartorius, United Kingdom
Whatman™ membrane filter paper 0.45μM	GE Healthcare, USA

4.1.4 Instruments

Analytical balance EG420-3NM	Kern, Germany
15T solariX XR FT-ICR mass spectrometer	Burker Daltonics, USA
Automatic pipettes	Eppendorf AG, Germany
Centrifuge 5804R	Eppendorf, Germany
Centrifuge Eppendorf MiniSpin	Eppendorf, Germany
Centrifuge Hermle Z323K	Hermle Labortechnik GmbH, Germany
Centrifuge Sigma 8K	Sigma, USA
FPLC	GE Healthcare, USA
Gallenkamp Orbital Incubator shaker	Gemini BV, Netherlands
Incubator HT Multitron	Infors, Germany
NanoDrop One	Thermo scientific, USA
Peristaltic pump Ecoline	Ismatec, Germany
pH Meter 3305	P Lab, Czech Republic
Sonicator 3000	Misonix, Inc., USA
electrophoresis	Bio-Rad Laboratories, USA
Thermal block	Grant, UK
Vortex ZX3	VELP Scientifica, Italy

4.2 Experimental methods

4.2.1 Expression and purification of 14-3-3 protein

Our lab has been working with 14-3-3 protein family for a long time and we possess all of its seven isoforms, whose purification protocol doesn't differ significantly. Gene encoding human 14-3-3 η cloned within the recombinant plasmid pET-15b with an N-terminal histidine tag (6 \times consecutive histidine residues) and for the purpose of protein expression; we transformed *Escherichia coli* (*E.coli*) bacterial strain BL21 (DE3) with it and prepared a glycerol stock that is stored on -80 °C.

To express 14-3-3 η , first we inoculated the 5 ml pre-cultures (LB medium with the appropriate antibiotic, in this case ampicillin) with the swab of the glycerol stock. We left them to incubate and grow on 37 °C with continuous shaking at 200 rpm for proper aeration. The next day, we poured 5ml pre-culture per 1 l LB media (with the appropriate amount of antibiotics, ampicillin). Culture was grown at 37 °C with shaking at 190 rpm until optical density (OD₆₀₀) became 0.6. The temperature was lowered to 30 °C and at OD 0.8, the culture induced by IPTG (final concentration of 0.5 mM). Bacterial culture was left to grow with constant shaking overnight (18-20 hrs) at 30 °C. After incubation, cell culture was centrifuged at 3000 rpm for 20 minutes. Cell pellet was suspended in a lysis buffer (50 ml/1 l cell pellet, (see table 4.1)) and subsequently frozen at -80°C, which also contributed to cell lysis.

Purification of 14-3-3 η started with thawing the cell suspension. Afterwards, we incubated it with lysozyme (100 μ g/ml) by stirring at 4 °C for 20 min, to make the cell more prone to lysis (lysozyme cleaves peptidoglycans of the cell wall). Final step of cell lysis was done by sonication, which disrupts the cell wall and cell membrane by ultrasound. It lasted for 15 minutes, on ice, with the pulse power 55 W and with each cycle consisting of 10 s ON and 30 s OFF. It is necessary to perform sonication on ice and to have breaks within the cycle to avoid overheating and subsequent protein denaturation. Afterwards, the sonicate was centrifuged at 13500 rpm for 45 min to separate insoluble components from solution. We collected the supernatant.

The next step was protein purification by nickel chelation chromatography (Fig. 4.1). Aforementioned, all the protein contains 6 \times His tag, which will allow us to separate the pure protein from everything else from the supernatant.

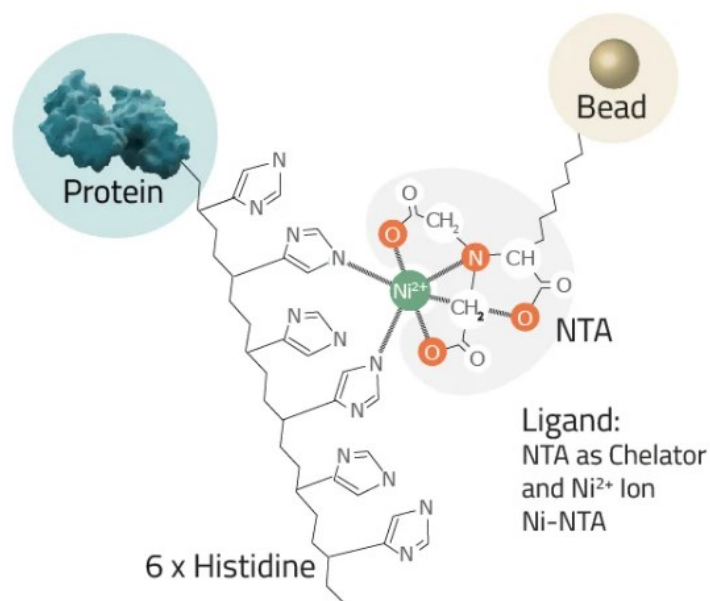


Figure 4.1: Ni-NTA affinity chromatography using 6× His tag. A schematic representation of a principle behind Ni-NTA affinity chromatography in which NTA and Ni²⁺ forms a chelator complex. Nickel ion attaches to two imidazole rings on a His-tag of protein (Figure taken from Cube Biotech website).

Protein purification by Ni NTA affinity chromatography is based on the coordination bond created between Ni²⁺ cations and free nitrogen of the imidazole ring of histidine. This allows the protein with the His-tag to bind to the column. At the elution step, the addition of high concentration of imidazole displaces the protein from the column. In the case of 14-3-3 proteins, about 3 ml of sepharose resin (Chelating Sepharose Fast Flow, GE Healthcare, USA) was used. The column was regenerated and charged with 20 ml of 0.1 M nickel sulphate (NiSO₄). Then the column was pre equilibrated by using buffer E (see Table 4.1). The sonicate was absorbed on the equilibrated column with the slow flow and stirring. Subsequently, the column was washed using 300 ml of 10% (v/v) solution of buffer F (see Table 4.1) to remove non-specifically bound protein impurities. Finally, the target protein is eluted with buffer F having high concentration of imidazole.

Table 4.1: Buffers and their composition used for 14-3-3 η purification

Lysis Buffer	1 \times PBS + 1 M NaCl + 4 mM β Me + 2 mM Imidazole
Buffer E	1 \times PBS + 0.5 M NaCl + 2 mM β Me + 1 mM Imidazole
Buffer F	1 \times PBS + 0.5 M NaCl + 2 mM β Me + 0.6 M Imidazole

An imidazole (0.6 M) having a high concentration in the elution buffer may affect the stability of the protein, so dialysis was performed with a low salt/salt free buffer. In dialysis, we use selectively permeable porous membranes whose pores allow the free migration of small molecules, but prevent it for the molecules larger (> 14 kDa) than the diameter of membrane pores. This results in exchange of solvents, not solutes (protein). The sample was dialysed using a dialysis buffer containing 50 mM Tris-HCl (pH 8.0), 2 mM EDTA, 2 mM β -Mercaptoethanol (β ME). After two hours of dialysis, the protein concentration was checked and SDS-PAGE was run to check purity of protein. Then TEV protease (31.2 μ l/1 mg protein) was added to cleave the histidine tag from the protein. After being transferred to a new dialysis buffer, the protein was dialysed for the second time at 4°C for an overnight. SDS-PAGE was used to examine His-tag cleavage.

Anion exchange chromatography was used to further purify the 14-3-3 proteins. This purification was done with the help of FPLC AKTA Pure system (GE Healthcare, USA) using Mono Q Sepharose column (1 ml) (GE Healthcare, USA). This column contains charge positive ions that bind negatively charged molecules, mostly acidic proteins i.e. 14-3-3 (pI 4.67 to 5.14) at pH 8.0 dialysis buffer. In anion exchange chromatography, the column was first equilibrated with buffer A (Table 4.2). Then the protein sample was loaded in a column under slow flow. Subsequently, the protein is eluted with a gradient of buffer B. The quality of purified protein was checked by SDS-PAGE.

Table 4.2: Buffer composition of anion exchange chromatography

Buffer A	50 mM Tris-HCl (pH 8.0) + 2 mM DTT
Buffer B	50 mM Tris-HCl (pH 8.0) + 1 M NaCl + 2 mM DTT

The final step of purification was size exclusion chromatography done with HiLoad 26/600 column with SuperdexTM 75 column (GE Healthcare) using the AKTA pure FPLC system. The principle behind size exclusion chromatography is that particles are separated based on their molecular size (hydrodynamic radius) through the solid phase of the column. Larger particles in this chromatography flow through the column faster than small ones, which are trapped inside the differently sized pores of the column's resin.

Protein was concentrated using Vivaspin Turbo 15 centrifugation concentrators (MWCO 10 kDa) before protein loading to the FPLC. Size exclusion chromatography was run using a buffer 20 mM Tris-HCl (pH 7.5) + 150 mM NaCl + 1 mM TCEP + 10% (v/v) glycerol. Protein elution was monitored by the light absorption at 280 nm. The collected protein fractions were checked with SDS-PAGE and suitable fractions were pooled together. The final concentration of protein was measured using Nanodrop at 280 nm based on the molar absorption coefficient calculated from the primary protein structure.

4.2.2 Site directed mutagenesis of Nedd4-2

Our lab obtained the gene encoding the Nedd4-2 protein from Addgene (#83433)²²⁷. All of the Nedd4-2 truncated protein variants were prepared using the above Nedd4-2 gene as a template DNA for mutagenesis. I used two Nedd4-2 constructs that were already created in our lab, Nedd4-2¹⁹⁰⁻⁵⁸¹ and Nedd4-2¹⁸⁶⁻⁹⁷⁵, to prepare cysteine mutants. Both constructs were cloned into the expression vector pST39 with non-cleavable C-terminal his-tag (6× Histidine) and sequencing was done to verify that.

Nedd4-2 mutant variants were prepared using standard protocol of Quikchange site directed mutagenesis kit (Stratagene, California, USA). This comprises a PCR reaction that uses overlapping primers with missense mutations. Every step of the site directed mutagenesis process is shown in Fig. 4.2. At the end, the recombinant plasmid with a confirmed sequence was transformed into the BL21(DE3) expression vector.

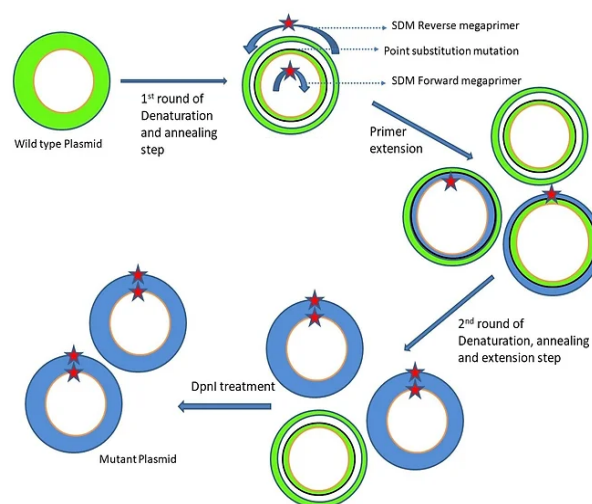


Figure 4.2: Site directed mutagenesis-Quick-change by Agilent illustrating the systematic process of site directed mutagenesis (Figure taken from biobulletins webpage).

The Nedd4-2¹⁹⁰⁻⁵⁸¹ contains only one cysteine residue. In order to produce cysteine variants, we prepared a template by changing the cysteine at position 341 to serine. The mutagenesis was done in a way that only a single cysteine was present in sequence and the other cysteine residues were mutated to serine residues. In the case of the Nedd4-2¹⁸⁶⁻⁹⁷⁵ variant, which contains six cysteine residues, the series of subsequent mutagenesis was necessary in order to achieve single cysteine variant. By using above described protocol, thirteen different Nedd4-2 variants in both Nedd4-2 constructs were generated and cysteine insertion in all mutants was confirmed by sequencing (Table 4.3):

Table 4.3: Nedd4-2 constructs details and positions of cysteine variants.

Construct	Domains present in the constructs	14-3-3 binding motifs in the constructs	Incorporated mutations for cysteine variants
Nedd4-2 ¹⁹⁰⁻⁵⁸¹	WW 1-4	S342, T367, S448	C341S, T209C, T218C, S389C, T414C, A508C, T522C, S571C
Nedd4-2 ¹⁸⁶⁻⁹⁷⁵	WW 1-4, HECT	S342, T367, S448	C702, C776, C853, C874, C942 (native cysteines in the HECT domain)

4.2.3 Expression and purification of Nedd4-2 protein variants

In the following chapters, the process of expression and purification of Nedd4-2 protein is described, which was necessary to perform the rest of the research.

4.2.3.1 Nedd4-2¹⁹⁰⁻⁵⁸¹ short variant for fluorescence measurements.

Nedd4-2¹⁹⁰⁻⁵⁸¹ wild type and seven variant proteins were expressed and purified by using the following procedure. The fusion proteins were expressed by *Escherichia coli* Bl21 (DE3) cells in LB media. Initially cell cultures were incubated at 37 °C until optical density (OD) became 0.5, similarly like with the expression of 14-3-3 η . The protein expression was induced with addition of 0.5 mM Isopropyl-beta-D-thiogalactoside (IPTG) at OD⁶⁰⁰=0.8. Cell cultures were incubated further at 18 °C overnight. Next day, cells were harvested by centrifugation at 3500 rpm for 20 mins. Cell pellets were resuspended into a lysis buffer containing 1× PBS, 1 M NaCl, 4 mM β Me, 2 mM imidazole and 0.01% (v/v) tergitol. The addition of tergitol (0.01%) to the lysis buffer improved the protein's stability, so we decided to keep 0.01% (v/v) tergitol in all of the buffers used throughout the purification. After thawing the cell pellet and incubating it with lysozyme, sonication was done for 10 minutes (pulse on – 5 sec, pulse off – 30 sec). Afterwards, the sonicate was centrifuged at 13500 rpm for 45 min at 4 °C.

The supernatant fraction protein was purified by affinity chromatography using a Chelating Sepharose Fast Flow column (GE Healthcare, USA) as per the standard protocol and final protein was eluted with 10 ml of buffer F containing 1× PBS + 0.5 M NaCl + 2 mM β Me + 0.6 M Imidazole + 0.01% (w/v) tergitol. The protein was immediately loaded on the FPLC system and purified using Hiload column Superdex 75, 26/600 gl (GE Healthcare, USA). Following purification, the obtained protein quality was analysed using SDS-PAGE.

Phosphorylation of Nedd4-2 was done by incubating a mixture of the protein with 158 U of protein kinase A (PKA) per 1mg of recombinant protein in the buffer with the final concentration of 20 mM MgCl₂ and 0.75 mM ATP for 2 hours at 30 °C and also at 4°C for overnight. The next day, excess of ATP was removed by size exclusion chromatography using a Superdex 75, 10/300 gl column (GE Healthcare USA) and buffer 50 mM Tris-HCl (pH 7.5) + 100 mM NaCl + 1 mM EDTA. To confirm the phosphorylation status, native TBE-PAGE was done with non-phosphorylated Nedd4-2, phosphorylated Nedd4-2 and their known binding partner 14-3-3 η .

Labeling of protein using thiol reactive probe 1,5-IAEDANS was done as described²²⁸. The approximate concentration of the protein used for labelling was 2.0-8.5 μM . A stock of 15 mM 1,5-IAEDANS was dissolved in DMSO. After mixing the label and protein at a molar ratio of 40:1 (using 40 moles of probe for every 1 mol of protein), the mixture was incubated for 2 hours at 30 °C, followed by overnight incubation at 4 °C. Afterwards, the separation of the labelled protein and dye was done by size exclusion chromatography with a Superdex75, 10/300 gl column (GE Healthcare USA) with buffer containing 50 mM Tris-HCl (pH7.5) + 100 mM NaCl + 1 mM EDTA + 10% glycerol.

The labelling incorporation stoichiometry was determined using a spectrophotometer by comparing the protein absorbance peak at 280 nm with absorbance peak at 336 nm of bound 1,5-IAEDANS (ext. coefficient 5700 $\text{M}^{-1} \text{cm}^{-1}$) (Molecular Probes, Eugene, OR). The CMS facility BIOCEV's mass spectrometry confirmed that proteins were phosphorylated and labelled at appropriate positions.

4.2.3.2 Purification of the Nedd4-2¹⁸⁶⁻⁹⁷⁵ long variant for fluorescence measurements.

This Nedd4-2¹⁸⁶⁻⁹⁷⁵ construct contained five cysteine residues at HECT domains. By using site directed mutagenesis approach five different Nedd4-2 variants prepared, that contained only one out of five native cysteines, while the rest were mutated to a serine (C702S, C776S, C853S, C874S, C942S).

Nedd4-2¹⁸⁶⁻⁹⁷⁵ C942 was the only variant out of the five protein variants that was expressed and purified as a stable and soluble protein; it was purified using the following method. Nedd4-2¹⁸⁶⁻⁹⁷⁵ variants were expressed and purified by Ni^{2+} NTA affinity chromatography using the same protocol as the Nedd4-2¹⁹⁰⁻⁵⁸¹ variant.

The purified protein was subsequently repurified by size exclusion chromatography using Hiload column Superdex 200, 26/600 gl (GE Healthcare, USA). SDS-PAGE was used to analyze quality and purity at each stage. Protein was phosphorylated as described above and again performed the size exclusion chromatography using Superdex 200, 10/300 gl column (GE Healthcare USA). Protein was concentrated using vivaspin turbo 15 (10 kDa) concentrator. Native TBE-PAGE was run to see interaction of the Nedd4-2 variant with 14-3-3 proteins.

Furthermore, Nedd4-2¹⁸⁶⁻⁹⁷⁵ protein was labelled by 1,5-IAEDANS using the same method as described further.

4.2.4 Mass spectrometry (MS)

Mass spectrometry (MS) is a powerful analytical technique used to separate and identify ionized particles based on their mass-to-charge ratios (m/z). It consists of several key components: an ion source, a mass analyzer, a detector, and a computer for data analysis. The ion source ionizes sample molecules, the mass analyzer sorts ions based on their masses, the detector measures ion abundances, and the computer manages the data. One widely used ionization method is Matrix-Assisted Laser Desorption/Ionization (MALDI), first introduced by Koichi Tanaka and further developed by Michael Karas and Franz Hillenkamp²²⁹. With MALDI, biomolecules of all sizes, from tiny metabolites to large proteins, can be analyzed by applying a matrix coating and ionizing them with a laser beam²³⁰⁻²³³.

The most common mass analyzer for MS is the time-of-flight (TOF) analyzer, which sorts ions based on their flight times. Tandem mass spectrometry allows for structural analysis by fragmenting ions and analyzing the resulting fragments. Molecular identification is achieved by comparing the obtained molecular weights with those in a database. Overall, selecting the appropriate combination of ionization method and mass analyzer is essential for successful MS analysis²³⁴.

The mass spectrometric analysis was carried out at BIOCEV, CMS facility. The following is the typical procedure for a mass spectrometric experiment. Proteins were diluted into a buffer containing 50 mM ammonium carbonate. Free cysteine was alkylated with 30 mM iodoacetamide for 30 minutes at room temperature in the dark, and cysteine was reduced with 10 mM DTT for 45 minutes at 60 °C. Digestion by trypsin continued overnight at 37°C with a 1:20 (w/w) enzyme to protein ratio. Peptides were loaded on a trap column (Luna Omega 5 μ m Polar C18 100 Å, 20× 0.3 mm, Phenomenex) and desalted for 5 min at a flow rate of 20 μ L/min.

Moreover, using a capillary UHPLC system (Agilent Technologies) and a reversed phase C18 column (Luna Omega 3 μ m Polar C18 100 Å, 150 x 0.3 mm, Phenomenex), the proteins were separated at a flow rate of 10 μ l/min under the following gradient conditions: 1–10% B in 1 minute, 10–45% B in 19 minutes, and 45–95% B in 5 minutes were the times for which solvent A and solvent B were, respectively, 0.1% formic acid in 98% acetonitrile and 2.0% acetonitrile

in water. Times ToF pro mass spectrometer (Bruker Daltonics) was immediately linked to the heated column, which was maintained at 50°C. PASEF mode was in use on the instrument. Data was processed using the Bioinformatics Solutions, Canada-based Peaks Studio X software, and it was compared to the Nedd4-2 protein database. The peptides' FDR was set to 1%.

4.2.5 Differential scanning fluorimetry (DSF)

Differential Scanning Fluorimetry (DSF) is a method used to measure protein stability. In the conventional approach, researcher uses a hydrophobic fluorescent dye that binds to the hydrophobic (folded) regions as they become exposed due to high temperatures, while the machine detects changes in the fluorescence signal. (Fig. 4.3.).

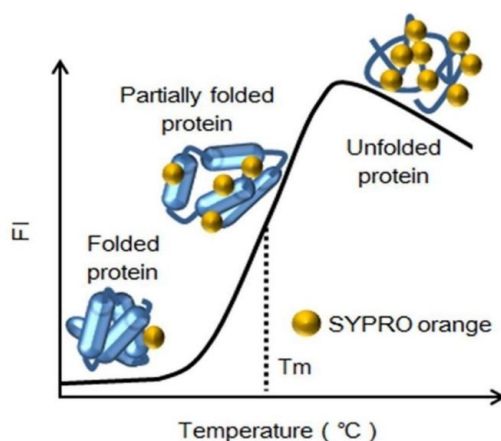


Figure 4.3: A schematic diagram of Differential scanning fluorimetry. The Fluorescence Intensity (FI) curve shows the change in fluorescence intensity of SYPRO orange dye as it becomes attached to an incrementally denatured test protein (Figure taken from Miyazaki *et. al.* 2017)²³⁵.

Protein stability is dependent on the Gibbs free energy of unfolding (ΔG_u). With the increase of temperature, at a certain point ΔG_u reaches equilibrium (equals 0), which means that the concentrations of folded and unfolded proteins are the same. This temperature is called melting temperature (T_m)^{235, 236, 237}.

This unfolding transition, discernible through differential analysis, offers critical information on the thermal stability of the biomolecule. The Fluorescence Intensity curve is a function of temperature and is sigmoidal (Fig. 4.3), which is further described by a two-state transition. To calculate the inflection point of this transition curve (T_m), by using the Boltzmann equation

(eq.1). The slope of the curve is defined by LL (minimum intensity) and UL values (maximum intensity), while the melting temperature is calculated by determining the maximum of the first derivative.

$$y = LL + \frac{(UL-LL)}{1 + \exp\left(\frac{T_m-x}{a}\right)} \quad (1)$$

The dyes used for DSF need to favour non-polar environments (hydrophobic sites on the denatured protein) and be quenched within polar solutions. Common dye of choice is SYPRO orange, mostly because of its high signal-to-noise ratio. Its second strength is that it requires a high excitation wavelength (~500nm), which lowers the possibility that a small molecule could cause random quenching^{238,239}.

DSF is usually done using a real-time PCR instrument, because it allows easy manipulation and monitoring of temperature changes. DSF performed on such an instrument is a convenient method of choice for screening different conditions proteins could be in, because it only requires only small amounts and low concentrations.

Using DSF, the thermal stability of Nedd4-2 mutants were determined by measuring the midpoint temperatures of the protein-unfolding transition (T_m). DSF was carried out using a LightCycler 480 II device (Roche Applied Science, Germany). Nedd4-2¹⁹⁰⁻⁵⁸¹ and Nedd4-2¹⁸⁶⁻⁹⁷⁵ protein variations were evaluated in 8 × concentrated Sypro Orange (Sigma-Aldrich, St. Louis, MO, USA) in a total reaction volume of 50 µL in a 96-well microtiter plate (Roche Applied Science) at concentrations of 0.144 – 0.37 mg/ml and 0.185 mg/ml, respectively. Protein was in a buffer containing 100 mM HEPES (pH 7.5) and 150 mM NaCl. Excitation wavelength fluorescence was set at 465 nm and emission wavelength was 580 nm. The values of the melting temperatures T_m corresponding to the inflection points of the denaturation curves were evaluated and were determined as the minima of the first negative derivatives of these curves using the ROCHE LightCycler 480 SW 1.5 software^{238,239}.

4.2.6 Fluorescence Spectroscopy

Fluorescence is a type of photoluminescence caused by photons excitation of a molecule to an electronic excited state. Some molecules, such as chlorophyll and proteins containing the amino acid residues tryptophan (Trp), phenylalanine (Phe), and tyrosine (Tyr), are intrinsically

fluorescent. Other fluorescent molecules are created deliberately from non-fluorescent systems by introducing fluorescent organic dyes or tags. After absorbing a photon, a fluorescent specie becomes excited from its ground to one of the various vibrational excited electronic states. If the excited molecule collides with other molecules, it loses vibrational energy (falls to the lowest vibrational state) which is a phenomenon called vibrational relaxation (VR). A Jablonski diagram is commonly utilized to illustrate this procedure (Fig. 4.4).

After excitation, the molecule emits a photon of a different energy (therefore frequency and wavelength). This causes the drop down to the ground electronic singlet state. Because of that, in fluorescent spectroscopy to be able to determine the structure of vibrational levels, it is necessary to analyse light frequencies and their intensities.

Jablonski diagram (Fig. 4.4) is a graphical representation that is often used to describe the photophysical processes that take place between the absorption and emission of light. In this diagram, the ground and first electronic states are typically represented as S_0 and S_1 , respectively. Fluorophores are molecules that, when stimulated by photons, emit light. It can occupy various vibrational energy levels, in these electronic states, often labelled as 0, 1, 2, and so forth.

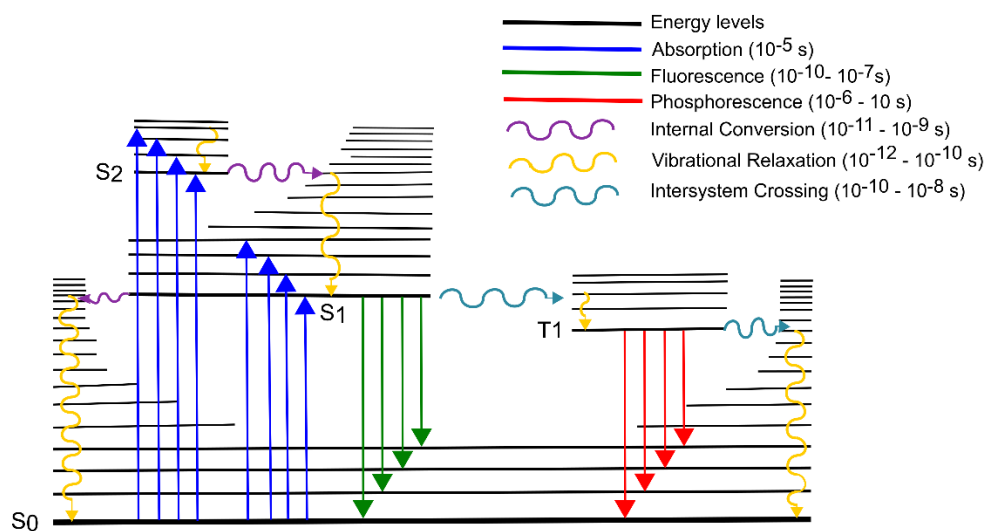


Figure 4.4: Jablonski diagram. Jablonski diagram with absorption (in blue), non-radiative transition (in red) and fluorescence (in green) vibrational levels included (Figure inspired from Edinburg instruments webpage).

From the lowest level of the first singlet electronic excited state, the molecule can undergo either nonradiative transition or fluorescent light emission to return to its ground singlet electronic state. According to quantum mechanical principles, the molecule can end up in any vibrational state of the electronic ground state upon radiative transition. However, the probability of a particular vibronic transition depends on the square of the overlap of vibrational wave functions of the initial and final state (Franck-Condon principle). In addition, fluorescence emission might be blocked if the ground and excited singlet states' vibrational levels overlap. In such a case, the molecule returns to the ground state through nonradiative internal conversion (IC). In addition to fluorescence emission, some fluorophores can exhibit phenomena of intersystem crossing (ISC).

Because of spin-orbit coupling, ISC consists of molecule transitioning the excited singlet to a triplet electronic state. The triplet state has a total spin value of 1. Phosphorescence is a phenomenon of the radiative transition from the excited triplet state to the ground state. Because the transition between states of different multiplicity (singlet to triplet or triplet to singlet) is forbidden (due to the spin selection rule), phosphorescence is considerably slower than fluorescence, which is an allowed transition (singlet to singlet).

With a fluorescence lifetime of roughly 10 nanoseconds (10^{-9} seconds), fluorescence emission rates often correspond to 10^8 s^{-1} . An essential feature of fluorescence is the Stokes shift, which is the difference in the energy of absorbed and emitted photons (molecule emits a lower-energy or longer-wavelength photon after absorbing one with a higher frequency or energy). The Stokes shift phenomenon is mostly caused by solvent molecule rearrangement and vibrational relaxation²⁴⁰⁻²⁴⁴.

Fluorescence quenching

Fluorescence quenching is a phenomenon where the fluorescence intensity of the fluorophore decreases due to interaction of quencher molecules. There are a number of examples when that might happen, some of which are collisional contacts, energy transfers, formation of complexes, excited-state reactions. The decrease of fluorescence emission therefore manifests through different mechanisms. Fluorescence quenching provides insights into molecular interactions and localization of fluorophores in proteins and membranes. Volume expansion within the solution, solvent viscosity influencing diffusion speeds, and molecular interaction between the

fluorophore and quencher all have an impact on the quenching process. During the lifetime of the excited state, quenchers can diffuse over moderate distances and affect measurements of lifetime or fluorescence intensity. Overall, fluorescence quenching is a highly useful technique that is applicable to many scientific fields for examining molecular environments, researching protein-protein interactions, and evaluating diffusion dynamics. There are two main types of fluorescence quenching: dynamic quenching and static quenching.

- **Dynamic Quenching:** In dynamic quenching, the excited fluorophore and the quencher molecule collide with one another. The excited state decays non-radiatively as a result of this collision, lowering the intensity of the fluorescence emission. In dynamic quenching, the rate of quenching is closely correlated with the quencher molecule concentration and follows the Stern-Volmer equation (eq.2):

$$F_0/F=1 + K_{SV}[Q] \quad (2)$$

where F_0 and F are the fluorescence intensities in the absence and presence of the quencher, respectively, K_{SV} is the Stern-Volmer quenching constant, and $[Q]$ is the concentration of the quencher. Common quenchers involved in dynamic quenching include molecular oxygen (O_2), heavy metals, and certain organic molecules.

- **Static Quenching:** Static quenching happens when the quencher and the fluorophore form non-fluorescent complex ground-state complex) even before excitation. This complex absorbs excitation energy but does not emit fluorescence upon relaxation to the ground state. Even at relatively low quencher concentrations, the fluorescence intensity decreases with static quenching. Static quenching is inapplicable to the Stern-Volmer equation. Depending on the type of interaction, the binding between the quencher and the fluorophore may be irreversible or reversible. Biomolecules, organic dyes, and specific metal ions are typical examples of static quenchers.

Fluorescence quenching has extensive application in fluorescence spectroscopy, fluorescence microscopy, enzyme kinetics, ligand-receptor binding, and protein-protein interactions²⁵³.

Fluorescence Lifetime

Fluorescence lifetime is another photophysical parameter of interest that characterizes energy relaxation and dynamics of the studied fluorophore. It can additionally describe dynamic

quenching, molecular rotation and the energy transfer between different electronic states. It characterizes the average duration a molecule remains in an excited state before emitting a photon and returning to its ground state, playing a pivotal role across scientific domains such as biochemistry, molecular biology, materials science, and medical diagnostics. A profound understanding of fluorescence lifetime offers invaluable insights into molecular structure, interactions, and dynamics.

Several factors influence fluorescence lifetime such as solvent polarity, pH, temperature, and presence of other molecules can influence the rate of excited-state processes. Fluorescence lifetimes are measured experimentally using a variety of methods, such as Time-Domain Fluorescence Spectroscopy, Time-Correlated Single Photon Counting (TCSPC), Frequency-Domain Fluorimetry, etc²⁴⁵.

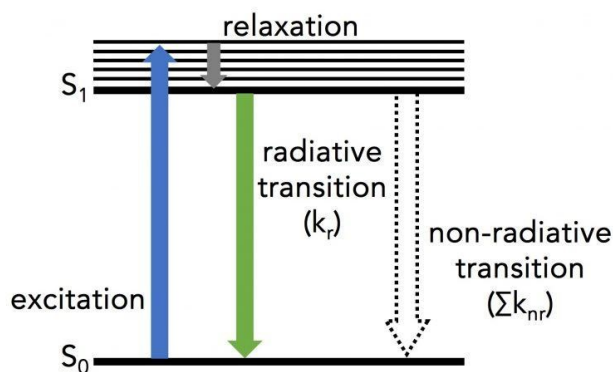


Figure 4.5: Jablonski diagram depicting the excitation and relaxation of a single molecule. (Figure taken from Edinburg instruments webpage)

Fluorescence lifetime (τ) of the molecule in Fig. 4.5 is calculating using the following equation (eq.3):

$$\tau = \frac{1}{k_r + \sum k_{nr}} \quad (3)$$

Fluorescence isn't a precise phenomenon, so that is the reason fluorescence lifetime is only the average time a fluorophore will be in the excited state, before falling to the ground state. This means only a few individual molecules will have emission that has $t = \tau$, but if you take a large population of the same fluorophore, τ value will be the average²⁴⁵⁻²⁵⁰.

Intensity decay of the population of molecules, $I(t)$, is calculated using the following equation (eq.4):

$$I(t) = I_0 e^{-(t/\tau)} \quad (4)$$

$I(t)$ is the intensity decay as a function of time (follows a single exponential model), I_0 the initial intensity, t time passed from the moment of excitation and τ the fluorescence lifetime.

4.2.6.1 Time-resolved fluorescence intensity and anisotropy decay measurements

Time-resolved fluorescence intensity and anisotropy decay measurements are two important techniques used in fluorescence spectroscopy to gather information about the dynamics and environment of fluorescent molecules.

Time-resolved fluorescence intensity measurements involve monitoring the emission of fluorescence from a sample over time with a high temporal resolution. This technique allows scientists to study the decay kinetics of fluorescence emission following excitation. By analyzing the fluorescence decay curve, information about the molecular environment, such as local viscosity, temperature, pH, and molecular interactions, can be obtained. Time-resolved fluorescence intensity measurements are typically performed using a pulsed excitation source, such as a laser, to generate short bursts of excitation energy. The fluorescence emission is then detected using a sensitive detector, such as a photomultiplier tube or a CCD camera, with a fast response time. By recording the fluorescence signal at various time intervals after excitation, the decay kinetics of the fluorescence can be analyzed using mathematical models, such as exponential fitting, to extract information about the sample. Applications of time-resolved fluorescence intensity include studying protein folding dynamics, investigating molecular interactions, probing conformational changes in biomolecules, and characterizing the properties of fluorescent probes and dyes used in biological assays and imaging techniques.

Fluorescence anisotropy measurements are used to probe the rotational motion of fluorescent molecules in solution. It provides information about the molecular size, shape, and rotational freedom of the fluorophores, as well as their interactions with surrounding molecules. Fluorescence anisotropy measurements are based on the principle that the polarization of emitted fluorescence is dependent on the orientation of the fluorophores at the time of excitation. When a polarized light source, such as a polarized laser beam, excites a sample

containing fluorescent molecules, the emitted fluorescence will retain some degree of polarization, which is characterized by the anisotropy value. Anisotropy is defined as the ratio of the difference in fluorescence intensity parallel (I_{\parallel}) and perpendicular (I_{\perp}) to the excitation polarization axis, normalized by the total intensity ($I_{\parallel} + 2I_{\perp}$).

Mathematically, it can be expressed as (eq.5):

$$r = \frac{I_{\parallel} - I_{\perp}}{I_{\parallel} + 2I_{\perp}} \quad (5)$$

Denoted are: anisotropy (r), the fluorescence intensity that is parallel to the excitation polarization axis (I_{\parallel}) and the fluorescence intensity that is normal to the excitation polarization axis (I_{\perp}).

Fluorescence anisotropy is dependent on the position, specifically rotational mobility, of fluorescent molecules. An increase in anisotropy indicates restricted rotational motion, whereas a decrease suggests increased molecular motion or rotational freedom. In addition, the analysis of time-resolved fluorescence anisotropy decays can provide useful information about the conformational behaviour of studied proteins. Therefore, this technique is widely used in protein-protein interaction studies and monitoring conformational changes in biomolecules. In summary, time-resolved fluorescence intensity and anisotropy decay measurements are powerful techniques in fluorescence spectroscopy that provide valuable insights into the dynamics, interactions, and structural characteristics of fluorescent molecules and their environment^{245,251-254}.

All time-resolved intensity decay and anisotropy fluorescence experiments were measured by the time correlated photon counting method as described previously^{255,256}. Briefly, fluorimeter which was used for this purpose, it consisted of a femtosecond titanium-sapphire laser (model Chameleon Ultra II and Pulse Picker HP), detector based on individual counting of photons (single photon counting detector) and photomultiplier (Hamamatsu, R3809U-50). Dansyl fluorophore was excited at 355 nm using the monochromator (Horiba, H-20; with a stack of glass OG420 long-pass and dielectric LP520 filters placed in front of the input slit) and data was collected at 535 nm. Intensity decay was accumulated (magic-angle conditions, 1024 channels, time resolution 195ps/channel) until about 1.5×10^5 counts when the decay maximum were reached. Polarized decays for fluorescence anisotropy were acquired quasi-

simultaneously (switching time between components lasted 30 s). Samples were placed in a thermostatic holder.

All experiments were done at 23°C. The proteins used (Nedd4-2¹⁹⁰⁻⁵⁸¹ protein variants: C209, C218, C389, C414, C508, C522 and C571; Nedd4-2¹⁸⁶⁻⁹⁷⁵ C942; 14-3-3 η) were in the same buffer (50mM Tris-HCl pH 7.5, 100mM NaCl, 1mM EDTA and 10% (w/v) glycerol – all components purchased from Sigma-Aldrich, St. Louis, MO, USA). Concentration ranges for Nedd4-2 constructs were within 1.6-4 μ M, while for 14-3-3 η 4-8 μ M. To analyse fluorescence intensity and anisotropy decays it was necessary to use model-independent SVD-MEM²⁵⁶.

Fluorescence intensity decays were assumed to be multiexponential according to equation (6)

$$I(t) = \sum_i \alpha_i \cdot \exp(-t/\tau_i) \quad (6)$$

where, τ_i are the lifetimes of the excited states and α_i are the respective amplitudes. Emissive decay of $I(t)$ was analyzed by the maximum entropy method²⁵⁶. The program generates sets of amplitudes α_i , which represent the distribution of excited lifetime's status. The mean lifetime of the excited state was calculated as (eq.7):

$$\tau_{mean} = \frac{\sum_i \alpha_i \tau_i^2}{\sum_i \alpha_i \tau_i} \quad (7)$$

All time-resolved fluorescence measurements were carried out under the guidance of prof. RNDr. Petr Heřman, CSc. and Mgr. Dita Strachotová, Ph.D. from the Institute of Physics, Faculty of Mathematics and Physics, Charles University and all the equations in the following text were taken from the literature²⁴⁵.

The fluorescence anisotropy decay $r(t)$ was obtained by simultaneous time-resolved by measuring parallel $I_{\parallel}(t)$ and perpendicular $I_{\perp}(t)$ components of fluorescence intensity. To evaluate data, the maximum entropy method was used²⁵⁶. Anisotropy of fluorescence $r(t)$ was analyzed for a set of exponentials according to equation (8)

$$r(t) = \sum_i \beta_i' \cdot \exp(-t/\phi_i') \quad (8)$$

β_i' represents distribution of rotational-correlation time's ϕ_i' .

Additionally β_i' depends on the initial anisotropy r_0 according to equation (9)

$$\sum_i \beta_i = r_0 \quad (9)$$

Equation (9) typically, 100 spin-correlation times uniformly spaced at log scale and 100 lifetimes equidistantly spaced in the logarithmic time-scale for the Maximum Entropy Method (MEM) analysis²⁵⁶.

4.2.6.2 Time-resolved acrylamide quenching measurements

Changes in the mean fluorescence lifetime after adding acrylamide aliquots (dissolved in the same buffer as the proteins) were used to construct Stern-Volmer (SV) plots. They were fitted by the modified Stern-Volmer equation (eq.10)²⁵⁷ transformed to the form of:

$$\frac{\tau_0}{\tau} = \frac{(k_q\tau_0[Q]+1)}{(k_q\tau_0[Q]f_b+1)} \quad (10)$$

Legend: τ_0 – mean fluorescence lifetime in the absence of quencher, τ – mean fluorescence lifetime in the presence of quencher, $[Q]$ – concentration of acrylamide, k_q – bimolecular quenching constant, f_b – inaccessible fraction of the fluorophore.

4.2.7 Limited proteolysis

Limited proteolysis was done using proteolytic enzyme trypsin, to cleave proteins in a selective manner. The idea behind limited proteolysis is that certain amino acid residues, such as arginine or lysine for trypsin, are usually the targets of particular peptide bond cleavage by proteolytic enzymes within proteins. Peptide bonds C-terminal to arginine or lysine residues are broken by trypsin. Under carefully monitored experimental settings, including buffer composition, temperature, reaction duration, and enzyme concentration, limited proteolysis is carried out. These circumstances are designed to cause the protein to partially breakdown, producing a variety of different-length protein fragments^{258–262}.

Measurement was performed in the protein buffer: 50 mM Tris-HCl pH 8.0, 500mM NaCl, 1mM TCEP, 10% (w/v) glycerol, 0.01% tergitol. Each sample contained 50pmol of phosphorylated Nedd4-2¹⁸⁶⁻⁹⁷⁵ wild type construct either with or without 100pmol 14-3-3 η (so the ratio between them would be 1:2, respectively). They were digested by trypsin at 25°C, either for 10, 20 or 30 minutes (protease : protein = 1 : 1000, w/w). Undigested protein served as the 0 time point. To stop the digestion, reactions were quenched by adding SDS-PAGE

loading buffer and boiling for 5 minutes at 95°C. The results were resolved by SDS-PAGE. Density of selected bands that represent degradation of Nedd4-2 (at noted time-points) were quantified using Image Lab software. Statistical significance was determined using student t-test (Bio-Rad).

4.2.8 Chemical crosslinking coupled with mass spectrometry

Chemical crosslinking coupled with mass spectrometry (XL-MS) is a versatile technique, providing valuable information about the spatial arrangement of interacting residues within a biomolecular assembly.

Chemical crosslinking involves the covalent linkage of proximal amino acid residues within a protein or between different subunits of a complex. This is achieved by introducing bifunctional reagents that possess two reactive groups capable of forming covalent bonds with specific functional groups on amino acids. The goal is to capture information about proximal residues within a protein or between interacting proteins in a complex. The choice of crosslinking reagent is crucial, as it determines the types of bonds that will form. Reagents with specific chemical functionalities, such as amino-reactive or carboxyl-reactive groups, allow for selective targeting of particular amino acid side chains. Crosslinking agents which are used in this dissertation includes disuccinimidyl suberate (DSS), disuccinimidyl glutarate (DSG) which helps in obtaining low-resolution structural information about large and dynamic complexes. The length and flexibility of the crosslinking reagent play a critical role in determining the spatial constraints of the crosslinked residues.

Mass spectrometry measurements with coupled chemical crosslinking were performed additionally to obtain further structural information about Nedd4-2 alone and together with 14-3-3 proteins. Sample preparation consisted of overnight dialysis (buffer composition: 20 mM HEPES pH 7.5, 150 mM NaCl and 1 mM TCEP). Nedd4-2 and 14-3-3 were mixed in a 1:2 molar ratio. Different homobifunctional crosslinking agents were prepared from fresh stock solutions (10 mg/ml, dissolved in DMSO) and were added to samples in a 50× molar excess. Reaction volume was 20 µl and the reaction lasted for 1 h at room temperature.

Quantitative studies consisted of mixing Nedd4-2¹⁸⁶⁻⁹⁷⁵ by itself or with 2× molar excess of 14-3-3 η with 50× molar excess of light (12 C) and heavy (13 C) disuccinimidyl adipate (DSA, purchased from Creative Molecules). Incubation lasted for 30 minutes, at room temperature.

Afterwards, Nedd4-2¹⁸⁶⁻⁹⁷⁵ with 14-3-3 η (labelled with 13 C) and Nedd4-2¹⁸⁶⁻⁹⁷⁵ alone (labelled with 12 C) were mixed together in a 1:1 ratio. Next step consisted of overnight trypsin digestion (enzyme : protein = 1 : 20, w/w) at 37°C. The next day, sample was injected into the Luna Omega 3 μ m Polar C18 100 Å 150 \times 0.3 mm column (Phenomenex) which was desalted at a 10 μ l/min flow rate for 5 min.

Eluted proteins were separated by reversed-phase chromatography. This was done using the same column (heated at 50°C) with a 10 μ l/min flow rate using a capillary UHPLC 1290 system (Agilent Technologies) with a gradient sequence of 1-10% for 1 min, 10-45% for 19 min, and 45-95% for 5 min of buffer solvent A (0.1% formic acid, 98% acetonitrile in water) in buffer solvent B (0.1% formic acid, 2% acetonitrile in water). Column was directly connected to 15T solariX XR FT-ICR mass spectrometer (Bruker Daltonics, USA) operated in a positive data-dependent mode. Data obtained from this experiment was exported using Data Analysis v. 5.3 software (Bruker Daltonics, USA). In order to identify cross-linked samples, StavroX software was used.

The modifications were set as variable methionine oxidation and fixed cysteine carbamidomethylation. The -NH₂ group of lysine and the N-terminus of the peptides were considered as the modification sites for DSA and BS3. A 3-ppm value was set for the mass error threshold, and manual curation was done for all assigned fragments. Crosslinking coupled with mass spectrometry experiments and the following data processing was done in collaboration with RNDr. Petr Pompach, Ph.D., and Mgr. Pavla Vaňková, Ph.D. employed at the facility of the Institute of the Academy of Sciences of the Czech Republic in BIOCEV.

Fixed carbamidomethylation of cysteine and variable methionine oxidation were set as modifications. The modification sites of DSG and DSS were N-termini, lysine, serine, threonine and tyrosine. The mass error threshold was set to 1 ppm, and all assigned fragments were manually curated. To identify cross-linked peptides, Links software was used. The no overlapping isotopes of peptides cross-linked with 12 C and 13 C DSA were used to calculate isotope ratios.

4.2.9 Protein crystallography

Protein crystallography is a method used to determine the atomic structure of proteins. This technique provides valuable insights into protein function and aids in the design of therapeutic agents. Basic principle behind that is, the individual arrangement of atoms, molecules, or ions within a crystal is called a crystal structure. Crystal structure consists of a motif, collection of atoms (molecules/ions) arranged in a certain way and a lattice. Crystal lattice represents a three-dimensional collection of points that are repeated regularly. Motifs are located on the points of the lattice. Unit cell is an abstract term that represents a “box” (whose vertices match to the aforementioned points) that contains 1 motif which will be repeated throughout the whole lattice. Parameters of the lattice represent the length of the unit cell edges and angles between them.

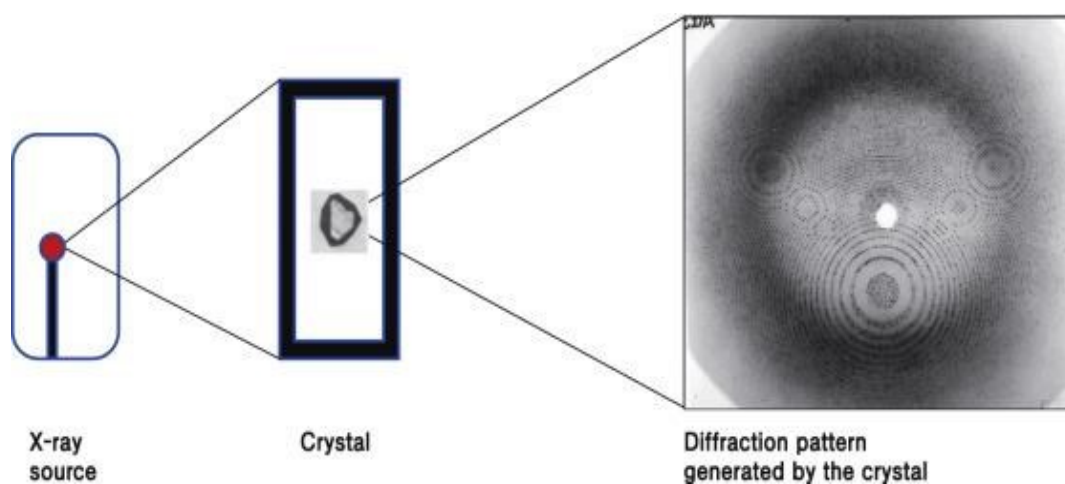


Figure 4.6: The X-ray crystallography principle. The virus particles' crystals produce a diffraction pattern that can be used to determine the high-resolution capsid structure (Figure taken from Wang-Shick Ryu, 2017)²⁶³.

X-ray crystallography is a field which uses X-ray diffraction to determine the geometry or the form of a specific molecule (that has the ability to crystallize). It is based on possibility of X-rays to elastically scatter from molecules whose interatomic spacing within the crystal is comparable to the wavelength of X-rays. After they impact the crystal, they scatter in a variety of directions. From this detected diffraction pattern (contains information of the angles and intensities of the scattered beams), it is possible to determine the arrangement of atoms within the crystal (Fig. 4.6) and therefore its three-dimensional image. Vast number of molecules are

known to be able to crystallize (metals, minerals, salts, biological molecules, semiconductors). The advancement of numerous scientific disciplines has been greatly aided by X-ray crystallography²⁶³⁻²⁶⁵.

According to Bragg's law, an interference pattern of the waves in an incident X-ray beam arises when X-rays are incident on a crystal with regularly ordered atoms. Crystal structure and identification of crystalline compounds can be ascertained by X-ray diffraction. In addition, it can be used to assess the size of the crystallites, the residual stress on the crystals, and the distribution of the crystal orientation inside the material.

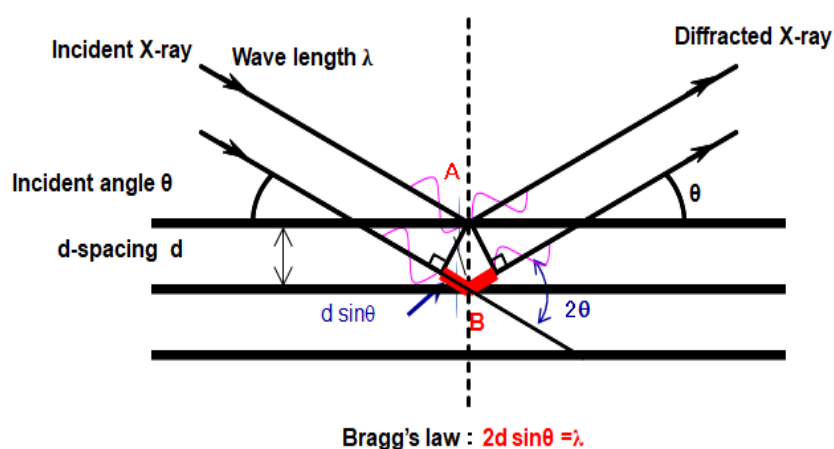


Figure 4.7: Schematic representation of the Bragg equation. The grid represents a two-dimensional crystal lattice with a set of imaginary planes. When X-rays strike a crystal at an angle θ , coherent diffraction (in phase) occurs when the difference in distance travelled ($2d\sin\theta$) equals an integral number of the wavelength ($n\lambda$) (Figure is taken from Toray Research Center, Inc webpage).

These reflections only happen in specific circumstances that meet the requirements of the Bragg's equation (Fig. 4.7). Denoted on the figure are: d – distance between atomic planes, θ – angle of the incident X-ray beam, n – integer (1, 2, 3... n). X-ray beam can reflect off a nearby atomic plane, and take a longer path (still parallel). In order to have constructive interference, path length difference needs to be equal to an integer value of the incident X-ray beams^{264,265}.

We attempted to crystallize the complex between 14-3-3 γ Δ C construct and Nedd4-2 peptide (possesses the phosphorylation site S342: LRSCpSVTDAV) in a 1:2 ratio. All proteins were in the buffer with the same composition (20 mM HEPES pH 7, 2 mM MgCl₂ and 1 mM TCEP). Crystallization was done using the hanging-drop vapour-diffusion method. Temperature was

291 K. Crystals of 14-3-3 γ Δ C:pepS342 peptide complex were grown in 3 μ l drops: 1 μ l of the protein complex with 16.5 mg/ml concentration and 2 μ l of precipitating solution (100 mM sodium citrate (pH 5.6), 200 mM potassium sodium tartrate, and 1.8 M ammonium sulphate). 30% (v/v) PEG 400 was used as a cryoprotectant. Crystals were flash frozen in liquid nitrogen before data collection¹¹⁸.

5. Results

5.1 Mutagenesis, expression, purification and labelling of recombinant proteins.

As previously described in chapter 4.2 experimental methods, all Nedd4-2 and 14-3-3 proteins were expressed and purified according to standard protocol. This section shows particular results of the individual expressions and purifications of the 14-3-3 and Nedd4-2 proteins, as well as the subsequent phosphorylation and labelling of the Nedd4-2 protein. The results of each purification stage was as follows:

5.1.1 Site directed mutagenesis of Nedd4-2 protein

A previous work done in our laboratory suggested that the 14-3-3 protein alters the interactions between the structured domains of Nedd4-2, causing a structural rearrangement of Nedd4-2¹¹⁸. In order to better understand 14-3-3:Nedd4-2 interaction and to study its effect on individual Nedd4-2 domains, we mapped the positions of each Nedd4-2 domain in order to insert a single cysteine at different positions (Fig. 5.1).

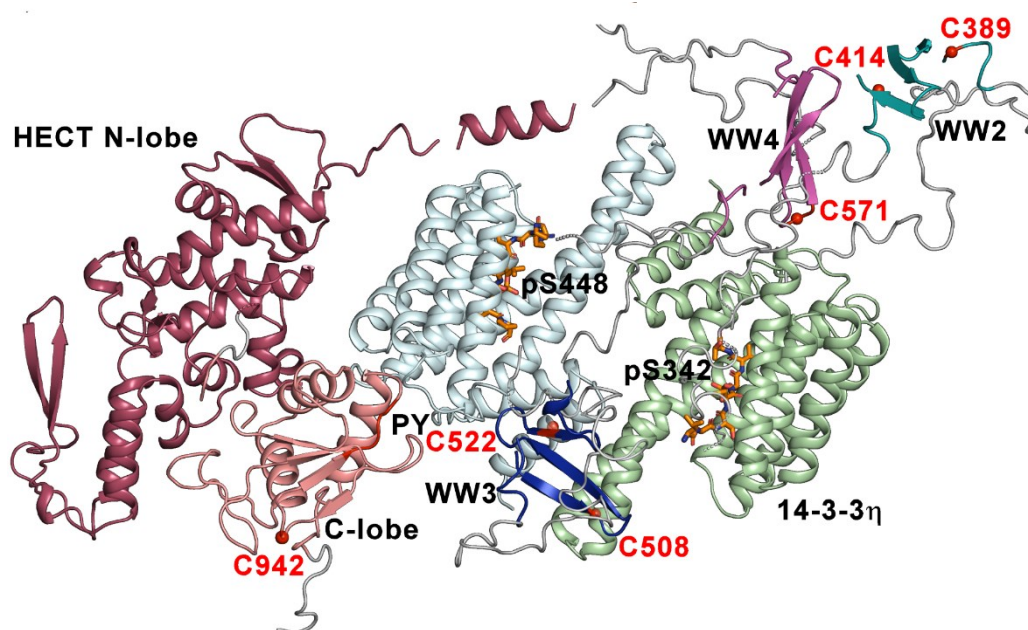


Figure 5.1: Selected positions of Nedd4-2 residues for incorporation of cysteine residues and subsequent labelling with IAEDANS. The SAXS-based model of the pNedd4-2¹⁸⁶⁻⁹⁷⁵:14-3-3 η complex. Nedd4-2 domains: WW2, WW3, WW4, and HECT. Orange sticks represent the phosphorylated 14-3-3 binding motifs of Nedd4-2 (PDB: 6ZBT and 6ZC9). Red balls represent the selected positions for cysteine incorporation in Nedd4-2 domains (Figure is taken from Joshi R. *et al* 2022)²⁶⁶.

In this work, we used two Nedd4-2 constructs: Nedd4-2¹⁹⁰⁻⁵⁸¹ and Nedd4-2¹⁸⁶⁻⁹⁷⁵, which lack N-terminal C2 domain. Nedd4-2¹⁹⁰⁻⁵⁸¹ contained all three phosphorylation sites and all four WW domains. The second construct, Nedd4-2¹⁸⁶⁻⁹⁷⁵, contained four WW domains and HECT domain including all three phosphorylation sites (Fig. 5.2)

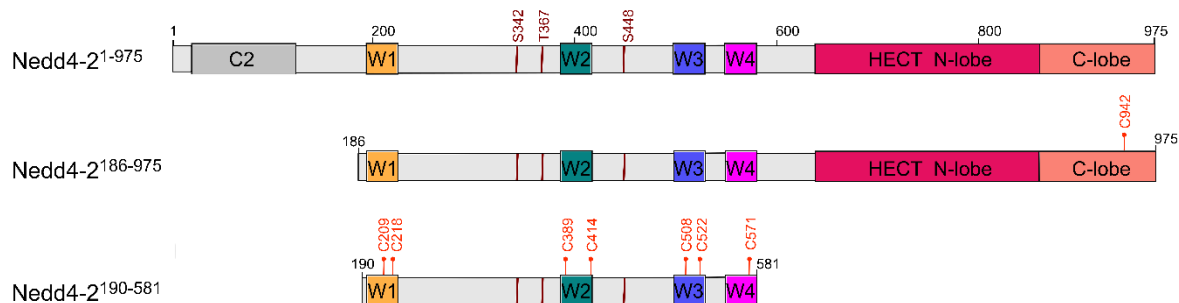


Fig. 5.2: Schematic representation of Nedd4-2 full-length protein and its constructs. Domains are represented by following colours: C2 domain – grey, WW1-4 domains – yellow, teal, blue and magenta (respectively), N-lobe of the HECT domain – salmon, C-lobe of the HECT domain – raspberry. Three 14-3-3 binding sites (S342, T367, and S448) are marked with red lines. Underneath are shown two shorter constructs, Nedd4-2¹⁸⁶⁻⁹⁷⁵ and Nedd4-2¹⁹⁰⁻⁵⁸¹ (along with their mutated variants, labelled in red), that were used in the present study. Cysteine residues that were labeled by 1,5-IAEDANS are marked with red dots. (Figure is taken from Joshi R. et al 2022)²⁶⁶.

The Nedd4-2¹⁹⁰⁻⁵⁸¹ sequence consists only of a single cysteine residue at position C341. Thus, we initially created a template by mutation into C341S. Following that, we performed more modifications by substituting the cysteine residue at the specific location (T209C, S218C, S389C, T414C, A508C, T522C, and S571C) using site directed mutagenesis approach.

Nedd4-2¹⁸⁶⁻⁹⁷⁵ consists of five cysteine at positions (C702, C776, C853, C874 and C942) in the HECT domain. Initially, we performed the mutation at position C341S to prepare a template. Afterwards, we did further mutations using this template, in a way that just one cysteine remains and the other four have been replaced to serine. Eight variants of Nedd4-2 containing a single cysteine were prepared, from out of eight; seven single cysteine variants of Nedd4-2¹⁹⁰⁻⁵⁸¹ (C209, C218, C389, C414, C508, C522, and C571) and one single cysteine variants of Nedd4-2¹⁸⁶⁻⁹⁷⁵ (C942) (Table 5.1). Sequencing confirmed that cysteine had been incorporated in both Nedd4-2 constructs.

Table 5.1 Nedd4-2 cysteine mutants

Construct	Domains present in the constructs	Incorporated locations of cysteine variants	Incorporation of cysteine confirmed by sequencing
Nedd4-2 ¹⁹⁰⁻⁵⁸¹	WW 1-4	C341, T209, T218, S389, T414 A508, T522, S571	Yes
Nedd4-2 ¹⁸⁶⁻⁹⁷⁵	WW 1-4, HECT	C702, C776, C853, C874, C942	Yes

5.1.2 Expression and purification of Nedd4-2¹⁹⁰⁻⁵⁸¹ variant

Since the majority of cysteine variants were produced using a Nedd4-2¹⁹⁰⁻⁵⁸¹ construct for fluorescence measurements, that construct was crucial in my study.

The Nedd4-2¹⁹⁰⁻⁵⁸¹ variants were purified according to the previous section (4.2.3.1). As better-quality protein is required for protein labelling and the following fluorescence measurement. Nedd4-2 was first purified using Ni²⁺ NTA affinity chromatography and the resulting protein was eluted with 10 ml of elution buffer (buffer F). The obtained protein is further purified by size-exclusion chromatography using Superdex 75 HiLoad 26/600 column (GE Healthcare, USA). SDS-PAGE was run after every purification step to check quality of protein (Fig.5.3). Since the purification outcomes for every Nedd4-2 variants were nearly same, so just one SDS PAGE gel image of Nedd4-2¹⁹⁰⁻⁵⁸¹ C508 is shown.

Differential scanning fluorimetry was used to assess the stability of each variant protein; all variations were found to be stable (see chapter DSF). In order to form a complex with 14-3-3 proteins, the protein was then phosphorylated (see method section). Native TBE PAGE was used to check that the Nedd4-2 could form a complex with the 14-3-3 protein (Fig.5.3). The phosphorylation at the expected position has been confirmed using mass spectrometry analysis at the CMS facility, BIOCEV. All Nedd4-2¹⁹⁰⁻⁵⁸¹ variants typically yielded ~2-3 mg protein from a 3 l cell culture. The protein was either stored at -80 °C or used further for 1,5-IAEDANS labelling.

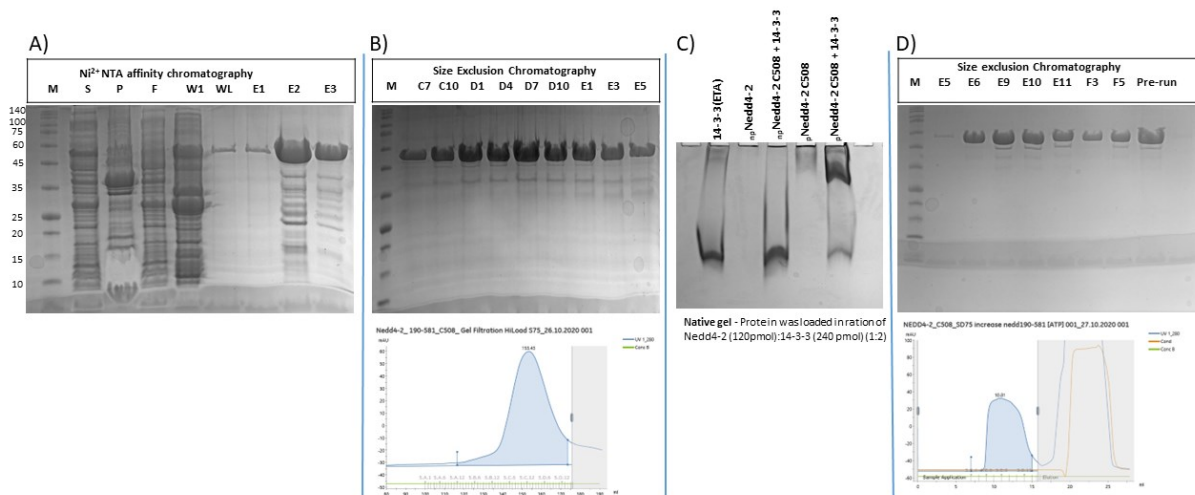


Figure 5.3: Expression and purification of Nedd4-2¹⁹⁰⁻⁵⁸¹ C508 variant protein (A) SDS PAGE (12%) after protein purification by Ni²⁺ NTA affinity chromatography (B) Eluted fractions by size exclusion chromatography using Superdex 75 HiLoad 26/600 column, SDS-PAGE (12%) and corresponding chromatogram (C) Native TBE PAGE gel of non-phosphorylated and phosphorylated Nedd4-2; phosphorylated Nedd4-2 forms a complex with 14-3-3 (D) Final protein purification by size-exclusion chromatography, SDS-PAGE gel after. The selected fractions (shown in the blue colour in chromatogram) were collected. Protein standards are indicated as M and eluted fraction shown with respective numbers.

5.1.3 Expression and purification of Nedd4-2¹⁸⁶⁻⁹⁷⁵ variants

Only the Nedd4-2¹⁸⁶⁻⁹⁷⁵ C942 variant protein was stable and soluble among the five variants. Thermal stability of this variant was also analysed by DSF analysis. Non cleavable, N-terminal His-tagged protein was expressed and purified using the optimized protocol, as mentioned before (section 4.2.3.2). This protocol was the same as for the Nedd4-2¹⁹⁰⁻⁵⁸¹, so the fusion protein was purified in the same manner. But the size exclusion chromatography was performed using Superdex 75 HiLoad 26/600 column (GE Healthcare, USA) big column, despite the fact that the Nedd4-2¹⁸⁶⁻⁹⁷⁵ mutant protein has a bigger molecular weight than the Nedd4-2¹⁹⁰⁻⁵⁸¹ proteins. SDS-PAGE was run after every purification step and on (Fig. 5.4) it is visible that the protein is soluble and of good quality. After size-exclusion chromatography, protein was phosphorylated by PKA. Native PAGE confirmed the binding of Nedd4-2¹⁸⁶⁻⁹⁷⁵ C942 with 14-3-3 protein. The typical purification yield was about 3 mg from 3L of cell culture. Afterwards, this protein was used for 1,5-IEADANS labelling or stored at -80 °C.

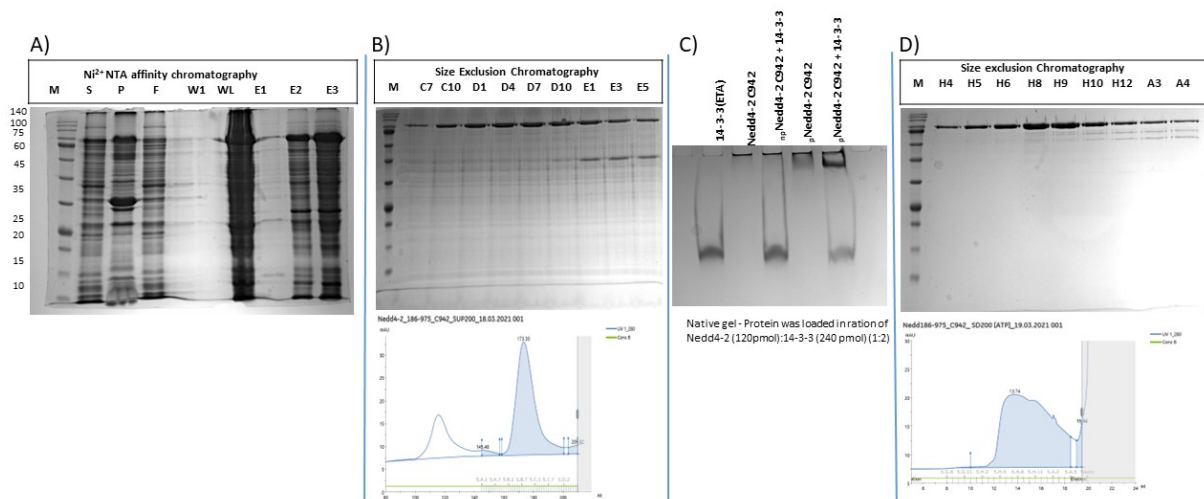


Figure 5.4: Expression and purification of Nedd4-2¹⁸⁶⁻⁹⁷⁵ C942 variant protein (A) Ni²⁺ - NTA affinity chromatography purification SDS PAGE (12%) (B) protein purification by size exclusion chromatography using Superdex 75 HiLoad 26/600 column, SDS PAGE (12%) and chromatogram (C) Native TBE PAGE gel of non-phosphorylated and phosphorylation Nedd4-2¹⁸⁶⁻⁹⁷⁵ – it is visible only phosphorylated protein can bind 14-3-3 (D) Final size-exclusion chromatography performed to remove ATP from protein after phosphorylation reaction, SDS-PAGE gel. The collected fractions are shown as the blue area under the curve of the chromatogram. M indicates protein standards marker and eluted fraction shown with respective numbers.

5.1.4 Expression and purification of 14-3-3 protein

The 14-3-3 proteins were purified using standardized protocols, as described (section 4.2.1). 14-3-3 η isoform was used mainly in this work. The 14-3-3 η protein was expressed using *E. coli* strain BL21(DE3) expression system. The 14-3-3 protein was purified using a series of purification steps, beginning with Ni²⁺ NTA affinity chromatography, followed by anion exchange chromatography, and finally size exclusion chromatography using a Superdex 75 HiLoad 26/600 column. The obtained results of expression and purification of 14-3-3 η from 4L cell culture are as follows (Fig. 5.5).

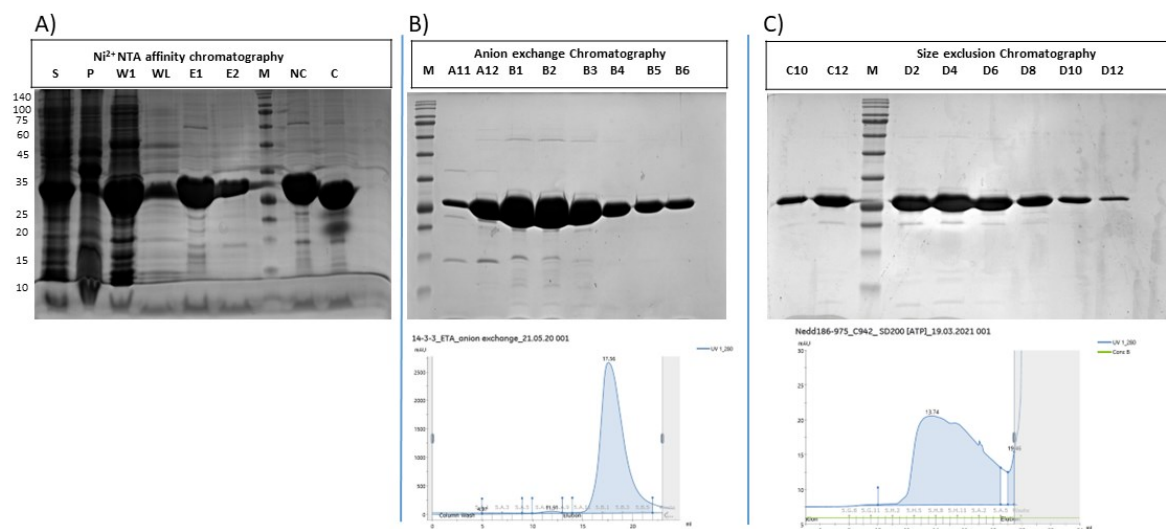


Figure 5.5: The 14-3-3 η protein expression and protein purity following all purification steps A) SDS gel following Ni²⁺ NTA affinity chromatography and B) Anion exchange chromatography gel C) size exclusion chromatography using 15% SDS PAGE.

5.2 Assessing the protein stability by DSF

In order to assess protein unfolding, DSF monitors fluorescence changes with temperature. The Nedd4-2 mutant's thermal stability was analysed by differential scanning fluorimetry which measure thermally induced protein denaturation (See.4.2.6). Using the Roche Light Cyclers 480 SW 1.5 software, the melting temperature values (T_m), which correspond to the melting curves' inflection points, were determined as the minimum of the negative first derivative. The final results were taken from the means of three measurements. Using DSF, the protein unfolding transition's midpoint temperatures (T_m) were determined for each Nedd4-2 mutant in order to evaluate their stability. All Nedd4-2 variants showed similar T_m values, with the exception of Nedd4-2¹⁹⁰⁻⁵⁸¹ C508 (Table 5.2). The Nedd4-2¹⁹⁰⁻⁵⁸¹ C508 variant's somewhat decreased T_m could be the result of the altered WW3 domain taking on a different conformation.

Table 5.2. Thermal stability of Nedd4-2 variants. (Table taken from Joshi *et.al.* 2022)²⁶⁶.

Sr. No.	Nedd4-2 construct	Nedd4-2 variants	<i>T_m</i> (°C)
1	Nedd4-2 ¹⁹⁰⁻⁵⁸¹	C209	54.2 ± 0.1
2		C218	55.3 ± 0.1
3		C389	53.6 ± 0.1
4		C414	55.7 ± 0.2
5		C508	51.06 ± 0.05
6		C522	56.5 ± 0.2
7		C571	54.4 ± 0.3
8		WT	56.29 ± 0.05
9	Nedd4-2 ¹⁸⁶⁻⁹⁷⁵	C942	41.34 ± 0.06
10		WT	39.5 ± 0.4

5.3 Labelling of recombinant proteins by 1,5-IAEDANS

Purified Nedd4-2 protein variants were labelled with 1,5-IAEDANS dye in order to measure by fluorescence spectroscopy. Fluorescence labelling was confirmed by LC-MS technique at CMS, BIOCEV (refer to the attached publication I: Joshi *et al.* 2022 in supplement)²⁶⁶. By this approach, we were able to monitor local conformational changes in different regions of Nedd4-2 protein (Fig.5.3).

Table 5.3 Parameters of individual Nedd4-2 variants and concentration after 1,5 IEADANS labelling.

Sr. No.	Labelled Protein variants by 1,5-IAEDANS on position	Stock Conc. (mg/ml)	Stock Conc. (µM)	Molecular weight (Da)
1	Nedd4-2 ¹⁹⁰⁻⁵⁸¹ C389	0.378	8.39	45020
2	Nedd4-2 ¹⁹⁰⁻⁵⁸¹ C209	0.240	5.39	45020
3	Nedd4-2 ¹⁹⁰⁻⁵⁸¹ C218	0.092	2.00	45020
4	Nedd4-2 ¹⁹⁰⁻⁵⁸¹ C414	0.247	5.53	45020
5	Nedd4-2 ¹⁹⁰⁻⁵⁸¹ C508	0.187	4.17	45020
6	Nedd4-2 ¹⁹⁰⁻⁵⁸¹ C522	0.212	4.74	45020
7	Nedd4-2 ¹⁹⁰⁻⁵⁸¹ C571	0.080	1.8	45020
8	Nedd4-2 ¹⁸⁶⁻⁹⁷⁵ C942	0.159	1.74	132244
9	14-3-3η	6.91	243.42	28412

5.4 Time-resolved fluorescence intensity and anisotropy decay measurements

It was shown before that 14-3-3 not only interacts with Nedd4-2 protein but also limits its interaction with target substrates such as membrane proteins^{117,225}. Thus, 14-3-3 is a known negative downregulator of Nedd4-2's. Although the exact molecular mechanism underlying this regulation is still unclear. For that reason, we chose to employ the fluorescence spectroscopic measurements using fluorescently labelled protein variants (Table 5.3).

In our previous study by Pohl et al., we demonstrated that the interaction between 14-3-3 protein and Nedd4-2 lead to structural rearrangements in the WW domains and the N- and C-lobes of the HECT domains of Nedd4-2 protein. To study the effects of 14-3-3 η on Nedd4-2 domains, we performed time-resolved fluorescence intensity measurements, using 1,5-IAEDANS labelled cysteine variants of Nedd4-2¹⁹⁰⁻⁵⁸¹ and Nedd4-2¹⁸⁶⁻⁹⁷⁵. 1,5-IAEDANS dye is sensitive to changes in its microenvironment, undergoes changes in fluorescence properties, mainly in quantum yield and emission lifetime based on polarity of surroundings.

Fluorescence lifetime measurements were useful in detecting subtle solvation and conformational changes upon 14-3-3 binding. Due to the complex decay patterns observed, we utilized mean fluorescence lifetime (τ mean) as a sensitive qualitative indicator of changes in the local environments of 1,5-IAEDANS-labelled cysteines. The emission lifetimes of C209 and C218 from the WW1 domain were quite short compared to the other mutants (15.4 and 15.1 ns, respectively), and they were unaffected by 14-3-3 η binding (Fig.5.6 and Table 5.4). Protein variants from WW2 (C389, C414) and WW3 (C508) domains showed the highest τ mean values (17.0, 16.7, and 16.8 respectively), indicating a less polar fluorophore microenvironment. Proteins variants C522 from the WW3 domain, C571 from the WW4 domain, and C942 from the C-lobe of the HECT domain exhibited comparatively lower τ mean values.

The most significant effect of 14-3-3 η binding was found on WW3 domain mutants C508 and C522, where τ mean increased by approximately 1.4 ns. The binding of 14-3-3 protein also affected mutants C389, C414, and C571 from the WW2 and WW4 domains, which displayed higher τ mean in the complex; this effect was most apparent in the C389 variation, where τ mean increased by approximately 0.7 ns. This may be the result of conformational changes in Nedd4-2 caused by 14-3-3, which may have an impact on interactions with dansyl fluorophore

and/or direct interaction with 14-3-3 η , which may influence dansyl solvation. On the other hand, the mutant variant containing the C942 in the C-lobe of HECT domain, which was tagged with 1,5-IAEDANS, showed a 0.3 ns reduction in the τ mean, suggesting that there were more contacts with the polar environment. This might be related to either higher solvation or quenching interactions. This implies that the structure of the Nedd4-2 C-lobe in the apo-state is influenced by 14-3-3 binding. (Fig. 5.6 and Table 5.4)

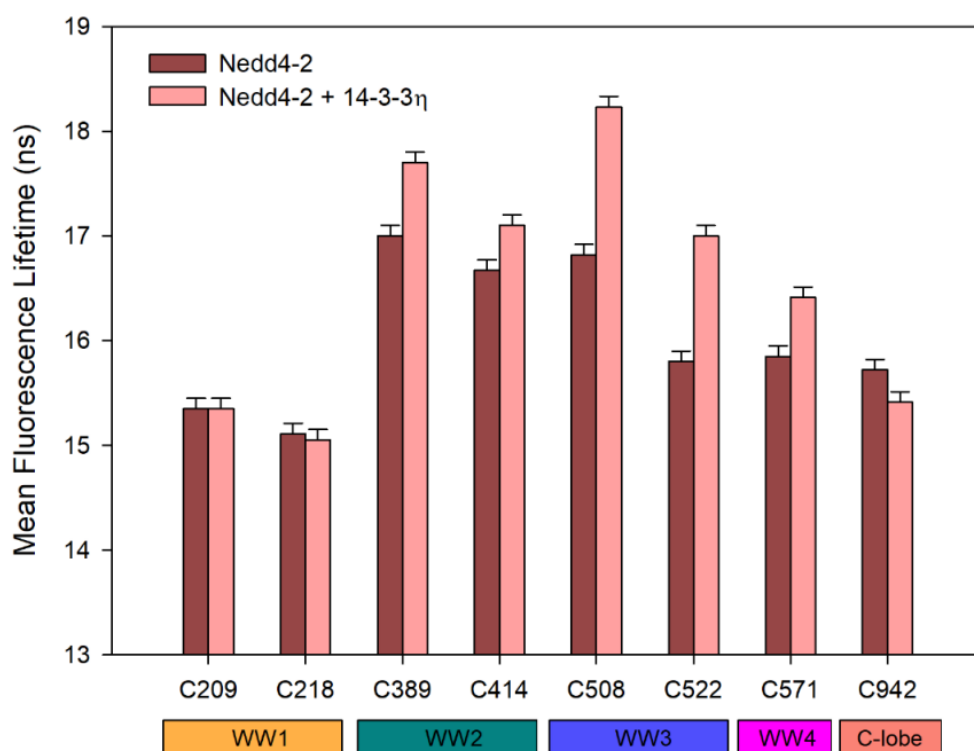


Figure 5.6: Nedd4-2 variants and 14-3-3 binding's dependent changes in mean fluorescence lifetime. The positions of cysteine residues labelled with 1,5-IAEDANS within the Nedd4-2 domains can be seen at the bottom. WW1: C209 and C218, WW2: C389 and C414, WW3: C508 and C522, WW4: C571. Catalytic C942 corresponds to the C-lobe of the HECT domain. Each error bar showing the standard deviation (Figure taken from Joshi *et.al.* 2022)²⁶⁶.

Table 5.4 Summary of the time-resolved IAEDANS fluorescence measurements²⁶⁶

Nedd4-2 variant	$\tau_{mean}^{a,b}$ (ns)	$k_q (\times 10^{-8})$ ($M^{-1} s^{-1}$) ^h	F_b	$\varphi_1^{c,d}$ (ns)		φ_2^e (ns)		φ_3^e (ns)		φ_4^f (ns)		φ_5^g (ns)	
Nedd4-2¹⁹⁰⁻⁵⁸¹													
C209	15.4	4.3	0.27	0.1	0.19	1.4	0.05	9.5	0.05	79	0.06		
C209 + 14-3-3 η	15.4	4.6	0.29	0.1	0.17	0.5	0.05	3.9	0.04	15	0.02	>200	0.06
C218	15.1	7.1	0.15	0.1	0.27	0.5	0.01	2.6	0.02	17	0.03	170	0.01
C218 + 14-3-3 η	15.1	6.9	0.30	0.1	0.26	0.5	0.03	3.9	0.01	15	0.02	>200	0.02
C389	17.0	2.7	0.30	0.1	0.08	1.1	0.04	3.9	0.07	26	0.13	>200	0.04
C389 + 14-3-3 η	17.7	1.5	0.28	0.1	0.08	1.6	0.04	6.5	0.05	50	0.11	>200	0.06
C414	16.7	2.6	0.31	0.1	0.08	1.4	0.06	6.6	0.07	35	0.10	>200	0.03
C414 + 14-3-3 η	17.1	2.0	0.31	0.1	0.08	1.9	0.06	9.4	0.07	97	0.04	>200	0.08
C508	16.8	2.7	0.25	0.1	0.10	1.3	0.02	4	0.06	12	0.08	79	0.07
C508 + 14-3-3 η	18.2	1.5	0.22	0.1	0.07	0.6	0.03	3.8	0.05	16	0.05	>200	0.14
C522	15.8	3.6	0.33	0.1	0.08	1.1	0.07	6.1	0.09	39	0.07	>200	0.03
C522 + 14-3-3 η	17.0	1.7	0.31	0.1	0.09	1.4	0.05	6.2	0.05	47	0.08	>200	0.07
C571	15.9	3.2	0.32	0.1	0.09	1.9	0.10	14.1	0.08	67	0.03	>200	0.03
C571 + 14-3-3 η	16.4	1.8	0.26	0.1	0.09	1.1	0.06	6.0	0.07	76	0.08	>200	0.05
Nedd4-2¹⁸⁶⁻⁹⁷⁵													
C942	15.7	5.5	0.49										
C942 + 14-3-3 η	15.4	7.4	0.56										

^aMean lifetimes were calculated as $\tau_{mean} = \sum_i f_i \tau_i$, where f_i is an intensity fraction of the i -th lifetime component τ_i .

^bSD = ± 0.1 ns.

^cAnisotropies $r(t)$ for a series of exponential were analysed using a model-independent maximum entropy method, with no presumptions regarding the shape of the correlation time distributions²⁵², $r(t) = \sum_k (\beta_k \exp(-t/\varphi_k))$, where amplitudes β_k represent the distribution of the correlation times φ_k . β_n presented in the table are peaks of the distribution positioned at correlation times φ_n .

^eInaccessible fraction, SD = ± 0.02 .

^fBimolecular quenching constant, SD = $\pm 0.2 (\times 10^{-8} M^{-1}s^{-1})$

5.4.1 Time-resolved emission polarization anisotropy measurements

We assumed that interactions with 14-3-3 η could affect certain residues' solvent exposure and mobility. To address this question, we used time-resolved emission polarization anisotropy measurements to determine segmental motions in cysteine tagged with 1,5 IAEDANS in order to investigate this. Table 5.4 presents the summarised results for seven Nedd4-2¹⁹⁰⁻⁵⁸¹ variations. Unfortunately, low signal intensity prevented accurate observations of time-resolved fluorescence anisotropy for Nedd4-2¹⁸⁶⁻⁹⁷⁵ C942. Five different classes of correlational times were identified by the polarization anisotropy decays, suggesting complex dynamics. The fluorophore itself initially moved slowly (3.8 to 9.5 ns and 12 to 97 ns), most likely due to the asymmetric rotor rotating freely²⁴¹. Then, faster (0.1 to 1.9 ns) motions were seen. Because of

finite dansyl lifespan, the largest component, ϕ_5 , may have represented movement of the Nedd4-2:14-3-3 complex, albeit poorly resolved with possible modest aggregation.

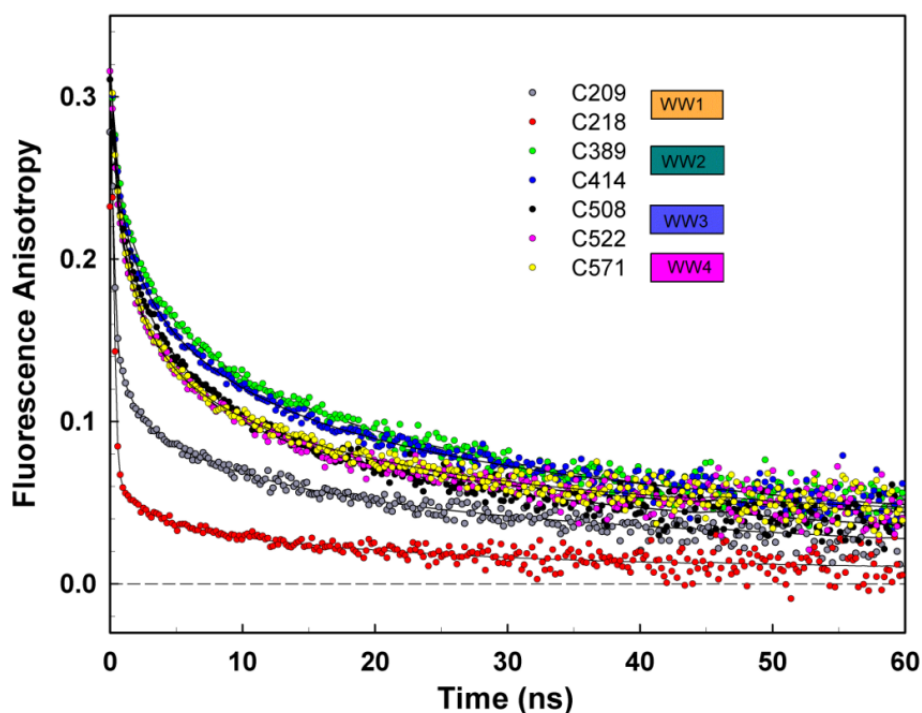


Figure 5.7: Nedd4-2's WW domains show various mobilities. Nedd4-2¹⁹⁰⁻⁵⁸¹ variants fluorescence anisotropy decays which were labelled with 1,5-IAEDANS (Figure taken from Joshi *et.al.* 2022)²⁶⁶.

The 1,5-IAEDANS-labelled Nedd4-2¹⁹⁰⁻⁵⁸¹ time-resolved fluorescence anisotropy decays showed three different groups according to dansyl mobility (see Fig.5.7). The change in the total amplitudes of the fast anisotropy decay components (β_{FAST}) was used to measure the amount of segmental mobility and changes induced by 14-3-3 binding. A higher β_{FAST} value reflected reduced steric hindrance in the fast-depolarizing motion of the fluorophore, likely correlating with increased internal protein mobility. C208 and C218 from the WW1 domain were in the first group with the highest internal mobility (with β_{FAST} values of 0.24 and 0.28, respectively), suggesting significant amount of solvent exposure. C218 appeared to be the most mobile mutant, suggesting a high degree of exposure to the solvent (Fig. 5.8). The elevated solvent exposure of C209 and C218 is further supported by their relatively short emission lifetimes of 15.4 and 15.1 ns, respectively (as indicated in the table 5.4). The WW2 domain's C389 and C414 mutants (with β_{FAST} values of 0.11 and 0.14, respectively) made up the second group, which had the maximum internal rigidity with longer emission lifetimes of 17.0 and 16.7

ns, respectively, suggested a less polar environment (Table 5.4). The third group was composed of mutants with intermediate internal flexibility from the WW3 and WW4 domains. Mutants in these groups showed similar fluorescence anisotropy decays in the unliganded form, indicating similar internal mobilities and general hydrodynamic properties of the protein (see Fig. 5.8 and Table 5.4).

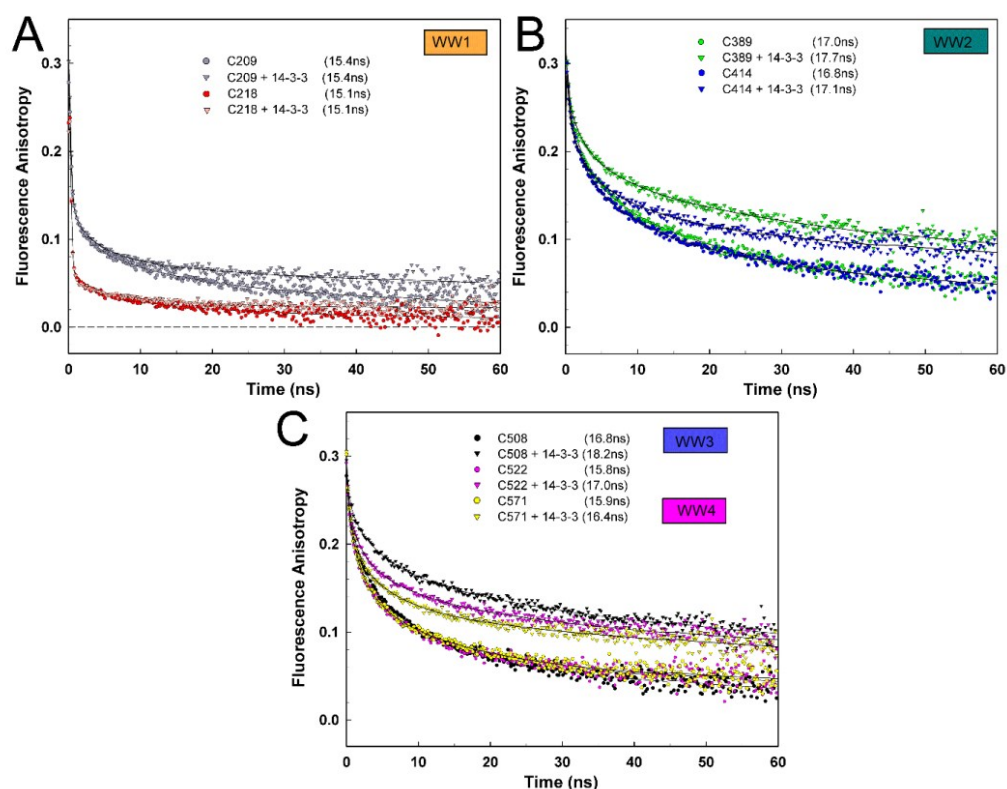


Figure 5.8: Influence of 14-3-3 η on the fluorescence anisotropy decays of WW domains of Nedd4-2 variants. Each panel represents a WW domain: (A) WW1, (B) WW2 domain, (C) WW3 and WW4 domain (Figure taken from Joshi *et.al.* 2022)²⁶⁶.

5.4.2 Time-resolved fluorescence quenching experiments

In order to investigate the changes in Nedd4-2 structure caused by interaction with 14-3-3 protein, we performed a time-resolved quenching experiment using eight variants of Nedd4-2¹⁹⁰⁻⁵⁸¹ and Nedd4-2¹⁸⁶⁻⁹⁷⁵. We did fluorescence quenching experiments to determine the accessibility of fluorophores to acrylamide. In order to achieve this, we used a time-resolved experiment to reduce the effects of static quenching, an issue that frequently occurs in research

that depends on intensity-based quenching. Consequently, our data revealed Stern-Volmer graphs that displayed curvature (See Fig. Suppl.S10-S13 in Joshi R.2022). The presence of curvature indicates the presence of separate groups of fluorophores that show varying degrees of sensitivity to the quenching agent, acrylamide.

Proteins can exhibit dynamic conformational heterogeneity, causing proteins to fluctuate between different structural states. These states provide different degrees of accessibility to dansyl. To make things easier, we have classified dansyl into two main categories: one that is accessible and the other that is completely inaccessible. In general, we saw that the proportion of dansyl in the inaccessible state (F_b) remained relatively stable among all mutants, usually around 0.3, except for the C218 mutant, which had a lower F_b . The bimolecular quenching constant (k_q) values, derived from fitting the Stern-Volmer plots, are summarized in Table 5.4 and Figure 5.9.

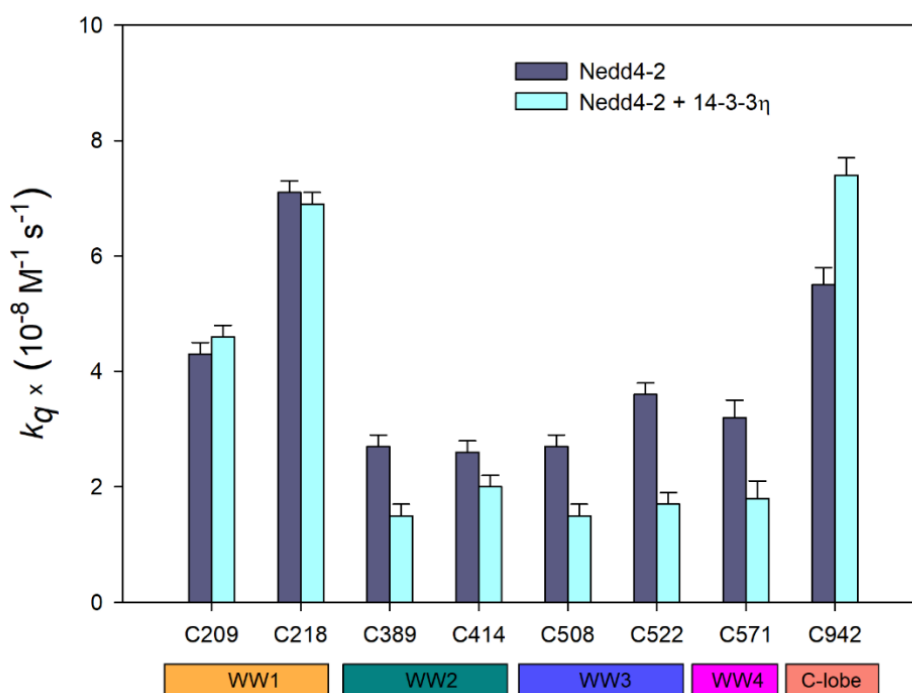


Figure 5.9: 14-3-3 η effect on the distinct bimolecular quenching constant of different Nedd4-2 mutants. (Figure taken from Joshi *et.al.* 2022)²⁶⁶

The results of our quenching experiments suggest that the presence of 14-3-3 η does not have significant effects on the quenching efficiency of the C209 and C218 mutants in the WW1

domain. Their bimolecular quenching constant (k_q) were 4.3 and $7.1 \times 10^{-8} \text{ M}^{-1}\text{s}^{-1}$, respectively. This indicates that dansyl is extensively exposed to the aquatic environment, regardless of the presence of 14-3-3. Out of all the mutations, C218 had the greatest ability to interact with the quencher. This was consistent with its heightened internal movement and reduced emission duration. Only this mutant exhibited significant changes in F_b upon interaction with 14-3-3, resulting in a clear deviation in the quenching curves. However, unbound C218 exhibited around 50% less F_b compared to other mutants, suggesting reduced conformational heterogeneity. Nevertheless, the F_b value of C218 in the presence of 14-3-3 η was similar to that of other mutants, indicating that WW1 is exposed to the solvent and there is a fast depolarization of anisotropy (Fig. 5.8, Table 5.4).

When we investigated mutants from the WW2, WW3, and WW4 domains, we observed a substantial decrease in k_q when bound to the 14-3-3 protein. However, the C942 mutant, which is located in the HECT domain, had a higher k_q value after 14-3-3 binding. While small F_b changes have been observed among these mutants, the reduction in k_q caused by 14-3-3 binding varied: approximately 23% for C414, 44% for C389, C508, and C571, and 53% for C522 (Fig. 5.9). These results were consistent with our anisotropy data, showing the effects of 14-3-3 binding on dansyl rotational mobility in the C508 mutant, whereas the rigid C414 mutant had the least obvious effect. The C942 mutant, on the other hand, exhibited the opposite behaviour, with a 35% rise in k_q upon 14-3-3 binding, which was connected with a decreased mean fluorescence lifetime after binding to the 14-3-3 protein. (Fig.5.9)

5.5 Structural characterization of Nedd4-2¹⁸⁶⁻⁹⁷⁵:14-3-3 η complex by chemical crosslinking coupled mass spectrometry (XL-MS)

Due to the limited structural data of full-length Nedd4-2 and 14-3-3 protein complex available, we did the chemical cross-linking coupled to mass spectrometry measurements (XL-MS) at CMS facility, BIOCEV. Using the crosslinking agent DSG and DSS with Nedd4-2¹⁸⁶⁻⁹⁷⁵ alone and in complex with 14-3-3 η . The obtained results revealed 14-3-3 dependent structural modifications in Nedd4-2. We observed 14 intramolecular cross-linked residues in Nedd4-2 apo form and 13 intramolecular distance restraints in Nedd4-2¹⁸⁶⁻⁹⁷⁵ in complexes with 14-3-3 η (Figs. 5.10a, 5.10b). Most of the crosslinks were found in both conditions, such as the one between K598 from the HECT domain and T275 from the WW1-WW2 linker. In other words,

once the complex has been formed, the distance between these two points remains constant (Fig. 5.10a, 5.10b). Crosslinks between the WW2 domain and the WW1-WW2 linker (K395-T275) and between WW2 and the HECT domain (K398-K822 and K398-S932) were only found in the apo form of Nedd4-2¹⁸⁶⁻⁹⁷⁵. Crosslinks between the WW2-WW3 and WW3-WW4 linkers (S538-S428) and WW3 with the C-lobe of HECT (K531-K935) were identified solely in the complexed form of Nedd4-2¹⁸⁶⁻⁹⁷⁵. These findings show that the creation of this complex affects the WW2 domain's location relative to the HECT domain and other WW domains in Nedd4-2¹⁸⁶⁻⁹⁷⁵.

For the quantitative intramolecular crosslinks of Nedd4-2¹⁸⁶⁻⁹⁷⁵ in the presence and absence of 14-3-3 η we used 12C and 13C-labelled disuccinimidyl adipate (DSA) in a 1:1 ratio to crosslink Nedd4-2¹⁸⁶⁻⁹⁷⁵ alone and the complex with 14-3-3 η (Fig. 5.10a, b-in green). Upon complex formation, only the abundances of crosslinks considerably changed showing that Nedd4-2 residues K531 from the WW3 domain and K607 from the HECT domain (Fig. 5.10b) are mostly cross-linked in the absence of 14-3-3 η . In contrast, the crosslink between Nedd4-2 residues H186, which precedes the WW1 domain, and K639 from the N-terminus of the HECT domain (Fig. 5.10b), largely formed in the presence of 14-3-3 η . Crosslinking Nedd4-2¹⁸⁶⁻⁹⁷⁵:14-3-3 η mixtures in 1:2 stoichiometry with disuccinimidyl suberate (DSS) and DSG resulted in eight intermolecular crosslinks (Fig. 5.10a, b). Crosslinks connect the 14-3-3 η ligand binding groove's α -helices (α 3, α 5, and α 9) to the WW3 and HECT domains, as well as α 2 and α 6 to the HECT domain. The 14-3-3 η and Nedd4-2 areas are expected to have direct interactions within the complex. Our crosslinking studies show that 14-3-3 η interacts with Nedd4-2's WW3 and HECT domains, causing alterations in their relative places.

In XL-MS data analysis from the full-length Nedd4-2:14-3-3 complex, observed most of intermolecular cross-links between the WW3 domains of Nedd4-2 and the 14-3-3, shown (Fig. 5.10). Also, multiple intramolecular cross-links have been found between the Nedd4-2 domains, shown in figure 5.10.

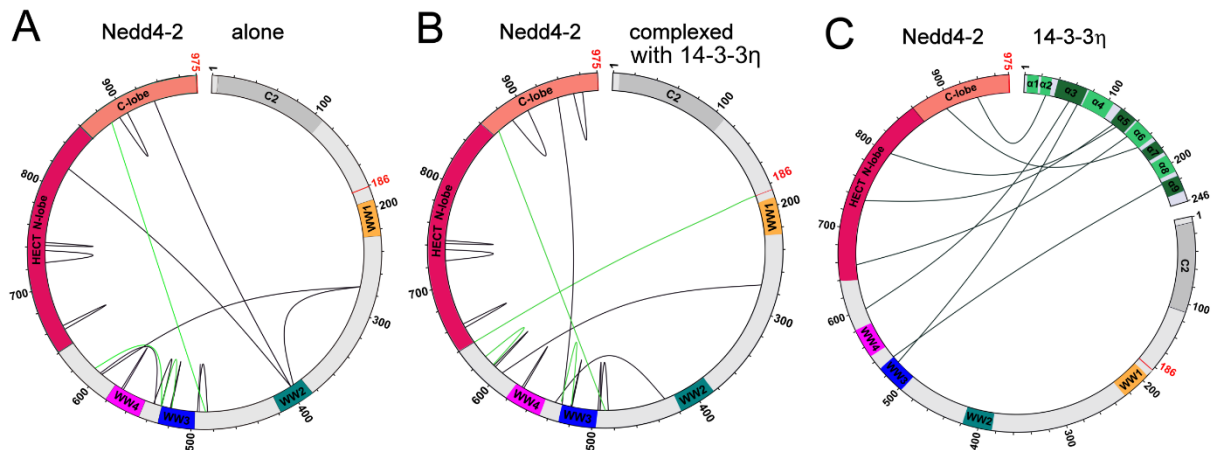


Figure 5.10: Identified crosslinks of Nedd4-2¹⁸⁶⁻⁹⁷⁵ in apo and complexed form with 14-3-3 η protein. Figure showing identified cross-linked peptides using crosslinking agent DSS and DSG (black lines). Quantitative crosslinks by DSA (light green). A) Position of intramolecular cross-linked residues in Nedd4-2 alone. Nedd4-2 domains have distinct colours in the following ways. The C2 domain (grey color, which is not a part of this construct), the WW domains (WW1 – yellow colour, WW2 - dark green colour, WW3 – blue colour, WW4 – purple colour) and the HECT N-lobe (red colour) and HECT C-lobe of domain (salmon colour) B) Positions of intramolecular crosslinks of pNedd4-2 protein identified in the presence of 14-3-3 protein. C) Positions of intermolecular crosslinks between the 14-3-3 protein and pNedd4-2. Helices of protein 14-3-3 are indicated in green and helices forming the binding groove are in dark green (Figure taken from Pohl *et.al.* 2021)¹¹⁸.

5.6 Limited proteolysis - protection against proteolytic cleavage

To investigate the functional role of 14-3-3 η protein on Nedd4-2¹⁸⁶⁻⁹⁷⁵, we performed limited proteolysis experiments using trypsin cleavage (Fig. 5.11). This assay allowed us to identify susceptible regions of Nedd4-2 to proteolysis. Previous reports indicate that 14-3-3 proteins play protective roles with various proteins such as caspase-2 and phosphocin^{172,173,267,268}. In our experiments, we performed limited proteolysis with trypsin using four different time intervals (Fig. 5.11A). Results showed that Nedd4-2¹⁸⁶⁻⁹⁷⁵ is highly prone to proteolysis when alone, but when complexed with 14-3-3 η , its degradation is significantly slowed down. Using mass spectrometry analysis after 30 minutes of trypsin digestion, we observed that the N-terminus containing WW1 and WW2 domains, with phosphorylation sites S342 and T367, is the most sensitive region to trypsin digestion. Notably, bands around 60 kDa corresponded to the Nedd4-2 sequence 446–975, with the first identified peptide phosphorylated at S448. Our findings clearly demonstrate that Nedd4-2 undergoes rapid degradation alone, but in the presence of 14-3-3 η , degradation is significantly reduced. The degradation of Nedd4-2 *in vitro* was halved in

the presence of 14-3-3 η (Fig. 5.11B), indicating that 14-3-3 protein acts as a protective agent against proteolytic degradation. In summary, our results show that 14-3-3 η binding protects the S448 binding motif, WW3-4, and the HECT domains at C terminal region of Nedd4-2 from proteolytic degradation. These findings are consistent with our fluorescence analysis results, indicating that 14-3-3 η stabilizes Nedd4-2 by influencing its structural dynamics.

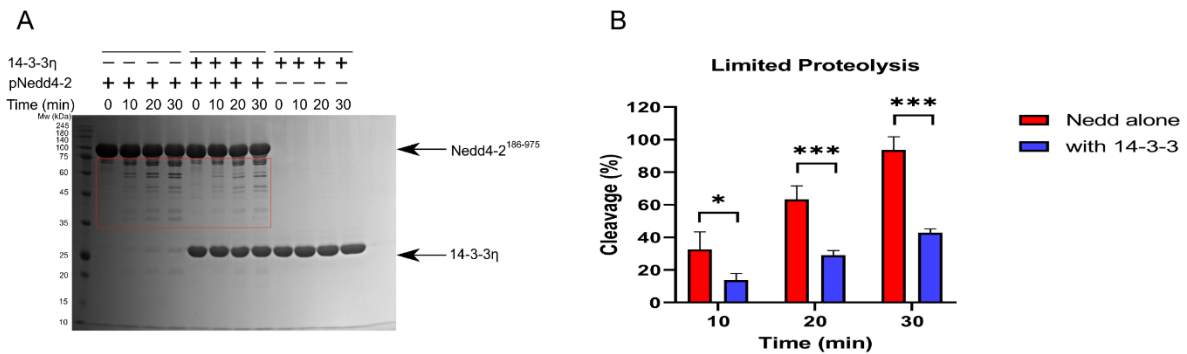


Figure 5.11: Limited proteolysis confirmed that 14-3-3 protein protects pNedd4-2¹⁸⁶⁻⁹⁷⁵ from proteolytic cleavage. A) Trypsin digestion of phosphorylated Nedd4-2¹⁸⁶⁻⁹⁷⁵ was performed at 10, 20, and 30 min. time intervals in the absence and presence of 14-3-3 B) The experiment used a protease/Nedd4-2 ratio of 1:1000 (w/w), and the reactions were terminated by boiling the samples in an SDS/PAGE loading buffer. The red rectangle represents the observed degradation of Nedd4-2¹⁸⁶⁻⁹⁷⁵. ImageLab software was used to measure the density of degradation bands of Nedd4-2¹⁸⁶⁻⁹⁷⁵, both with and without 14-3-3 η . The error bars indicate the standard deviation of four separate experiments (Figure taken from Joshi *et.al.* 2022)²⁶⁶.

5.7 Protein structure determination.

Previous research on the interaction between phosphorylated Nedd4-2 variants and 14-3-3 proteins indicated that motifs containing phosphorylated residues at positions S342 and S448 are crucial for a strong interaction with 14-3-3¹¹⁸. In order to investigate further this interaction at the atomic level, we did protein crystallization using 14-3-3 $\gamma\Delta C$ and a phosphorylated peptide derived from the 14-3-3 binding motif pS342 in the native sequence of Nedd4-2. The 14-3-3 $\gamma\Delta C$ protein, lacking 15 residues at the C-terminus, was selected for this study due to the high quality of the crystals.

We co-crystallized this protein with the Nedd4-2 phosphopeptides (LRSCpSVTDAV), which carries the first phosphorylation site at S342. The resulting complex, two 14-3-3 dimers in the asymmetric unit coupled to phosphopeptides, crystallised in the trigonal space group R3. (PDB

ID: 6ZBT, Fig.5.12). To determine the structure of the pep-S342:14-3-3 γ Δ C complexes, we used molecular replacement techniques with 14-3-3 γ (PDB ID: 2B05) as a search model, followed by refinement to final resolutions of 1.8 Å.

The crystal structure obtained in this study was consistent with our previously published findings¹¹⁸. The highest quality diffraction data were obtained for the Nedd4-2pS342/14-3-3 γ Δ C complex crystals. However, only seven residues of Nedd4-2 were visible in the final electron density map, with the last three residues likely being disordered. The structure revealed that the phosphopeptides adopted extended conformations within the ligand-binding groove of 14-3-3, similar to other 14-3-3: phosphopeptides complexes. Specific connections were observed between the phosphorylated serine at position 342 (pSer342) and certain amino acid side chains of 14-3-3 proteins, including Arg57, Arg132, Lys50, and Tyr133, as well as indirect interactions facilitated by water molecules with Asp129 and Asn178 of 14-3-3. Additionally, hydrogen bonds were identified between the main-chain atoms of Nedd4-2 residues Cys341 and Val343 and the side chains of 14-3-3 residues Asn229 and Asn178, respectively. Furthermore, the side chain of Nedd4-2 Ser340 formed a polar contact with the side-chain residues Trp233 and Glu185 of 14-3-3.

My colleague Mgr. Dana Kalábová crystallized 14-3-3 γ Δ C with phosphopeptides. Diffraction analysis of this crystal, molecular replacement and structure validation was done with the help of my supervisor RNDr. Veronika Obsilova, PhD. Then the structure is submitted to the PDB database with PDB ID: 6ZBT.

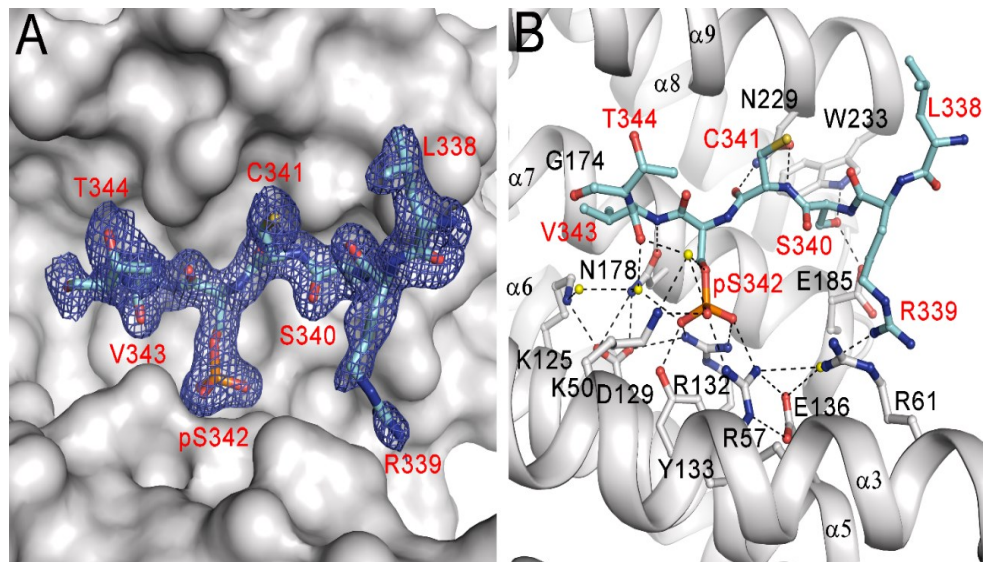


Figure 5.12: Solved crystal structure of complex of phosphopeptides Nedd4-2_pS342 (LRScpSVTDAV) and 14-3-3 $\gamma\Delta C$ protein. (A) The 14-3-3 $\gamma\Delta C$: pep-S342 complex's crystal structure, solved at 1.61 Å resolution through molecular replacement and refinement. The contour of the 2Fo-Fc electron density map is at 1 σ . (PDB ID – 6ZBT) (B) Polar contacts (black lines) between the Nedd4-2 pSer342 binding site (red) and the residues of 14-3-3 γ (black). Water molecules are shown as yellow spheres (Figure taken from Pohl *et.al.* 2021)¹¹⁸.

6. Discussion

Nedd4-2 is crucial in the ubiquitination of membrane-bound proteins, responsible for various diseases like epilepsy, hypertension, and cystic fibrosis. Its regulation involves phosphorylation-triggered binding to the adaptor protein 14-3-3, which has different effects in different tissues. For example, in the brain, the interaction between Nedd4-2 and 14-3-3 induces the ubiquitination of AMPA receptor's GluA1 subunit. Conversely, ENaC's ubiquitination is reduced in the kidney upon binding to 14-3-3, leading to increased sodium absorption by elevating ENaC surface expression²⁷⁰. Despite the importance of this interaction, detailed structural information regarding the regulation of Nedd4-2 by 14-3-3 remained unknown. Our study sheds light on the structural aspects of this interaction. In our previous study, we found that 14-3-3 interaction induces a structural rearrangement in Nedd4-2, affecting its domain and likely modulating substrate ubiquitination. These findings underscore the broader regulatory role of 14-3-3 to target for Nedd4-2-related diseases.

Numerous studies have shown that Nedd4-2's WW domains play important roles in various eukaryotic signalling cascades. These WW domains recognize PY motifs in proteins such as ENaC subunits, SGK1, ACK1, and WNK1. Nedd4-2 has four WW domains that have distinct sequences, suggesting that every domain is going to have a different role. *In vitro* study using surface plasmon resonance showed that Nedd4-2 WW2 and WW3 domains bind to SGK1 both independently and cooperatively, whereas only WW3 and WW4 domains interact with ENaC¹¹⁶. These results verify a proposed model in which SGK1 initially binds to the WW2 and WW3 domains of Nedd4-2, moreover, phosphorylation of Nedd4-2 leads to binding of scaffolding 14-3-3 protein and subsequently dissociation of Nedd4-2 from ENaC²⁷⁰. However, the exact mechanisms underlying the modulation of Nedd4-2 by 14-3-3 proteins are not fully understood yet and require further investigation²⁷⁵⁻²⁷⁸.

In our recent study, we utilized a combination of SAXS, cross-linking, and crystallography to examine the structural characteristics of the Nedd4-2:14-3-3 η complex. Our findings revealed significant changes in the interactions within Nedd4-2's structured domains upon binding to 14-3-3 η ¹¹⁸. This shows the potential impact of complex formation on the accessibility of Nedd4-2's catalytic HECT domain and WW domains individually. To delve deeper, we used time-resolved dansyl fluorescence spectroscopy to examine the conformational changes, mobility, and solvent accessibility of Nedd4-2's WW and HECT domains induced by

binding with 14-3-3 η . Our results clearly shows direct interaction between 14-3-3 η and WW3 and WW4 domains, indicated by a substantial increase in dansyl fluorescence lifetime and a reduction in solvent accessibility and mobility of IAEDANS-labelled Cysteine residues at positions 508, 522, and 571 (see Fig.5.6, 5.8C, and 5.9). Furthermore, the observed blue shift in emission spectra, approximately 4-5 nm for C508 and C522 residues and 1 nm for C571 upon binding with 14-3-3 η , corroborates this finding (Joshi et al, Fig.S19)²⁶⁶. Comparison with the spectra of free IAEDANS in water and DMSO suggests a less polar microenvironment, further supporting our conclusions (Joshi *et al*, Fig.S20)²⁶⁶.

The observed changes in the 1,5-IAEDANS microenvironment, mobility, and quencher accessibility are likely due to two mechanisms: conformational changes caused by 14-3-3 η protein binding to the Nedd4-2 WW3 and WW4 domains, and direct interaction with labelled cysteine residues, which shields them from polar solvents and restricts their mobility. The fluorescence properties of 1,5 IAEDANS-labelled Cys residues at positions 389 and 414 in the WW2 domain had a lower impact on interaction with 14-3-3 η . Despite having the lowest internal mobility of Nedd4-2's four WW domains, 14-3-3 η binding had only a little effect on the WW2 domain's movement (see fig.5.7, 5.8B). Nonetheless, complex formation caused some structural changes near this domain, as demonstrated by the increased τ_{mean} . Furthermore, the drop in k_q values and a modest blue spectral shift show that the WW2 domain has reduced solvent accessibility after binding with 14-3-3 η . IAEDANS-Cys at positions 209 and 218 inside the WW1 domain, on the other hand, had no effect on their fluorescence lifetimes or apparent k_q when bound to 14-3-3 η . Regardless of the presence of 14-3-3 η , this domain showed strong internal mobility, a short emission lifetime, and high quenching of IAEDANS emission. (see fig.5.6, 5.8A and 5.9). In summary, these results suggest that the WW1 domain is relaxed and highly solvent-accessible, while 14-3-3 η binding has little effect on 1,5 IAEDANS-C209 emission spectrum. However, the existence of a blue-shifted shoulder on 1,5 IAEDANS-C218's emission spectra in the presence of 14-3-3 η implies that structural heterogeneity has increased in this location. Overall, binding of 14-3-3 η had no substantial effect on the WW1 domain's interactions or structure. However, the changes in structure caused by the 14-3-3 η binding extend to Nedd4-2's catalytic HECT domain, as shown by a study of the fluorescence properties of 1,5-IAEDANS labelled C942 within the active region of the HECT domain (see fig.5.6, 5.9).

Our results revealed conformational changes in Nedd4-2 domains induced by the presence of 14-3-3, shedding light on the mechanistic aspects of their interaction.

Nedd4-2 regulates Na⁺ transport in mammalian cells^{120,275–277}. It binds to the PY motif of the epithelial sodium channel ENaC, causing ubiquitination and a decrease in Na⁺ transit. In contrast, phosphorylation of Nedd4-2 by different kinases stimulates interaction with 14-3-3 proteins, blocking ENaC ubiquitination and resulting in ENaC continued activity on the cellular surface²⁷⁷. Our fluorescence spectroscopy results, together with recent structural insights into both Nedd4-2 alone and the Nedd4-2:14-3-3 η complex, give insight into the mechanism behind the 14-3-3-mediated inhibition of Nedd4-2 binding to ENaC¹¹⁸. Structural studies of Nedd4-2 and in complex with 14-3-3 η show that when 14-3-3 η is absent, the WW2 and WW3 domains interact with the HECT domain (see fig.5.10). However, when 14-3-3 η binds, these connections are disrupted, resulting in WW3 being sequestered into the central channel of the 14-3-3 η dimer and away from the HECT domain (see fig.5.6, fig.5.9) Furthermore, our current model suggest interactions between 14-3-3 η and the WW4 and HECT domains. Consistent with these structural predictions, our time-resolved fluorescence measurements, combined with the limited proteolysis results reported in this study, confirm the interactions between 14-3-3 η and the WW3 and WW4 domains, as well as the structural changes within the HECT domain during complex formation. Furthermore, our results show that complex formation reduces the mobility and solvent accessibility of the WW2-4 domains, most likely due to steric masking by 14-3-3 η binding.

It is most likely that the 14-3-3-mediated physical restriction of WW domains is responsible for regulating Nedd4-2 function. Additionally, the relative position of both HECT lobes to each other is directly influenced by 14-3-3, which would cause an impact of the catalytic activity of this enzyme. We make this hypothesis based on the fact that the IAEDANS moiety bound to C942²⁷⁸, a catalytic residue, behaves differently once Nedd4-2 is in a complex in comparison to when it is by itself. Which would be a consequence of the structural change within the catalytic domain. In conclusion, our fluorescence spectroscopic study of the Nedd4-2:14-3-3 η complex shows that steric hindrance in the WW3 and WW4 domains, together with conformational changes in the catalytic domain, contribute to the regulation of Nedd4-2 activities via 14-3-3 binding. Furthermore, these findings open the way for further exploration

of the 14-3-3:Nedd4-2 interface for possible therapeutic intervention in Nedd4-2-related diseases such as Parkinson's disease, kidney disease, hypertension and others.

Recently some studies on the development of small-molecule therapeutics that enhance protein-protein interactions within 14-3-3 protein complexes have yielded some promising outcomes, in the same approach²⁷⁹. Our findings suggest that besides phosphorylation motifs, Nedd4-2 interacts with 14-3-3 η through additional regions such as WW3 and WW4 domains. By targeting that interaction interface between these proteins, it may be possible to develop novel inhibitors that disrupt Nedd4-2 function, offering an alternative or complementary approach to existing strategies for treating diseases.

Overall, the results presented here provide a deeper understanding of the molecular mechanisms regulating the interaction between Nedd4-2 and 14-3-3 η , highlighting its importance in cellular homeostasis and offering promising prospects for therapeutic intervention.

7. Conclusion

Our research successfully addressed the regulation of the ubiquitin ligase Nedd4-2 by the 14-3-3 η protein using integrated structural biology approaches.

- Nedd4-2 variants were efficiently prepared using a site-directed mutagenesis approach. We successfully optimized the expression and purification protocols for Nedd4-2¹⁹⁰⁻⁵⁸¹ and Nedd4-2¹⁸⁶⁻⁹⁷⁵ variants, resulting in a sufficient yield of soluble proteins.
- Nedd4-2 variants have been found to be stable and suitable for further experiments using DSF analysis. As well as Nedd4-2 variants were forming complex with 14-3-3 η protein in binding stoichiometry 1:2 (monomer of Nedd4-2: dimer of 14-3-3 η).
- All Nedd4-2 variants were appropriately labelled with 1,5-IAEDANS dye, followed by fluorescence measurements. The fluorescence spectroscopy analysis of the Nedd4-2:14-3-3 η complex indicates that binding of 14-3-3 η protein to Nedd4-2 causes the steric hindrance of the WW3 and WW4 domains and the conformational change in the catalytic HECT domain.
- Chemical crosslinking experiments provided valuable data on the spatial proximity between Nedd4-2 and 14-3-3 η , offering further insights into their binding mechanism.
- Limited proteolysis experiment has demonstrated that the 14-3-3 η protein binding protects Nedd4-2 from proteolytic degradation *in vitro*.
- The crystal structure of the Nedd4-2pS342:14-3-3 $\gamma\Delta$ C was refined at 1.8 Å resolution and provided a detailed molecular view of the interaction of 14-3-3 protein with the Nedd4-2 phosphorylation site pS342.
- Collectively, all these findings provide insight into the regulatory mechanisms of Nedd4-2 and its interaction with 14-3-3 η protein, which could have possible explanation and future implications for treatments of Nedd4-2-related diseases.

8. Literature

1. Krishna, R. G. & Wold, F. Post-Translational Modification of Proteins. in *Advances in Enzymology - and Related Areas of Molecular Biology* (ed. Meister, A.) 265–298 (John Wiley & Sons, Inc., Hoboken, NJ, USA, 2006). doi:10.1002/9780470123133.ch3.
2. Mann, M. & Jensen, O. N. Proteomic analysis of post-translational modifications. *Nat. Biotechnol.* **21**, 255–261 (2003).
3. Nørregaard Jensen, O. Modification-specific proteomics: characterization of post-translational modifications by mass spectrometry. *Curr. Opin. Chem. Biol.* **8**, 33–41 (2004).
4. Eichler, J. & Adams, M. W. W. Posttranslational Protein Modification in *Archaea*. *Microbiol. Mol. Biol. Rev.* **69**, 393–425 (2005).
5. Yang, X.-J. Multisite protein modification and intramolecular signaling. *Oncogene* **24**, 1653–1662 (2005).
6. Jensen, O. N. Interpreting the protein language using proteomics. *Nat. Rev. Mol. Cell Biol.* **7**, 391–403 (2006).
7. Karve, T. M. & Cheema, A. K. Small Changes Huge Impact: The Role of Protein Posttranslational Modifications in Cellular Homeostasis and Disease. *J. Amino Acids* **2011**, 207691 (2011).
8. Hershko, A. & Ciechanover, A. The Ubiquitin System. *Annu. Rev. Biochem.* **67**, 425–479 (1998).
9. Wiesner, S. *et al.* Autoinhibition of the HECT-Type Ubiquitin Ligase Smurf2 through Its C2 Domain. *Cell* **130**, 651–662 (2007).
10. Ramazi, S. & Zahiri, J. Post-translational modifications in proteins: resources, tools and prediction methods. *Database J. Biol. Databases Curation* **2021**, baab012 (2021).
11. Goldknopf, I. L. & Busch, H. Isopeptide linkage between nonhistone and histone 2A polypeptides of chromosomal conjugate-protein A24. *Proc. Natl. Acad. Sci. U. S. A.* **74**, 864–868 (1977).
12. Goldstein, G. *et al.* Isolation of a polypeptide that has lymphocyte-differentiating properties and is probably represented universally in living cells. *Proc. Natl. Acad. Sci. U. S. A.* **72**, 11–15 (1975).
13. Hunt, L. T. & Dayhoff, M. O. Amino-terminal sequence identity of ubiquitin and the nonhistone component of nuclear protein A24. *Biochem. Biophys. Res. Commun.* **74**, 650–655 (1977).
14. Yau, R. & Rape, M. The increasing complexity of the ubiquitin code. *Nat. Cell Biol.* **18**, 579–586 (2016).
15. Wang, X., Herr, R. A. & Hansen, T. H. Ubiquitination of Substrates by Esterification. *Traffic Cph. Den.* **13**, 19–24 (2012).
16. Haas, A. L., Warms, J. V., Hershko, A. & Rose, I. A. Ubiquitin-activating enzyme. Mechanism and role in protein-ubiquitin conjugation. *J. Biol. Chem.* **257**, 2543–2548 (1982).
17. Cappadocia, L. & Lima, C. D. Ubiquitin-like Protein Conjugation: Structures, Chemistry, and Mechanism. *Chem. Rev.* **118**, 889–918 (2018).

18. Finley, D., Özkaynak, E. & Varshavsky, A. The yeast polyubiquitin gene is essential for resistance to high temperatures, starvation, and other stresses. *Cell* **48**, 1035–1046 (1987).
19. Hershko, A., Ciechanover, A., Heller, H., Haas, A. L. & Rose, I. A. Proposed role of ATP in protein breakdown: conjugation of protein with multiple chains of the polypeptide of ATP-dependent proteolysis. *Proc. Natl. Acad. Sci. U. S. A.* **77**, 1783–1786 (1980).
20. Sims, J. J. & Cohen, R. E. Linkage-specific avidity defines the lysine 63-linked polyubiquitin binding preference of Rap80. *Mol. Cell* **33**, 775–783 (2009).
21. Sato, Y. *et al.* Structural basis for specific recognition of Lys 63-linked polyubiquitin chains by tandem UIMs of RAP80. *EMBO J.* **28**, 2461–2468 (2009).
22. Komander, D. & Rape, M. The Ubiquitin Code. *Annu. Rev. Biochem.* **81**, 203–229 (2012).
23. Nakagawa, T. & Nakayama, K. Protein monoubiquitylation: targets and diverse functions. *Genes Cells* **20**, 543–562 (2015).
24. Grice, G. L. & Nathan, J. A. The recognition of ubiquitinated proteins by the proteasome. *Cell. Mol. Life Sci.* **73**, 3497–3506 (2016).
25. Vijay-kumar, S., Bugg, C. E. & Cook, W. J. Structure of ubiquitin refined at 1.8 Å resolution. *J. Mol. Biol.* **194**, 531–544 (1987).
26. Ries, L. From recognition to reaction: Mechanistic analysis of the interactions of the HECT ligase E6AP with ubiquitin. (2020).
27. Chau, V. *et al.* A Multiubiquitin Chain Is Confined to Specific Lysine in a Targeted Short-Lived Protein. *Science* **243**, 1576–1583 (1989).
28. Meyer, H.-J. & Rape, M. Enhanced Protein Degradation by Branched Ubiquitin Chains. *Cell* **157**, 910–921 (2014).
29. Wang, C. *et al.* TAK1 is a ubiquitin-dependent kinase of MKK and IKK. *Nature* **412**, 346–351 (2001).
30. Tokunaga, F. *et al.* Involvement of linear polyubiquitylation of NEMO in NF- κ B activation. *Nat. Cell Biol.* **11**, 123–132 (2009).
31. Flotho, A. & Melchior, F. Sumoylation: A Regulatory Protein Modification in Health and Disease. *Annu. Rev. Biochem.* **82**, 357–385 (2013).
32. Abidi, N. & Xirodimas, D. P. Regulation of cancer-related pathways by protein NEDDylation and strategies for the use of NEDD8 inhibitors in the clinic. *Endocr. Relat. Cancer* **22**, T55–T70 (2015).
33. Gâtel, P., Piechaczyk, M. & Bossis, G. Ubiquitin, SUMO, and Nedd8 as Therapeutic Targets in Cancer. in *Proteostasis and Disease* (eds. Barrio, R., Sutherland, J. D. & Rodriguez, M. S.) vol. 1233 29–54 (Springer International Publishing, Cham, 2020).
34. Chanarat, S. UBL5/Hub1: An Atypical Ubiquitin-Like Protein with a Typical Role as a Stress-Responsive Regulator. *Int. J. Mol. Sci.* **22**, 9384 (2021).
35. Liu, F. & Walters, K. J. Multitasking with ubiquitin through multivalent interactions. *Trends Biochem. Sci.* **35**, 352–360 (2010).
36. Metzger, M. B., Hristova, V. A. & Weissman, A. M. HECT and RING finger families of E3 ubiquitin ligases at a glance. *J. Cell Sci.* **125**, 531–537 (2012).

37. Hershko, A. Ubiquitin: Roles in protein modification and breakdown. *Cell* **34**, 11–12 (1983).
38. Gong, X. *et al.* The structure and regulation of the E3 ubiquitin ligase HUWE1 and its biological functions in cancer. *Invest. New Drugs* **38**, 515–524 (2020).
39. Tanaka, K., Waxman, L. & Goldberg, A. L. ATP serves two distinct roles in protein degradation in reticulocytes, one requiring and one independent of ubiquitin. *J. Cell Biol.* **96**, 1580–1585 (1983).
40. Walz, J. *et al.* 26S Proteasome Structure Revealed by Three-dimensional Electron Microscopy. *J. Struct. Biol.* **121**, 19–29 (1998).
41. Komander, D., Clague, M. J. & Urbé, S. Breaking the chains: structure and function of the deubiquitinases. *Nat. Rev. Mol. Cell Biol.* **10**, 550–563 (2009).
42. Groettrup, M., Pelzer, C., Schmidtke, G. & Hofmann, K. Activating the ubiquitin family: UBA6 challenges the field. *Trends Biochem. Sci.* **33**, 230–237 (2008).
43. Lee, I. & Schindelin, H. Structural Insights into E1-Catalyzed Ubiquitin Activation and Transfer to Conjugating Enzymes. *Cell* **134**, 268–278 (2008).
44. Lv, Z., Williams, K. M., Yuan, L., Atkison, J. H. & Olsen, S. K. Crystal structure of a human ubiquitin E1–ubiquitin complex reveals conserved functional elements essential for activity. *J. Biol. Chem.* **293**, 18337–18352 (2018).
45. Lv, Z. *et al.* Molecular mechanism of a covalent allosteric inhibitor of SUMO E1 activating enzyme. *Nat. Commun.* **9**, 5145 (2018).
46. Haas, A. L. & Rose, I. A. The mechanism of ubiquitin activating enzyme. A kinetic and equilibrium analysis. *J. Biol. Chem.* **257**, 10329–10337 (1982).
47. Michelle, C., Vourc’h, P., Mignon, L. & Andres, C. R. What Was the Set of Ubiquitin and Ubiquitin-Like Conjugating Enzymes in the Eukaryote Common Ancestor? *J. Mol. Evol.* **68**, 616–628 (2009).
48. Yang, Q., Zhao, J., Chen, D. & Wang, Y. E3 ubiquitin ligases: styles, structures and functions. *Mol. Biomed.* **2**, 23 (2021).
49. Schelpe, J., Monté, D., Dewitte, F., Sixma, T. K. & Rucktooa, P. Structure of UBE2Z Enzyme Provides Functional Insight into Specificity in the FAT10 Protein Conjugation Machinery. *J. Biol. Chem.* **291**, 630–639 (2016).
50. Ye, Y. & Rape, M. Building ubiquitin chains: E2 enzymes at work. *Nat. Rev. Mol. Cell Biol.* **10**, 755–764 (2009).
51. Wenzel, D. M., Stoll, K. E. & Klevit, R. E. E2s: structurally economical and functionally replete. *Biochem. J.* **433**, 31–42 (2011).
52. Stewart, M. D., Ritterhoff, T., Klevit, R. E. & Brzovic, P. S. E2 enzymes: more than just middle men. *Cell Res.* **26**, 423–440 (2016).
53. Varshavsky, A. The Ubiquitin System, Autophagy, and Regulated Protein Degradation. *Annu. Rev. Biochem.* **86**, 123–128 (2017).
54. Nakayama, K. I. & Nakayama, K. Ubiquitin ligases: cell-cycle control and cancer. *Nat. Rev. Cancer* **6**, 369–381 (2006).

55. Whatley, B. R., Li, L. & Chin, L.-S. The ubiquitin–proteasome system in spongiform degenerative disorders. *Biochim. Biophys. Acta BBA - Mol. Basis Dis.* **1782**, 700–712 (2008).
56. Ponts, N. *et al.* Unraveling the Ubiquitome of the Human Malaria Parasite. *J. Biol. Chem.* **286**, 40320–40330 (2011).
57. Wenzel, D. M. & Klevit, R. E. Following Ariadne’s thread: a new perspective on RBR ubiquitin ligases. *BMC Biol.* **10**, 24 (2012).
58. Zheng, N. & Shabek, N. Ubiquitin Ligases: Structure, Function, and Regulation. *Annu. Rev. Biochem.* **86**, 129–157 (2017).
59. Deshaies, R. J. & Joazeiro, C. A. P. RING Domain E3 Ubiquitin Ligases. *Annu. Rev. Biochem.* **78**, 399–434 (2009).
60. Metzger, M. B., Pruneda, J. N., Klevit, R. E. & Weissman, A. M. RING-type E3 ligases: Master manipulators of E2 ubiquitin-conjugating enzymes and ubiquitination. *Biochim. Biophys. Acta BBA - Mol. Cell Res.* **1843**, 47–60 (2014).
61. Spratt, D. E., Walden, H. & Shaw, G. S. RBR E3 ubiquitin ligases: new structures, new insights, new questions. *Biochem. J.* **458**, 421–437 (2014).
62. Christensen, D. E., Brzovic, P. S. & Klevit, R. E. E2–BRCA1 RING interactions dictate synthesis of mono- or specific polyubiquitin chain linkages. *Nat. Struct. Mol. Biol.* **14**, 941–948 (2007).
63. Wang, M., Cheng, D., Peng, J. & Pickart, C. M. Molecular determinants of polyubiquitin linkage selection by an HECT ubiquitin ligase. *EMBO J.* **25**, 1710–1719 (2006).
64. Berndsen, C. E. & Wolberger, C. New insights into ubiquitin E3 ligase mechanism. *Nat. Struct. Mol. Biol.* **21**, 301–307 (2014).
65. Riley, B. E. *et al.* Structure and function of Parkin E3 ubiquitin ligase reveals aspects of RING and HECT ligases. *Nat. Commun.* **4**, 1982 (2013).
66. Wenzel, D. M., Lissounov, A., Brzovic, P. S. & Klevit, R. E. UBCH7 reactivity profile reveals parkin and HHARI to be RING/HECT hybrids. *Nature* **474**, 105–108 (2011).
67. Scheffner, M. & Staub, O. HECT E3s and human disease. *BMC Biochem.* **8**, S6 (2007).
68. Simonson, S. J. S., Difilippantonio, M. J. & Lambert, P. F. Two Distinct Activities Contribute to Human Papillomavirus 16 E6’s Oncogenic Potential. *Cancer Res.* **65**, 8266–8273 (2005).
69. Huibregtse, J. M., Scheffner, M., Beaudenon, S. & Howley, P. M. A family of proteins structurally and functionally related to the E6-AP ubiquitin-protein ligase. *Proc. Natl. Acad. Sci.* **92**, 2563–2567 (1995).
70. Huibregtse, J. M., Scheffner, M. & Howley, P. M. A cellular protein mediates association of p53 with the E6 oncoprotein of human papillomavirus types 16 or 18. *EMBO J.* **10**, 4129–4135 (1991).
71. Duda, D. M. *et al.* Structure of HHARI, a RING-IBR-RING Ubiquitin Ligase: Autoinhibition of an Ariadne-Family E3 and Insights into Ligation Mechanism. *Structure* **21**, 1030–1041 (2013).
72. Walden, H. & Rittinger, K. RBR ligase–mediated ubiquitin transfer: a tale with many twists and turns. *Nat. Struct. Mol. Biol.* **25**, 440–445 (2018).

73. Pickrell, A. M. & Youle, R. J. The Roles of PINK1, Parkin, and Mitochondrial Fidelity in Parkinson's Disease. *Neuron* **85**, 257–273 (2015).
74. Rotin, D., Staub, O. & Haguenaer-Tsapis, R. Ubiquitination and Endocytosis of Plasma Membrane Proteins: Role of Nedd4/Rsp5p Family of Ubiquitin-Protein Ligases. *J. Membr. Biol.* **176**, 1–17 (2000).
75. Rotin, D. & Kumar, S. Physiological functions of the HECT family of ubiquitin ligases. *Nat. Rev. Mol. Cell Biol.* **10**, 398–409 (2009).
76. Zou, X., Levy-Cohen, G. & Blank, M. Molecular functions of NEDD4 E3 ubiquitin ligases in cancer. *Biochim. Biophys. Acta BBA - Rev. Cancer* **1856**, 91–106 (2015).
77. Rizo, J. & Südhof, T. C. Mechanics of membrane fusion. *Nat. Struct. Biol.* **5**, 839–842 (1998).
78. Plant, P. J., Yeager, H., Staub, O., Howard, P. & Rotin, D. The C2 Domain of the Ubiquitin Protein Ligase Nedd4 Mediates Ca²⁺-dependent Plasma Membrane Localization. *J. Biol. Chem.* **272**, 32329–32336 (1997).
79. Macias, M. J., Wiesner, S. & Sudol, M. WW and SH3 domains, two different scaffolds to recognize proline-rich ligands. *FEBS Lett.* **513**, 30–37 (2002).
80. Kato, Y., Ito, M., Kawai, K., Nagata, K. & Tanokura, M. Determinants of Ligand Specificity in Groups I and IV WW Domains as Studied by Surface Plasmon Resonance and Model Building. *J. Biol. Chem.* **277**, 10173–10177 (2002).
81. Kato, Y. *et al.* Common Mechanism of Ligand Recognition by Group II/III WW Domains. *J. Biol. Chem.* **279**, 31833–31841 (2004).
82. Kamadurai, H. B. *et al.* Insights into ubiquitin transfer cascades from a structure of a UbcH5B~Ubiquitin-HECTNEDD4L complex. *Mol. Cell* **36**, 1095–1102 (2009).
83. Verdecia, M. A. *et al.* Conformational Flexibility Underlies Ubiquitin Ligation Mediated by the WWP1 HECT Domain E3 Ligase. *Mol. Cell* **11**, 249–259 (2003).
84. Bruce, M. C. *et al.* Regulation of Nedd4-2 self-ubiquitination and stability by a PY motif located within its HECT-domain. *Biochem. J.* **415**, 155–163 (2008).
85. Bernassola, F., Karin, M., Ciechanover, A. & Melino, G. The HECT Family of E3 Ubiquitin Ligases: Multiple Players in Cancer Development. *Cancer Cell* **14**, 10–21 (2008).
86. Ingham, R. J., Gish, G. & Pawson, T. The Nedd4 family of E3 ubiquitin ligases: functional diversity within a common modular architecture. *Oncogene* **23**, 1972–1984 (2004).
87. de Bie, P. & Ciechanover, A. Ubiquitination of E3 ligases: self-regulation of the ubiquitin system via proteolytic and non-proteolytic mechanisms. *Cell Death Differ.* **18**, 1393–1402 (2011).
88. Mund, T. & Pelham, H. R. B. Control of the activity of WW-HECT domain E3 ubiquitin ligases by NDFIP proteins. *EMBO Rep.* **10**, 501–507 (2009).
89. Ciechanover, A. Intracellular protein degradation: From a vague idea thru the lysosome and the ubiquitin–proteasome system and onto human diseases and drug targeting. *Biochim. Biophys. Acta BBA - Proteins Proteomics* **1824**, 3–13 (2012).
90. Perry, W. L. *et al.* The itchy locus encodes a novel ubiquitin protein ligase that is disrupted in a18H mice. *Nat. Genet.* **18**, 143–146 (1998).

91. Shaw, A. Z. *et al.* Phosphorylation of either Ser16 or Thr30 does not disrupt the structure of the Itch E3 ubiquitin ligase third WW domain. *Proteins Struct. Funct. Bioinforma.* **60**, 558–560 (2005).
92. Yang, C. *et al.* Negative Regulation of the E3 Ubiquitin Ligase Itch via Fyn-Mediated Tyrosine Phosphorylation. *Mol. Cell* **21**, 135–141 (2006).
93. Scialpi, F. *et al.* Itch self-polyubiquitylation occurs through lysine-63 linkages. *Biochem. Pharmacol.* **76**, 1515–1521 (2008).
94. Lin, J.-H., Deng, G., Huang, Q. & Morser, J. KIAP, a Novel Member of the Inhibitor of Apoptosis Protein Family. *Biochem. Biophys. Res. Commun.* **279**, 820–831 (2000).
95. Zhu, H., Kavsak, P., Abdollah, S., Wrana, J. L. & Thomsen, G. H. A SMAD ubiquitin ligase targets the BMP pathway and affects embryonic pattern formation. *Nature* **400**, 687–693 (1999).
96. Kavsak, P. *et al.* Smad7 Binds to Smurf2 to Form an E3 Ubiquitin Ligase that Targets the TGF β Receptor for Degradation. *Mol. Cell* **6**, 1365–1375 (2000).
97. Lu, Y.-H., Wang, K., He, R. & Xi, T. Knockdown of Survivin and Upregulation of p53 Gene Expression by Small Interfering RNA Induces Apoptosis in Human Gastric Carcinoma Cell Line SGC-823. *Cancer Biother. Radiopharm.* **23**, 727–734 (2008).
98. Cheng, S. Y. & Zhang, Y. E. Smurfs have “fused” into the asymmetric division of stem cells. *Protein Cell* **2**, 2–4 (2011).
99. Jiang, H., Dempsey, D. R. & Cole, P. A. Ubiquitin Ligase Activities of WWP1 Germline Variants K740N and N745S. *Biochemistry* **60**, 357–364 (2021).
100. Soond, S. M. & Chantry, A. Selective targeting of activating and inhibitory Smads by distinct WWP2 ubiquitin ligase isoforms differentially modulates TGF β signalling and EMT. *Oncogene* **30**, 2451–2462 (2011).
101. Yeung, B., Ho, K.-C. & Yang, X. WWP1 E3 Ligase Targets LATS1 for Ubiquitin-Mediated Degradation in Breast Cancer Cells. *PLoS ONE* **8**, e61027 (2013).
102. Maddika, S. *et al.* WWP2 is an E3 ubiquitin ligase for PTEN. *Nat. Cell Biol.* **13**, 728–733 (2011).
103. Flaszka, M., Gorman, P., Roylance, R., Canfield, A. E. & Baron, M. Alternative Splicing Determines the Domain Structure of WWP1, a Nedd4 Family Protein. *Biochem. Biophys. Res. Commun.* **290**, 431–437 (2002).
104. Miyazaki, M. [The treatments of hepatic metastasis from pancreato-biliary cancer]. *Nihon Geka Gakkai Zasshi* **104**, 717–720 (2003).
105. Miyazaki, K. *et al.* NEDL1, a Novel Ubiquitin-protein Isopeptide Ligase for Dishevelled-1, Targets Mutant Superoxide Dismutase-1. *J. Biol. Chem.* **279**, 11327–11335 (2004).
106. Kwak, Y.-D. *et al.* Upregulation of the E3 ligase NEDD4-1 by Oxidative Stress Degrades IGF-1 Receptor Protein in Neurodegeneration. *J. Neurosci.* **32**, 10971–10981 (2012).
107. Cao, X. R. *et al.* Nedd4 Controls Animal Growth by Regulating IGF-1 Signaling. *Sci. Signal.* **1**, (2008).

108. Wang, S., Liu, F., Li, X. & Dong, P. [Research of the expression of PTEN in squamous cell carcinoma of larynx by the tissue chip technology]. *Lin Chuang Er Bi Yan Hou Tou Jing Wai Ke Za Zhi J. Clin. Otorhinolaryngol. Head Neck Surg.* **21**, 1081–1084 (2007).
109. Wang, J. *et al.* Calcium Activates Nedd4 E3 Ubiquitin Ligases by Releasing the C2 Domain-mediated Auto-inhibition. *J. Biol. Chem.* **285**, 12279–12288 (2010).
110. Itani, O. A., Campbell, J. R., Herrero, J., Snyder, P. M. & Thomas, C. P. Alternate promoters and variable splicing lead to hNedd4-2 isoforms with a C2 domain and varying number of WW domains. *Am. J. Physiol.-Ren. Physiol.* **285**, F916–F929 (2003).
111. Garrone, N. F., Blazer-Yost, B. L., Weiss, R. B., Lalouel, J.-M. & Rohrwasser, A. A human polymorphism affects NEDD4L subcellular targeting by leading to two isoforms that contain or lack a C2 domain. *BMC Cell Biol.* **10**, 26 (2009).
112. Albesa, M., Grilo, L. S., Gavillet, B. & Abriel, H. Nedd4-2-dependent ubiquitylation and regulation of the cardiac potassium channel hERG1. *J. Mol. Cell. Cardiol.* **51**, 90–98 (2011).
113. Caohuy, H., Jozwik, C. & Pollard, H. B. Rescue of Δ F508-CFTR by the SGK1/Nedd4-2 Signaling Pathway. *J. Biol. Chem.* **284**, 25241–25253 (2009).
114. Harvey, K. F., Dinudom, A., Cook, D. I. & Kumar, S. The Nedd4-like Protein KIAA0439 Is a Potential Regulator of the Epithelial Sodium Channel. *J. Biol. Chem.* **276**, 8597–8601 (2001).
115. Kamynina, E., Debonneville, C., Bens, M., Vandewalle, A. & Staub, O. A novel mouse Nedd4 protein suppresses the activity of the epithelial Na⁺ channel. *FASEB J.* **15**, 204–214 (2001).
116. Staub, O. *et al.* WW domains of Nedd4 bind to the proline-rich PY motifs in the epithelial Na⁺ channel deleted in Liddle's syndrome. *EMBO J.* **15**, 2371–2380 (1996).
117. Ichimura, T. *et al.* 14-3-3 Proteins Modulate the Expression of Epithelial Na⁺ Channels by Phosphorylation-dependent Interaction with Nedd4-2 Ubiquitin Ligase. *J. Biol. Chem.* **280**, 13187–13194 (2005).
118. Pohl, P., Joshi, R., Petrvalska, O., Obsil, T. & Obsilova, V. 14-3-3-protein regulates Nedd4-2 by modulating interactions between HECT and WW domains. *Commun. Biol.* **4**, 899 (2021).
119. Snyder, P. M., Olson, D. R., Kabra, R., Zhou, R. & Steines, J. C. cAMP and Serum and Glucocorticoid-inducible Kinase (SGK) Regulate the Epithelial Na⁺ Channel through Convergent Phosphorylation of Nedd4-2. *J. Biol. Chem.* **279**, 45753–45758 (2004).
120. Manning, J. A. & Kumar, S. Physiological Functions of Nedd4-2: Lessons from Knockout Mouse Models. *Trends Biochem. Sci.* **43**, 635–647 (2018).
121. Boase, N. A. *et al.* Respiratory distress and perinatal lethality in Nedd4-2-deficient mice. *Nat. Commun.* **2**, 287 (2011).
122. Shi, P. P. *et al.* Salt-sensitive hypertension and cardiac hypertrophy in mice deficient in the ubiquitin ligase Nedd4-2. *Am. J. Physiol.-Ren. Physiol.* **295**, F462–F470 (2008).
123. Minegishi, S. *et al.* An isoform of Nedd4-2 is critically involved in the renal adaptation to high salt intake in mice. *Sci. Rep.* **6**, 27137 (2016).

124. Dibbens, L. M. *et al.* *NEDD4-2* as a potential candidate susceptibility gene for epileptic photosensitivity. *Genes Brain Behav.* **6**, 750–755 (2007).
125. Laedermann, C. J. *et al.* Dysregulation of voltage-gated sodium channels by ubiquitin ligase *NEDD4-2* in neuropathic pain. *J. Clin. Invest.* **123**, 3002–3013 (2013).
126. Yavuz, Y. *et al.* Therapeutic effect of magnesium sulphate on carbon monoxide toxicity-mediated brain lipid peroxidation. *Eur. Rev. Med. Pharmacol. Sci.* **17 Suppl 1**, 28–33 (2013).
127. Aitken, A. 14-3-3 proteins: A historic overview. *Semin. Cancer Biol.* **16**, 162–172 (2006).
128. Dubois, T. *et al.* 14-3-3 Is Phosphorylated by Casein Kinase I on Residue 233. *J. Biol. Chem.* **272**, 28882–28888 (1997).
129. Ma, Y. *et al.* Sphingosine Activates Protein Kinase A Type II by a Novel cAMP-independent Mechanism. *J. Biol. Chem.* **280**, 26011–26017 (2005).
130. Wang, W. & Shakes, D. C. Molecular evolution of the 14-3-3 protein family. *J. Mol. Evol.* **43**, 384–398 (1996).
131. Cau, Y., Valensin, D., Mori, M., Draghi, S. & Botta, M. Structure, Function, Involvement in Diseases and Targeting of 14-3-3 Proteins: An Update. *Curr. Med. Chem.* **25**, 5–21 (2018).
132. Obsil, T. & Obsilova, V. Structural basis of 14-3-3 protein functions. *Semin. Cell Dev. Biol.* **22**, 663–672 (2011).
133. Ichimura, T., Taoka, M., Hozumi, Y., Goto, K. & Tokumitsu, H. 14-3-3 Proteins directly regulate Ca^{2+} /calmodulin-dependent protein kinase kinase α through phosphorylation-dependent multisite binding. *FEBS Lett.* **582**, 661–665 (2008).
134. Gardino, A. K., Smerdon, S. J. & Yaffe, M. B. Structural determinants of 14-3-3 binding specificities and regulation of subcellular localization of 14-3-3-ligand complexes: A comparison of the X-ray crystal structures of all human 14-3-3 isoforms. *Semin. Cancer Biol.* **16**, 173–182 (2006).
135. Lim, G. E. *et al.* 14-3-3 ζ coordinates adipogenesis of visceral fat. *Nat. Commun.* **6**, 7671 (2015).
136. Mhaweck, P. 14-3-3 proteins—an update. *Cell Res.* **15**, 228–236 (2005).
137. Wang, Y. *et al.* *C. elegans* 14-3-3 proteins regulate life span and interact with SIR-2.1 and DAF-16/FOXO. *Mech. Ageing Dev.* **127**, 741–747 (2006).
138. Le, T. P., Vuong, L. T., Kim, A.-R., Hsu, Y.-C. & Choi, K.-W. 14-3-3 proteins regulate Tctp–Rheb interaction for organ growth in *Drosophila*. *Nat. Commun.* **7**, 11501 (2016).
139. Nam, S., Le, T. P., Chung, S. & Choi, K.-W. Tctp regulates the level and localization of Foxo for cell growth in *Drosophila*. *Cell Death Discov.* **8**, 146 (2022).
140. Pennington, K., Chan, T., Torres, M. & Andersen, J. The dynamic and stress-adaptive signaling hub of 14-3-3: emerging mechanisms of regulation and context-dependent protein–protein interactions. *Oncogene* **37**, 5587–5604 (2018).
141. Thomas, D., Guthridge, M., Woodcock, J. & Lopez, A. 14-3-3 Protein Signaling in Development and Growth Factor Responses. in *Current Topics in Developmental Biology* vol. 67 285–303 (Elsevier, 2005).
142. Fan, X. *et al.* 14-3-3 Proteins Are on the Crossroads of Cancer, Aging, and Age-Related Neurodegenerative Disease. *Int. J. Mol. Sci.* **20**, 3518 (2019).

143. Lu, L. *et al.* Deregulated 14-3-3 ζ and methionine adenosyltransferase α 1 interplay promotes liver cancer tumorigenesis in mice and humans. *Oncogene* **40**, 5866–5879 (2021).
144. Muslin, A. J., Tanner, J. W., Allen, P. M. & Shaw, A. S. Interaction of 14-3-3 with Signaling Proteins Is Mediated by the Recognition of Phosphoserine. *Cell* **84**, 889–897 (1996).
145. Truong, A. B., Masters, S. C., Yang, H. & Fu, H. Role of the 14-3-3 C-terminal loop in ligand interaction. *Proteins Struct. Funct. Bioinforma.* **49**, 321–325 (2002).
146. Wilker, E. W., Grant, R. A., Artim, S. C. & Yaffe, M. B. A Structural Basis for 14-3-3 σ Functional Specificity* \blacklozenge . *J. Biol. Chem.* **280**, 18891–18898 (2005).
147. Liu, D. *et al.* Crystal structure of the zeta isoform of the 14-3-3 protein. *Nature* **376**, 191–194 (1995).
148. Xiao, B. *et al.* Structure of a 14-3-3 protein and implications for coordination of multiple signalling pathways. *Nature* **376**, 188–191 (1995).
149. Yang, X. *et al.* Structural basis for protein–protein interactions in the 14-3-3 protein family. *Proc. Natl. Acad. Sci.* **103**, 17237–17242 (2006).
150. Bridges, D. & Moorhead, G. B. G. 14-3-3 proteins: a number of functions for a numbered protein. *Sci. STKE Signal Transduct. Knowl. Environ.* **2005**, re10 (2005).
151. Zhu, H. *et al.* Origin of a folded repeat protein from an intrinsically disordered ancestor. *eLife* **5**, e16761 (2016).
152. Das, A. K., Cohen, P. W. & Barford, D. The structure of the tetratricopeptide repeats of protein phosphatase 5: implications for TPR-mediated protein-protein interactions. *EMBO J.* **17**, 1192–1199 (1998).
153. Sluchanko, N. N. & Gusev, N. B. Oligomeric structure of 14-3-3 protein: what do we know about monomers? *FEBS Lett.* **586**, 4249–4256 (2012).
154. Haladová, K. *et al.* The combination of hydrogen/deuterium exchange or chemical cross-linking techniques with mass spectrometry: mapping of human 14-3-3 ζ homodimer interface. *J. Struct. Biol.* **179**, 10–17 (2012).
155. Jones, D. H., Ley, S. & Aitken, A. Isoforms of 14-3-3 protein can form homo- and heterodimers in vivo and *in vitro*: implications for function as adapter proteins. *FEBS Lett.* **368**, 55–58 (1995).
156. Verdoodt, B., Benzinger, A., Popowicz, G. M., Holak, T. A. & Hermeking, H. Characterization of 14-3-3 σ Dimerization Determinants: Requirement of Homodimerization for Inhibition of Cell Proliferation. *Cell Cycle* **5**, 2920–2926 (2006).
157. Liang, X., Butterworth, M. B., Peters, K. W., Walker, W. H. & Frizzell, R. A. An Obligatory Heterodimer of 14-3-3 β and 14-3-3 ϵ Is Required for Aldosterone Regulation of the Epithelial Sodium Channel. *J. Biol. Chem.* **283**, 27418–27425 (2008).
158. Kligys, K., Yao, J., Yu, D. & Jones, J. C. R. 14-3-3 ζ/τ heterodimers regulate Slingshot activity in migrating keratinocytes. *Biochem. Biophys. Res. Commun.* **383**, 450–454 (2009).
159. Rittinger, K. *et al.* Structural Analysis of 14-3-3 Phosphopeptide Complexes Identifies a Dual Role for the Nuclear Export Signal of 14-3-3 in Ligand Binding. *Mol. Cell* **4**, 153–166 (1999).

160. Yaffe, M. B. *et al.* The Structural Basis for 14-3-3:Phosphopeptide Binding Specificity. *Cell* **91**, 961–971 (1997).
161. Ganguly, S. *et al.* Melatonin synthesis: 14-3-3-dependent activation and inhibition of arylalkylamine *N*-acetyltransferase mediated by phosphoserine-205. *Proc. Natl. Acad. Sci.* **102**, 1222–1227 (2005).
162. Würtele, M., Jelich-Ottmann, C., Wittinghofer, A. & Oecking, C. Structural view of a fungal toxin acting on a 14-3-3 regulatory complex. *EMBO J.* **22**, 987–994 (2003).
163. Ottmann, C. *et al.* Phosphorylation-independent interaction between 14-3-3 and exoenzyme S: from structure to pathogenesis. *EMBO J.* **26**, 902–913 (2007).
164. Sluchanko, N. N. & Gusev, N. B. Moonlighting chaperone-like activity of the universal regulatory 14-3-3 proteins. *FEBS J.* **284**, 1279–1295 (2017).
165. Psenakova, K. *et al.* 14-3-3 protein directly interacts with the kinase domain of calcium/calmodulin-dependent protein kinase kinase (CaMKK2). *Biochim. Biophys. Acta BBA - Gen. Subj.* **1862**, 1612–1625 (2018).
166. Johnson, C. *et al.* Bioinformatic and experimental survey of 14-3-3-binding sites. *Biochem. J.* **427**, 69–78 (2010).
167. Masters, S. C., Pederson, K. J., Zhang, L., Barbieri, J. T. & Fu, H. Interaction of 14-3-3 with a Nonphosphorylated Protein Ligand, Exoenzyme S of *Pseudomonas aeruginosa*. *Biochemistry* **38**, 5216–5221 (1999).
168. Fu, H., Coburn, J. & Collier, R. J. The eukaryotic host factor that activates exoenzyme S of *Pseudomonas aeruginosa* is a member of the 14-3-3 protein family. *Proc. Natl. Acad. Sci.* **90**, 2320–2324 (1993).
169. Wang, B. *et al.* Isolation of High-Affinity Peptide Antagonists of 14-3-3 Proteins by Phage Display. *Biochemistry* **38**, 12499–12504 (1999).
170. Petosa, C. *et al.* 14-3-3 ζ Binds a Phosphorylated Raf Peptide and an Unphosphorylated Peptide via Its Conserved Amphipathic Groove. *J. Biol. Chem.* **273**, 16305–16310 (1998).
171. Toleman, C. A. *et al.* Structural basis of O-GlcNAc recognition by mammalian 14-3-3 proteins. *Proc. Natl. Acad. Sci.* **115**, 5956–5961 (2018).
172. Horvath, M., Petrvalska, O., Herman, P., Obsilova, V. & Obsil, T. 14-3-3 proteins inactivate DAPK2 by promoting its dimerization and protecting key regulatory phosphosites. *Commun. Biol.* **4**, 986 (2021).
173. Obsilova, V. & Obsil, T. Structural insights into the functional roles of 14-3-3 proteins. *Front. Mol. Biosci.* **9**, 1016071 (2022).
174. Ottmann, C. Small-molecule modulators of 14-3-3 protein–protein interactions. *Bioorg. Med. Chem.* **21**, 4058–4062 (2013).
175. Stevers, L. M. *et al.* Modulators of 14-3-3 Protein–Protein Interactions. *J. Med. Chem.* **61**, 3755–3778 (2018).
176. Masters, S. C. & Fu, H. 14-3-3 Proteins Mediate an Essential Anti-apoptotic Signal. *J. Biol. Chem.* **276**, 45193–45200 (2001).
177. Cao, W. *et al.* Targeting 14-3-3 protein, difopein induces apoptosis of human glioma cells and suppresses tumor growth in mice. *Apoptosis* **15**, 230–241 (2010).

178. Zhao, J. *et al.* Discovery and structural characterization of a small molecule 14-3-3 protein-protein interaction inhibitor. *Proc. Natl. Acad. Sci.* **108**, 16212–16216 (2011).
179. Glas, A. *et al.* Constrained Peptides with Target-Adapted Cross-Links as Inhibitors of a Pathogenic Protein–Protein Interaction. *Angew. Chem. Int. Ed.* **53**, 2489–2493 (2014).
180. Takemoto, Y. *et al.* Chemistry and Biology of Moverastins, Inhibitors of Cancer Cell Migration, Produced by *Aspergillus*. *Chem. Biol.* **12**, 1337–1347 (2005).
181. Tashiro, E. & Imoto, M. Screening and target identification of bioactive compounds that modulate cell migration and autophagy. *Bioorg. Med. Chem.* **24**, 3283–3290 (2016).
182. Acevedo, S. F., Tsigkari, K. K., Grammenoudi, S. & Skoulakis, E. M. C. *In Vivo* Functional Specificity and Homeostasis of Drosophila 14-3-3 Proteins. *Genetics* **177**, 239–253 (2007).
183. Gogl, G. *et al.* Hierarchized phosphotarget binding by the seven human 14-3-3 isoforms. *Nat. Commun.* **12**, 1677 (2021).
184. Yang, H.-Y., Wen, Y.-Y., Chen, C.-H., Lozano, G. & Lee, M.-H. 14-3-3 σ Positively Regulates p53 and Suppresses Tumor Growth. *Mol. Cell. Biol.* **23**, 7096–7107 (2003).
185. Ferguson, A. T. *et al.* High frequency of hypermethylation at the 14-3-3 σ locus leads to gene silencing in breast cancer. *Proc. Natl. Acad. Sci.* **97**, 6049–6054 (2000).
186. Oecking, C., Eckerskorn, C. & Weiler, E. W. The fusicoccin receptor of plants is a member of the 14-3-3 superfamily of eukaryotic regulatory proteins. *FEBS Lett.* **352**, 163–166 (1994).
187. Molzan, M. *et al.* Stabilization of Physical RAF/14-3-3 Interaction by Cotylenin A as Treatment Strategy for RAS Mutant Cancers. *ACS Chem. Biol.* **8**, 1869–1875 (2013).
188. Rose, R. *et al.* Identification and Structure of Small-Molecule Stabilizers of 14 – 3 – 3 Protein–Protein Interactions. *Angew. Chem. Int. Ed.* **49**, 4129–4132 (2010).
189. Sato, S. *et al.* Metabolite Regulation of Nuclear Localization of Carbohydrate-response Element-binding Protein (ChREBP). *J. Biol. Chem.* **291**, 10515–10527 (2016).
190. Sijbesma, E. *et al.* Structure-based evolution of a promiscuous inhibitor to a selective stabilizer of protein–protein interactions. *Nat. Commun.* **11**, 3954 (2020).
191. Stevers, L. M. *et al.* Macrocyclic-stabilization of its interaction with 14-3-3 increases plasma membrane localization and activity of CFTR. *Nat. Commun.* **13**, 3586 (2022).
192. Wiltfang, J. *et al.* Isoform Pattern of 14-3-3 Proteins in the Cerebrospinal Fluid of Patients with Creutzfeldt-Jakob Disease. *J. Neurochem.* **73**, 2485–2490 (1999).
193. Layfield, R. *et al.* Neurofibrillary tangles of Alzheimer’s disease brains contain 14-3-3 proteins. *Neurosci. Lett.* **209**, 57–60 (1996).
194. Ostrerova, N. *et al.* α -Synuclein Shares Physical and Functional Homology with 14-3-3 Proteins. *J. Neurosci.* **19**, 5782–5791 (1999).
195. Chen, H.-K. *et al.* Interaction of Akt-Phosphorylated Ataxin-1 with 14-3-3 Mediates Neurodegeneration in Spinocerebellar Ataxia Type 1. *Cell* **113**, 457–468 (2003).
196. Lu, J. *et al.* 14-3-3 ζ Cooperates with ErbB2 to Promote Ductal Carcinoma In Situ Progression to Invasive Breast Cancer by Inducing Epithelial-Mesenchymal Transition. *Cancer Cell* **16**, 195–207 (2009).

197. Xu, J. *et al.* 14-3-3 ζ Turns TGF- β 's Function from Tumor Suppressor to Metastasis Promoter in Breast Cancer by Contextual Changes of Smad Partners from p53 to Gli2. *Cancer Cell* **27**, 177–192 (2015).
198. Gu, Y. *et al.* 14-3-3 ζ binds the proteasome, limits proteolytic function and enhances sensitivity to proteasome inhibitors. *Leukemia* **32**, 744–751 (2018).
199. Lage-Vickers, S. *et al.* The expression of YWHAZ and NDRG1 predicts aggressive outcome in human prostate cancer. *Commun. Biol.* **4**, 103 (2021).
200. Zhang, Y. *et al.* 14-3-3 ϵ : a protein with complex physiology function but promising therapeutic potential in cancer. *Cell Commun. Signal.* **22**, 72 (2024).
201. Berg, D., Holzmann, C. & Riess, O. 14-3-3 proteins in the nervous system. *Nat. Rev. Neurosci.* **4**, 752–762 (2003).
202. Boston, P. F., Jackson, P. & Thompson, R. J. Human 14-3-3 Protein: Radioimmunoassay, Tissue Distribution, and Cerebrospinal Fluid Levels in Patients with Neurological Disorders. *J. Neurochem.* **38**, 1475–1482 (1982).
203. Steinacker, P., Aitken, A. & Otto, M. 14-3-3 proteins in neurodegeneration. *Semin. Cell Dev. Biol.* **22**, 696–704 (2011).
204. Betters, R. K. *et al.* Characterization of the Tau Interactome in Human Brain Reveals Isoform-Dependent Interaction with 14-3-3 Family Proteins. *eneuro* **10**, ENEURO.0503-22.2023 (2023).
205. Montine, T. J. *et al.* National Institute on Aging–Alzheimer's Association guidelines for the neuropathologic assessment of Alzheimer's disease: a practical approach. *Acta Neuropathol. (Berl.)* **123**, 1–11 (2012).
206. Rubio, M. P. *et al.* 14-3-3-affinity purification of over 200 human phosphoproteins reveals new links to regulation of cellular metabolism, proliferation and trafficking. *Biochem. J.* **379**, 395–408 (2004).
207. Benzinger, A., Muster, N., Koch, H. B., Yates, J. R. & Hermeking, H. Targeted Proteomic Analysis of 14-3-3 ζ , a p53 Effector Commonly Silenced in Cancer. *Mol. Cell. Proteomics* **4**, 785–795 (2005).
208. Seger, R. & Krebs, E. G. The MAPK signaling cascade. *FASEB J. Off. Publ. Fed. Am. Soc. Exp. Biol.* **9**, 726–735 (1995).
209. Hekman, M. *et al.* Reversible Membrane Interaction of BAD Requires two C-terminal Lipid Binding Domains in Conjunction with 14-3-3 Protein Binding. *J. Biol. Chem.* **281**, 17321–17336 (2006).
210. Foote, M. & Zhou, Y. 14-3-3 proteins in neurological disorders. *Int. J. Biochem. Mol. Biol.* **3**, 152–164 (2012).
211. Qing, Y. *et al.* Dysregulated 14-3-3 Family in Peripheral Blood Leukocytes of Patients with Schizophrenia. *Sci. Rep.* **6**, 23791 (2016).
212. Schubert, K. O., Föcking, M. & Cotter, D. R. Proteomic pathway analysis of the hippocampus in schizophrenia and bipolar affective disorder implicates 14-3-3 signaling, aryl hydrocarbon receptor signaling, and glucose metabolism: Potential roles in GABAergic interneuron pathology. *Schizophr. Res.* **167**, 64–72 (2015).

213. Saia-Cereda, V. M., Cassoli, J. S., Martins-de-Souza, D. & Nascimento, J. M. Psychiatric disorders biochemical pathways unraveled by human brain proteomics. *Eur. Arch. Psychiatry Clin. Neurosci.* **267**, 3–17 (2017).
214. Watanabe, K. *et al.* Role of 14-3-3 protein and oxidative stress in diabetic cardiomyopathy. *Acta Physiol. Hung.* **96**, 277–287 (2009).
215. Kosaka, Y. *et al.* 14-3-3 ϵ Plays a Role in Cardiac Ventricular Compaction by Regulating the Cardiomyocyte Cell Cycle. *Mol. Cell. Biol.* **32**, 5089–5102 (2012).
216. Qu, J.-H. *et al.* Proteomic Landscape and Deduced Functions of the Cardiac 14-3-3 Protein Interactome. *Cells* **11**, 3496 (2022).
217. Lim, J. W. *et al.* Cellular stress-related protein expression in Helicobacter pylori-infected gastric epithelial AGS cells. *Int. J. Biochem. Cell Biol.* **36**, 1624–1634 (2004).
218. Assossou, O. *et al.* Subcellular localization of 14-3-3 proteins in *Toxoplasma gondii* tachyzoites and evidence for a lipid raft-associated form. *FEMS Microbiol. Lett.* **224**, 161–168 (2003).
219. Weidner, J. M. *et al.* Migratory activation of parasitized dendritic cells by the protozoan *Toxoplasma gondii* 14-3-3 protein: Toxoplasma-induced hypermigration of dendritic cells. *Cell. Microbiol.* **18**, 1537–1550 (2016).
220. Aoki, H., Hayashi, J., Moriyama, M., Arakawa, Y. & Hino, O. Hepatitis C Virus Core Protein Interacts with 14-3-3 Protein and Activates the Kinase Raf-1. *J. Virol.* **74**, 1736–1741 (2000).
221. Kosaki, A., Yamada, K., Suga, J., Otaka, A. & Kuzuya, H. 14-3-3 β Protein Associates with Insulin Receptor Substrate 1 and Decreases Insulin-stimulated Phosphatidylinositol 3'-Kinase Activity in 3T3L1 Adipocytes. *J. Biol. Chem.* **273**, 940–944 (1998).
222. Wang, P. *et al.* Type 2 Diabetes Promotes Cell Centrosome Amplification via AKT-ROS-Dependent Signalling of ROCK1 and 14-3-3 σ . *Cell. Physiol. Biochem.* **47**, 356–367 (2018).
223. Munier, C. C., Ottmann, C. & Perry, M. W. D. 14-3-3 modulation of the inflammatory response. *Pharmacol. Res.* **163**, 105236 (2021).
224. Chow, K. T., Gale, M. & Loo, Y.-M. RIG-I and Other RNA Sensors in Antiviral Immunity. *Annu. Rev. Immunol.* **36**, 667–694 (2018).
225. Bhalla, V. *et al.* Serum- and Glucocorticoid-Regulated Kinase 1 Regulates Ubiquitin Ligase Neural Precursor Cell-Expressed, Developmentally Down-Regulated Protein 4-2 by Inducing Interaction with 14-3-3. *Mol. Endocrinol.* **19**, 3073–3084 (2005).
226. Lu, C., Pribanic, S., Debonneville, A., Jiang, C. & Rotin, D. The PY Motif of ENaC, Mutated in Liddle Syndrome, Regulates Channel Internalization, Sorting and Mobilization from Subapical Pool. *Traffic* **8**, 1246–1264 (2007).
227. Itani, O. A., Stokes, J. B. & Thomas, C. P. Nedd4–2 isoforms differentially associate with ENaC and regulate its activity. *Am. J. Physiol.-Ren. Physiol.* **289**, F334–F346 (2005).
228. Boura, E. *et al.* Both the N-terminal Loop and Wing W2 of the Forkhead Domain of Transcription Factor Foxo4 Are Important for DNA Binding. *J. Biol. Chem.* **282**, 8265–8275 (2007).

229. Karas, Michael. & Hillenkamp, Franz. Laser desorption ionization of proteins with molecular masses exceeding 10,000 daltons. *Anal. Chem.* **60**, 2299–2301 (1988).
230. Garrett, T. J. *et al.* Imaging of small molecules in tissue sections with a new intermediate-pressure MALDI linear ion trap mass spectrometer. *Int. J. Mass Spectrom.* **260**, 166–176 (2007).
231. Khatib-Shahidi, S., Andersson, M., Herman, J. L., Gillespie, T. A. & Caprioli, R. M. Direct Molecular Analysis of Whole-Body Animal Tissue Sections by Imaging MALDI Mass Spectrometry. *Anal. Chem.* **78**, 6448–6456 (2006).
232. Chaurand, P., Norris, J. L., Cornett, D. S., Mobley, J. A. & Caprioli, R. M. New Developments in Profiling and Imaging of Proteins from Tissue Sections by MALDI Mass Spectrometry. *J. Proteome Res.* **5**, 2889–2900 (2006).
233. Stoeckli, M., Staab, D., Staufenbiel, M., Wiederhold, K.-H. & Signor, L. Molecular imaging of amyloid β peptides in mouse brain sections using mass spectrometry. *Anal. Biochem.* **311**, 33–39 (2002).
234. Murayama, C., Kimura, Y. & Setou, M. Imaging mass spectrometry: principle and application. *Biophys. Rev.* **1**, 131–139 (2009).
235. Yasuyuki Miyazaki *et al.*, ‘Novel *In Vitro* Screening System Based on Differential Scanning Fluorimetry to Search for Small Molecules against the Disassembly or Assembly of HIV-1 Capsid Protein’, *Frontiers in Microbiology* 8 (24 July 2017): 1413, <https://doi.org/10.3389/fmicb.2017.01413>.
236. Kai Gao, Rick Oerlemans, and Matthew R. Groves, ‘Theory and Applications of Differential Scanning Fluorimetry in Early-Stage Drug Discovery’, *Biophysical Reviews* 12, no. 1 (February 2020): 85–104, <https://doi.org/10.1007/s12551-020-00619-2>.
237. Thaiesha A. Wright *et al.*, ‘Extraction of Thermodynamic Parameters of Protein Unfolding Using Parallelized Differential Scanning Fluorimetry’, *The Journal of Physical Chemistry Letters* 8, no. 3 (2 February 2017): 553–58, <https://doi.org/10.1021/acs.jpcclett.6b02894>.
238. Niesen, F. H., Berglund, H. & Vedadi, M. The use of differential scanning fluorimetry to detect ligand interactions that promote protein stability. *Nat. Protoc.* **2**, 2212–2221 (2007).
239. Ballone, A., Centorrino, F., Wolter, M. & Ottmann, C. Protein X-ray crystallography of the 14-3-3 ζ /SOS1 complex. *Data Brief* **19**, 1683–1687 (2018).
240. Senesi, N. & D’Orazio, V. FLUORESCENCE SPECTROSCOPY. in *Encyclopedia of Soils in the Environment* 35–52 (Elsevier, 2005). doi:10.1016/B0-12-348530-4/00211-3.
241. Albani, J. R. Fluorescence: Principles and Observables. in *Structure and Dynamics of Macromolecules: Absorption and Fluorescence Studies* 55–98 (Elsevier, 2004). doi:10.1016/B978-044451449-3/50002-2.
242. Misra, G. Fluorescence spectroscopy. in *Data Processing Handbook for Complex Biological Data Sources* 31–37 (Elsevier, 2019). doi:10.1016/B978-0-12-816548-5.00003-4.
243. Fleming, K. G. Fluorescence Theory. in *Encyclopedia of Spectroscopy and Spectrometry* 647–653 (Elsevier, 2017). doi:10.1016/B978-0-12-803224-4.00357-5.
244. Lakowicz, J. R. "In Principles of Fluorescence Spectroscopy." (2006): 97-155.

245. *Principles of Fluorescence Spectroscopy*. (Springer US, Boston, MA, 2006). doi:10.1007/978-0-387-46312-4.
246. Valeur, B. & Berberan-Santos, M. N. *Molecular Fluorescence: Principles and Applications*. (Wiley, 2012). doi:10.1002/9783527650002.
247. Jameson, D. M. *Introduction to Fluorescence*. (CRC Press, 2014). doi:10.1201/b16502.
248. Yasuda, R. Principle and Application of Fluorescence Lifetime Imaging for Neuroscience. in *Neurophotonics and Biomedical Spectroscopy* 53–64 (Elsevier, 2019). doi:10.1016/B978-0-323-48067-3.00003-2.
249. Boens, N. *et al.* Fluorescence Lifetime Standards for Time and Frequency Domain Fluorescence Spectroscopy. *Anal. Chem.* **79**, 2137–2149 (2007).
250. Jain, A., Blum, C. & Subramaniam, V. Fluorescence Lifetime Spectroscopy and Imaging of Visible Fluorescent Proteins. in *Advances in Biomedical Engineering* 147–176 (Elsevier, 2009). doi:10.1016/B978-0-444-53075-2.00004-6.
251. Bajar, B., Wang, E., Zhang, S., Lin, M. & Chu, J. A Guide to Fluorescent Protein FRET Pairs. *Sensors* **16**, 1488 (2016).
252. Diamandis, E. P. Immunoassays with time-resolved fluorescence spectroscopy: Principles and applications. *Clin. Biochem.* **21**, 139–150 (1988).
253. Teijeiro-Gonzalez, Y. *et al.* Time-Resolved Fluorescence Anisotropy and Molecular Dynamics Analysis of a Novel GFP Homo-FRET Dimer. *Biophys. J.* **120**, 254–269 (2021).
254. Bader, A. N., Hofman, E. G., Van Bergen En Henegouwen, P. M. P. & Gerritsen, H. C. Imaging of protein cluster sizes by means of confocal time-gated fluorescence anisotropy microscopy. *Opt. Express* **15**, 6934 (2007).
255. Kacirova, M. *et al.* Structural Characterization of Phosducin and Its Complex with the 14-3-3 Protein. *J. Biol. Chem.* **290**, 16246–16260 (2015).
256. Vecer, J. & Herman, P. Maximum Entropy Analysis of Analytically Simulated Complex Fluorescence Decays. *J. Fluoresc.* **21**, 873–881 (2011).
257. Lehrer, S. Solute perturbation of protein fluorescence. Quenching of the tryptophyl fluorescence of model compounds and of lysozyme by iodide ion. *Biochemistry* **10**, 3254–3263 (1971).
258. Suh, M.-J., Pourshahian, S. & Limbach, P. A. Developing limited proteolysis and mass spectrometry for the characterization of ribosome topography. *J. Am. Soc. Mass Spectrom.* **18**, 1304–1317 (2007).
259. Peng, B.-H., Lee, J. C. & Campbell, G. A. *In Vitro* Protein Complex Formation with Cytoskeleton-anchoring Domain of Occludin Identified by Limited Proteolysis. *J. Biol. Chem.* **278**, 49644–49651 (2003).
260. Meyer, E. L., Strutz, N., Gahring, L. C. & Rogers, S. W. Glutamate Receptor Subunit 3 Is Modified by Site-specific Limited Proteolysis Including Cleavage by γ -Secretase. *J. Biol. Chem.* **278**, 23786–23796 (2003).

261. Hijarrubia, M. J., Aparicio, J. F. & Martín, J. F. Domain Structure Characterization of the Multifunctional α -Aminoacidate Reductase from *Penicillium chrysogenum* by Limited Proteolysis. *J. Biol. Chem.* **278**, 8250–8256 (2003).
262. Krufft, V. & Wittmann-Liebold, B. Determination of peptide regions on the surface of the eubacterial and archaeobacterial ribosome by limited proteolytic digestion. *Biochemistry* **30**, 11781–11787 (1991).
263. Ryu, W.-S. Virus Structure. in *Molecular Virology of Human Pathogenic Viruses* 21–29 (Elsevier, 2017). doi:10.1016/B978-0-12-800838-6.00002-3.
264. Wlodawer, A., Minor, W., Dauter, Z. & Jaskolski, M. Protein crystallography for aspiring crystallographers or how to avoid pitfalls and traps in macromolecular structure determination. *FEBS J.* **280**, 5705–5736 (2013).
265. Bunaciu, A. A., Udriștioiu, E. G. & Aboul-Enein, H. Y. X-Ray Diffraction: Instrumentation and Applications. *Crit. Rev. Anal. Chem.* **45**, 289–299 (2015).
266. Joshi, R. *et al.* Nedd4-2 binding to 14-3-3 modulates the accessibility of its catalytic site and WW domains. *Biophys. J.* **121**, 1299–1311 (2022).
267. Kalabova, D. *et al.* Human procaspase-2 phosphorylation at both S139 and S164 is required for 14-3-3 binding. *Biochem. Biophys. Res. Commun.* **493**, 940–945 (2017).
268. Nutt, L. K. *et al.* Metabolic Control of Oocyte Apoptosis Mediated by 14-3-3 ζ -Regulated Dephosphorylation of Caspase-2. *Dev. Cell* **16**, 856–866 (2009).
269. Wright, K. M. *et al.* NEDD4L intramolecular Interactions regulate its auto- and substrate NaV1.5 ubiquitination. *J. Biol. Chem.* 105715 (2024) doi:10.1016/j.jbc.2024.105715.
270. Chandran, S. *et al.* Neural Precursor Cell-expressed Developmentally Down-regulated Protein 4-2 (Nedd4-2) Regulation by 14-3-3 Protein Binding at Canonical Serum and Glucocorticoid Kinase 1 (SGK1) Phosphorylation Sites. *J. Biol. Chem.* **286**, 37830–37840 (2011).
271. Sudol, M., Chen, H. I., Bougeret, C., Einbond, A. & Bork, P. Characterization of a novel protein-binding module — the WW domain. *FEBS Lett.* **369**, 67–71 (1995).
272. Snyder, P. M., Olson, D. R. & Thomas, B. C. Serum and Glucocorticoid-regulated Kinase Modulates Nedd4-2-mediated Inhibition of the Epithelial Na⁺Channel. *J. Biol. Chem.* **277**, 5–8 (2002).
273. Chan, W. *et al.* Down-regulation of Active ACK1 Is Mediated by Association with the E3 Ubiquitin Ligase Nedd4-2. *J. Biol. Chem.* **284**, 8185–8194 (2009).
274. Roy, A. *et al.* Alternatively spliced proline-rich cassettes link WNK1 to aldosterone action. *J. Clin. Invest.* **125**, 3433–3448 (2015).
275. Fotia, A. B. *et al.* Regulation of Neuronal Voltage-gated Sodium Channels by the Ubiquitin-Protein Ligases Nedd4 and Nedd4-2. *J. Biol. Chem.* **279**, 28930–28935 (2004).
276. Bhalla, V. & Hallows, K. R. Mechanisms of ENaC Regulation and Clinical Implications. *J. Am. Soc. Nephrol.* **19**, 1845–1854 (2008).
277. Snyder, P. M. Down-Regulating Destruction: Phosphorylation Regulates the E3 Ubiquitin Ligase Nedd4-2. *Sci. Signal.* **2**, (2009).

278. Wu, P.-Y. A conserved catalytic residue in the ubiquitin-conjugating enzyme family. *EMBO J.* **22**, 5241–5250 (2003).
279. Lorenzo Soini et al., ‘Identification of Molecular Glues of the SLP76/14-3-3 Protein–Protein Interaction’, *RSC Medicinal Chemistry* **12**, no. 9 (2021): 1555–64, <https://doi.org/10.1039/D1MD00172H>.

9. Internet sources

- <https://en.wikipedia.org/>
- <https://pubmed.ncbi.nlm.nih.gov/>
- <https://www.ncbi.nlm.nih.gov/protein/>
- <https://www.uniprot.org/>
- <https://www.rcsb.org/>
- <https://xiview.org/>
- <https://peterslab.org/MSTools/DrawHDXPlot/DrawHDXPlot.php>
- <https://www.addgene.org/>
- <https://cube-biotech.com/>
- <https://www.biobulletins.com/>
- <https://www.edinst.com/>
- <https://www.toray-research.co.jp/>

10. Published articles

10.1 Publication I

Joshi, R., Pohl, P., Strachotova, D., Herman, P., Obsil, T., Obsilova, V. **Nedd4-2 binding to 14-3-3 modulates the accessibility of its catalytic site and WW domains.** *Biophys. J.* **121**, 1299–1311 (2022).

IF²⁰²² = 3.4

Contribution:

I have performed most of the experiments; including site directed mutagenesis, preparation of all Nedd4-2 and 14-3-3 recombinant proteins. I optimized the protein purification of all single cysteine Nedd4-2 variants of constructs Nedd4-2¹⁹⁰⁻⁵⁸¹ and Nedd4-2¹⁸⁶⁻⁹⁷⁵ to obtain protein of sufficient yield and quality for subsequent biophysical characterization. I performed the differential scanning fluorimetry measurements and native gel electrophoresis. I performed and optimized protein labeling by 1,5-IAEDANS and prepared samples for fluorescence measurements. Finally, I performed limited proteolysis experiment and prepared the corresponding figures.

Nedd4-2 binding to 14-3-3 modulates the accessibility of its catalytic site and WW domains

Rohit Joshi,^{1,2} Pavel Pohl,¹ Dita Strachotova,³ Petr Herman,³ Tomas Obsil,^{1,2} and Veronika Obsilova^{1,*}

¹Department of Structural Biology of Signaling Proteins, Division BIOCEV, Institute of Physiology of the Czech Academy of Sciences, Czech Republic; ²Department of Physical and Macromolecular Chemistry, Faculty of Science, Charles University, Prague, Czech Republic; and ³Institute of Physics, Faculty of Mathematics and Physics, Charles University, Prague, Czech Republic

ABSTRACT Neural precursor cells expressed developmentally downregulated protein 4-2 (Nedd4-2), a homologous to the E6-AP carboxyl terminus (HECT) ubiquitin ligase, triggers the endocytosis and degradation of its downstream target molecules by regulating signal transduction through interactions with other targets, including 14-3-3 proteins. In our previous study, we found that 14-3-3 binding induces a structural rearrangement of Nedd4-2 by inhibiting interactions between its structured domains. Here, we used time-resolved fluorescence intensity and anisotropy decay measurements, together with fluorescence quenching and mass spectrometry, to further characterize interactions between Nedd4-2 and 14-3-3 proteins. The results showed that 14-3-3 binding affects the emission properties of AEDANS-labeled WW3, WW4, and, to a lesser extent, WW2 domains, and reduces their mobility, but not those of the WW1 domain, which remains mobile. In contrast, 14-3-3 binding has the opposite effect on the active site of the HECT domain, which is more solvent exposed and mobile in the complexed form than in the apo form of Nedd4-2. Overall, our results suggest that steric hindrance of the WW3 and WW4 domains combined with conformational changes in the catalytic domain may account for the 14-3-3 binding-mediated regulation of Nedd4-2.

SIGNIFICANCE Ubiquitin ligase Nedd4-2 phosphorylation at residues S342 and S448 triggers its association with 14-3-3 proteins, thus modulating Nedd4-2 function and the ubiquitination of various ion channels. Here, we labeled the individual structured Nedd4-2 domains with the environmentally sensitive extrinsic fluorophore 1,5-IAEDANS and performed fluorescence measurements. This allowed us to monitor the mobility and accessibility of the individual domains of Nedd4-2 upon 14-3-3 protein binding. Our data reveal that the steric hindrance of the WW3 and WW4 domains together with the conformational change in the catalytic domain may be responsible for the 14-3-3 binding-mediated regulation of Nedd4-2 functions. Therefore, 14-3-3-mediated changes in the accessibility and/or mobility of individual WW domains of Nedd4-2 may modulate different dynamic processes of membrane proteins ubiquitination.

INTRODUCTION

The Nedd4 family of mammalian homologous to the E6-AP carboxyl terminus (HECT) E3 ubiquitin ligases encompasses nine members, including neural precursor cell-expressed developmentally downregulated protein 4-2 (Nedd4-2). Nedd4-2 originated from the most conserved and ancestral member Nedd4 by gene duplication (1) and is only found in vertebrates, which primarily express this ubiquitin ligase in the lungs, kidneys, brain, and heart (2). In these organs, Nedd4-2 has been shown to modulate

epithelial sodium channel ENaC in the lungs and kidneys (3), the renal sodium-chloride symporter NCC (4), several voltage-gated sodium and potassium channels (5,6), and neural receptors (7), among other targets. Some of these targets include membrane proteins, whose activation is controlled by ubiquitination mediated by Nedd4-2. Accordingly, its malfunction has been linked to lung inflammation, Liddle syndrome, salt-sensitive hypertension, epilepsy, and developmental and end-stage renal disorders, highlighting its importance for human physiology (8–11).

The Nedd4-2 molecule consists of three spatially and functionally distinct domains, the N-terminal calcium/lipid binding (C2) domain, four repeats of 34 amino acids known as WW domains, and the HECT domain (Fig. 1 A). The C2 domain regulates protein function by mediating its

Submitted August 31, 2021, and accepted for publication February 15, 2022.

*Correspondence: veronika.obsilova@fgu.cas.cz or obsil@natur.cuni.cz

Editor: Samrat Mukhopadhyay.

<https://doi.org/10.1016/j.bpj.2022.02.025>

© 2022 Biophysical Society.



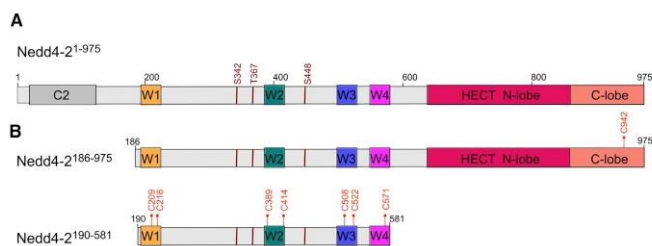


FIGURE 1 Domain structure of human Nedd4-2 and the protein constructs used in this study. (A) Schematic representation of the Nedd4-2 domain structure showing the positions of 14-3-3 binding motifs S342, T367, and S448; the Ca^{2+} lipid binding domain is shown in gray (denoted as C2), and the WW1-4 domains are shown in yellow, teal, blue, and magenta (denoted as W1-4). The N- and C-lobes of the HECT domain are shown in raspberry and salmon, respectively. (B) The constructs used in this study are Nedd4-2¹⁸⁶⁻⁹⁷⁵ (C942) and Nedd4-2¹⁹⁰⁻⁵⁸¹ (C209, C218, C389, C414, C508, C522, and C571). The positions of the cysteine residues used for 1,5-IAEDANS labeling are shown in red. To see this figure in color, go online.

translocation to phospholipid membranes in a response to enhanced cytosolic Ca^{2+} (12). Human Nedd4-2 contains four WW domains located between the C2 and the HECT domains. The WW domains (also known as WWP) are named after their two highly conserved tryptophan residues and proline residue. These domains preferentially bind to proline-rich motifs (PPXY) of regulated substrates because they contain a hydrophobic core bordered by beta sheets with several charged residues (13,14). The catalytic HECT domain catalyzes polyubiquitin chain assembly through a conserved, two-step mechanism, similarly to other HECT family members (15). This substrate ubiquitination by Nedd4-2 through substrate-linked ubiquitin chains promotes degradation and cell signaling (16). WW domains, in the same protein, show different substrate specificity *in vitro*. As such, Nedd4-2 may interact with various proteins through its WW domains *in vivo*.

In line with the above, the WW3 and WW4 domains of Nedd4-2 directly interact with all epithelial sodium channel (ENaC) subunits and play a key role in the feedback regulation of ENaC in mammalian cells (2,17). In turn, mouse Nedd4 uses all of its three WW domains to interact with ENaC (18), whereas WW2-4 of human Nedd4, which has four WW domains, are required for this interaction (19). Moreover, the WW domains of Nedd4-2 recognize the PY motif in its own HECT domain (20), and WW1 and WW2 interact with TRPV6 and decrease its ubiquitination rate (21). Nedd4-2 function and its substrate specificity are also modulated by phosphorylation and binding to adaptor proteins, which can have both inhibitory and activatory effects. Several protein kinases, such as PKA, Akt, Sgk1, JNK1, and IKK β , phosphorylate Nedd4-2 at S342, T367, and S448 (22–27), thus triggering 14-3-3 protein binding (28–30).

14-3-3 proteins are a family of highly conserved dimeric proteins, which interact with hundreds of other proteins, thereby regulating their functions (31–34). 14-3-3 proteins recognize pSer/pThr-containing motifs, which are frequently located within disordered regions of their binding partners and far from structured functional domains (35–37). Nedd4-2 has three 14-3-3 binding motifs, but phosphorylated

S342 and S448 are the crucial residues that facilitate high-affinity 14-3-3 binding (30). Both motifs are located within disordered regions bordering the WW2 domain (Fig. 1 A). However, the exact role of 14-3-3 binding in regulating Nedd4-2 remains unclear. For example, Nedd4-2 interaction with 14-3-3 is known to both prevent the ubiquitination of ENaC, increasing ENaC activity (38), and promote the ubiquitination of the GluA1 subunit of the AMPA receptor (7). Nevertheless, we have recently performed a biophysical characterization of the complex between the phosphorylated Nedd4-2 and 14-3-3 η , showing that 14-3-3 binding induces a structural rearrangement of Nedd4-2 by altering interactions between its structured domains (30). Our structural analysis also suggested that the formation of this complex may affect the accessibility and/or the mobility of individual WW domains of Nedd4-2.

To test this hypothesis, in this study, we aimed to further characterize interactions between phosphorylated Nedd4-2 and 14-3-3 by investigating changes in the solvent accessibility and mobility of Nedd4-2 domains upon complex formation. For this purpose, we used various fluorescence spectroscopy methods, including time-resolved fluorescence intensity and anisotropy decay measurements and fluorescence quenching. The results clearly indicate that 14-3-3 η directly interacts with WW3 and WW4 domains and that the 14-3-3 η -protein-induced conformational change of Nedd4-2 involves not only the WW3 and WW4 domains but also its catalytic domain.

MATERIALS AND METHODS

Heterologous expression and purification of 14-3-3 protein

14-3-3 η was expressed and purified as described previously (30,39,40). In brief, 14-3-3 η was expressed in *E. coli* BL21(DE3) cells using three purification steps: affinity chromatography, followed by His₆-tag cleavage, anion-exchange chromatography (HiTrap Q column, GE Healthcare, Chicago, Illinois, USA), and size-exclusion chromatography (HiLoad Superdex 75, GE Healthcare) in a buffer containing 20 mM Tris-HCl (pH 7.5), 150 mM NaCl, 1 mM TCEP, and 10% (w/v) glycerol. The final protein was concentrated to 30 mg·mL⁻¹, frozen in liquid nitrogen, and stored in aliquots at -80°C (193.15 K).

Heterologous expression, purification, and phosphorylation of Nedd4-2

The coding sequence of Nedd4-2 (residues 190–581) was PCR amplified from the plasmid hNedd4-2 (residues 186–975) previously prepared in our laboratory (30). The PCR product containing residues 190–581 was ligated into the polycistronic pST39 vector *SacI/KpnI* restriction sites. The entire cloned region was confirmed by sequencing. Thirteen different Nedd4-2 mutants in both Nedd4-2 variants containing a single cysteine residue (Nedd4-2^{190–581} variant: T209C, S218C, S389C, T414C, A508C, T522C, S571C; Nedd4-2^{186–975} variant: C702S, C776S, C853S, C874S, C942S) were generated using the QuikChange kit (Stratagene, Santa Clara, California, USA), confirming all mutations by sequencing.

Nedd4-2^{190–581} WT and single cysteine variants were expressed as a fusion protein with 6× noncleavable His-tag at the C-terminus by isopropyl-1-thio-β-D-galactopyranoside induction for 18–20 h at 18°C in *E. coli* BL21 (DE3) cells. The pelleted cells were suspended in lysis buffer (1× PBS, 1 M NaCl, 4 mM β-mercaptoethanol, 2 mM imidazole, and 0.01% (v/v) Tergitol NP-40) and purified using a Chelating Sepharose Fast Flow column (GE Healthcare) and purified using the standard protocol, followed by gel filtration chromatography on a HiLoad 26/600 Superdex 75 pg column (GE Healthcare) in a buffer containing 20 mM Tris-HCl (pH 7.5), 500 mM NaCl, 1 mM TCEP, 10% glycerol (w/v), and 0.01% (v/v) Tergitol NP-40. Purified Nedd4-2^{190–581} was phosphorylated with 158 units of PKA (Promega, Santa Clara, California, USA) per milligram of recombinant protein in the presence of 0.75 mM ATP and 20 mM MgCl₂ by incubation at 30°C for 2 h and then overnight at 4°C. After phosphorylation, the protein was repurified using a size-exclusion chromatography Superdex 75 Increase 10/300 GL column (GE Healthcare) in a buffer containing 20 mM Tris-HCl (pH 7.5), 500 mM NaCl, 1 mM TCEP, and 10% glycerol (w/v).

Nedd4-2^{186–975} WT and single cysteine variants were expressed and purified as described previously (30).

Labeling of Nedd4-2 mutants by 1,5-IAEDANS

Nedd4-2^{190–581} contains only one cysteine residue at position 341. To prepare Nedd4-2^{190–581} specifically labeled with a fluorescence probe at different positions in the WW domains, we first replaced cysteine 341 by serine and then incorporated a single cysteine into seven different positions (C209, C218, C389, C414, C508, C522, and C571). Nedd4-2^{186–975} contains six cysteine residues. To prepare Nedd4-2^{186–975} specifically labeled with a fluorescence probe at different positions of the HECT domain, we mutated C341S and used this mutation as a template for subsequent mutagenesis of five cysteine residues present in the HECT domain. Mutagenesis was performed so that only a single cysteine was present and that all other cysteine residues were mutated to serine residues. Covalent modification of Nedd4-2 containing a single cysteine residue with the thiol-reactive probe 1,5-IAEDANS was performed as described before (41). In brief, the protein (2.0–8.5 μM) in 50 mM Tris-HCl (pH 7.5), 100 mM NaCl, 1 mM EDTA buffer, and label, were mixed at a molar ratio of 1:40 and incubated at 30°C for 2 h, and then at 4°C overnight in the dark. Subsequent gel filtration chromatography was performed in 50 mM Tris-HCl (pH 7.5), 100 mM NaCl, 1 mM EDTA, 10% glycerol (w/v) buffer (Sigma-Aldrich, St. Louis, MO) to remove free unreacted label. The incorporation stoichiometry was determined by comparing the peak protein absorbance at 280 nm with the absorbance of bound 1,5-IAEDANS measured at 336 nm using an extinction coefficient of 5700 M⁻¹ cm⁻¹ (Molecular Probes, Eugene, OR).

Mass spectrometry analysis

Proteins were diluted to 50 mM ammonium bicarbonate buffer. Cysteines were reduced with 10 mM DTT for 45 min at 60°C and free cysteines were alkylated with 30 mM iodoacetamide for 30 min at room temperature in the dark. Trypsin digestion proceeded overnight at 37°C with an enzyme/

protein ratio of 1:20 (w/w). Peptides were loaded on a trap column (Luna Omega 5 μm Polar C18 100 Å, 20 × 0.3 mm, Phenomenex, Torrance, California, USA) and desalted for 5 min at flow rate 20 μL/min. Peptides were then separated using a reversed-phase C18 column (Luna Omega 3 μm Polar C18 100 Å, 150 × 0.3 mm, Phenomenex) at a flow rate 10 μL/min with a capillary UHPLC system (Agilent Technologies, Santa Clara, California, USA) under the following gradient conditions: 1–10% B in 1 min, 10–45% B in 19 min, 45–95% B in 5 min, where solvent A was 0.1% formic acid and 2.0% acetonitrile in water, and solvent B was 0.1% formic acid in 98% acetonitrile. The column was heated at 50°C and directly connected to a timsTOF Pro mass spectrometer (Bruker Daltonics, Madison, Wisconsin, USA). The instrument was operating in PASEF mode. All data were processed by the PEAKS Studio X software (Bioinformatics Solutions, Waterloo, Ontario, Canada), searching against the database of Nedd4-2^{190–581} protein. The FDR was set to 1% for the peptides.

Differential scanning fluorimetry

The thermal stability of the Nedd4-2 mutants was checked by measuring the thermally induced protein denaturation, using differential scanning fluorimetry. Nedd4-2^{190–581} and Nedd4-2^{186–975} protein variants at concentrations of 0.144–0.37 and 0.185 mg·mL⁻¹, respectively, were tested in 8× concentrated Sypro Orange (Sigma-Aldrich) in a total reaction volume of 50 μL in buffer containing 100 mM HEPES (pH 7.5) and 150 mM NaCl on a LightCycler 480 Multiwell Plate 96 (Roche Applied Science, Penzberg, Germany). The melting temperature values, *T_m*, corresponding to the inflection points of the melting curves, were determined as the minima of the negative first derivative using the Roche LightCycler 480 SW 1.5 software (42,43). The final results are expressed as the means from three measurements.

Limited proteolysis

Samples containing 50 pmol of phosphorylated Nedd4-2^{186–975} WT with or without 100 pmol 14-3-3η were digested by trypsin for 10, 20, and 30 min at 25°C in a buffer containing 50 mM Tris-HCl (pH 8.0), 500 mM NaCl, 1 mM TCEP, 10% (w/v) glycerol, and 0.01% tertol (protease/protein ratio was 1:1000, w/w). Undigested protein served as the zero-time point. The reactions were terminated by adding SDS-PAGE sample loading buffer and boiling for 5 min. The results were analyzed by SDS-PAGE. The density of the bands resulting from the degradation of Nedd4-2 in respective time points were quantified using Image Lab software and Student's *t*-test (Bio-Rad, Hercules, California, USA).

Time-resolved fluorescence

Time-resolved fluorescence intensity and anisotropy decay measurements, as well as data analysis, were performed as described previously (44,45). In brief, the apparatus comprised pulsed frequency-tripled Ti:Sapphire laser (Chameleon Ultra II, Coherent, Santa Clara, California, USA) and time-correlated single-photon counting detection (SPC150, Becker & Hickl, Berlin, Germany) with cooled MCP-PMT (R3809U-50, Hamamatsu, Hamamatsu City, Shizuoka, Japan). Dansyl fluorescence was excited at 355 nm and collected at 535 nm on a monochromator (H-20, Horiba, Kyoto, Japan) with a stack of glass OG420 long-pass and dielectric LP520 filters placed in front of the input slit. The repetition frequency of the excitation pulses was lowered to 4 MHz by the pulse-picker (APE, Berlin, Germany). This corresponds to about 15 dansyl lifetimes (250 ns) allowing dansyl emission to completely decay to zero between the two successive excitation pulses. Intensity decays were accumulated under the magic-angle conditions, typically in 1024 channels with a time resolution of 195 ps/channel, until reaching approximately 1.5 × 10⁵ counts at the decay maximum. The instrument response function was measured by scattered excitation from the

diluted ludo solution. FWHM of the response function was about 120 ps, which is well below the decay channel time width. Polarized decays for fluorescence anisotropy were acquired quasi-simultaneously with a switching time between the components of 30 s. The samples were placed in a thermostatic holder.

All experiments were performed at 23°C in a 50 mM Tris-HCl (pH 7.5), 100 mM NaCl, 1 mM EDTA, and 10% (w/v) glycerol buffer (Sigma-Aldrich). The concentrations of Nedd4-2^{190–581} variants (C209, C218, C389, C414, C508, C522, and C571), Nedd4-2^{186–975} C942, and 14-3-3 η ranged from 1.6 to 4 and from 4 to 8 μ M, respectively. Both fluorescence intensity and anisotropy decays were analyzed using the model-independent singular value decomposition-maximum entropy method (45).

Fluorescence was assumed to decay multiexponentially

$$I(t) = \sum_i \alpha_i \cdot \exp(-t/\tau_i), \quad (1)$$

where τ_i stands for the fluorescence lifetime components, and α_i are the corresponding amplitudes. The mean emission lifetime was calculated as follows:

$$\tau_{mean} = \frac{\sum_i \alpha_i \tau_i^2}{\sum_i \alpha_i \tau_i}. \quad (2)$$

Fluorescence anisotropies $r(t)$ were determined by simultaneous resolution of $I_{\parallel}(t)$ and $I_{\perp}(t)$ polarized decays (46,47). The anisotropies were assumed to decay multiexponentially:

$$r(t) = \sum_i \beta'_i \cdot \exp(-t/\phi'_i), \quad (3)$$

where amplitudes β'_i represent the distribution of the correlation times ϕ'_i , $\sum \beta'_i = r_0$, and r_0 is the initial anisotropy. We typically used 100 correlation times and 100 lifetimes equidistantly spaced in the logarithmic time-scale for MEM analysis (45).

Dansyl quenching

Stem-Volmer plots were constructed from changes in mean fluorescence lifetime after adding acrylamide aliquots dissolved in the protein buffer. Stem-Volmer plots were fitted to the modified SV equation (48) transformed to the form of:

$$\tau_0/\tau = (k_q\tau_0[Q] + 1)/(k_q\tau_0[Q]F_b + 1), \quad (4)$$

where τ and τ_0 are the mean fluorescence lifetime with and without quencher, respectively, $[Q]$ is acrylamide concentration, k_q is the bimolecular quenching constant, and F_b stands for an inaccessible fraction of the fluorophore.

RESULTS

Construction of the Nedd4-2 protein mutants for dansyl fluorescence measurements

For further insight into interactions between Nedd4-2 and 14-3-3 η , we labeled the individual structured Nedd4-2 domains with the environmentally sensitive extrinsic fluorophore 1,5-IAEDANS and performed time-resolved fluorescence intensity and anisotropy decay measurements, in addition to time-resolved collisional quenching of dansyl-labeled pro-

teins. For this purpose, we used two Nedd4-2 variants: Nedd4-2^{190–581} containing both 14-3-3 binding sites, S342 and S448, and all four WW domains, and Nedd4-2^{186–975}, also containing the HECT domain (Fig. 1 B) (30). Both proteins exhibited sufficient solubility and stability for biophysical studies. A previous study has shown that the Nedd4-2^{186–975} and 14-3-3 η form a complex with a 1:2 stoichiometry and $K_D < 50$ nM (30). Therefore, the concentration used for fluorescence studies enables that $\sim 99\%$ of proteins are bound in the complex.

The sequence of Nedd4-2^{190–581} contains a single cysteine residue at position C341 preceding the first phosphorylation site, that is, the 14-3-3 binding motif S342. For this reason, we first mutated C341 to serine and subsequently introduced a single cysteine residue at several positions of interest (mutations T209C, S218C, S389C, T414C, A508C, T522C, and S571C) to specifically label the proteins with 1,5-IAEDANS. The longer construct, Nedd4-2^{186–975}, contains five additional cysteine residues in the HECT domain at positions C702, C776, C853, C874, and C942. Thus, we first introduced the C341S mutation and then proceeded with the step-by-step mutagenesis of other Cys residues to prepare single cysteine-containing variants. Unfortunately, of all Nedd4-2^{186–975} mutant variants, only Nedd4-2^{186–975} with Cys at position 942 yielded a soluble and stable protein. In total, eight single cysteine-containing Nedd4-2 variants were prepared: seven with the Nedd4-2^{190–581} construct (C209, C218, C389, C414, C508, C522, and C571) and one with the Nedd4-2^{186–975} construct (C942). These cysteine residues are located in five different regions of Nedd4-2: C209 and C218 in the WW1 domain, C389 and C414 in the WW2 domain, C508 and C522 in the WW3 domain, C571 in the WW4 domain, and C942 in the active site of the C-lobe of the HECT domain (Fig. 1 B).

The stability of all Nedd4-2 mutants was assessed by measuring the midpoint temperatures of the protein unfolding transition (T_m) by differential scanning calorimetry. No substantial differences in T_m were observed in all Nedd4-2 variants, except for Nedd4-2^{190–581} C508 (Table 1). The slightly lower T_m of the Nedd4-2^{190–581} C508 variant may reflect a different conformation of the mutated WW3 domain. The binding of all phosphorylated Nedd4-2 mutant variants to 14-3-3 η was confirmed by native gel electrophoresis (Fig. S1). The single cysteine-containing variants of Nedd4-2 were labeled with the extrinsic fluorophore 1,5-IAEDANS, confirming the successful modification of all proteins by LC-MS (Figs. S2–S10).

14-3-3 η protein binding affects the conformation of Nedd4-2 WW3, WW4, and the active site of the HECT domain: Time-resolved fluorescence lifetime measurements

We have recently shown that 14-3-3 η binding triggers the structural rearrangement of Nedd4-2 (30), which could

TABLE 1 Stability of individual Nedd4-2 mutant variants

Nedd4-2 ^{190–581} variant	T_m (°C)
C209	54.2 ± 0.1
C218	55.3 ± 0.1
C389	53.6 ± 0.1
C414	55.7 ± 0.2
C508	51.06 ± 0.05
C522	56.5 ± 0.2
C571	54.4 ± 0.3
WT	56.29 ± 0.05
Nedd4-2 ^{186–975} variant	T_m (°C)
WT	41.34 ± 0.06
C942	39.5 ± 0.4

Midpoint temperatures of the protein unfolding transition (T_m) for Nedd4-2 WT and mutants, as determined by differential scanning fluorimetry. Uncertainties are expressed as the SE values calculated from three experiments.

include conformational changes in the WW and HECT domains. To gather more detailed information about structural changes in individual Nedd4-2 domains induced by their interaction with 14-3-3 η , we performed time-resolved fluorescence intensity measurements of all eight AEDANS-labeled cysteine variants of Nedd4-2^{190–581} and Nedd4-2^{186–975} in the absence and presence of 14-3-3 η . As an environmentally sensitive fluorophore, AEDANS changes its quantum yield and emission lifetime with the polarity of its microenvironment (49). Fluorescence lifetime measurements can therefore sensitively monitor subtle changes in dansyl solvation and/or conformational changes induced by 14-3-3 η binding (Fig. 2; Table 2).

All AEDANS-labeled Nedd4-2 proteins exhibited multi-exponential decays, typically containing two major and up to two minor components. Examples of decays and lifetime distributions are shown in Figs. S16 and S17. Since the protein is expected to scan a conformational space and the individual components are difficult to unequivocally assign, we used the mean fluorescence lifetime (τ_{mean}) as a qualitative indicator of changes in the local environment of AEDANS-labeled cysteines. AEDANS-labeled Nedd4-2^{190–581}C209 and Nedd4-2^{190–581}C218 (both Cys are located in the WW1 domain) exhibited relatively short emission lifetimes, 15.4 and 15.1 ns, respectively, unresponsive to 14-3-3 η binding. Conversely, AEDANS-labeled Nedd4-2^{190–581}C389, Nedd4-2^{190–581}C414, and Nedd4-2^{190–581}C508 (Cys located in WW2 and WW3 domains) exhibited the highest τ_{mean} of 17.0, 16.7 and 16.8 ns, respectively, in the absence of 14-3-3 η , indicating a less polar fluorophore microenvironment (49). Lower τ_{mean} values were also detected for Nedd4-2^{190–581}C522 (the WW3 domain), Nedd4-2^{190–581}C571 (the WW4 domain), and Nedd4-2^{186–975}C942 (the C-lobe of the HECT domain).

The strongest effect of 14-3-3 η binding was observed in AEDANS moieties attached within the WW3 domain (Nedd4-2^{190–581}C508 and Nedd4-2^{190–581}C522), whose τ_{mean} values increased by ~ 1.4 ns. AEDANS-labeled

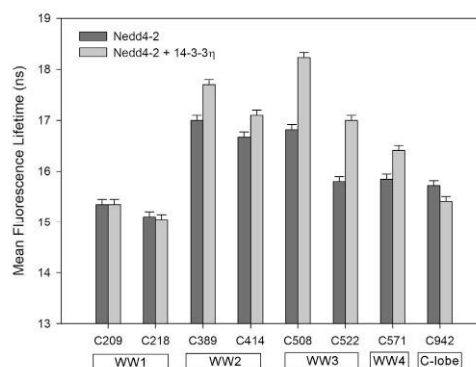


FIGURE 2 Mean fluorescence lifetimes of Nedd4-2 variants and their changes upon 14-3-3 η binding. The positions of AEDANS-labeled cysteine residues within Nedd4-2 domains are indicated at the bottom. C209 and C218, WW1; C389 and C414, WW2; C414 and C508, WW3; C571, WW4; C942, the C-lobe of HECT domain. Each error bar reflects the standard deviation of a single-curve data analysis.

Nedd4-2^{190–581}C389, C414, and C571 mutants (Cys in WW2 and WW4 domains) also exhibited significantly increased τ_{mean} in the presence of 14-3-3 η , particularly the Nedd4-2^{190–581}C389 variant (the WW2 domain), whose increase in τ_{mean} was close to 0.7 ns. As the dansyl fluorophore is known to exhibit an increased τ_{mean} in a less polar environment (49), these changes in τ_{mean} may result from 14-3-3 η -induced conformational changes in Nedd4-2, which affect interactions between dansyl moieties and amino acid residues in their vicinity. Alternatively, the increase in τ_{mean} may reflect reduced polar contacts and modulated dansyl solvation due to a direct interaction of the fluorophore with bound 14-3-3 η .

In contrast to C389, the AEDANS-labeled catalytic C942 in the active site of the HECT domain revealed a decrease in τ_{mean} by 0.3 ns, which can be interpreted as increased contacts with the polar environment resulting from increased solvation and/or quenching interactions near this residue. This suggests that 14-3-3 η binding induces conformational changes within the active site of Nedd4-2 HECT domain (Fig. 2; Table 2).

14-3-3 η protein binding reduces the mobility of Nedd4-2 WW domains: Time-resolved fluorescence anisotropy decay measurements

To investigate how 14-3-3 η binding affects the mobility of Nedd4-2 AEDANS-labeled domains, we performed time-resolved emission polarization anisotropy measurements. For all seven variants of Nedd4-2^{190–581}, the results are summarized in Table 2. Unfortunately, we were unable to prepare Nedd4-2^{186–975}C942 in a concentration comparable with the other mutants. Low emission intensity called for longer measurement times, stronger excitation, and larger

TABLE 2 Summary of the time-resolved AEDANS fluorescence measurements

Nedd4-2 variant	$\tau_{mean}^{a,b}$ (ns)	$k_d (\times 10^{-8})$	F_b	$\varphi_1^{c,d}$		φ_2^e		φ_3^e		φ_4^f		φ_5^g	
		$(M^{-1} s^{-1})^h$		(ns)	β_1^c	(ns)	β_2	(ns)	β_3	(ns)	β_4	(ns)	β_5
Nedd4-2¹⁹⁰⁻⁵⁸¹													
C209	15.4	4.3	0.27	0.1	0.19	1.4	0.05	9.5	0.05	79	0.06		
C209 + 14-3-3 η	15.4	4.6	0.29	0.1	0.17	0.5	0.05	3.9	0.04	15	0.02	>200	0.06
C218	15.1	7.1	0.15	0.1	0.27	0.5	0.01	2.6	0.02	17	0.03	170	0.01
C218 + 14-3-3 η	15.1	6.9	0.30	0.1	0.26	0.5	0.03	3.9	0.01	15	0.02	>200	0.02
C389	17.0	2.7	0.30	0.1	0.08	1.1	0.04	3.9	0.07	26	0.13	>200	0.04
C389 + 14-3-3 η	17.7	1.5	0.28	0.1	0.08	1.6	0.04	6.5	0.05	50	0.11	>200	0.06
C414	16.7	2.6	0.31	0.1	0.08	1.4	0.06	6.6	0.07	35	0.10	>200	0.03
C414 + 14-3-3 η	17.1	2.0	0.31	0.1	0.08	1.9	0.06	9.4	0.07	97	0.04	>200	0.08
C508	16.8	2.7	0.25	0.1	0.10	1.3	0.02	4	0.06	12	0.08	79	0.07
C508 + 14-3-3 η	18.2	1.5	0.22	0.1	0.07	0.6	0.03	3.8	0.05	16	0.05	>200	0.14
C522	15.8	3.6	0.33	0.1	0.08	1.1	0.07	6.1	0.09	39	0.07	>200	0.03
C522 + 14-3-3 η	17.0	1.7	0.31	0.1	0.09	1.4	0.05	6.2	0.05	47	0.08	>200	0.07
C571	15.9	3.2	0.32	0.1	0.09	1.9	0.10	14.1	0.08	67	0.03	>200	0.03
C571 + 14-3-3 η	16.4	1.8	0.26	0.1	0.09	1.1	0.06	6.0	0.07	76	0.08	>200	0.05
Nedd4-2¹⁸⁶⁻⁹⁷⁵													
C942	15.7	5.5	0.49										
C942 + 14-3-3 η	15.4	7.4	0.56										

^aMean lifetimes were calculated as $\tau_{mean} = \sum_i f_i \tau_i$, where f_i is an intensity fraction of the i th lifetime component τ_i , see also Eq. 2.

^bSD = ± 0.1 ns. The SD is a conservative upper estimate derived from the deconvolution analysis of single decay curves. Similarly were derived SDs of all other MEM-derived parameters (63).

^cAnisotropies $r(t)$ were analyzed for a series of exponentials using a model-independent maximum entropy method without setting prior assumptions about the shape of the correlation time distributions (45), $r(t) = \sum_k (\beta_k \exp(-t/\varphi_k))$, where amplitudes β_k represent the distribution of the correlation times φ_k . β_n presented in the table are areas of peaks positioned at correlation times φ_n . SD of β_n is ± 0.01 .

^dShortest resolvable correlation time rounded to the first significant digit, SD < ± 0.1 ns.

^eSD = ± 0.2 ns.

^fSD = ± 5 ns.

^gDue to the finite dansyl emission lifetime this correlation time has a larger uncertainty with highly asymmetrical standard deviations. The uncertainty to the + direction (+SD) is much larger than to the - direction (-SD). This is indicated by the "greater than" (>) symbol. The exact value of this correlation time cannot be more accurately determined.

^hInaccessible fraction, SD = ± 0.02 , apparent bimolecular quenching constant, SD = $\pm 0.2 (\times 10^{-8} M^{-1} s^{-1})$. The standard deviations result from the fitting uncertainty of single quenching curves (64).

light exposure of the sample. Consequently, resulting progressive photobleaching prevented reliable collection of sequentially measured polarized decays and evaluation of the Nedd4-2¹⁸⁶⁻⁹⁷⁵/C942 emission anisotropy.

The AEDANS fluorescence anisotropy decays were complex, usually with five classes of correlational times. Typical data are shown in Fig. S18. The first two correlation times likely reflect the fast hindered motion of the AEDANS fluorophore itself ($\varphi_1 \sim 0.1$ and $\varphi_2 \sim 0.5$ –1.9 ns). The slower decay components φ_3 and φ_4 , with correlation times ranging from 2.6 to 14 ns and from 12 to 97 ns, respectively, reflect slower internal movements and components arising from the free rotation of the generally asymmetric rotor (46). The longest φ_5 , poorly resolved due to the finite dansyl lifetime, reflects the slow rotational movement of the Nedd4-2:14-3-3 η complex ($M_w = 150$ kDa). The φ_5 component is generally modulated by the asymmetry of the complex (47) and it may also reflect minor aggregation.

Based on the position of the label, the time-resolved fluorescence anisotropy decays of AEDANS-labeled Nedd4-2¹⁹⁰⁻⁵⁸¹ mutants can be separated into three distinct groups with different extent of the dansyl mobilities (Fig. 3) re-

flected by the depolarization amplitudes β_i . The extent of segmental motion of the AEDANS-labeled cysteines of Nedd4-2¹⁹⁰⁻⁵⁸¹ and/or their 14-3-3 η binding-induced changes can be assessed by visual comparison of the initial part of the anisotropy decay of each mutant variant and from the amplitude β_1 . The higher the β_1 is, the lower the steric hindrance of the fast-depolarizing motion of the fluorophore and the higher the internal protein mobility will be. According to these correlations, C209 and C218 from the WW1 domain formed the group with the highest internal mobility ($\beta_1 = 0.19$ and 0.27, respectively). C218 was the AEDANS-labeled cysteine with the highest angular mobility, which suggest its high accessibility to the solvent and quencher molecules. The large extent of the fast initial fluorescence depolarization is clearly shown in Fig. 4 A). The proposed high solvent accessibility of AEDANS-labeled C209 and C218 is supported by their relatively short emission lifetimes, 15.4 and 15.1 ns, respectively (Table 2). The group with the lowest internal mobility contains the C389 and C414 from the WW2 domain ($\beta_1 = 0.08$). As expected, the high protein rigidity near C389 and C414 residues is accompanied by longer emission lifetimes of 17.0 and

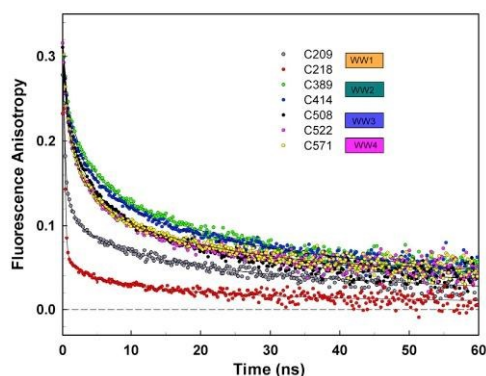


FIGURE 3 WW domains of Nedd4-2 exhibit different mobilities. Fluorescence anisotropy decays of AEDANS-labeled Nedd4-2^{190–581} variants. To see this figure in color, go online.

16.7 ns, respectively, thus suggesting a less polar dansyl microenvironment (Table 2). In the third group, Nedd4-2^{190–581} mutants with cysteines inserted into the WW3 and WW4 domains (C508, C522, and C571) showed intermediate internal flexibility. In the apo form, the mutants with cysteines in the WW2-4 domains exhibited almost identical fluorescence anisotropy decays, indicating the similar internal mobilities of dansyl-labeled protein segments and the similar overall hydrodynamic properties of the whole protein (Fig. 3; Table 2).

Time-resolved dansyl fluorescence anisotropy measurements performed in the presence of 14-3-3 η revealed that complex formation does not lower the high mobility of the dansyl moiety at C209 and C218 within the WW1 domain because the anisotropy decays initially overlap (Fig. 4 A). This overlap correlates with the unchanged τ_{mean} (Table 2).

The mobilities of all other mutants differed upon complex formation. Fig. 4 B demonstrates that the segmental mobility of the most rigid C389 and C414 mutants (the WW2 domain) further decreased, particularly in the C389 mutant, as shown by the elevation of the corresponding anisotropy curve. Since Nedd4-2^{190–581}C389:14-3-3 η and Nedd4-2^{190–581}C414:14-3-3 η complexes have the same molecular weight, the slower initial depolarization should be caused by the decrease in dansyl mobility. The increase in fluorescence lifetime by 0.7 and 0.4 ns (Table 2) correlates with the observed decrease in the internal mobility of segments containing AEDANS-labeled C389 and C414, respectively.

A similar behavior was observed in the last group of mutants with cysteine residues in WW3 and WW4 domains (C508, C522, and C571) (Fig. 4 C). Although the anisotropy decays of these Nedd4-2^{190–581} variants in the absence of 14-3-3 η seem to be similar, the presence of 14-3-3 η signifi-

cantly reduced their dansyl mobility in the following order: C571, C522, and C508 (Fig. 4 C). Fluorescence lifetime values increased in the same order upon 14-3-3 η binding (Table 2). Among all other mutants, Nedd4-2^{190–581}C508 exhibited the highest rigidization and a considerable lifetime increase of 1.4 ns. This increase likely reflects a conformational transition in the C508-containing WW3 domain combined with an increase in the solvent shielding of its dansyl group.

14-3-3 η protein binding decreases the accessibility of Nedd4-2 WW3 and WW4 domains to the quencher, conversely increasing the accessibility of the HECT C-lobe: Time-resolved acrylamide quenching measurements

To further explore 14-3-3-induced structural changes in Nedd4-2, we performed time-resolved quenching experiments with all eight variants of Nedd4-2^{190–581} and Nedd4-2^{186–975}, probing fluorophore accessibility to acrylamide. This time-resolved approach eliminates static quenching effects, which often complicate intensity-based quenching experiments and result in curved Stern-Volmer plots. Fluorescence decays of Nedd4-2 labeled by a single AEDANS fluorophore typically contained two closely spaced major peaks accompanied by up to two minor peaks, as shown in Figs. S16 and S17. Being aware of the same simplification, we represented decays by τ_{mean} that allowed as to reduce data, construct a single Stern-Volmer plot for each mutant, and retrieve an apparent collisional quenching constants for the each variant. As shown in Figs. S11–S14, this approach led to curved Stern-Volmer plots that indicate at least two classes of the fluorophore with different accessibilities to the collisional quencher, that is, acrylamide. Although the underlying molecular mechanism remains unknown, a likely explanation is the dynamic conformational heterogeneity of the proteins, fluctuating between conformations with different dansyl accessibilities. Hence, for another simplification, we assumed two classes of dansyl only, i.e., accessible and fully inaccessible forms. The values of the apparent bimolecular quenching constant k_q determined by fitting the Stern-Volmer plots are presented in Table 2 and compared in Fig. 5. Generally, the inaccessible fractions of dansyl (F_b) were similar across all mutants ~ 0.3 , except for Nedd4-2^{190–581}C218, whose F_b was lower.

The quenching experiments revealed that 14-3-3 η binding does not significantly affect the quenching efficiency of C209, or C218 in the WW1 domain, with an apparent k_q of 4.3 and $7.1 \times 10^{-8} \text{ M}^{-1} \text{ s}^{-1}$, respectively (Table 2; Fig. S11). This lack of an effect suggests a high dansyl accessibility to the quencher molecules dissolved in the aqueous environment, regardless of the presence of 14-3-3 η . Among the mutants, Nedd4-2^{190–581}C218 exhibited the highest accessibility to the quencher, in line with the highest internal mobility of C218 and the shortest emission lifetime (Table 2). Moreover, only this mutant showed a significant change in F_b

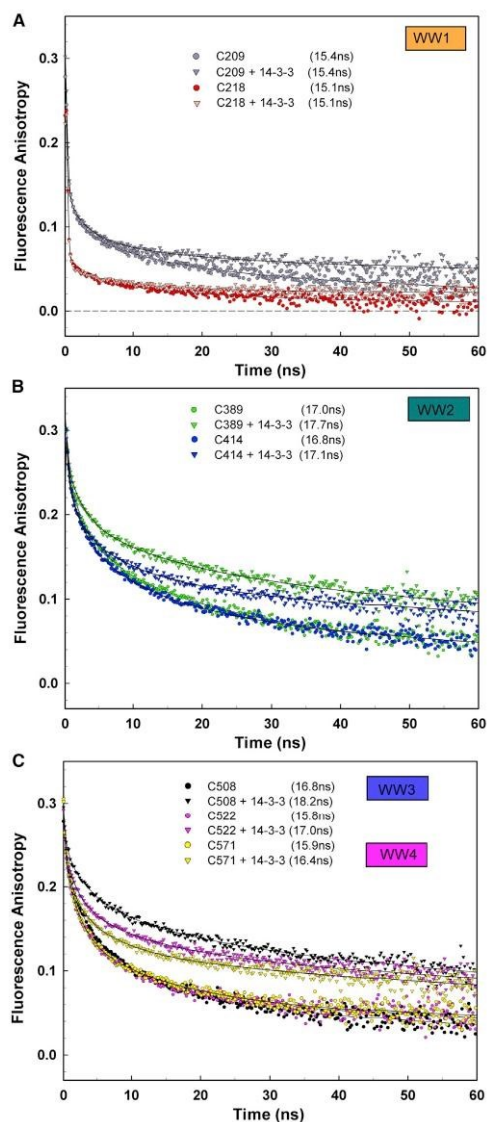


FIGURE 4 14-3-3 η binding affects the mobility of Nedd4-2 WW domains. Fluorescence anisotropy decays of Nedd4-2 variants with AEDANS-labeled individual WW domains in the absence and presence of 14-3-3 η . (A) WW1 domain variants C209 and C218, (B) WW2 domain variants C389 and C414, and (C) WW3 and WW4 domain variants C508, C522, and C571. To see this figure in color, go online.

upon 14-3-3 η binding, which is the only reason for the dramatic change in the shape of the quenching curves, as shown in Fig. S11. Although the molecular mechanism is still unknown, unbound Nedd4-2^{190–581}C218 has approximately two times lower F_b than the other mutants. This difference indicates that the conformational heterogeneity of dansyl at position 218 in the WW1 domain is lower in the unbound protein. The steady-state emission spectra of Nedd4-2^{190–581}C218 are shown in Fig. S19. In contrast to the other mutants, the spectrum in the presence of 14-3-3 η displays a blue-shifted shoulder, which is consistent with the quenching experiment and suggests the appearance of new conformers upon 14-3-3 η binding.

All mutants with cysteine residues in WW2-4 domains exhibited a significantly decreased k_q after 14-3-3 η protein binding and only minor changes in F_b . Only the Nedd4-2^{186–975}C942 mutant with dansyl positioned in the HECT domain displayed an increased value of k_q upon 14-3-3 η binding. The relative decrease in k_q induced by 14-3-3 η binding was approximately 23% for Nedd4-2^{190–581}C414, 44% for Nedd4-2^{190–581}C389, C508, and C571, and 53% for Nedd4-2^{190–581}C522 (Fig. 5). These changes are also in line with the results from our fluorescence anisotropy measurements, because the strongest effect of 14-3-3 η binding on dansyl rotational mobility was identified in the Nedd4-2^{190–581}C508 mutant (Fig. 4 C) and the weakest in the rigid Nedd4-2^{190–581}C414 (Figs. 2 and 4 B). In contrast, the Nedd4-2^{186–975}C942 exhibited the opposite behavior, with a 35% increase in k_q in the presence of 14-3-3 η , matching the decrease in τ_{mean} after 14-3-3 η binding (Figs. S14 and 5).

14-3-3 protein binding protects the WW3 and WW4 domains of Nedd4-2 from proteolytic degradation in vitro

Our previous structural characterization of Nedd4-2^{186–975} and its complex with 14-3-3 η based on SAXS and chemical cross-linking coupled to MS (30), and the fluorescence spectroscopy data gathered in this study, suggest that 14-3-3 η protein binding alters interactions between its structured domains, consequently changing their mobility and solvent exposure. To further corroborate these findings, we investigated which Nedd4-2 regions are sensitive to proteolysis in the absence and presence of 14-3-3 η . For this purpose, we performed limited proteolysis experiments with trypsin (Figs. 6 A and S15). The results of Nedd4-2 digestion with low trypsin levels revealed that Nedd4-2^{186–975} alone is highly sensitive to proteolysis, whereas adding 14-3-3 η significantly slowed the degradation of Nedd4-2^{186–975} (Fig. 6 B).

Mass spectrometry analysis of the Nedd4-2 fragments after 30 min of digestion with trypsin in the absence and presence of 14-3-3 η showed that the most sensitive Nedd4-2 region, in both cases, is the N-terminus of our Nedd4-2^{186–975} construct containing the WW1 and WW2 domains

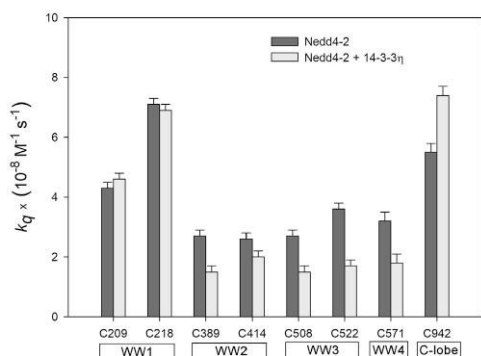


FIGURE 5 14-3-3 η binding affects the solvent exposure of Nedd4-2 domains, as shown by the apparent bimolecular quenching constants of AEDANS-labeled Nedd4-2 cysteine variants in the absence and presence of 14-3-3 η . Each error bar reflects the standard deviation of a single-curve data analysis.

and the phosphorylation sites S342 and T367, because the bands with an apparent $M_w \sim 60$ kDa correspond to the Nedd4-2 sequence 446–975 (the first peptide identified from the N-terminus was peptide 446–462, phosphorylated at S448, with an m/z signal of 1736.86). Peptides containing the preceding phosphorylation sites S342 and T367 (the peptide 339–362 phosphorylated at S342 with an m/z signal of 2383.06 and the peptide 365–394 phosphorylated at T367 with an m/z signal of 3207.44) were detected only in control samples without trypsin. Combined, these data indicate that 14-3-3 η binding protects the 14-3-3 binding motif S448 and the WW3-4 and HECT domains at the C-terminus of Nedd4-2 against proteolytic degradation, and are thus in line with the results from our fluorescence analysis (Fig. 4).

DISCUSSION

Nedd4-2 WW domains function as protein interaction modules and participate in a wide range of eukaryotic signaling processes, as shown in numerous studies (50,51). These WW domains of Nedd4-2 bind PY motifs present in ENaC subunits (17) and in SGK1, ACK1, and WNK1 (52–54). Nedd4-2 contains four WW domains with different sequences. Therefore, each WW domain likely has a specific function.

In this study, we analyzed the domain specificity of Nedd4-2 to two binding partners, namely ENaC and SGK1. The *in vitro* characterization of the binding of individual domains of Nedd4-2 by surface plasmon resonance demonstrated that WW2 and WW3 bind to SGK1 both individually and cooperatively, whereas only WW3 and WW4 bind to ENaC (17,55,56). The findings of Wiemuth et al. support a model where SGK binds to WW2 and WW3 and then phosphorylates Nedd4-2 and pulls it back from the ENaC (56).

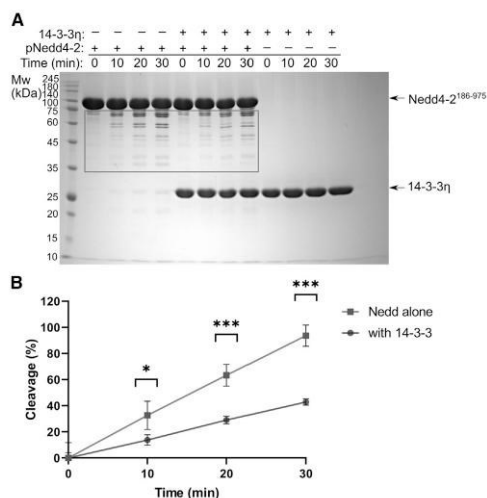


FIGURE 6 Limited proteolysis assay showing the protective effect of 14-3-3 to pNedd4-2^{186–975}. (A) Phosphorylated Nedd4-2^{186–975} in the absence and presence of 14-3-3 η digested with trypsin for 10, 20, and 30 min. The protease/Nedd4-2 ratio was 1:1000 (w/w). The reactions were stopped by boiling the samples with SDS/PAGE loading buffer at the times indicated before SDS-PAGE analysis. The black rectangle marks the quantified region. Unedited gel image is provided in supporting material (Fig. S15). (B) The density of the bands representing degraded Nedd4-2^{186–975} in the presence and absence of 14-3-3 η were quantified in ImageLab (Bio-Rad). Error bars represent the standard deviation of four independent experiments. Asterisks indicate significant differences, according to Student's *t*-tests comparing relative changes between samples with and without 14-3-3 η at selected time points (* $p \leq 0.01$, *** $p \leq 0.0001$).

Nedd4-2 phosphorylation triggers the binding of scaffolding 14-3-3 proteins, which further modulate Nedd4-2 function, albeit through mechanisms not yet fully understood (29). Our recently reported structural characterization of the Nedd4-2:14-3-3 η complex based on SAXS, cross-linking, and crystallography data suggested that 14-3-3 η binding alters interactions between the structured domain of Nedd4-2, thus indicating that complex formation may affect the accessibility of the catalytic HECT and/or individual WW domains (30). To test this hypothesis, we studied the 14-3-3 η -induced conformational changes, mobility, and solvent accessibility of individual WW domains and HECT domains of Nedd4-2 by time-resolved dansyl fluorescence.

The data reported here clearly indicate that 14-3-3 η directly interacts with WW3 and WW4 domains, as shown by the large increase in dansyl fluorescence lifetime and by the decrease in solvent accessibility and mobility of AEDANS-labeled Cys residues at positions 508, 522, and 571 (Table 2; Figs. 2, 4 C, and 5). The blue shift of the emission spectra of about 4–5 nm for labeled Cys508 and Cys522 residues and ~ 1 nm for Cys571 upon 14-3-3 η binding is consistent with this conclusion, Fig. S19. The shift indicates a less polar

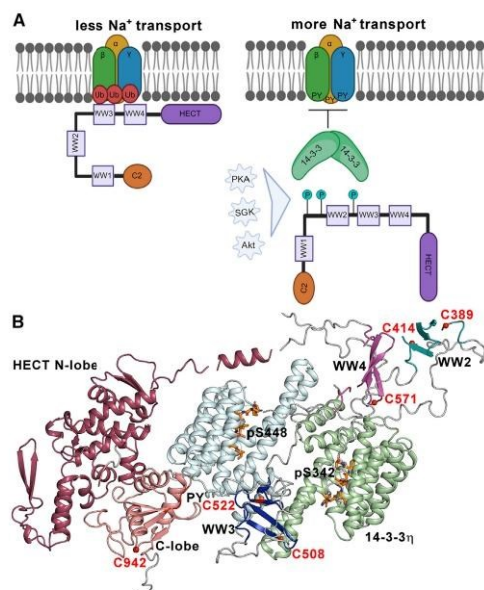


FIGURE 7 Phosphorylation followed by 14-3-3 binding regulates Nedd4-2. (A) Nedd4-2 binds to ENaC PY motifs and catalyzes its ubiquitination, reducing the rate of sodium transport and consequently the surface expression of these channels. Phosphorylation by various kinases (PKA, SGK, and Akt) triggers 14-3-3 protein binding, which sterically blocks WW domains and affects the structure of the active site, thereby preventing Nedd4-2 binding to ENaC and its ubiquitination. The 14-3-3 binding motifs S342, T367, and S448 are shown as teal circles with P. (B) Positions of AEDANS-labeled cysteine residues in the SAXS-based model of the pNedd4-2^{186–975}:14-3-3 η complex (30). The 14-3-3 η protomers are shown in pale green and pale cyan. In the HECT domain of Nedd4-2^{186–975}, the N-lobe is indicated in raspberry and the C-lobe in salmon. WW2, WW3, and WW4 domains are indicated in teal, blue, and magenta, respectively. Phosphorylated 14-3-3 binding motifs of Nedd4-2 are shown as orange sticks (PDB: 6ZBT and 6ZC9 (30)). The positions of the cysteine residues in the WW2, WW3, WW4, and HECT domains labeled by AEDANS are indicated as red balls. The WW1 domain is not shown. The PY motif (L⁹⁴⁸PPY⁹⁵¹) is shown in red. To see this figure in color, go online.

microenvironment, as shown in Fig. S20 for free AEDANS in water and DMSO. The observed changes can be interpreted as a modulation of the AEDANS microenvironment, mobility, and quencher accessibility due to at least two distinct actions: 1) the 14-3-3 η -protein-induced conformational change involving Nedd4-2 WW3 and WW4 domains, and/or 2) the direct contact of the 14-3-3 η protein with these labeled cysteine residues and consequent shielding from the polar solvent and restriction of their mobility.

The fluorescence properties of AEDANS-labeled Cys residues at positions 389 and 414 within the WW2 domain were affected by 14-3-3 η binding to a lesser extent. The mobility of the WW2 domain, which exhibited the lowest

internal mobility of all four WW domains of Nedd4-2 (Fig. 3), was only weakly affected by 14-3-3 η binding (Fig. 4 B). Nevertheless, as in the WW3 and WW4 domains, complex formation induced some structural changes near this domain, as indicated by the increase in τ_{mean} . The decrease in k_q values (Table 2; Figs. 2 and 5) and a slight blue spectral shift (Fig. S19) suggest decreased solvent accessibility of the WW2 domain after 14-3-3 η binding.

In contrast, the fluorescent lifetimes and apparent k_q of AEDANS-Cys at positions 209 and 218 within the WW1 domain remained unaffected by 14-3-3 η . This domain exhibits high internal mobility, high collisional quenching of the AEDANS emission, and short emission lifetimes, both in the absence and in the presence of 14-3-3 η . Taking together, this indicates that WW1 is relaxed and highly accessible to the solvent (Table 2; Figs. 2, 3, 4 A and 5).

While emission spectrum of AEDANS-C209 is also insensitive to 14-3-3 η binding, the appearance of blue-shifted shoulder on the emission spectrum of AEDANS-C218 in the presence of 14-3-3 η suggests binding-induced increase of the conformational heterogeneity in this region (Fig. S19). Considering the above, 14-3-3 η does not affect considerably the interactions and structure of the WW1 domain, but the 14-3-3 η binding-induced conformational change of Nedd4-2 also involves its catalytic domain, as shown by analysis of the fluorescent properties of AEDANS-labeled C942 within the active site of the HECT domain (Table 2; Figs. 2 and 5). Nedd4-2 is key regulator of Na⁺ transport in mammalian cells (3,57–59). When cells need to reduce Na⁺ transport, Nedd4-2 binds to the PY motif of the epithelial sodium channel ENaC and catalyzes its ubiquitination. Conversely, when increased Na⁺ transport is required, Nedd4-2 is phosphorylated by various kinases, which induces 14-3-3 protein binding and blocks ENaC ubiquitination. As a result, ENaC remains permanently active on the cellular surface (Fig. 7 A) (reviewed in (58)).

Our fluorescence spectroscopy measurements, together with a recent structural analysis of apo Nedd4-2 and the Nedd4-2:14-3-3 η complex (30), suggest a plausible mechanism for this 14-3-3-mediated inhibition of Nedd4-2 binding to ENaC (Fig. 7). Models of apo Nedd4-2 and its complex with 14-3-3 η indicate that the WW2 and WW3 domains, in the apo form, interact with the HECT domain and that these interactions are disrupted in the presence of 14-3-3 η , which apparently sequesters WW3 into the central channel of its dimeric molecule, away from the HECT domain (Fig. 7 B). This model of the complex also suggests interactions of 14-3-3 η with WW4 and HECT domains.

In line with these models, our time-resolved fluorescence measurements (Figs. 2, 3, 4, and 5), together with the results of limited proteolysis (Fig. 6) reported in this study, confirm the interactions between 14-3-3 η and WW3 and WW4 domains and the structural change within the HECT domain upon complex formation. Moreover, our

time-resolved fluorescence anisotropy and quenching measurements show that complex formation decrease the mobility and solvent accessibility of WW2-4, most likely because 14-3-3 η binding sterically masks these domains. Therefore, this physical obstruction of WW domains may be responsible for the 14-3-3-dependent modulation of Nedd4-2 functions.

In a second modulatory mechanism, 14-3-3 directly interacts with the HECT domain, changes the relative positions of the N- and C-lobes of the HECT domain (30), and thus may also affect the catalytic activity of this domain. Indeed, our experiments revealed that the AEDANS moiety attached to C942, which is a catalytic residue (60), exhibits a somewhat lower τ_{mean} and a considerably higher accessibility to the solvent in the complexed form than in the apo form (Figs. 2 and 5), thus indicating a structural change within the catalytic core of the enzyme.

In conclusion, the fluorescence spectroscopy analysis of the Nedd4-2:14-3-3 η complex reported in this study indicates that the steric hindrance of the WW3 and WW4 domains, together with the conformational change in the catalytic domain, may be responsible for the 14-3-3 binding-mediated regulation of Nedd4-2 functions. Moreover, our data provide a platform for future studies targeting the 14-3-3:Nedd4-2 interface for potential therapeutic purposes for treating Nedd4-2-related diseases, such as Parkinson and kidney disease, hypertension, etc. Recent advances in the development of small-molecule compounds that stabilize protein-protein interactions in 14-3-3 protein complexes have demonstrated the feasibility of this approach. For example, Ottmann's group recently identified compounds able to stabilize complexes between 14-3-3 and the adaptor protein SLP76 (61) or the p65 subunit of NF- κ B (62). Our finding that Nedd4-2 interacts with 14-3-3 η not only through phosphorylated motifs, but also other regions, including WW3 and WW4 domains, suggests the presence of a sufficiently large binding interface that could be targeted by small-molecule compounds as an alternative or complementary strategy in suppressing the activity of Nedd4-2.

SUPPORTING MATERIAL

Supporting material can be found online at <https://doi.org/10.1016/j.bpj.2022.02.025>.

AUTHOR CONTRIBUTIONS

V.O. and T.O. conceived the study and provided scientific guidance. R.J. performed mutagenesis, prepared the recombinant proteins, performed protein labeling by 1,5-IAEDANS, the differential scanning fluorimetry measurements, and limited proteolysis, in addition to preparing samples for fluorescence measurements. P.P. prepared the recombinant proteins. D.S. and P.H. performed the fluorescence measurements and analyzed the fluorescence data. V.O. and T.O. wrote the paper. All co-authors revised the manuscript.

ACKNOWLEDGMENTS

This study was funded by the Czech Science Foundation (to V.O., grant no. 20-00058S), the Grant Agency of Charles University (to R.J., grant no. 348421), the Czech Academy of Sciences (to R.V.O. grant no. 67985823 of the Institute of Physiology). We thank the Czech Infrastructure for Integrative Structural Biology (CIISB) for access to the CMS facilities at BIOCEV (project LM2018127 by MEYS). P.H. and D.S. acknowledge the institutional support UNCE/SCI/010. We also thank Dr. Petr Pompach for mass spectrometry analysis and Dr. Carlos V. Melo for proofreading the article.

REFERENCES

1. Yang, B., and S. Kumar. 2010. Nedd4 and Nedd4-2: closely related ubiquitin-protein ligases with distinct physiological functions. *Cell Death Differ.* 17:68–77.
2. Itani, O. A., J. R. Campbell, ..., C. P. Thomas. 2003. Alternate promoters and variable splicing lead to hNedd4-2 isoforms with a C2 domain and varying number of WW domains. *Am. J. Physiol. Ren. Physiol.* 285:F916–F929.
3. Fotia, A. B., J. Ekberg, ..., S. Kumar. 2004. Regulation of neuronal voltage-gated sodium channels by the ubiquitin-protein ligases Nedd4 and Nedd4-2. *J. Biol. Chem.* 279:28930–28935.
4. Arroyo, J. P., D. Lagnaz, ..., O. Staub. 2011. Nedd4-2 modulates renal Na⁺-Cl⁻ cotransporter via the aldosterone-SGK1-Nedd4-2 pathway. *J. Am. Soc. Nephrol.* 22:1707–1719.
5. Kamynina, E., C. Debonneville, M. Bens, A. Vandewalle, and O. Staub. 2001. A novel mouse Nedd4 protein suppresses the activity of the epithelial Na⁺ channel. *FASEB J.* 15:204–214.
6. Ekberg, J., F. Schuetz, ..., D. J. Adams. 2007. Regulation of the voltage-gated K(+) channels KCNQ2/3 and KCNQ3/5 by ubiquitination. Novel role for Nedd4-2. *J. Biol. Chem.* 282:12135–12142.
7. Zhu, J., K. Y. Lee, ..., N. P. Tsai. 2017. Epilepsy-associated gene Nedd4-2 mediates neuronal activity and seizure susceptibility through AMPA receptors. *PLoS Genet.* 13:e1006634.
8. Broix, L., H. Jagline, ..., J. Chelly. 2016. Mutations in the HECT domain of NEDD4L lead to AKT-mTOR pathway deregulation and cause periventricular nodular heterotopia. *Nat. Genet.* 48:1349–1358.
9. Popovic, D., D. Vucic, and I. Dikic. 2014. Ubiquitination in disease pathogenesis and treatment. *Nat. Med.* 20:1242–1253.
10. Rizzo, F., and O. Staub. 2015. NEDD4-2 and salt-sensitive hypertension. *Curr. Opin. Nephrol. Hypertens.* 24:111–116.
11. Vanli-Yavuz, E. N., O. Ozdemir, ..., B. Baykan. 2015. Investigation of the possible association of NEDD4-2 (NEDD4L) gene with idiopathic photosensitive epilepsy. *Acta Neurol. Belg.* 115:241–245.
12. Corbalan-Garcia, S., and J. C. Gomez-Fernandez. 2014. Signaling through C2 domains: more than one lipid target. *Biochim. Biophys. Acta.* 1838:1536–1547.
13. Bork, P., and M. Sudol. 1994. The WW domain: a signalling site in dystrophin? *Trends Biochem. Sci.* 19:531–533.
14. Chen, H. L., and M. Sudol. 1995. The WW domain of Yes-associated protein binds a proline-rich ligand that differs from the consensus established for Src homology 3-binding modules. *Proc. Natl. Acad. Sci. U.S.A.* 92:7819–7823.
15. Todaro, D. R., A. C. Augustus-Wallace, ..., A. L. Haas. 2017. The mechanism of neural precursor cell expressed developmentally down-regulated 4-2 (Nedd4-2)/NEDD4L-catalyzed polyubiquitin chain assembly. *J. Biol. Chem.* 292:19521–19536.
16. French, M. E., J. L. Klosowiak, ..., T. Hunter. 2017. Mechanism of ubiquitin chain synthesis employed by a HECT domain ubiquitin ligase. *J. Biol. Chem.* 292:10398–10413.

17. Fotia, A. B., A. Dinudom, ..., S. Kumar. 2003. The role of individual Nedd4-2 (KIAA0439) WW domains in binding and regulating epithelial sodium channels. *FASEB J.* 17:70–72.
18. Harvey, K. F., A. Dinudom, ..., S. Kumar. 1999. All three WW domains of murine Nedd4 are involved in the regulation of epithelial sodium channels by intracellular Na^+ . *J. Biol. Chem.* 274:12525–12530.
19. Snyder, P. M., D. R. Olson, ..., D. B. Bucher. 2001. Multiple WW domains, but not the C2 domain, are required for inhibition of the epithelial Na^+ channel by human Nedd4. *J. Biol. Chem.* 276:28321–28326.
20. Bruce, M. C., V. Kanelis, ..., D. Rotin. 2008. Regulation of Nedd4-2 self-ubiquitination and stability by a PY motif located within its HECT-domain. *Biochem. J.* 415:155–163.
21. Zhang, W., T. Na, ..., J. B. Peng. 2010. Down-regulation of intestinal apical calcium entry channel TRPV6 by ubiquitin E3 ligase Nedd4-2. *J. Biol. Chem.* 285:36586–36596.
22. Ichimura, T., H. Yamamura, ..., T. Isobe. 2005. 14-3-3 proteins modulate the expression of epithelial Na^+ channels by phosphorylation-dependent interaction with Nedd4-2 ubiquitin ligase. *J. Biol. Chem.* 280:13187–13194.
23. Snyder, P. M., D. R. Olson, ..., J. C. Steines. 2004. cAMP and serum and glucocorticoid-inducible kinase (SGK) regulate the epithelial Na^+ channel through convergent phosphorylation of Nedd4-2. *J. Biol. Chem.* 279:45753–45758.
24. Bhalla, V., D. Daidie, ..., D. Pearce. 2005. Serum- and glucocorticoid-regulated kinase 1 regulates ubiquitin ligase neural precursor cell-expressed, developmentally down-regulated protein 4-2 by inducing interaction with 14-3-3. *Mol. Endocrinol.* 19:3073–3084.
25. Lee, I. H., A. Dinudom, ..., D. I. Cook. 2007. Akt mediates the effect of insulin on epithelial sodium channels by inhibiting Nedd4-2. *J. Biol. Chem.* 282:29866–29873.
26. Hallows, K. R., V. Bhalla, ..., D. Pearce. 2010. Phosphopeptide screen uncovers novel phosphorylation sites of Nedd4-2 that potentiate its inhibition of the epithelial Na^+ channel. *J. Biol. Chem.* 285:21671–21678.
27. Edinger, R. S., J. Lebowitz, ..., K. R. Hallows. 2009. Functional regulation of the epithelial Na^+ channel by I κ B kinase- β occurs via phosphorylation of the ubiquitin ligase Nedd4-2. *J. Biol. Chem.* 284:150–157.
28. Nagaki, K., H. Yamamura, ..., T. Ichimura. 2006. 14-3-3 Mediates phosphorylation-dependent inhibition of the interaction between the ubiquitin E3 ligase Nedd4-2 and epithelial Na^+ channels. *Biochemistry.* 45:6733–6740.
29. Chandran, S., H. Li, ..., V. Bhalla. 2011. Neural precursor cell-expressed developmentally down-regulated protein 4-2 (Nedd4-2) regulation by 14-3-3 protein binding at canonical serum and glucocorticoid kinase 1 (SGK1) phosphorylation sites. *J. Biol. Chem.* 286:37830–37840.
30. Pohl, P., R. Joshi, ..., V. Obsilova. 2021. 14-3-3-protein regulates Nedd4-2 by modulating interactions between HECT and WW domains. *Commun. Biol.* 4:899.
31. Mackintosh, C. 2004. Dynamic interactions between 14-3-3 proteins and phosphoproteins regulate diverse cellular processes. *Biochem. J.* 381 (Pt 2):329–342.
32. Obsilova, V., and T. Obsil. 2020. The 14-3-3 proteins as important allosteric regulators of protein kinases. *Int. J. Mol. Sci.* 21:8824.
33. Sluchanko, N. N. 2018. Association of multiple phosphorylated proteins with the 14-3-3 regulatory hubs: problems and perspectives. *J. Mol. Biol.* 430:20–26.
34. Gogl, G., K. V. Tugaeva, ..., N. N. Sluchanko. 2021. Hierarchized phosphotarget binding by the seven human 14-3-3 isoforms. *Nat. Commun.* 12:1677.
35. Sluchanko, N. N., and D. M. Bustos. 2019. Intrinsic disorder associated with 14-3-3 proteins and their partners. *Prog. Mol. Biol. Transl. Sci.* 166:19–61.
36. Bustos, D. M. 2012. The role of protein disorder in the 14-3-3 interaction network. *Mol. Biosyst.* 8:178–184.
37. Horvath, M., O. Petrvalska, ..., T. Obsil. 2021. 14-3-3 proteins inactivate DAPK2 by promoting its dimerization and protecting key regulatory phosphosites. *Commun. Biol.* 4:986.
38. Rotin, D., and O. Staub. 2012. Nedd4-2 and the regulation of epithelial sodium transport. *Front Physiol.* 3:212.
39. Obsil, T., R. Ghirlando, ..., F. Dyda. 2001. Crystal structure of the 14-3-3zeta:serotonin N-acetyltransferase complex. a role for scaffolding in enzyme regulation. *Cell.* 105:257–267.
40. Obsilova, V., P. Herman, ..., T. Obsil. 2004. 14-3-3zeta C-terminal stretch changes its conformation upon ligand binding and phosphorylation at Thr232. *J. Biol. Chem.* 279:4531–4540.
41. Boura, E., J. Silhan, ..., T. Obsil. 2007. Both the N-terminal loop and wing W2 of the forkhead domain of transcription factor Foxo4 are important for DNA binding. *J. Biol. Chem.* 282:8265–8275.
42. Niesen, F. H., H. Berglund, and M. Vedadi. 2007. The use of differential scanning fluorimetry to detect ligand interactions that promote protein stability. *Nat. Protoc.* 2:2212–2221.
43. Ballone, A., F. Centorrino, ..., C. Ottmann. 2018. Protein X-ray crystallography of the 14-3-3zeta/SOS1 complex. *Data Brief.* 19:1683–1687.
44. Kacirova, M., D. Kosek, ..., T. Obsil. 2015. Structural characterization of phosphoducin and its complex with the 14-3-3 protein. *J. Biol. Chem.* 290:16246–16260.
45. Vecer, J., and P. Herman. 2011. Maximum entropy analysis of analytically simulated complex fluorescence decays. *J. Fluorescence.* 21:873–881.
46. Lakowicz, J. R. 2006. Principles of Fluorescence Spectroscopy. Springer.
47. Lakowicz, J. R. 1983. Principles of Fluorescence Spectroscopy. Plenum Press.
48. Lehrer, S. S. 1971. Solute perturbation of protein fluorescence. The quenching of the tryptophyl fluorescence of model compounds and of lysozyme by iodide ion. *Biochemistry.* 10:3254–3263.
49. Yong, W., I. Tsukasa, ..., T. Fujio. 1994. Dansyl- β -cyclodextrins as fluorescent sensors responsive to organic compounds. *Bull. Chem. Soc. Jpn.* 67:1598–1607.
50. Sudol, M., H. I. Chen, ..., P. Bork. 1995. Characterization of a novel protein-binding module—the WW domain. *FEBS Lett.* 369:67–71.
51. Staub, O., and D. Rotin. 1996. WW domains. *Structure.* 4:495–499.
52. Snyder, P. M., D. R. Olson, and B. C. Thomas. 2002. Serum and glucocorticoid-regulated kinase modulates Nedd4-2-mediated inhibition of the epithelial Na^+ channel. *J. Biol. Chem.* 277:5–8.
53. Chan, W., R. Tian, ..., E. Manser. 2009. Down-regulation of active ACK1 is mediated by association with the E3 ubiquitin ligase Nedd4-2. *J. Biol. Chem.* 284:8185–8194.
54. Roy, A., L. Al-Qusairi, ..., A. R. Subramanya. 2015. Alternatively spliced proline-rich cassettes link WNK1 to aldosterone action. *J. Clin. Invest.* 125:3433–3448.
55. Asher, C., I. Sinha, and H. Garty. 2003. Characterization of the interactions between Nedd4-2, ENaC, and sgk-1 using surface plasmon resonance. *Biochim. Biophys. Acta.* 1612:59–64.
56. Wiemuth, D., J. S. Lott, ..., F. J. McDonald. 2010. Interaction of serum- and glucocorticoid regulated kinase 1 (SGK1) with the WW-domains of Nedd4-2 is required for epithelial sodium channel regulation. *PLoS One.* 5:e12163.
57. Bhalla, V., and K. R. Hallows. 2008. Mechanisms of ENaC regulation and clinical implications. *J. Am. Soc. Nephrol.* 19:1845–1854.
58. Snyder, P. M. 2009. Down-regulating destruction: phosphorylation regulates the E3 ubiquitin ligase Nedd4-2. *Sci. Signal.* 2:pe41.

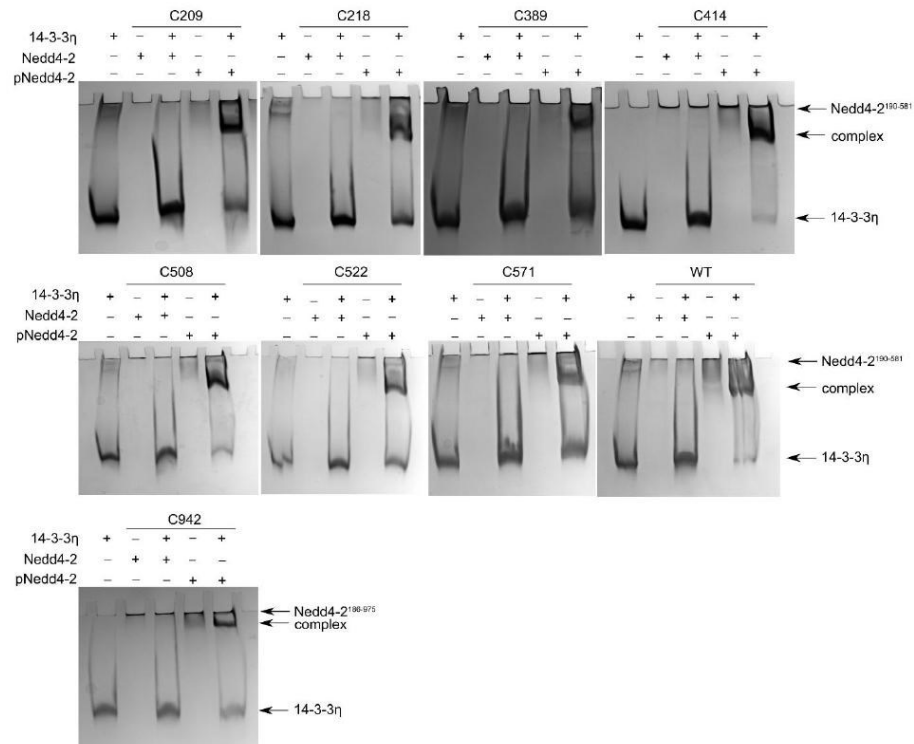
59. Manning, J. A., and S. Kumar. 2018. Physiological functions of Nedd4-2: lessons from knockout mouse models. *Trends Biochem. Sci.* 43:635–647.
60. Wu, P. Y., M. Hanlon, ..., C. M. Pickart. 2003. A conserved catalytic residue in the ubiquitin-conjugating enzyme family. *EMBO J.* 22:5241–5250.
61. Soini, L., M. Redhead, ..., C. Ottmann. 2021. Identification of molecular glues of the SLP76/14-3-3 protein-protein interaction. *RSC Med. Chem.* 12:1555–1564.
62. Wolter, M., D. Valenti, ..., C. Ottmann. 2021. An exploration of chemical properties required for cooperative stabilization of the 14-3-3 interaction with NF-kappaB-Utilizing a reversible covalent tethering approach. *J. Med. Chem.* 64:8423–8436.
63. Bryan, R. K. 1990. Maximum entropy analysis of oversampled data problems. *Eur. Biophys. J.* 18:165–174.
64. Marquardt, D. W. 1963. An algorithm for least-squares estimation of Nonlinear parameters. *J. Soc. Ind. Appl. Math.* 11:431–441.

Biophysical Journal, Volume 121

Supplemental information

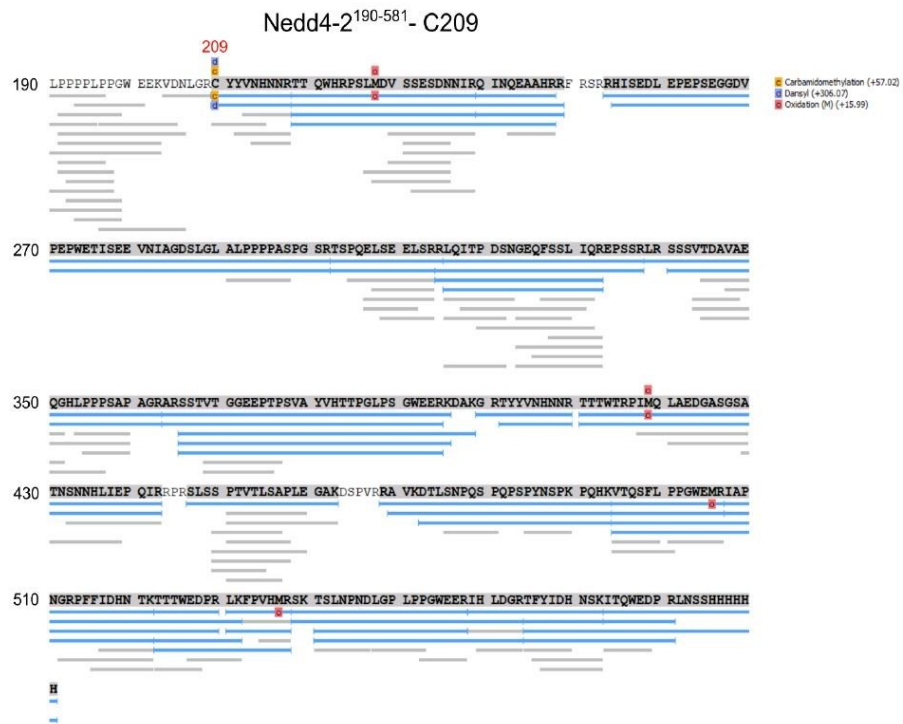
Nedd4-2 binding to 14-3-3 modulates the accessibility of its catalytic site and WW domains

Rohit Joshi, Pavel Pohl, Dita Strachotova, Petr Herman, Tomas Obsil, and Veronika Obsilova

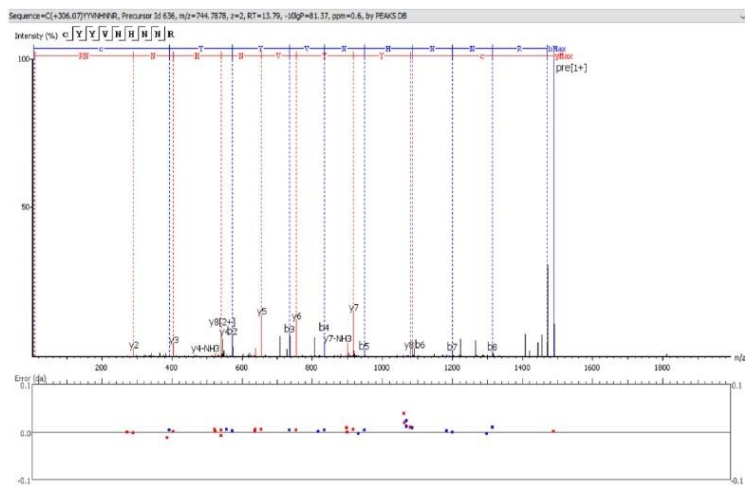


Supplemental Figure S1. Characterization of the interaction between single cysteine variants of Nedd4-2¹⁹⁰⁻⁵⁸¹ and Nedd4-2¹⁸⁶⁻⁹⁷⁵ and 14-3-3η in solution. 12% TBE-PAGE showing the phosphorylation-dependent formation of a complex between single cysteine variants of pNedd4-2¹⁹⁰⁻⁵⁸¹ (C209, C218, C389, C414, C508, C522, C571 and WT) or pNedd4-2¹⁸⁶⁻⁹⁷⁵ C942 and 14-3-3η after loading 240 pmol of 14-3-3η and 120 pmol of Nedd4-2 or pNedd4-2 on the native gel, respectively.

A



B



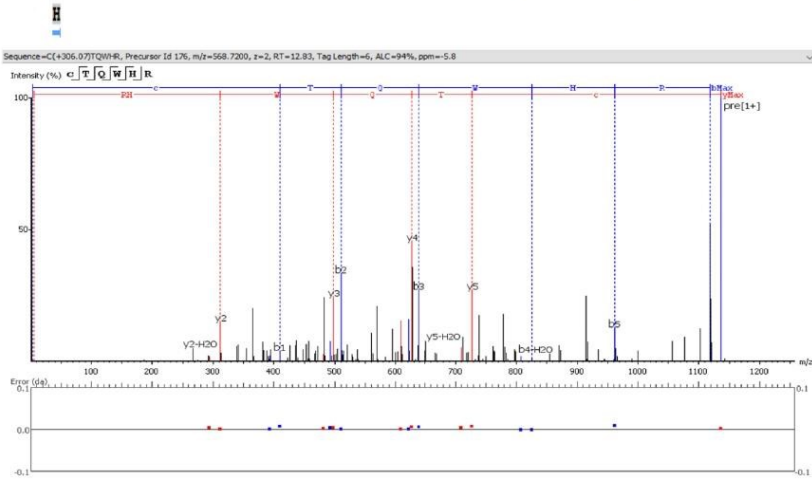
Supplemental Figure S2. Verification of dansyl labeling of Nedd4-2¹⁹⁰⁻⁵⁸¹ at C209 from WW1 domain. **A.** Peptide mapping of pNedd4-2¹⁹⁰⁻⁵⁸¹ after digestion with immobilized pepsin. All peptides identified by ESI-MS/MS (timsToF Pro) are shown as blue bars. Grey bars represent *de novo* peptides. **B.** Fragmentation spectrum of dansyl labelled peptide.

A

Nedd4-2¹⁹⁰⁻⁵⁸¹ - C218



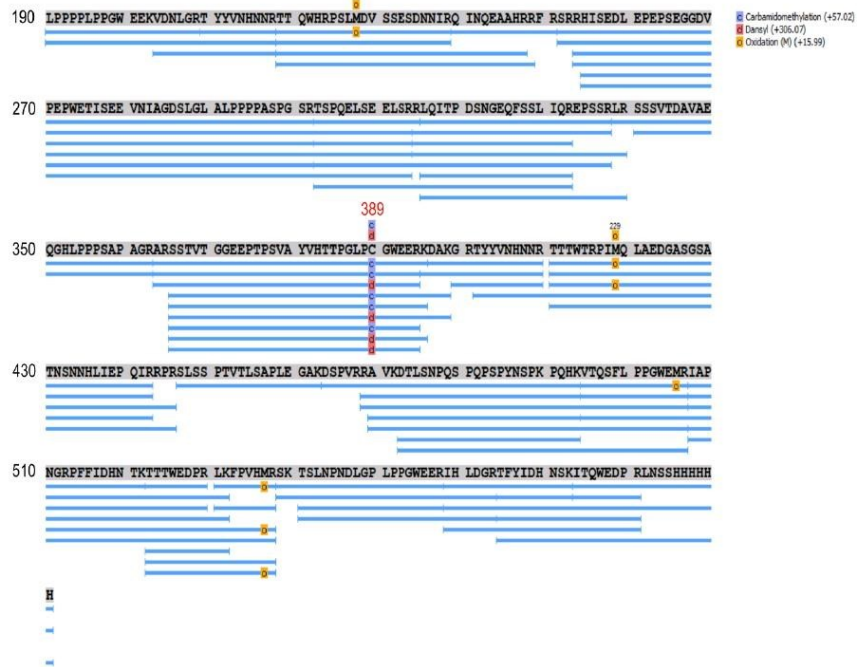
B



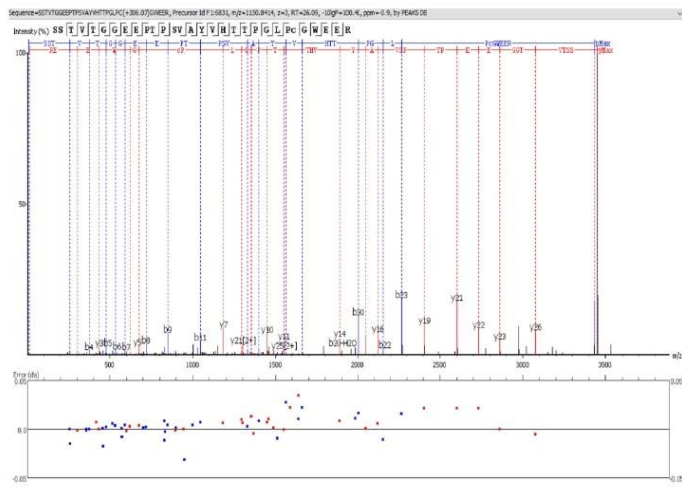
Supplemental Figure S3. Verification of dansyl labeling of Nedd4-2¹⁹⁰⁻⁵⁸¹ at C218 from the WW1 domain. **A.** Peptide mapping of pNedd4-2¹⁹⁰⁻⁵⁸¹ after digestion with immobilized pepsin. All peptides identified by ESI-MS/MS (timsToF Pro) are shown as blue bars. Grey bars represent *de novo* peptides. **B.** Fragmentation spectrum of the dansyl labelled peptide.

A

Nedd4-2¹⁹⁰⁻⁵⁸¹-C389



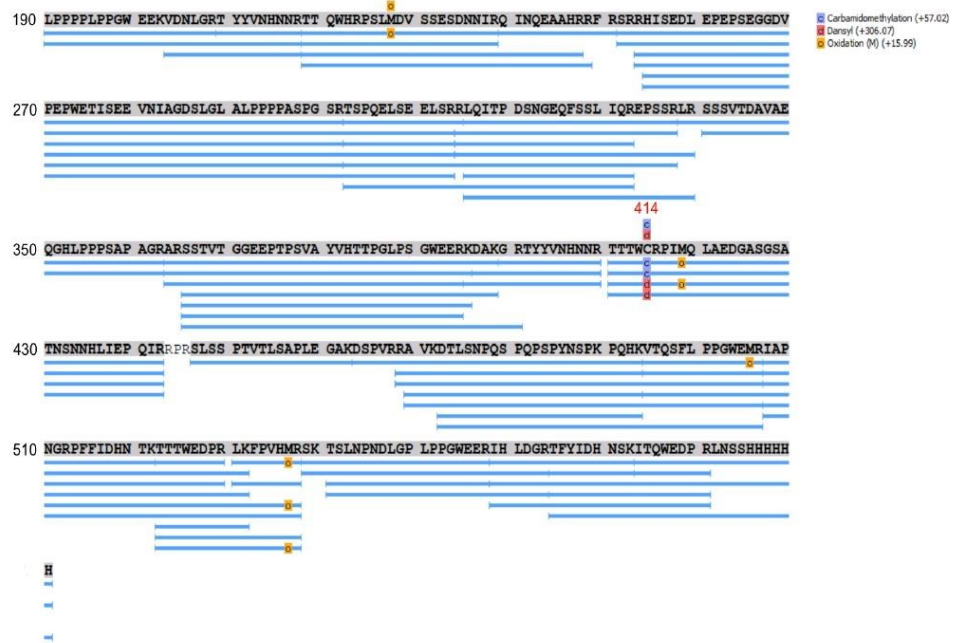
B



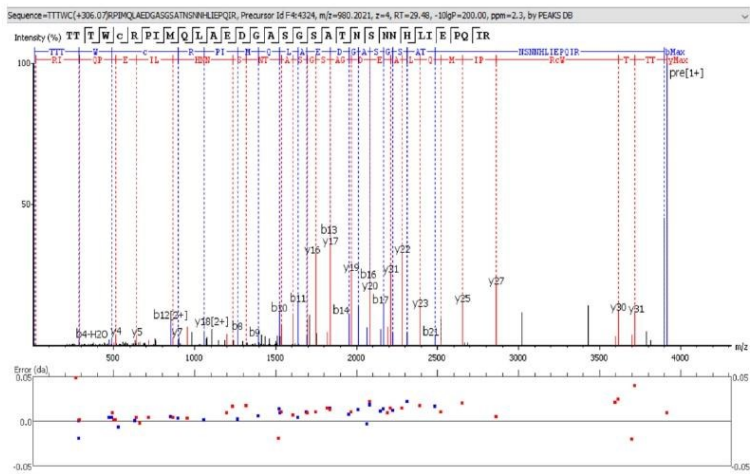
Supplemental Figure S4. Verification of dansyl labeling of Nedd4-2¹⁹⁰⁻⁵⁸¹ at C389 from the WW2 domain. **A.** Peptide mapping of pNedd4-2¹⁹⁰⁻⁵⁸¹ after digestion with immobilized pepsin. All peptides identified by ESI-MS/MS (timsToF Pro) are shown as blue bars. Grey bars represent *de novo* peptides. **B.** Fragmentation spectrum of the dansyl labelled peptide.

A

Nedd4-2¹⁹⁰⁻⁵⁸¹- C414



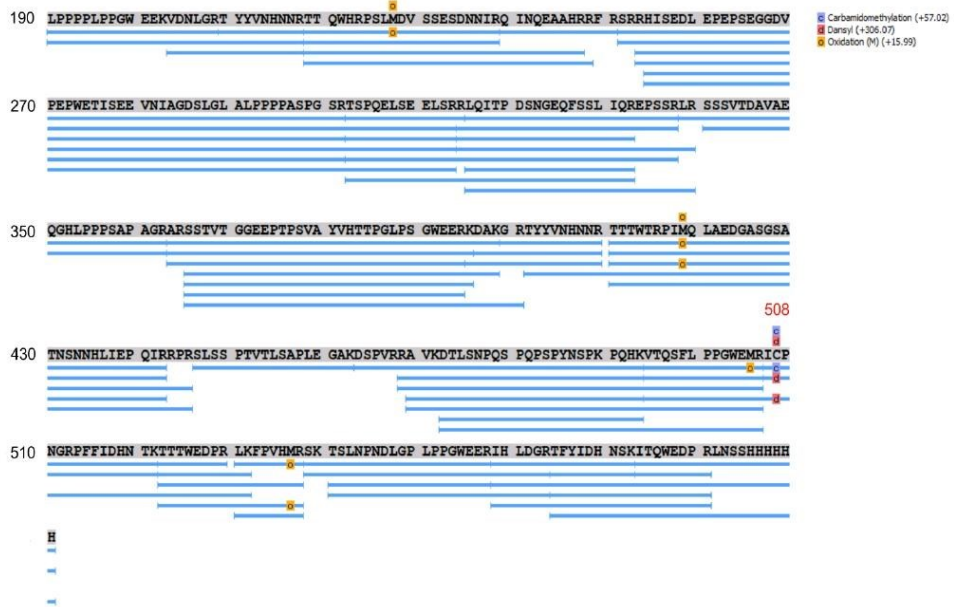
B



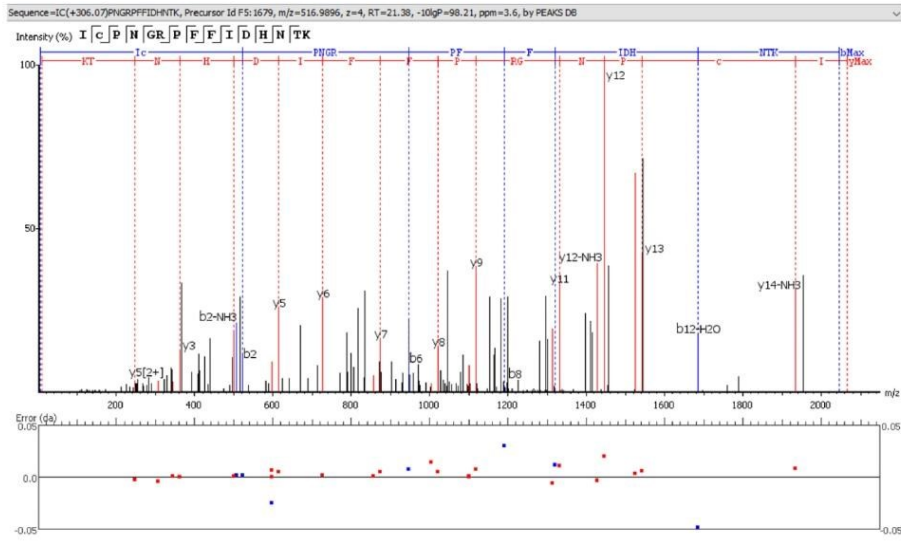
Supplemental Figure S5. Verification of dansyl labeling of Nedd4-2¹⁹⁰⁻⁵⁸¹ at C414 from the WW2 domain. **A.** Peptide mapping of pNedd4-2¹⁹⁰⁻⁵⁸¹ after digestion with immobilized pepsin. All peptides identified by ESI-MS/MS (timsToF Pro) are shown as blue bars. Grey bars represent *de novo* peptides. **B.** Fragmentation spectrum of the dansyl labelled peptide.

A

Nedd4-2¹⁹⁰⁻⁵⁸¹- C508



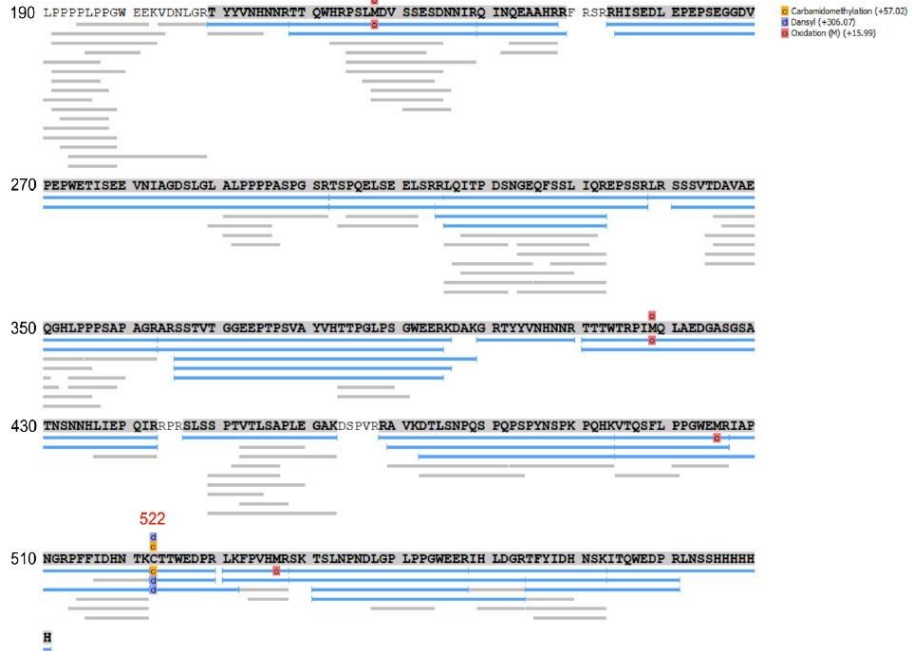
B



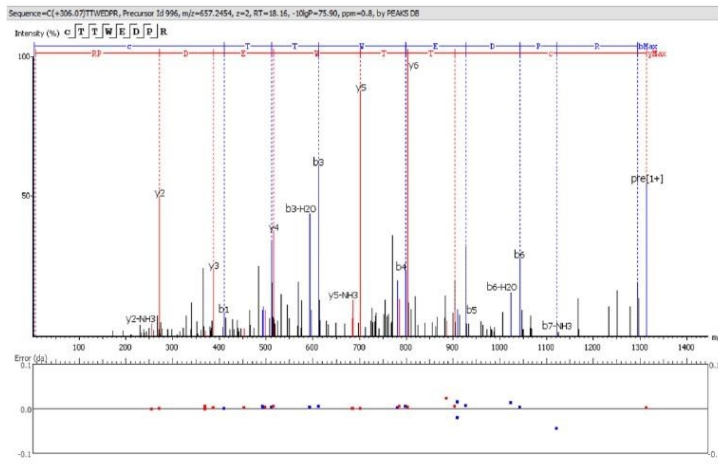
Supplemental Figure S6. Verification of dansyl labeling of Nedd4-2¹⁹⁰⁻⁵⁸¹ at C508 from the WW3 domain. **A.** Peptide mapping of pNedd4-2¹⁹⁰⁻⁵⁸¹ after digestion with immobilized pepsin. All peptides identified by ESI-MS/MS (timsToF Pro) are shown as blue bars. Grey bars represent *de novo* peptides. **B.** Fragmentation spectrum of the dansyl labelled peptide.

A

Nedd4-2¹⁹⁰⁻⁵⁸¹- C522



B



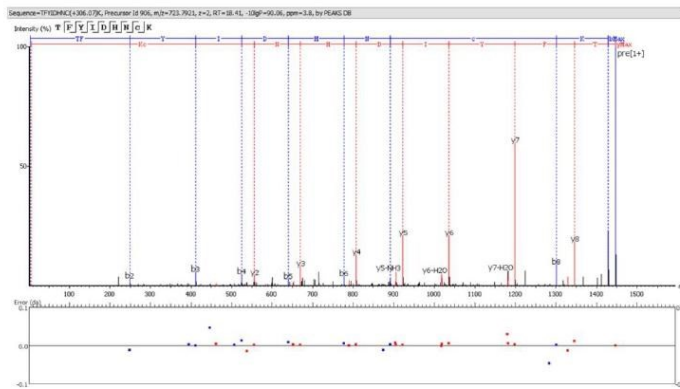
Supplemental Figure S7. Verification of dansyl labeling of Nedd4-2¹⁹⁰⁻⁵⁸¹ at C522 from the WW3 domain. **A.** Peptide mapping of pNedd4-2¹⁹⁰⁻⁵⁸¹ after digestion with immobilized pepsin. All peptides identified by ESI-MS/MS (timsToF Pro) are shown as blue bars. Grey bars represent *de novo* peptides. **B.** Fragmentation spectrum of the dansyl labelled peptide.

A

Nedd4-2¹⁹⁰⁻⁵⁸¹- C571



B

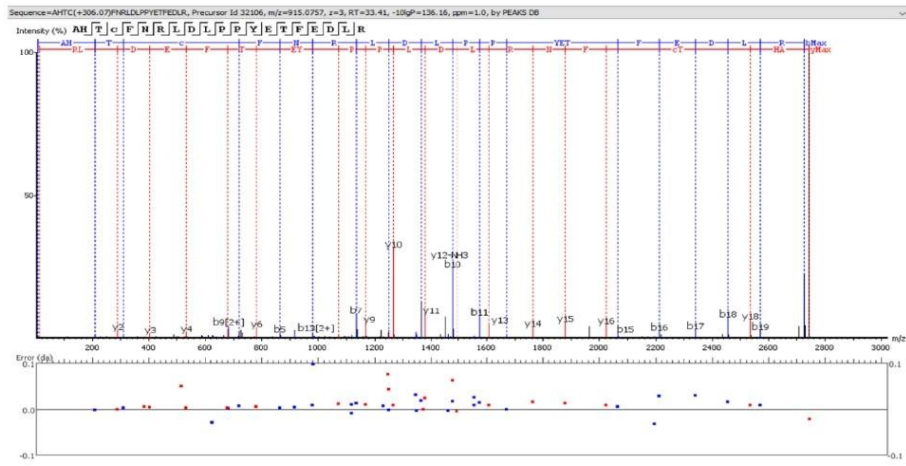


Supplemental Figure S8. Verification of dansyl labeling of Nedd4-2¹⁹⁰⁻⁵⁸¹ at C571 from the WW4 domain. **A.** Peptide mapping of pNedd4-2¹⁹⁰⁻⁵⁸¹ after digestion with immobilized pepsin. All peptides identified by ESI-MS/MS (timsToF Pro) are shown as blue bars. Grey bars represent *de novo* peptides. **B.** Fragmentation spectrum of the dansyl labelled peptide.

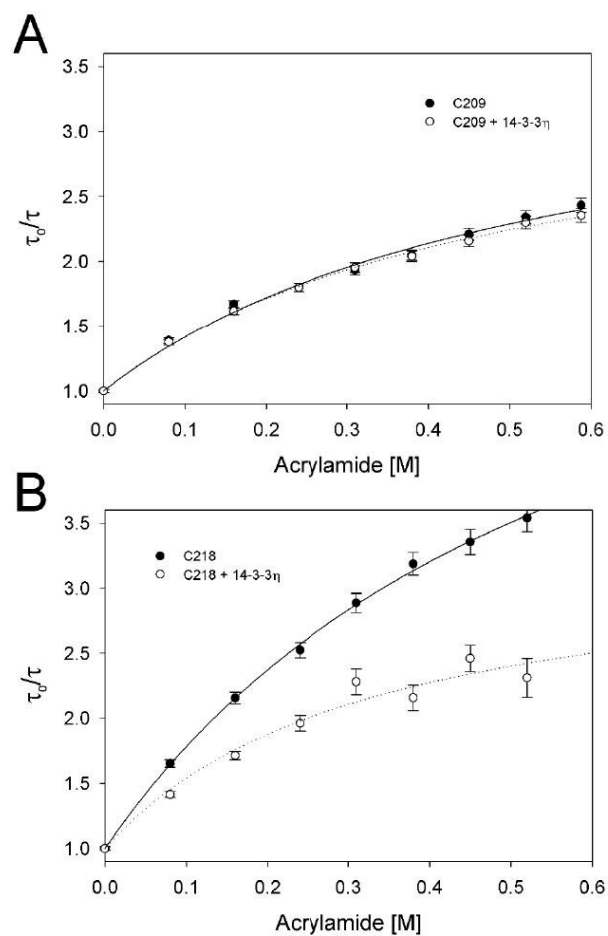
Nedd4-2¹⁸⁶⁻⁹⁷⁵_ C942



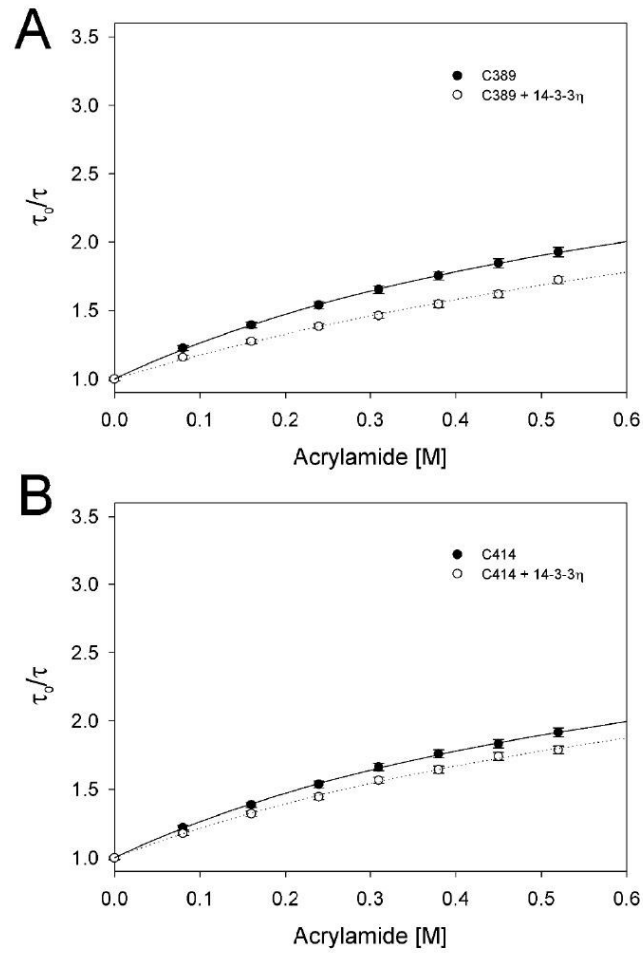
Supplemental Figure S9. Verification of dansyl labeling of Nedd4-2¹⁸⁶⁻⁹⁷⁵ at C942 from the C-lobe of HECT domain. Peptide mapping of pNedd4-2¹⁸⁶⁻⁹⁷⁵ after digestion with immobilized pepsin. All peptides identified by ESI-MS/MS (timsToF Pro) are shown as blue bars. Grey bars represent *de novo* peptides.



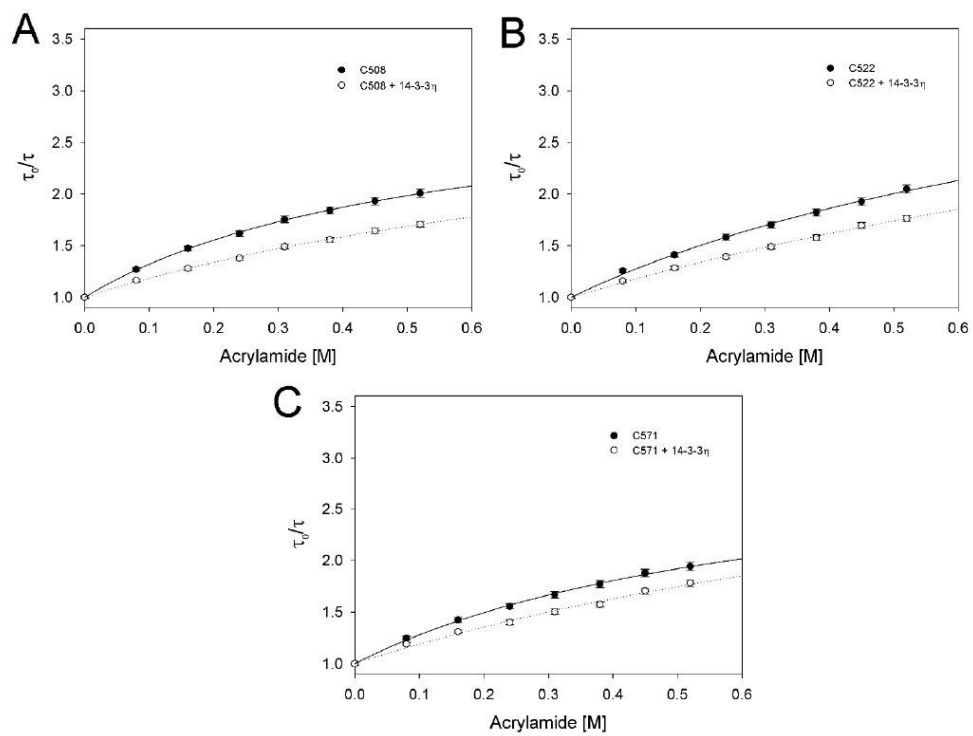
Supplemental Figure S10. Verification of dansyl labeling of Nedd4-2¹⁸⁶⁻⁹⁷⁵ at C942 from the C-lobe of HECT domain. Fragmentation spectrum of dansyl labelled peptide identified by ESI-MS/MS (timsToF Pro).



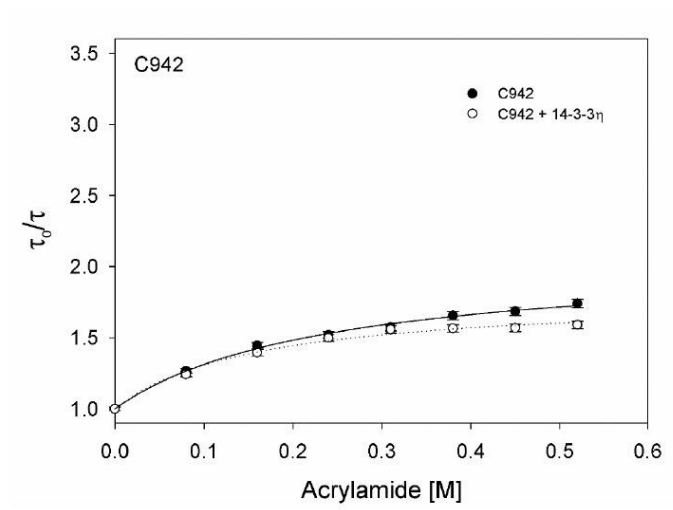
Supplemental Figure S11. Results of acrylamide quenching of dansyl fluorescence of C209 (A) and C218 (B) of Nedd4-2¹⁹⁰⁻⁵⁸¹ from the WW1 domain.



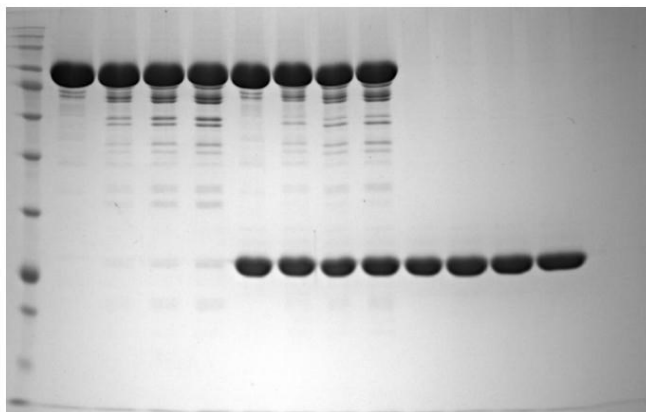
Supplemental Figure S12. Results of acrylamide quenching of dansyl fluorescence of C389 (A) and C414 (B) of Nedd4-2¹⁹⁰⁻⁵⁸¹ from the WW2 domain.



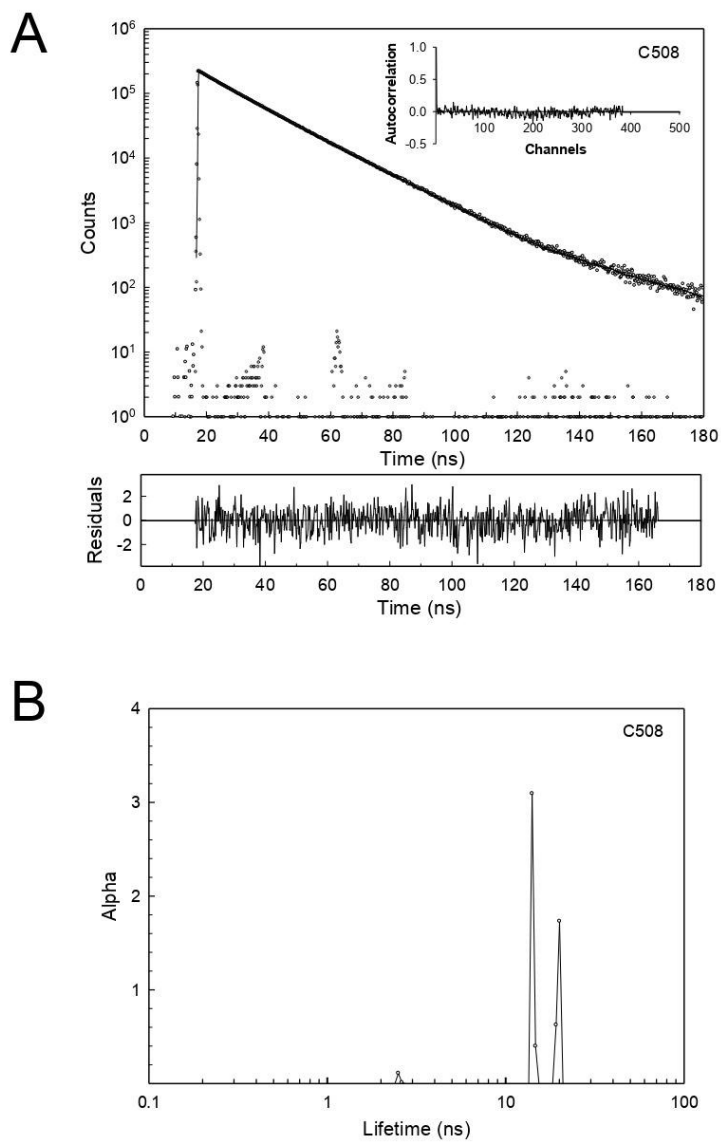
Supplemental Figure S13. Results of acrylamide quenching of dansyl fluorescence of C508 (A), C522 (B) and 571 (C) of Nedd4-2¹⁹⁰⁻⁵⁸¹ from the WW3 and WW4 domains.



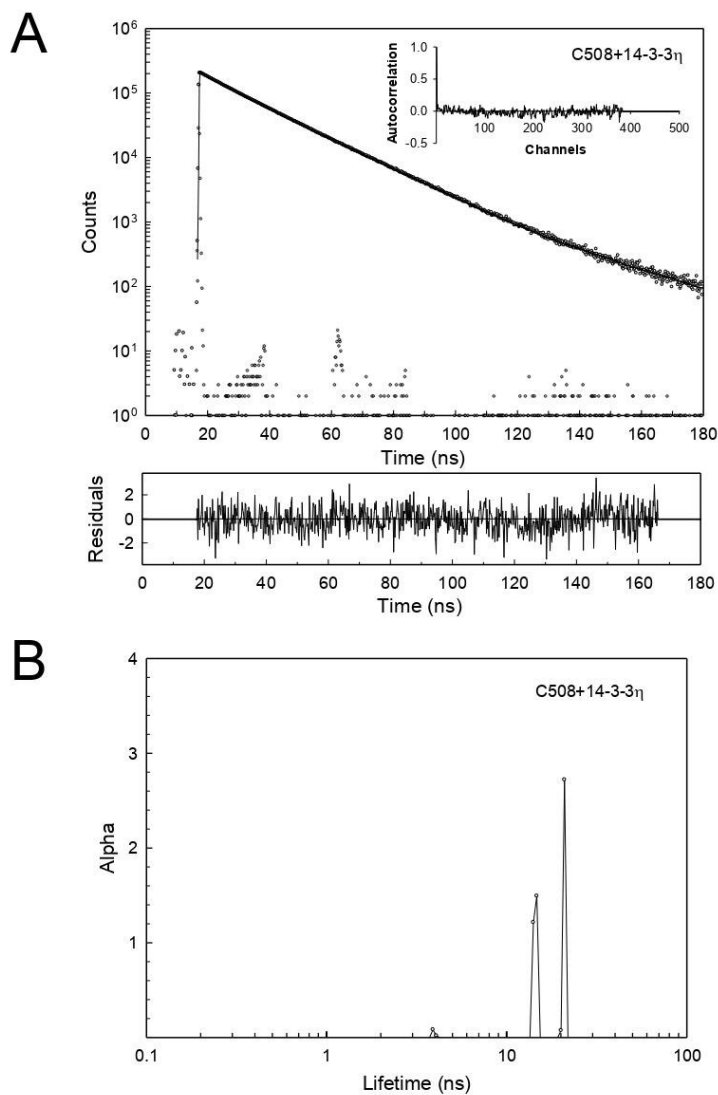
Supplemental Figure S14. Results of acrylamide quenching of dansyl fluorescence of C942 of Nedd4-2¹⁸⁶⁻⁹⁷⁵ from the HECT domain.



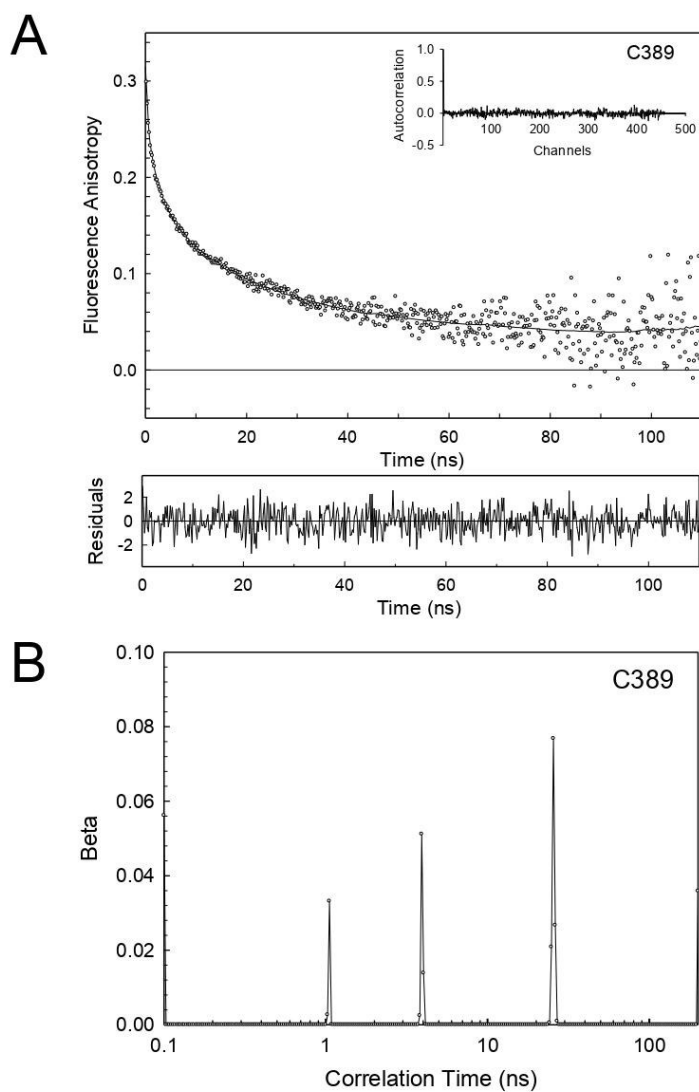
Supplemental Figure S15. Limited proteolysis assay showing the protective effect of 14-3-3 to pNedd4-2¹⁸⁶⁻⁹⁷⁵. Phosphorylated Nedd4-2¹⁸⁶⁻⁹⁷⁵ in the absence and presence of 14-3-3 η digested with trypsin for 10, 20 and 30 min. The protease/Nedd4-2 ratio was 1:1000 (w/w). The reactions were stopped by boiling the samples with SDS/PAGE loading buffer at the times indicated, before SDS-PAGE analysis. Unedited gel image corresponds to Figure 6A.



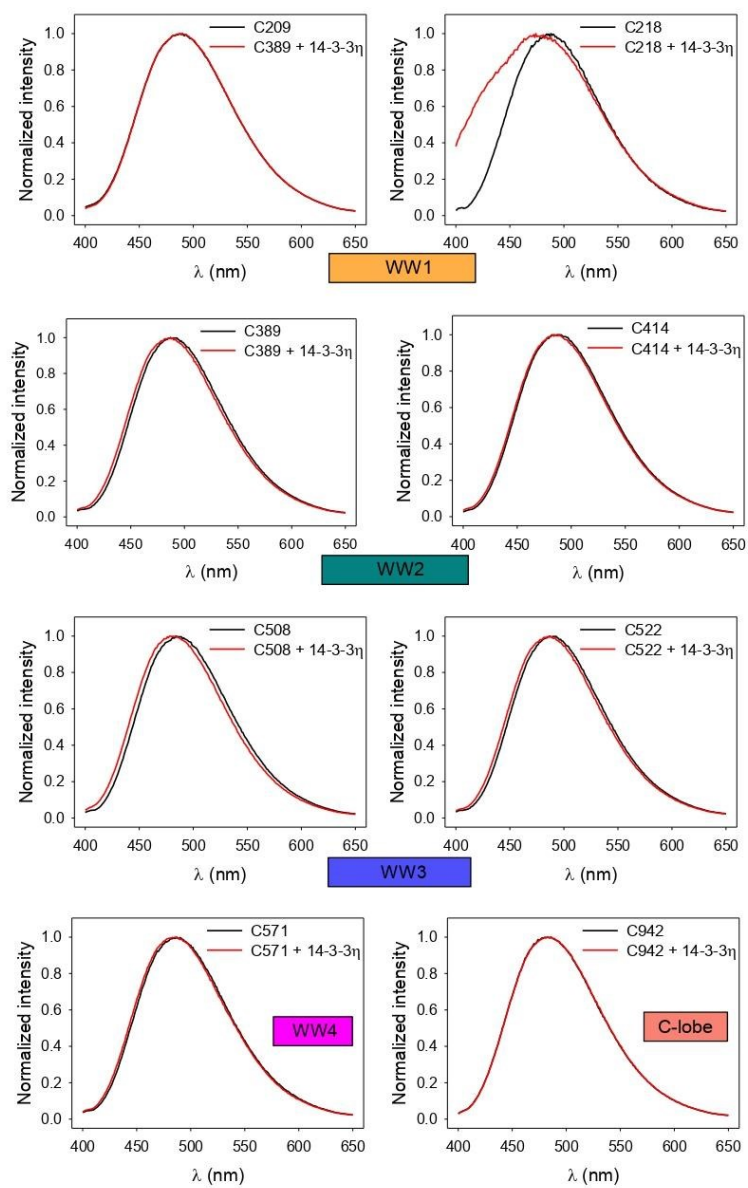
Supplemental Figure S16. Typical fluorescence decay of AEDANS-labelled Nedd4-2. Emission decay (A) and lifetime distribution (B) of AEDANS-labelled Nedd4-2¹⁸⁶⁻⁹⁷⁵ C508.



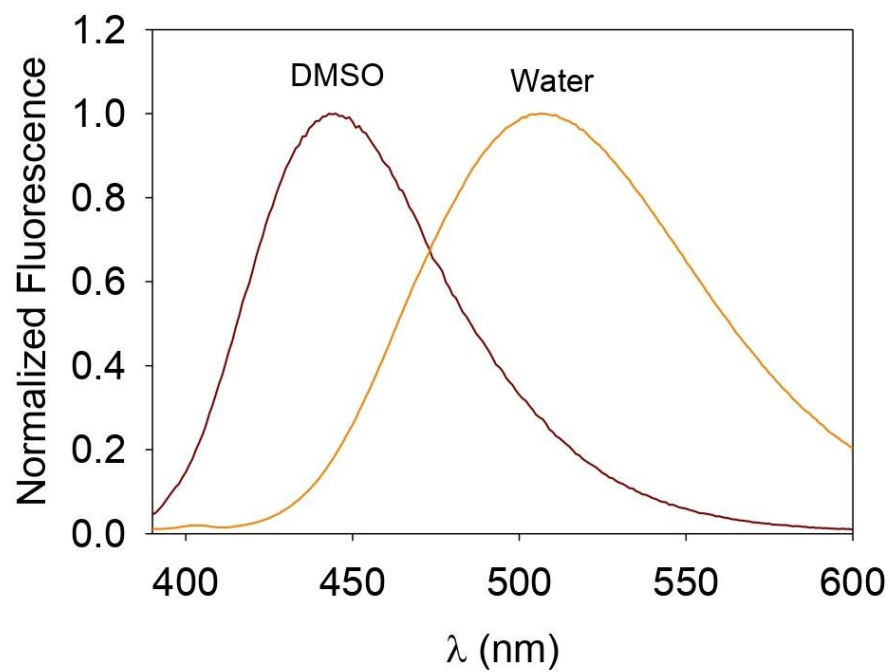
Supplemental Figure S17. Typical fluorescence decay of AEDANS-labelled Nedd4-2 in the presence of 14-3-3. Emission decay (A) and lifetime distribution (B) of AEDANS-labelled Nedd4-2¹⁸⁶⁻⁹⁷⁵ C508 in the presence of 14-3-3 η .



Supplemental Figure S18. Typical fluorescence anisotropy data of AEDANS-labelled Nedd4-2. Fluorescence anisotropy decay (A) and correlation time distribution (B) of AEDANS-labelled Nedd4-2¹⁸⁶⁻⁹⁷⁵ C389.



Supplemental Figure S19. Emission spectra of Dansyl-labeled Nedd4-2 variants in the absence (black) and the presence (red) 14-3-3η. The emission was excited at 355 nm.



Supplemental Figure S20. Emission spectra of free AEDANS in DMSO and water, excitation wavelength was 355 nm.

10.2 Publication II



Pohl, P., **Joshi, R.**, Petrvalska, O., Obsil, T., Obsilova, V. **14-3-3-protein regulates Nedd4-2 by modulating interactions between HECT and WW domains.** *Commun. Biol.* **4**, 899 (2021).

IF²⁰²¹ = 6.268

Contribution:

I have prepared recombinant Nedd4-2 and 14-3-3 protein variants for further experiments. In addition, I have prepared the protein samples for chemical cross-linking coupled to mass spectrometry experiments, optimized the conditions of this experiment and prepared corresponding figures. Moreover, I have refined the protein structure of Nedd4-2pS342:14-3-3 $\gamma\Delta$ C complex.

14-3-3-protein regulates Nedd4-2 by modulating interactions between HECT and WW domains

Pavel Pohl^{1,2}, Rohit Joshi^{1,3}, Olivia Petrvalska^{1,3}, Tomas Obsil^{1,3} [✉] & Veronika Obsilova^{1,3} [✉]

Neural precursor cell expressed developmentally down-regulated 4 ligase (Nedd4-2) is an E3 ubiquitin ligase that targets proteins for ubiquitination and endocytosis, thereby regulating numerous ion channels, membrane receptors and tumor suppressors. Nedd4-2 activity is regulated by autoinhibition, calcium binding, oxidative stress, substrate binding, phosphorylation and 14-3-3 protein binding. However, the structural basis of 14-3-3-mediated Nedd4-2 regulation remains poorly understood. Here, we combined several techniques of integrative structural biology to characterize Nedd4-2 and its complex with 14-3-3. We demonstrate that phosphorylated Ser³⁴² and Ser⁴⁴⁸ are the key residues that facilitate 14-3-3 protein binding to Nedd4-2 and that 14-3-3 protein binding induces a structural rearrangement of Nedd4-2 by inhibiting interactions between its structured domains. Overall, our findings provide the structural glimpse into the 14-3-3-mediated Nedd4-2 regulation and highlight the potential of the Nedd4-2:14-3-3 complex as a pharmacological target for Nedd4-2-associated diseases such as hypertension, epilepsy, kidney disease and cancer.

¹Department of Structural Biology of Signaling Proteins, Division BIOCEV, Institute of Physiology of the Czech Academy of Sciences, Vestec, Czech Republic. ²2nd Faculty of Medicine, Charles University, Prague, Czech Republic. ³Department of Physical and Macromolecular Chemistry, Faculty of Science, Charles University, Prague, Czech Republic. ✉email: obsil@natur.cuni.cz; veronika.obsilova@fgu.cas.cz

The neural precursor cell expressed developmentally down-regulated 4 (Nedd4-2) is a member of the HECT E3 ubiquitin ligase family. As such, this enzyme targets proteins for ubiquitination in mammalian programmed cell death^{1,2}. Mouse knockout studies have confirmed that Nedd4-2 plays a key role in animal physiology by regulating multiple substrates, including the epithelial sodium channel (ENaC). High ENaC activity and blood pressure with aberrant renal Na⁺ reabsorption are observed in Liddle syndrome resulting from mutations in its Nedd4-2-interacting motif^{3,4}. In addition to regulating ion transport, Nedd4-2 controls cellular trafficking in different tissues, modulating multiple signaling pathways through these interactions. Unsurprisingly, respiratory distress, hypertension, and electrolyte imbalance and kidney disease stand out among the pathological consequences of Nedd4-2 dysregulation, in line with mouse studies associating numerous SNPs in the Nedd4-2 gene with these conditions and with multiple tumor types^{5,6}. Therefore, potential therapeutic interventions may be developed by targeting the ubiquitin system for drug development via Nedd4-2 interactions⁷.

Developing such strategies targeting Nedd4-2 requires thoroughly understanding the structural-functional relationships of this protein. Fortunately, all nine members of the Nedd4 family of mammalian HECT E3 ligases have a similar modular multi-domain architecture, typically consisting of an N-terminal C2 domain, two-to-four WW domains, which contain two conserved tryptophan residues and a proline residue, and a C-terminal catalytic HECT domain^{5,8} (see Fig. 1). The N-terminal C2 domain enables Ca²⁺-dependent binding to membrane phospholipids, whereas the WW domains specifically bind short protein motifs, either PPXY or LPXY (where X indicates any amino acid), as well as proline-rich motifs of substrate proteins⁹. Through its four WW domains, Nedd4-2 may, nevertheless, interact with many different proteins, and even with several proteins simultaneously, because these domains show different substrate specificities, suggesting distinctive roles¹⁰. HECT domain is a bilobed domain whose N-terminal N-lobe interacts with E2 enzymes and whose C-terminal C-lobe contains the catalytic cysteine (Cys⁹⁴² in Nedd4-2). The C-lobe can freely move around the flexible joint loop connecting this lobe to the N-lobe in the L-shaped structure^{11,12}. Furthermore, inter- or intramolecular interactions between WW domains and the PY motif (L⁹⁴⁸PPY⁹⁵¹) located within the HECT domain likely inhibit Nedd4-2 auto-ubiquitination, thus increasing its stability¹³. Accordingly, this interaction is disrupted by substrate binding, promoting Nedd4-2 self-ubiquitination and subsequent degradation. As a result, Nedd4-2 is downregulated upon target ubiquitination.

Nedd4-2 is also regulated by phosphorylation in response to changes in Na⁺ or in volume through several hormonal signaling

pathways. The first pathway is initiated by aldosterone, which induces SGK1 kinase-mediated Nedd4-2 phosphorylation on three sites (Ser³⁴², Thr³⁶⁷ and Ser⁴⁴⁸), and the second by vasopressin, which activates PKA kinase and phosphorylates Nedd4-2 on the same three residues¹⁴⁻¹⁷. Moreover, insulin signaling activates both Akt1 and SGK1 kinases and results in phosphorylation of Nedd4-2^{11,18}. In particular, Ser⁴⁴⁸ is also phosphorylated by IKK β kinase in association with SGK or PKA kinases, inhibiting Nedd4-2 binding to ENaC upon dual phosphorylation¹⁹. As expected in this context, Nedd4-2 Ser⁴⁴⁸ phosphorylation triggers 14-3-3 protein binding, which in turn inhibits the interaction between Nedd4-2 and its substrate ENaC^{20,21}. In fact, the 14-3-3 protein (eta isoform) is a known cofactor in SGK- and PKA-dependent regulation of human Nedd4-2²⁰⁻²². Concurrently, the region containing Ser⁴⁴⁸, located between the WW2 and WW3 domains, is conserved among various Nedd4-2 proteins, thus further supporting its importance for Nedd4-2 regulation. Further evidence on the other two phosphoserines, pSer³⁴² and pSer³⁶⁷, located in the linker between WW1 and WW2 domains, demonstrates their role as additional 14-3-3 binding motifs^{17,22,23}. Several 14-3-3 binding partners also have two or more 14-3-3 binding motifs for high-affinity binding to both protomers within the 14-3-3 dimer^{24,25}. However, the contribution of these individual motifs, especially of their phosphoserines pSer³⁴² and pSer³⁶⁷, to the stability of the Nedd4-2:14-3-3 complex and the mechanism whereby 14-3-3 binding modulates Nedd4-2 function remain elusive. Bridging these knowledge gaps may enable us to develop strategies for targeted modulation of Nedd4-2 functions. Thus, to enhance our understanding of the 14-3-3-mediated Nedd4-2 regulation, we prepared and biophysically and structurally characterized the 14-3-3 binding motifs of Nedd4-2 and two longer Nedd4-2 variants (Nedd4-2¹⁸⁶⁻⁹⁷⁵ and Nedd4-2³³⁵⁻⁴⁵⁵, Fig. 1) in complex with the 14-3-3 protein.

Results

Phosphorylated Nedd4-2 forms a stable complex with 14-3-3 with a 1:2 stoichiometry. To investigate the interaction between Nedd4-2 and 14-3-3 proteins, we prepared a full length Nedd4-2 construct (residues 1-975), but recombinant expression and purification of this construct yielded an insoluble protein. We then expressed N-terminally truncated Nedd4-2, missing the C2 domain (Nedd4-2¹⁸⁶⁻⁹⁷⁵), which was soluble and stable enough for biophysical and structural characterization upon purification. Purified Nedd4-2¹⁸⁶⁻⁹⁷⁵ was phosphorylated by PKA in vitro, and stoichiometric phosphorylation of all three known 14-3-3 binding motifs (Ser³⁴², Thr³⁶⁷ and Ser⁴⁴⁸) was confirmed by LC-MS analysis^{17,23}. Using the auto-ubiquitination assay¹³, we also tested the catalytic activity of Nedd4-2¹⁸⁶⁻⁹⁷⁵, which was reduced in the presence of the 14-3-3 η protein (Supplementary Fig. S1).

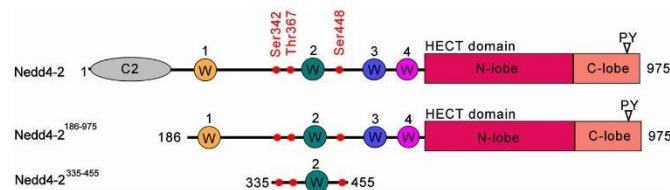


Fig. 1 Domain structure of human Nedd4-2 and the expression constructs used in this study. On the top, a schematic representation of the Nedd4-2 domain structure shows the relative positions of sites phosphorylated by PKA in vitro in red dots. Ser³⁴², Thr³⁶⁷ and Ser⁴⁴⁸ are 14-3-3 binding motifs. The Ca²⁺/lipid binding domain is shown in grey (denoted as C2), and the WW domains 1-4 (denoted as W) are shown in yellow, teal, blue and magenta. The HECT domain N- and C-lobes are shown in raspberry and salmon, respectively. The boundaries of two constructs used in this study are Nedd4-2¹⁸⁶⁻⁹⁷⁵ and Nedd4-2³³⁵⁻⁴⁵⁵.

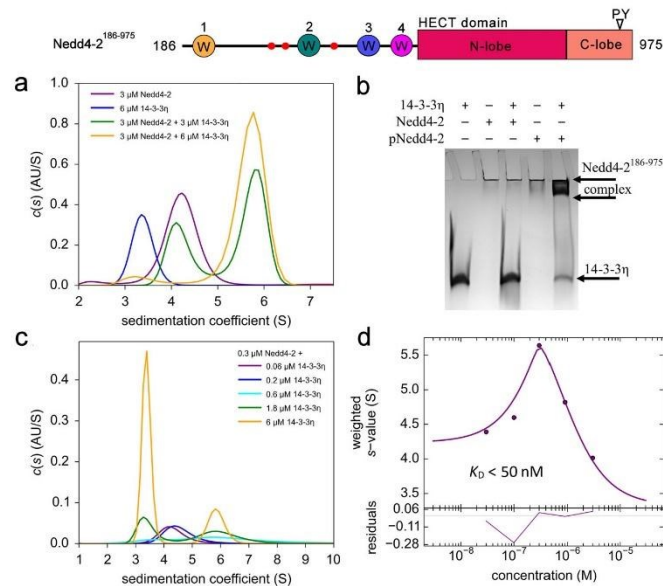


Fig. 2 Characterization of the interaction between Nedd4-2¹⁸⁶⁻⁹⁷⁵ and 14-3-3 in solution. **a** Continuous sedimentation coefficient distributions ($c(s)$) of 3 μM pNedd4-2¹⁸⁶⁻⁹⁷⁵ alone (purple), 6 μM 14-3-3 η alone (blue), and pNedd4-2¹⁸⁶⁻⁹⁷⁵:14-3-3 η complex mixed at 1:1 (green) and 1:2 (yellow) molar ratios. **b** 12% TBE-PAGE showing the phosphorylation-dependent formation of a complex between pNedd4-2¹⁸⁶⁻⁹⁷⁵ and 14-3-3 η after loading 240 pmol of 14-3-3 η and 120 pmol of Nedd4-2¹⁸⁶⁻⁹⁷⁵ or pNedd4-2¹⁸⁶⁻⁹⁷⁵ on the native gel, respectively. **c** Sedimentation coefficient distributions ($c(s)$) of mixtures of 300 nM pNedd4-2¹⁸⁶⁻⁹⁷⁵ with 0.06–6 μM 14-3-3 η . **d** Isotherm of weight-averaged sedimentation coefficients (s_w) derived from SV-AUC analysis of mixtures of 300 nM pNedd4-2¹⁸⁶⁻⁹⁷⁵ with 0.06–6 μM 14-3-3 η . Based on our estimates, the K_D value was lower than 50 nM, as further confirmed by global modeling.

Solution properties of Nedd4-2¹⁸⁶⁻⁹⁷⁵ and its interactions with 14-3-3 were characterized by sedimentation velocity analytical ultracentrifugation (SV AUC). The continuous sedimentation coefficient distributions ($c(s)$) of phosphorylated Nedd4-2¹⁸⁶⁻⁹⁷⁵ (pNedd4-2¹⁸⁶⁻⁹⁷⁵) and 14-3-3 η alone, a known Nedd4-2 binding partner²¹, revealed single peaks with weight-averaged sedimentation coefficients corrected to 20.0 °C and to the density of water ($s_{w(20,w)}$) of 4.8 S ($f/f_0 = 1.6$) and 3.8 S ($f/f_0 = 1.4$), respectively (Fig. 2a). The $s_{w(20,w)}$ of pNedd4-2¹⁸⁶⁻⁹⁷⁵ and 14-3-3 η correspond to M_w of ~95.9 kDa and ~57.4 kDa, respectively, suggesting that pNedd4-2¹⁸⁶⁻⁹⁷⁵ is protomeric in solution (theoretical $M_w = 91.7$ kDa), whereas 14-3-3 η forms stable dimers (theoretical $M_w = 56.8$ kDa), as expected. The analysis of $c(s)$ distributions of pNedd4-2¹⁸⁶⁻⁹⁷⁵:14-3-3 η mixtures also revealed the formation of a stable complex with a $s_{w(20,w)}$ of 6.5 S ($f/f_0 = 1.6$), which corresponds to a M_w of ~145 kDa, thus indicating a molar stoichiometry of 1:2 (a protomer of pNedd4-2¹⁸⁶⁻⁹⁷⁵ bound to a dimer of 14-3-3 η , with a theoretical M_w of 149 kDa) (Fig. 2a). The formation of this complex was also confirmed by native TBE-PAGE, which showed the phosphorylation-dependent interaction between Nedd4-2¹⁸⁶⁻⁹⁷⁵ and 14-3-3 η (compare lane 3 and 5) (Fig. 2b). To determine the apparent dissociation constant (K_D) of the pNedd4-2¹⁸⁶⁻⁹⁷⁵:14-3-3 η complex, five mixtures of pNedd4-2¹⁸⁶⁻⁹⁷⁵ and 14-3-3 η were prepared at different molar ratios (from 5:1 to 1:20) and analyzed by SV-AUC (Fig. 2c). Based on our direct modeling of SV-AUC data using the Lamm equation and on our analysis of the isotherm of weight-averaged sedimentation coefficient s values (s_w isotherm) as a function of 14-3-3 η concentration, the apparent K_D is lower than 50 nM

when using a Langmuir binding model assuming a reversible interaction between the 14-3-3 η dimer and one molecule of pNedd4-2¹⁸⁶⁻⁹⁷⁵ (Fig. 2d).

To examine the role of the HECT domain in the overall stability of the Nedd4-2:14-3-3 η complex, we also prepared a shorter variant Nedd4-2³³⁵⁻⁴⁵⁵ missing both the C2 and the HECT domains. This construct was considerably more soluble and stable than Nedd4-2¹⁸⁶⁻⁹⁷⁵. In the SV-AUC analysis of phosphorylated Nedd4-2³³⁵⁻⁴⁵⁵ (pNedd4-2³³⁵⁻⁴⁵⁵) alone, the single peak with a $s_{w(20,w)}$ of 1.4 ($f/f_0 = 1.5$) corresponds to a M_w of ~14 kDa (theoretical M_w 14 kDa). Accordingly, the absence of HECT domain should not affect Nedd4-2 oligomerization (Supplementary Fig. S2a). In turn, the analysis of pNedd4-2³³⁵⁻⁴⁵⁵ and 14-3-3 η mixtures showed the formation of a complex with a $s_{w(20,w)}$ of 4.5 S ($f/f_0 = 1.4$), which corresponds to a M_w of ~70 kDa and matches a molar stoichiometry of 1:2 (a protomer of pNedd4-2³³⁵⁻⁴⁵⁵ bound to a 14-3-3 η dimer, theoretical M_w 70 kDa) (Supplementary Fig. S2a). Both direct modeling of SV-AUC data (Supplementary Fig. S3a) and analysis of the s_w isotherm as a function of pNedd4-2³³⁵⁻⁴⁵⁵ concentration revealed an apparent K_D lower than 30 nM when using a binding model assuming a reversible interaction between the 14-3-3 η dimer and one molecule of pNedd4-2³³⁵⁻⁴⁵⁵ (Fig. 3b). These results indicate that the HECT domain is not essential for high-affinity Nedd4-2 binding to 14-3-3 η .

In addition, we prepared pNedd4-2³³⁵⁻⁴⁵⁵ to characterize 14-3-3 isoform binding specificity. As shown by native TBE-PAGE, pNedd4-2³³⁵⁻⁴⁵⁵ forms stable complexes with all human 14-3-3 protein isoforms (Supplementary Fig. S2b). Our findings

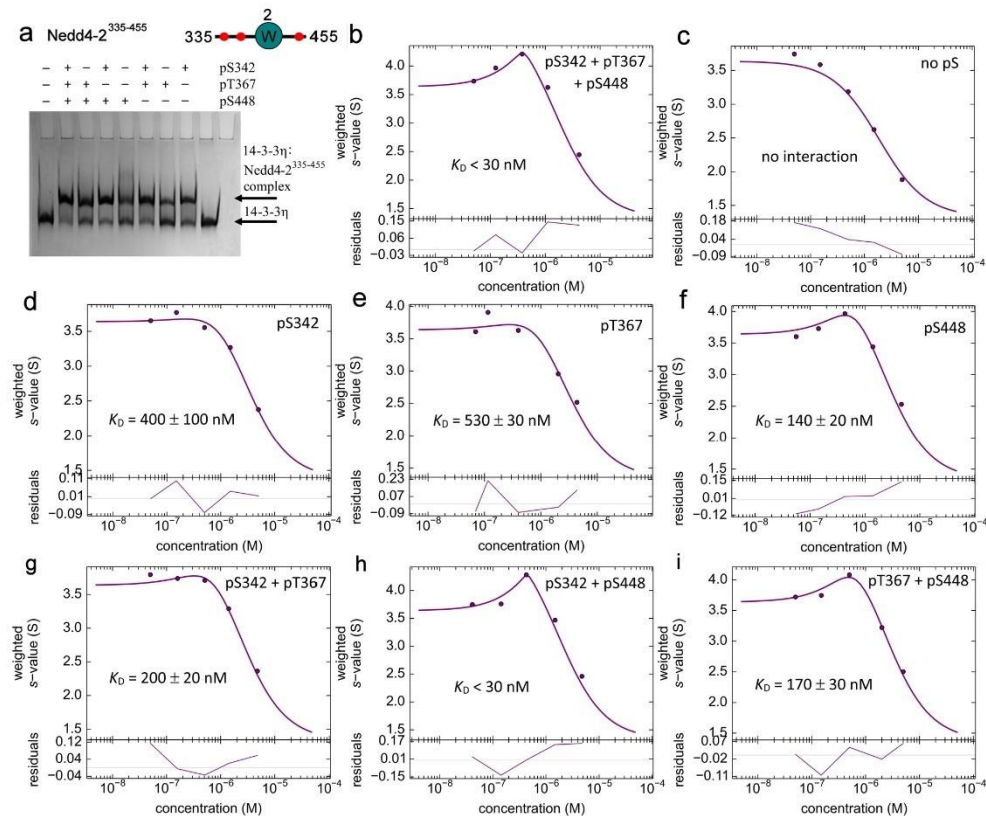


Fig. 3 Simultaneous phosphorylation of two 14-3-3 binding motifs pSer342 and pSer448 is required for tight complex formation between pNedd4-2335-455 and 14-3-3 η . **a** 12% Native TBE-PAGE showing the interaction between 14-3-3 η (240 pmol) and Nedd4-2335-455 variants without (no pS) or with one, two or three phosphorylation sites (120 pmol); 14-3-3 η protein alone was loaded on the penultimate lane. **b–i** Sedimentation velocity analytical ultracentrifugation analysis of the complexes between 14-3-3 η and pNedd4-2335-455 variants showing the s_w isotherms of 14-3-3 η and Nedd4-2 with all three phosphorylation sites pSer³⁴² + pThr³⁶⁷ + pSer⁴⁴⁸ (**b**), with no phosphorylation sites (**c**), with one phosphorylation site (pSer³⁴² (**d**), pThr³⁶⁷ (**e**) and pSer⁴⁴⁸ (**f**), or with two phosphorylation sites (pSer³⁴² + pThr³⁶⁷ (**g**), pSer³⁴² + pSer⁴⁴⁸ (**h**) and pThr³⁶⁷ + pSer⁴⁴⁸ (**i**)). The isotherms of weight-averaged sedimentation coefficients were constructed by SV-AUC analysis of mixtures of 1 μ M 14-3-3 η with Nedd4-2335-455 variants (0.05–5 μ M). The $c(s)$ distributions underlying the s_w data points are shown in Supplementary Fig. S3.

corroborate previous studies, which demonstrated that Nedd4-2 interacts with the 14-3-3 σ and η isoforms^{20,21,26} and with the 14-3-3 β,ϵ heterodimer²⁷.

High-affinity Nedd4-2 binding to 14-3-3 η requires both Ser³⁴² and Ser⁴⁴⁸ phosphorylation. All three putative 14-3-3 binding motifs of Nedd4-2 contain arginine residues at -5 and -3 positions with the respect to the phosphoresidue and a serine residue at -2 position. However, only the motif with Ser⁴⁴⁸ has a proline residue at +2 position, thus resembling the canonical 14-3-3 binding motif I (RSXpSXP). Considering their differences in primary structure, these three motifs likely differ in their binding affinities to 14-3-3^{25,28,29}. To characterize the importance of these phosphorylated motifs for Nedd4-2 binding to 14-3-3 η , we prepared three Nedd4-2³³⁵⁻⁴⁵⁵ mutants containing a single phosphorylation site (denoted as pS342, pT367 and pS448) by mutating the other phosphorylation sites to alanine and three Nedd4-2³³⁵⁻⁴⁵⁵ mutants with combinations of two

phosphorylation sites (denoted as pS342 + pT367, pS342 + pS448 and pT367 + pS448), in addition to a variant with all sites mutated to alanine (denoted as no pS), which was used as a negative control.

Differences in 14-3-3 η -protein binding affinity between all eight Nedd4-2³³⁵⁻⁴⁵⁵ variants (WT and mutants with none, one or two phosphosites) were tested by both native TBE-PAGE and SV-AUC analysis (Fig. 3 and Supplementary S2). Native TBE-PAGE revealed that only Nedd4-2³³⁵⁻⁴⁵⁵ no pS lost its ability to bind to 14-3-3 η because all other versions were able to form the complex (Fig. 3a). Among these variants, Nedd4-2³³⁵⁻⁴⁵⁵WT (Fig. 3b) and Nedd4-2³³⁵⁻⁴⁵⁵pS342 + pS448 (Fig. 3h) had the highest binding affinity (with K_D lower than 30 nM), as shown in a more quantitative analysis by SV-AUC. The results from our analytical ultracentrifugation analysis also highlighted that Nedd4-2:14-3-3 η -protein binding affinity was partly reduced (K_D = 140–200 nM) in singly phosphorylated Nedd4-2³³⁵⁻⁴⁵⁵pS448 (Fig. 3f), doubly phosphorylated Nedd4-2³³⁵⁻⁴⁵⁵pS342 + pT367 (Fig. 3g) and

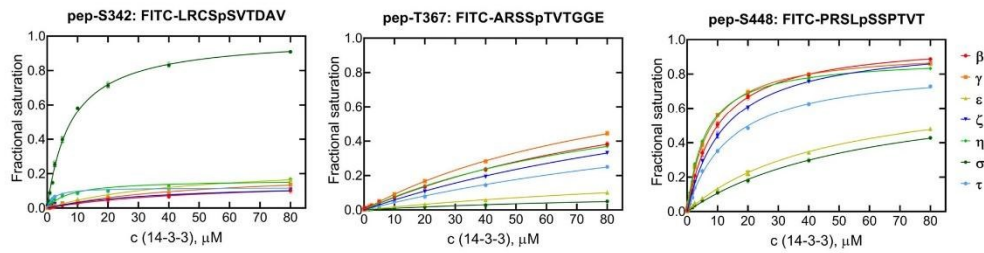


Fig. 4 14-3-3 isoform binding specificity of Nedd4-2 phosphomotifs. Binding of FITC-labeled phosphopeptides with 14-3-3 binding motifs of Nedd4-2 (pSer³⁴², pThr³⁶⁷ or pSer⁴⁴⁸) to all human 14-3-3 isoforms was characterized by FP titrations. The binding affinities of these peptides were determined by fitting FP data to a one-site binding model. The corresponding sequences of these peptides are shown at the top. Background polarization was subtracted from all values. Results are expressed as mean \pm SD ($n = 3$). Error bars are not visible if they are smaller than the size of the symbol.

Table 1 14-3-3 isoform binding specificity of individual 14-3-3 binding motifs of Nedd4-2.

	K_D^1 , μ M	K_D^1 , μ M
14-3-3 β	—	10.0 \pm 1.0
14-3-3 γ	—	7.2 \pm 0.7
14-3-3 ϵ	—	50.0 \pm 10.0
14-3-3 ζ	—	13.0 \pm 1.0
14-3-3 η	—	6.1 \pm 0.5
14-3-3 σ	7.8 \pm 0.8	60.0 \pm 10.0
14-3-3 τ	—	14.0 \pm 1.0

¹The apparent K_D values of the interaction between the peptide and 14-3-3 protein isoforms were determined by fluorescence polarization measurements of FITC-labeled Nedd4-2 peptides pep-S342 and pep-S448 peptides titrated with 14-3-3.

Nedd³³⁵⁻⁴⁵⁵pT367 + pS448 (Fig. 3i), significantly reduced ($K_D = 400 \pm 100$ nM and 530 ± 30 nM, respectively) in the singly phosphorylated variants Nedd³³⁵⁻⁴⁵⁵pS342 (Fig. 3d) and Nedd³³⁵⁻⁴⁵⁵pT367 (Fig. 3e) and undetected in Nedd³³⁵⁻⁴⁵⁵no pS (Fig. 3c). The binding affinities of our singly phosphorylated variants correlate with previous observations of their relative contribution to the cAMP-dependent regulation of Nedd (Ser⁴⁴⁸ > Ser³⁴² > Thr³⁶⁷)¹⁷. Therefore, bidentate interaction through pSer³⁴² and pSer⁴⁴⁸ affords the most stable complex between Nedd4-2 and 14-3-3 η in which pSer⁴⁴⁸ is the high affinity motif³⁰.

14-3-3 binding motifs of Nedd4-2 show distinct 14-3-3 isoform binding specificity. The interactions between isolated 14-3-3 binding motifs of Nedd4-2 and 14-3-3 protein isoforms were further characterized by fluorescence polarization (FP). For this purpose, we synthesized three decapeptides of known 14-3-3 binding motifs with phosphorylated pSer³⁴², pThr³⁶⁷ and pSer⁴⁴⁸ (denoted as pep-S342, pep-T367 and pep-S448) bordered by the amino acids from the natural sequence of Nedd4-2, with four amino acids before and another five after the corresponding phosphoresidue. We labelled all peptides N-terminally with fluorescein isothiocyanate (FITC) and characterized their binding to all human 14-3-3 protein isoforms by FP (Fig. 4 and Table 1). Our FP data revealed that all three phosphopeptides have relatively low binding affinities. The pep-S342 showed a measurable binding affinity only to 14-3-3 σ (K_D of ~ 7.8 μ M). In contrast, we were able to detect pep-T367 binding, albeit very weak, to all 14-3-3 isoforms except ϵ and σ . Lastly, we determined that pep-S448 binds to all 14-3-3 isoforms in the low micromolar range, showing the lowest K_D values (~ 6.1 and 7.2 μ M) when bound to isoforms η and γ , respectively. In addition, the K_D values of

synthetic phosphorylated peptides are two orders of magnitude higher than those of recombinant Nedd4-2 variants, indicating simultaneous binding of two motifs and/or the participation of regions other than phosphorylated motifs in the formation of the complex (Figs. 2 and 3). Overall, these results support our hypothesis that the pSer⁴⁴⁸ motif is the dominant 14-3-3 binding motif.

The 14-3-3 dimer simultaneously anchors both pSer³⁴² and pSer⁴⁴⁸ motifs of Nedd4-2. Because our AUC analysis suggested that the pSer³⁴² and pSer⁴⁴⁸ motifs are responsible for high-affinity Nedd4-2 binding to 14-3-3, we investigated the structural basis of their interaction with 14-3-3 in detail. For this purpose, we crystallized the peptides containing the pSer³⁴² and pSer⁴⁴⁸ motifs (pep-S342 and pep-S448) bound to 14-3-3 γ Δ C (lacking the 15 flexible residues at the C-terminus). The 14-3-3 γ isoform was selected based on crystal quality. Both phosphopeptide complexes crystallized in the trigonal space group R3 with two 14-3-3 dimers with bound phosphopeptides in the asymmetric unit (PDB ID: 6ZBT and 6ZC9, Table 2 and Fig. 5). The structures of the pep-S342:14-3-3 γ Δ C and pep-S448:14-3-3 γ Δ C complexes were solved by molecular replacement with 14-3-3 γ (PDB ID: 2B05) as a search model and refined to resolutions of 1.8 Å and 1.9 Å , respectively. The final electron densities of both peptides allowed us to trace seven of ten amino acids (Leu³³⁸ – Thr³⁴⁴) of pep-S342 and (Pro⁴⁴⁴ – Pro⁴⁵⁰) pep-S448 (Fig. 5a, c). In both cases, we were unable to trace the last three residues of each peptide, presumably due to disorder. The phosphate group, the main-chain conformation and other contacts in the 14-3-3-binding groove of both motifs were recognized similarly to those previously observed in other 14-3-3 protein complexes^{25,29,31–34}. The pSer³⁴² moiety of pep-S342 is coordinated through direct contacts enabled by side chains of the 14-3-3 residues Arg⁵⁷, Arg¹³², Lys⁵⁰ and Tyr¹³³ and by water-mediated contacts with 14-3-3 Asp¹²⁹ and Asn¹⁷⁸ (Fig. 5b). Other contacts include hydrogen bonds between the main-chain atoms of the Nedd4-2 residues Cys³⁴¹ and Val³⁴³ and the side chains of the 14-3-3 residues Asn²²⁹ and Asn¹⁷⁸, respectively. In addition, the side chain of Nedd4-2 Ser³⁴⁰ makes a polar contact with the side-chain residues Trp²³³ and Glu¹⁸⁵ of 14-3-3. Similar contacts between the phosphopeptide and 14-3-3 were also observed in the 14-3-3 γ Δ C:pep-S448 complex (Fig. 5d). The main difference is the absence of water-mediated contacts between Arg⁴⁴⁵ (–5 residue with the respect to pSer⁴⁴⁸) and the side chains of the 14-3-3 residues Arg⁵⁷, Arg⁶¹ and Glu¹³⁶.

Because the 14-3-3 binding motifs pSer³⁴² and pSer⁴⁴⁸ border the WW2 domain (Fig. 1), we assessed whether this domain

Table 2 Crystallographic data collection and refinement statistics.

Complex	pep-S342:14-3-3 γ Δ C	pep-S448:14-3-3 γ Δ C	Nedd4-2 ³³⁵⁻⁴⁵⁵ :14-3-3 η Δ C
PDB ID	6ZBT	6ZC9	7NMZ
Wavelength (Å)	0.9184	0.9184	1.3418
Space group	R 3:H	R 3:H	C121
Unit-cell parameters			
<i>a</i> , <i>b</i> , <i>c</i> (Å)	205.857 205.857 74.354	205.707 205.707 74.649	117.86 58.95 106.76
α , β , γ (°)	90.0 90.0 90.0	90.0 90.0 120.0	90 90.693 90
Asymmetric unit contents	Dimer of 14-3-3 γ Δ C with bound phosphopeptide	Dimer of 14-3-3 γ Δ C with bound phosphopeptide	Dimer of 14-3-3 η Δ C with bound Nedd4-2 containing pSer ³⁴² and pSer ⁴⁴⁸
Resolution range (Å) ^a	27.27 - 1.799 (1.864 - 1.799)	25.53 - 1.899 (1.967 - 1.899)	31.35 - 2.303 (2.385 - 2.303)
Unique reflections	108872 (10874)	92751 (9202)	32696 (3215)
Data multiplicity	5.81 (8.77)	5.84 (9.45)	4.73 (3.99)
Completeness (%)	99.88 (99.65)	99.76 (98.90)	99.85 (99.38)
$\langle I/\sigma(I) \rangle$	25.82 (2.9)	20.39 (1.81)	19.68 (1.94)
R_{meas}^b	0.041 (0.597)	0.051 (1.038)	0.064 (0.655)
R_{work}^c	0.2101 (0.2973)	0.2119 (0.3793)	0.1994 (0.2432)
R_{free}^c	0.2404 (0.3240)	0.2394 (0.3915)	0.2350 (0.2915)
No. of protein atoms	7332	7393	3718
No. of ligand atoms	40	40	
No. of waters	642	551	189
Average B factors (Å ²)	36.20	44.80	43.92
Protein	35.65	44.47	44.03
Ligand	49.35	57.13	
Water	41.72	48.36	41.82
R.m.s. ^d deviations from ideal values			
Bond lengths (Å)	0.003	0.004	0.003
Bond angles (°)	0.50	0.61	0.61
Ramachandran favored (%)	99.12	98.90	98.73
Ramachandran allowed (%)	0.88	1.10	1.27
Ramachandran outliers (%)	0	0	0

^aValues in parentheses are for the highest resolution shell.
^b $R_{\text{meas}} = \frac{\sum_{hkl} (|N(hkl)|/N(hkl) - 1)^2 \times \sum_{i,j} |I(hkl) - (hkl)|}{\sum_{hkl} \sum_{i,j} I(hkl)}$, where $I(hkl)$ is the intensity of reflection hkl , (hkl) is the mean intensity, $\frac{1}{N(hkl)} \sum_{i,j} I(hkl)$, and $N(hkl)$ the multiplicity.
^cThe free R value (R_{free}) was calculated using 5% of the reflections, which were omitted from the refinement.
^dR.m.s., root mean square.

participates in 14-3-3 binding by crystallizing the Nedd4-2³³⁵⁻⁴⁵⁵ construct in a complex with 14-3-3 η Δ C. The phosphorylation site Thr³⁶⁷ was mutated to Ala to prepare Nedd4-2³³⁵⁻⁴⁵⁵ phosphorylated only at Ser³⁴² and Ser⁴⁴⁸ for high-affinity binding and for homogeneous crystallization. The 14-3-3 η Δ C:Nedd4-2³³⁵⁻⁴⁵⁵ complex crystallized in the monoclinic space group C121, with one Nedd4-2 molecule bound to the 14-3-3 η Δ C dimer in the asymmetric unit. The structure was solved by molecular replacement with 14-3-3 η (PDB ID: 2C63) as a search model and refined to a resolution of 2.3 Å. Interpretable electron density was found for 21 residues, nine around the pSer³⁴² site and twelve around second pSer⁴⁴⁸ site (Leu³³⁸-Ala³⁴⁶ and Pro⁴⁴⁴-Ser⁴⁵⁵) (PDB ID code 7NMZ, Fig. 5e, Table 2). Although the structure revealed simultaneous binding to both phosphorylated motifs by a 14-3-3 η dimer, no electron density was found for the 97 residues between the phosphorylated motifs (Val³⁴⁷-Arg⁴⁴³), thus indicating that this region, including the WW2 domain, remains flexible when bound to 14-3-3 (Fig. 5e). The recognition of the phosphate group and contacts with the 14-3-3 ligand binding grooves are similar to those observed in the structures of the individual motifs (Fig. 5b, d). Other contacts were not detected in the crystal structures of short phosphopeptides, including the 14-3-3 residue Asn⁴³ from the α 3 helix of both protomers, which interacts with the main chain of the Nedd4-2 residues Ala³⁴⁶, Val⁴⁵², Thr⁴⁵³ and Ser⁴⁵⁵, and the polar contacts between the 14-3-3 residue Glu¹⁵ from the α 1 helix and the Nedd4-2 residues Thr⁴⁵³ and Ser⁴⁵⁵. A similar contacts have been previously observed in the structures of the Nth1:14-3-3 and caspase-2:14-3-3 complexes (PDB ID: 5N6N³² and 6SAD³³, respectively).

14-3-3 η interacts with the WW3 and HECT domains of Nedd4-2 and changes the relative positions of all Nedd4-2 domains. Nedd4-2¹⁸⁶⁻⁹⁷⁵ chemical crosslinking using the bifunctional agent disuccinimidyl glutarate (DSG) coupled to MS (XL-MS) with and without 14-3-3 η showed further 14-3-3 protein-mediated structural changes in Nedd4-2, highlighting 14 and 13 intramolecular distance constraints for Nedd4-2¹⁸⁶⁻⁹⁷⁵ in the free and complexed forms, respectively (Supplementary Table S1, S2, Fig. 6a, b). Many crosslinks were observed in both forms of Nedd4-2¹⁸⁶⁻⁹⁷⁵, for example, the crosslink between Lys⁵⁹⁸ from the HECT domain and Thr²⁷⁵ from the WW1-WW2 linker (#4 in Supplementary Table S1, #6 in Supplementary Table S2). In other words, when the complex is formed, the distance between these two regions remains unaltered (Fig. 6a, b). In contrast, crosslinks connecting the WW2 domain to the WW1-WW2 linker (Lys³⁹⁵-Thr²⁷⁵, #6 in Supplementary Table S1) and WW2 to the HECT domain (Lys³⁹⁸-Lys⁸²² and Lys³⁹⁸-Ser⁹³², #8 and 14 in Supplementary Table S1) were observed only in the free form of Nedd4-2¹⁸⁶⁻⁹⁷⁵. Conversely, crosslinks connecting the WW2-WW3 and WW3-WW4 linkers (Ser⁵³⁸-Ser⁴²⁸, #3 in Supplementary Table S2) and WW3 with the C-lobe of HECT (Lys⁵³¹-Lys⁹³⁵, #13 in Supplementary Table S2) were observed only in the complexed form of Nedd4-2¹⁸⁶⁻⁹⁷⁵. These findings confirm that the formation of this complex affects the position of the WW2 domain with respect to the HECT domain and other WW domains of Nedd4-2¹⁸⁶⁻⁹⁷⁵.

To quantify intramolecular Nedd4-2¹⁸⁶⁻⁹⁷⁵ crosslinks with and without 14-3-3 η , we crosslinked both Nedd4-2¹⁸⁶⁻⁹⁷⁵ alone and the Nedd4-2¹⁸⁶⁻⁹⁷⁵:14-3-3 η complex using ¹²C and ¹³C-labeled

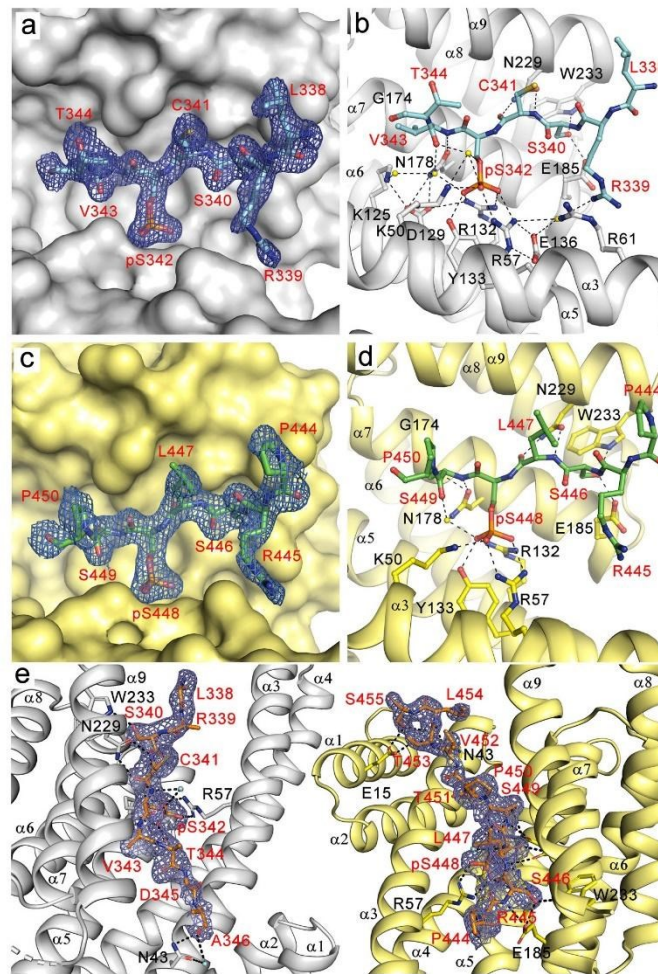


Fig. 5 Crystal structures of Nedd4-2 peptides containing the 14-3-3 binding motifs pSer342 and pSer448 bound to 14-3-3 γ and 14-3-3 η . **a** Detailed view of the crystal structure of the 14-3-3 γ Δ C:pep-S342 complex. The $2F_o - F_c$ electron density map is contoured at 1σ . **b** Polar contacts (black lines) between the residues of 14-3-3 γ (black) and the pSer³⁴² binding site of Nedd4-2 (red). Water molecules are shown as yellow spheres. **c** Detailed view of the crystal structure of the 14-3-3 γ Δ C:pep-S448 complex. The $2F_o - F_c$ electron density map is contoured at 1σ . **d** Polar contacts (black lines) between the residues of 14-3-3 γ (black) and the pSer⁴⁴⁸ binding site of Nedd4-2 (red). Water molecules are shown as yellow spheres. **e** Crystal structure of Nedd4-2³³⁵⁻⁴⁵⁵ containing two phosphorylation sites (pSer³⁴² and pSer⁴⁴⁸) bound to the 14-3-3 η Δ C dimer: Top view of the intervening linker sequence of the two 14-3-3-binding motifs of Nedd4-2 and of the polar contacts (black dashed lines). The final $2F_o - F_c$ electron density map is contoured at 0.8σ (blue mesh). Nedd4-2 residues are labeled in red, and 14-3-3 residues are labeled in black. Water molecules are shown as cyan spheres. Structure figures were generated using PYMOL.

disuccinimidyl adipate (DSA) in a 1:1 ratio (Supplementary Table S3, Fig. 6a, b – in green). Upon complex formation, only the abundances of crosslinks #1 and #3 significantly changed, indicating that Nedd4-2 residues Lys⁵³¹ from the WW3 domain and Lys⁶⁰⁷ from the HECT domain (#1 in Supplementary Table S3, Fig. 6b) are crosslinked mainly in the absence of 14-3-3 η . Conversely, the crosslink between the Nedd4-2 residues His¹⁸⁶, which precedes the WW1 domain, and Lys⁶³⁹ from the N-

terminus of the HECT domain (#3 in Supplementary Table S3, Fig. 6b) primarily formed in the presence of 14-3-3 η .

Crosslinking Nedd4-2¹⁸⁶⁻⁹⁷⁵:14-3-3 η mixtures (mixed in 1:2 stoichiometry) using disuccinimidyl suberate (DSS) and DSG yielded eight intermolecular crosslinks (Supplementary Table S4, Fig. 6c). Most of these crosslinks connect the α -helices that form the 14-3-3 η ligand binding groove (α 3, α 5 and α 9) with the WW3 domain and the HECT domain

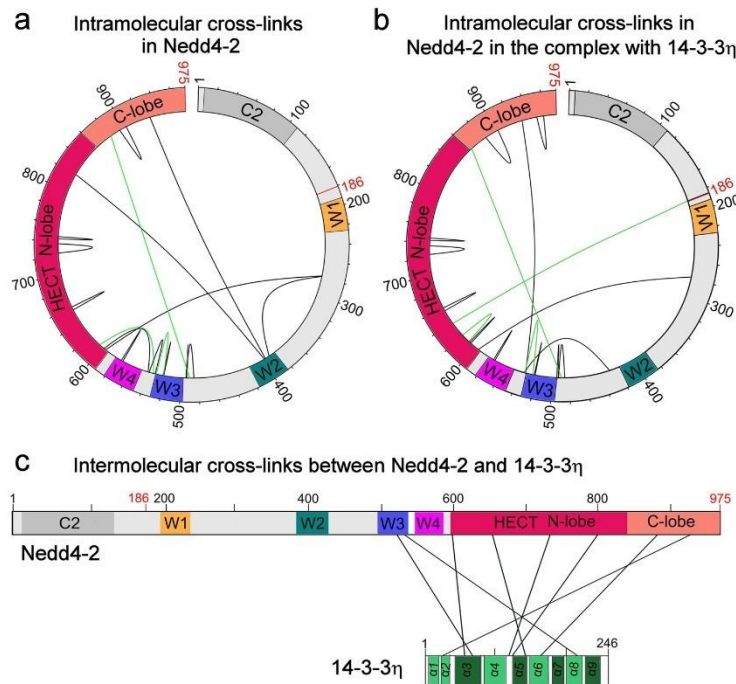


Fig. 6 Schematic representation of intra- and intermolecular crosslinks in Nedd4-2 and between Nedd4-2 and 14-3-3 η . **a** Schematic representation of intramolecular crosslinks of Nedd4-2¹⁸⁶⁻⁹⁷⁵ alone (black) with a 50-fold molar excess of DSG (Supplementary Table S1) and quantitative crosslinks with a 50-fold molar excess of 12 C and 13 C DSA in pale green (Supplementary Table S3). **b** Schematic representation of intramolecular crosslinks of Nedd4-2¹⁸⁶⁻⁹⁷⁵ in a complex with 14-3-3 η (black) with a 50-fold molar excess of DSG (Supplementary Table S2) and quantitative crosslinks with a 50-fold molar excess of 12 C and 13 C DSA in pale green (Supplementary Table S3). **c** Schematic representation of intermolecular crosslinks between Nedd4-2¹⁸⁶⁻⁹⁷⁵ and 14-3-3 η mixed at a 1:2 stoichiometry with a 50-fold molar excess of DSG or DSS (black) crosslinking agent (Supplementary Table S4). Nedd4-2¹⁸⁶⁻⁹⁷⁵ diagram: the C2 domain, not present in the Nedd4-2¹⁸⁶⁻⁹⁷⁵ construct, is shown in grey, the WW domains (denoted as W1-4) are shown in yellow, teal, blue and magenta, and the HECT domain N- and C-lobes are shown in raspberry and salmon, respectively. The beginning and the end of the Nedd4-2¹⁸⁶⁻⁹⁷⁵ construct are labeled in red. 14-3-3 η diagram: colored regions represent α -helices of the 14-3-3 molecule (shown in green), and the helices that form the ligand binding groove (α 3, α 5, α 7 and α 9) are colored in dark green. This figure was prepared using the xiVIEW (<https://xiview.org/>) and Inkscape (<http://www.inkscape.org/>) programs.

(crosslinks #1-3 and #5, 6), and the 14-3-3 η helices α 2 and α 6 with the HECT domain (crosslinks #4, 7 and 8). Most likely, these 14-3-3 η and Nedd4-2 regions directly interact with each other in the complex. The combined results from our crosslinking experiments demonstrate that 14-3-3 η interacts with the WW3 and HECT domains of Nedd4-2 and changes the relative positions of all Nedd4-2 domains.

14-3-3 η binding blocks interactions between WW domains and the HECT domain of Nedd4-2. To gain structural insights into the 14-3-3-mediated regulation of Nedd4-2, we tried to crystallize the Nedd4-2¹⁸⁶⁻⁹⁷⁵:14-3-3 η complex, but all our crystallization trials were unsuccessful. For this reason, we performed size-exclusion chromatography (SEC) coupled to small angle x-ray scattering (SAXS) analysis of Nedd4-2¹⁸⁶⁻⁹⁷, 14-3-3 η and the Nedd4-2¹⁸⁶⁻⁹⁷⁵:14-3-3 η complex.

Scattering data from two regions of the elution peak of Nedd4-2¹⁸⁶⁻⁹⁷⁵ alone were analyzed (Supplementary Fig. S4a). Based on our Guinier analysis, the data from the top of the peak of Nedd4-2¹⁸⁶⁻⁹⁷⁵ revealed the presence of aggregates, whereas the data from the right shoulder of the elution peak showed homogenous

particles with consistent R_g values of \sim 4.4 nm and an estimated M_w of \sim 101 kDa, in line with the theoretical M_w of Nedd4-2¹⁸⁶⁻⁹⁷⁵ (92 kDa; Supplementary Fig. S4b and Table 3). In turn, scattering data from the top of the elution peak of 14-3-3 η indicated homogenous particles with an estimated M_w of 56 kDa, matching the theoretical M_w of 14-3-3 η dimer (57 kDa) (Supplementary Fig. S4c, d and Table 3). The Nedd4-2¹⁸⁶⁻⁹⁷⁵:14-3-3 η complex was prepared with the 1:2 stoichiometry at a concentration 60 μ M, which is approximately three orders of the magnitude higher than the K_D value derived from SV-AUC (\sim 50 nM, Fig. 2). The complex eluted as a single peak and frames from two regions of the elution profile were analyzed (Supplementary Fig. S4e). As in Nedd4-2¹⁸⁶⁻⁹⁷⁵, the Guinier plot of the scattering data from the top of the elution peak indicated the presence of aggregates, but the scattering data from the right side of the peak showed a R_g of \sim 4.8 nm and a M_w of \sim 157 kDa, corroborating the theoretical M_w of the Nedd4-2¹⁸⁶⁻⁹⁷⁵:14-3-3 η complex with a 1:2 stoichiometry (149 kDa) (Supplementary Fig. S4f).

After calculating distance distribution functions $P(r)$, we found similar values of maximal distance within the particle (D_{max}) of

Table 3 Structural parameters determined from SEC-SAXS data.

Sample	R_g (nm) ^c	R_g (nm) ^d	D_{max} (nm)	V_p ^e (nm ³)	M_w ^f (kDa)	M_w ^g (kDa)
Nedd4-2 ¹⁸⁶⁻⁹⁷⁵ (1) ^a	4.67 ± 0.01	4.92 ± 0.01	18.3	218	125	92
Nedd4-2 ¹⁸⁶⁻⁹⁷⁵ (2) ^b	4.39 ± 0.02	4.54 ± 0.02	16.9	192	101	92
14-3-3 η	2.93 ± 0.01	2.94 ± 0.01	8.6	87	56	57
14-3-3 η :Nedd4-2 ¹⁸⁶⁻⁹⁷⁵ (1) ^a	4.95 ± 0.01	5.14 ± 0.01	18.1	277	170	149
14-3-3 η :Nedd4-2 ¹⁸⁶⁻⁹⁷⁵ (2) ^b	4.79 ± 0.01	4.92 ± 0.01	17.2	253	157	149

^aBased on frames from the top of the elution peak from SEC.
^bBased on frames from the right side of the elution peak from SEC.
^cCalculated using the Guinier approximation⁸².
^dCalculated using GNOM⁷³.
^eExcluded volume of the hydrated particle (Porod volume).
^fMolecular weight estimate based on a consensus Bayesian assessment method⁷⁶.
^gTheoretical molecular weights of proteins alone and the Nedd4-2¹⁸⁶⁻⁹⁷⁵:14-3-3 η complex (with 1:2 stoichiometry).

Nedd4-2¹⁸⁶⁻⁹⁷⁵ and its complex with 14-3-3 η (Fig. 7a and Table 3). Concurrently, the dimensionless Kratky plot of scattering data ($(sR_g)^2 I(s)/I_0$ versus sR_g) suggested their conformational flexibility, as indicated by the bell-shaped profiles of the complex and Nedd4-2¹⁸⁶⁻⁹⁷⁵ alone with maxima of 1.2 at $sR_g \sim 2.1$ and 1.4 at $sR_g \sim 2.2$, respectively (Fig. 7b, green and red trace) because the scattering data on a compact globular particle such as 14-3-3 η (Fig. 7b, blue trace) peaks at 1.104 at sR_g value of ~ 1.73 . Nevertheless, the complex exhibits a lower conformational flexibility than Nedd4-2¹⁸⁶⁻⁹⁷⁵ alone.

By combining rigid body modeling of SAXS profiles with distance constraints assessed by crosslinking coupled to MS (Supplementary Tables S1-S4), we calculated models of Nedd4-2¹⁸⁶⁻⁹⁷⁵ alone and in a complex with 14-3-3 η . The best-scoring CORAL model of Nedd4-2¹⁸⁶⁻⁹⁷⁵ alone fitted the experimental SAXS data with a χ^2 of 1.26 (Supplementary Fig. S5) and matched all intramolecular crosslinks (Supplementary Table S1 and S3). In this model, the WW2 and WW3 domains (in teal and blue, respectively) are positioned close to the HECT domain, WW2 is located between the N- and C-lobes and WW3 interacts with the C-lobe of the HECT domain (Fig. 7c). In turn, WW1 and WW4 are distant from the catalytic domain (Supplementary Fig. S5). This arrangement corroborates a previous report by Grimsey et al.³⁵. According to these authors, in the closed, autoinhibited form of Nedd4-2, the HECT domain interacts with the region preceding the WW3 domain.

The Nedd4-2¹⁸⁶⁻⁹⁷⁵:14-3-3 η complex was first modeled as a 14-3-3 η dimer attached to Nedd4-2 via pSer³⁴² and pSer⁴⁴⁸-containing motifs and assuming that the whole HECT domain is a rigid body. However, the models derived from these simulations did not fit well the experimental SAXS data and had χ^2 values of ~ 6.4 . Therefore, we subsequently allowed the N- and C-lobes of HECT to move freely with respect to each other. From these simulations, the best-scoring CORAL model (Supplementary Fig. S6) showed a considerably better agreement with the experimental SAXS data (χ^2 of 1.63), matching all intermolecular crosslinks (Supplementary Table S4), the intramolecular crosslinks of complexed Nedd4-2 (Supplementary Table S2 and S3) and the ab initio shape reconstruction (Supplementary Fig. S6b, S4f). The model of the complex suggests that the WW3 domain of Nedd4-2 (shown in blue) is positioned within the central channel of the 14-3-3 η dimer and interacts with the 14-3-3 η helices $\alpha 1$, $\alpha 3$ and $\alpha 9$ (Fig. 7d). The HECT domain is located outside the central channel of 14-3-3 η dimer, its C-lobe (shown in salmon) is close to the 14-3-3 η $\alpha 8$ - $\alpha 9$ loop, and the N-lobe (shown in raspberry) is positioned near the 14-3-3 η helices $\alpha 6$ and $\alpha 8$. Although the HECT domain interacts with one 14-3-3 η protomer, the WW4 and WW2 domains are located above the second 14-3-3 η protomer, far from the HECT domain (Supplementary Fig. S6a). Thus, by comparison with the model of Nedd4-2¹⁸⁶⁻⁹⁷⁵ alone,

14-3-3 η binding changed the relative positions of the structured domains of Nedd4-2, including the N- and C-lobes of HECT, where the C-lobe interacts with the helices $\alpha 6$, $\alpha 7$ and $\alpha 10$ of the N-lobe. Taken together, our SAXS and crosslinking data highlight that 14-3-3 binding induces a conformational rearrangement of Nedd4-2 by changing the relative positions and interactions of its structured domains, including the N- and C-lobes of the catalytic HECT domain, and by masking the surface of the WW3 domain.

Discussion

Nedd4-2 primarily ubiquitinates membrane-bound proteins, such as channels and receptors, and its dysfunction leads to multiple diseases, including epilepsy, hypertension, cystic fibrosis, pulmonary edema or Liddle syndrome³⁶⁻⁴⁰. Previous studies have shown that Nedd4-2 phosphorylation triggers binding to the adaptor protein 14-3-3 and that this interaction may have different functional consequences depending on the tissue. In the brain, for example, this interaction promotes the ubiquitination of the GluA1 subunit of the AMPA receptor³⁶. In contrast, in the kidney, Nedd4-2 binding to 14-3-3 weakens ENaC ubiquitination, thereby increasing sodium absorption by elevating the surface expression of ENaC²². However, key structural aspects of the 14-3-3-mediated regulation of Nedd4-2 have remained unclear until now. Thus, our study provides detailed structural insights into the interaction between 14-3-3 protein and Nedd4-2 by combining several structural biology approaches.

The interaction between the 14-3-3 protein and Nedd4-2 is mediated by phosphorylation of three residues bordering WW2 domain: pSer³⁴², pThr³⁶⁷ and pSer⁴⁴⁸ (Fig. 1)^{17,23}. Because 14-3-3 protein dimers frequently interact with their binding partners by simultaneously anchoring two phosphorylated motifs separated by at least 20 amino acid residues⁴¹, we hypothesized that the interaction between 14-3-3 and Nedd4-2 is also mediated by such bidentate binding. Our LC-MS analysis confirmed that Nedd4-2 is phosphorylated by PKA in vitro on all three aforementioned sites. Mutating all three residues abolished Nedd4-2 binding to the 14-3-3 protein, whereas simultaneous phosphorylation of the Ser³⁴² and Ser⁴⁴⁸ sites led to the highest affinity binding of Nedd4-2 to the 14-3-3 η dimer, in the nanomolar range ($K_D < 30$ nM) (Fig. 3, S3). The binding affinity decreased upon single phosphorylation of Ser⁴⁴⁸ or other double phosphorylation combinations involving Ser⁴⁴⁸. Our fluorescence polarization measurements also highlighted the importance of the Ser⁴⁴⁸-containing motif for high-affinity Nedd4-2 binding to 14-3-3 η . Concurrently, our crystallographic analysis of the phosphorylated Nedd4-2³³⁵⁻⁴⁵⁵ bound to 14-3-3 η confirmed the bidentate interaction with the 14-3-3 dimer through both 14-3-3 binding motifs, pSer³⁴² and pSer⁴⁴⁸, also showing that the complex establishes more contacts than the structures of the isolated singly phosphorylated motifs (Fig. 5). These findings support the

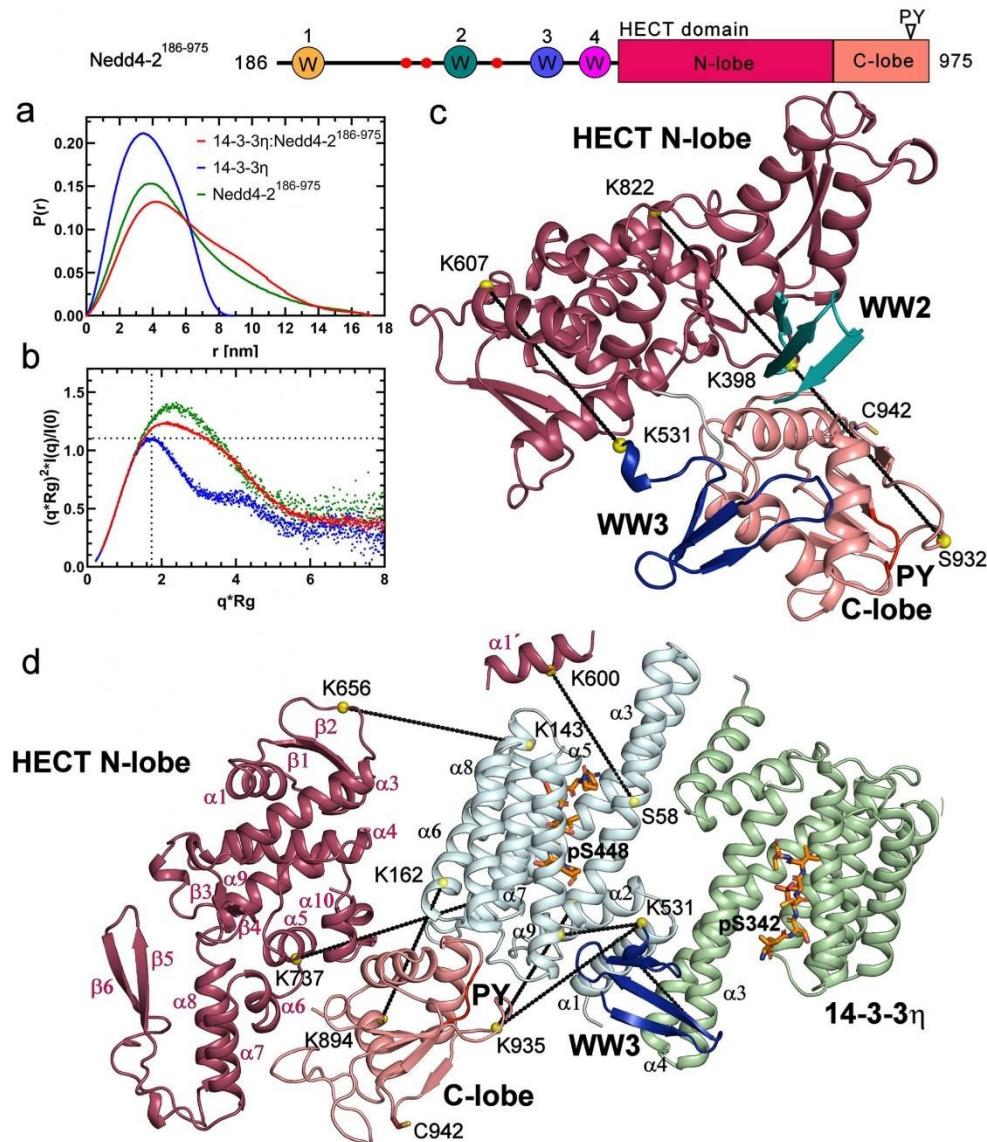


Fig. 7 SAXS-based structural modeling of the pNedd4-2¹⁸⁶⁻⁹⁷⁵;14-3-3 η complex and pNedd4-2¹⁸⁶⁻⁹⁷⁵. **a** Plot of the distance distribution functions $P(r)$, with maximum particle dimensions (D_{max}) of 169, 89 and 172 Å for Nedd4-2¹⁸⁶⁻⁹⁷⁵, 14-3-3 η and the 14-3-3 η :pNedd4-2¹⁸⁶⁻⁹⁷⁵ complex, respectively. **b** Dimensionless Kratky plots are shown in green for Nedd4-2¹⁸⁶⁻⁹⁷⁵, in blue for 14-3-3 η , and in red for the 14-3-3 η :pNedd4-2¹⁸⁶⁻⁹⁷⁵ complex. The dotted lines mark the value of 1.104 for $sR_g = 1.73$, denoting the peak of a perfectly globular particle. **c** Crosslinked domains from the best-scoring CORAL model of Nedd4-2¹⁸⁶⁻⁹⁷⁵. The full model is shown in Supplementary Fig. S5. **d** Crosslinked domains from the best-scoring CORAL model of the Nedd4-2¹⁸⁶⁻⁹⁷⁵;14-3-3 η complex. The full model is shown in Supplementary Fig. S6. The 14-3-3 η protomers are shown in pale green and pale cyan. In the HECT domain of Nedd4-2¹⁸⁶⁻⁹⁷⁵, the N-lobe is indicated in raspberry and the C-lobe in salmon. WW1, WW2, WW3 and WW4 domains are indicated in yellow, teal, blue and magenta, respectively. Phosphorylated 14-3-3 binding motifs of Nedd4-2 are shown as orange sticks (PDB ID: 6ZBT and 6ZC9, this work). α atoms of crosslinked residues are shown as yellow spheres. The PY motif (L⁹⁴⁸PPY⁹⁵¹) is shown in red, and the catalytic residue Cys⁹⁴² is shown as a stick. The elements in the HECT N-lobe secondary structure are numbered according to⁸¹.

assumptions that the key residue for 14-3-3 protein binding is Ser⁴⁴⁸, phosphorylated by either SGK or PKA, and that the interaction between Nedd4-2 and 14-3-3 η depends on a Pro residue located at position +2 from pSer⁴⁴⁸^{17,20,22}. Although pSer⁴⁴⁸ alone promotes Nedd4-2 binding to 14-3-3, our data clearly show that the most stable interaction involves simultaneous binding of two phosphorylated motifs. In line with our results, decreased phosphorylation of Nedd4-2 at Ser³⁴² has been recently shown to promote its association with ribosomal proteins during endoplasmic reticulum stress⁴², but whether this process also involves changes in the interaction between Nedd4-2 and 14-3-3 is still unknown. Nevertheless, our structural analysis of this interaction did show that 14-3-3 changes the relative positions of all Nedd4-2 domains.

14-3-3 proteins are well known to regulate their binding partners by modulating their structure and/or masking structural and functional features on their surface. The conformational change upon the 14-3-3 protein binding was demonstrated for the serotonin N-acetyltransferase (AANAT), an enzyme that controls the daily rhythm in melatonin synthesis. The 14-3-3 binding modulates structure of the substrate binding sites of AANAT, thereby increasing the affinity of AANAT for its substrates with an accompanying increase in activity^{43,44}. In our previous work on 14-3-3-mediated regulation of the neutral trehalase Nth1, we demonstrated that 14-3-3 protein triggers its enzyme activity by stabilizing the interaction between its catalytic and regulatory domains³². Another example of 14-3-3-induced structural changes upon binding is the negative regulation of B-RAF kinase, which 14-3-3 protein maintains in an inactive state by blocking the membrane recruitment of B-RAF and by preventing B-RAF kinase dimerization through steric occlusion of its domains^{45,46}. Our results suggest that the 14-3-3-mediated regulation of Nedd4-2 requires simultaneous binding of two phosphorylated motifs followed by both the conformational change and steric occlusion of several functional domains, thus resembling regulations mentioned above. The CORAL model of Nedd4-2¹⁸⁶⁻⁹⁷⁵ alone indicated close interactions between the HECT and WW2/3 domains and full exposure of the WW1 and WW4 domains to the solvent (Fig. 7c and S5). This arrangement of domains corroborates previous evidence of the interaction between WW domains of Nedd4-2 and its own weak PY motif located within the C-lobe of HECT (Fig. 7c)^{13,47}. On the other hand, 14-3-3 binding blocked interactions between HECT and WW2/3 by sequestering WW3 within the central channel of the 14-3-3 dimer and by weakening the interaction between the N- and C-lobes of the HECT domain (Fig. 7d and S6a). Furthermore, in a complex with 14-3-3, the WW4 domain of Nedd4-2 is located near the surface of the 14-3-3 η dimer, whereas WW1 and WW2 are fully exposed to the solvent (Supplementary Fig. S6a). Such position of WW2, far from the surface of the 14-3-3 η dimer, may also explain why we were unable to trace this domain in the electron density map of Nedd4-2³³⁵⁻⁴⁵⁵ bound to 14-3-3 η (Fig. 5e). Because WW domains presumably mediate the interaction between Nedd4-2 and its substrates, such occlusions or exposures likely affect substrate ubiquitination, accounting for the 14-3-3-mediated modulation of the ubiquitination of some Nedd4-2 substrates^{36,48-50}. Considering the above, our data provide the structural glimpse into 14-3-3-mediated Nedd4-2 regulation, showing that 14-3-3 protein regulates multidomain binding partners through several common mechanisms, either promoting or blocking interdomain interactions and sterically occluding functional surfaces, among other alterations.

In conclusion, Nedd4-2 is phosphorylated on multiple sites by PKA, but dual phosphorylation on the sites Ser³⁴² and Ser⁴⁴⁸ mediates high-affinity Nedd4-2 bonding to 14-3-3 η . Upon binding, 14-3-3 η induces a structural rearrangement of Nedd4-2

by altering interactions between the structured domains of Nedd4-2, including the N- and C-lobes of the catalytic HECT domain. Changes in the exposure of WW domains may explain how 14-3-3 modulates the ubiquitination of some Nedd4-2 substrates. For this reason, further studies should be conducted to identify the exact mechanisms of 14-3-3-dependent regulation of ubiquitination of particular substrates and to assess whether these mechanisms include variations in Nedd4-2 phosphorylation and whether the suggested conformational change of the HECT domain has any functional consequences. For now, our findings lay the foundations for future research aimed at understanding the versatile regulatory roles of 14-3-3 proteins in the regulation of signaling pathways and processes linked to protein degradation through the ubiquitin-proteasome system. Such studies are particularly relevant because many other E3 ubiquitin protein ligases, e.g., parkin, ZNRF2, CBL, ITCH and SMURF1, are also regulated in a 14-3-3-dependent manner⁵¹⁻⁵⁶. Moreover, recent advances in the development of small molecule compounds targeting protein-protein interactions have demonstrated the potential to modulate the activity of key 14-3-3 binding partners in various physiological processes by targeting their distinct interactions with 14-3-3⁵⁷. In this context, the interaction between Nedd4-2 and 14-3-3 proteins should be a promising target for the treatment of Nedd4-2-associated diseases.

Methods

Heterologous expression and purification of 14-3-3 protein isoforms. All seven 14-3-3 protein isoforms (β , γ , ϵ , ζ , η , σ and τ) and the C-terminally truncated 14-3-3 γ isoform (14-3-3 γ AC, residues 1-235) were expressed in *E. coli* BL21(DE3) cells (Novagen) using a modified pET-15b plasmid with a TEV cleavage site. After affinity chromatography, the His₆-tag was cleaved by TEV protease, followed by anion-exchange chromatography (HiTrap Q column; GE Healthcare)^{43,58}. The final purification step was size-exclusion chromatography (HiLoad Superdex 75; GE Healthcare) in a buffer containing 20 mM Tris-HCl (pH 7.5), 150 mM NaCl, 5 mM DTT and 10% (w/v) glycerol. All isoforms were concentrated to 30 mg.ml⁻¹, frozen in liquid nitrogen and stored in aliquots in -80 °C (193.15 K).

Heterologous expression, purification and phosphorylation of Nedd4-2.

Nedd4-2 coding sequences (residues 335-455 and 186-975) were PCR-amplified from the plasmid hNedd4-2 (a gift from Christie Thomas, Addgene plasmid # 83433)⁵⁹. The PCR product containing residues 335-455 was ligated into the pRSFDuet-1 (Novagen) using the *NcoI/NofI* restriction sites. Modified pRSFDuet-1 contained the sequence of the His₆-tagged GB1 domain of protein G inserted into the first multiple cloning site (a gift from Evzen Boura, IOCB CAS). The PCR product, including residues 186-975, was subcloned into the expression vector pST39 (a gift from Evzen Boura, IOCB CAS) using the *XbaI/KpnI* restriction sites. The entire cloned regions were confirmed by sequencing. Mutations of Nedd4-2 with a different number of PKA phosphorylation sites (at positions 342, 367 and 448) were generated by mutating other sites to alanine, using the QuikChangeTM approach (Stratagene), and confirmed by sequencing. Oligo sequences are provided in Supplementary Table S5.

Nedd4-2 fusion proteins were expressed as fusion proteins with an N-terminal His₆-GB1-tagged fusion protein (Nedd4-2³³⁵⁻⁴⁵⁵ variant) or a non-cleavable 6 × His-tag at the C-terminus (Nedd4-2¹⁸⁶⁻⁹⁷⁵ variant) in *Escherichia coli* BL21 (DE3) (Novagen) cells grown in Luria-Bertani media, inducing expression by adding 0.5 mM IPTG (isopropyl β -D-1-thiogalactopyranoside) at OD⁶⁰⁰ = 0.8 for 20 h at 18 °C. The pelleted cells were suspended in lysis buffer (1 × PBS, 1 M NaCl, 4 mM β -mercaptoethanol and 2 mM imidazole) and purified using a Chelating Sepharose[®] Fast Flow column (GE Healthcare), according to the standard protocol. For Nedd4-2¹⁸⁶⁻⁹⁷⁵, Tergitol NP-40 (Sigma) was added to all buffers at a final concentration of 0.01% (v/v).

The eluted Nedd4-2³³⁵⁻⁴⁵⁵ protein and its variants were dialyzed against the buffer containing 20 mM Tris-HCl (pH 7.5), 2 mM EDTA, 2 mM 2-mercaptoethanol and 10% (w/v) glycerol. The His₆-GB1 tag was cleaved by incubation with the TEV protease (750 U of TEV per 1 mg of fusion protein) in dialysis overnight at 4 °C. Nedd4-2³³⁵⁻⁴⁵⁵ was phosphorylated by incubation at 30 °C for 2 h and then overnight at 4 °C with 1300 U of PKA (Promega) per 1 mg of protein in the presence of 0.75 mM ATP and 20 mM MgCl₂. TEV and PKA were removed through another immobilized metal affinity chromatography and subsequent size-exclusion chromatography using a HiLoad[™] 26/600 Superdex[™] 75 pg column (GE Healthcare) in a buffer containing 20 mM Tris-HCl (pH 7.5), 150 mM NaCl, 1 mM TCEP and 10% (w/v) glycerol. The typical yield was 5 mg of pure protein per one liter of LB media.

The eluted Nedd4-2¹⁸⁶⁻⁹⁷⁵ was purified by size-exclusion chromatography directly after Ni²⁺ affinity chromatography, using a HiLoad[™] 26/600 Superdex[™]

200 µg column (GE Healthcare) in a buffer containing 50 mM Tris-HCl (pH 8.0), 500 mM NaCl, 1 mM TCEP and 10% (w/v) glycerol and 0.01% (v/v) NP-40. Purified Nedd4-2¹⁸⁶⁻⁹⁷⁵ was phosphorylated with 250 U of PKA (Promega) per mg of protein in the presence of 0.75 mM ATP and 20 mM MgCl₂ and incubated at 30 °C for 3 h followed by size-exclusion chromatography using a Superdex™ 200 Increase 10/300 GL column (GE Healthcare) in a buffer containing 50 mM Tris-HCl (pH 8.0), 500 mM NaCl, 1 mM TCEP and 10% (w/v) glycerol. The typical yield was 2 mg of pure protein per one liter of LB media.

The level of the phosphorylation of both proteins was confirmed by the mass spectrometry service provided by CMS Biocore.

Heterologous expression and purification of Uba1, Ube2d2 and Ub. The coding sequences of mouse Uba1 (ubiquitin-like modifier-activating enzyme 1), mouse Ube2d2 (ubiquitin-conjugating enzyme E2D2) and human Ub were kindly provided by Dr. Silhan (IOCB, CAS). Both enzymes and human ubiquitin were expressed in *Escherichia coli* BL21 (DE3) cells (Novagen). The E1 enzyme Uba1 was subcloned into a pET28a plasmid with a TEV-cleavable 6 × His-tag at the N-terminus and expressed at 16 °C O/N. The E2 enzyme Ube2d2 and human ubiquitin Ub were subcloned into a pET15b plasmid with a TEV-cleavable 6 × His-tag at the N-terminus and expressed at 25 °C O/N. All these fusion proteins were expressed in Luria-Bertani media by induction at OD⁶⁰⁰ = 0.8 for 20 h. The pelleted cells were suspended in lysis buffer (1 × PBS, 1 M NaCl, 4 mM β-mercaptoethanol and 2 mM imidazole) and purified using a Chelating Sepharose™ Fast Flow column (GE Healthcare) according to the standard protocol. The fusion proteins were dialyzed into a buffer containing 20 mM Tris-HCl (pH 7.5), 150 mM NaCl, 2 mM DTT and 10% (w/v) glycerol. The His₆-tag of Uba1 and Ube2d2 were cleaved by incubation with TEV protease at 30 °C for 2 h. The final purity of all proteins was confirmed by size-exclusion chromatography on Superdex™ 200 Increase 10/300 GL (GE Healthcare) or Superdex™ 75 Increase 10/300 GL (GE Healthcare) columns in a buffer containing 20 mM Tris-HCl (pH 7.5), 150 mM NaCl, 2 mM DTT and 10% (w/v) glycerol. The proteins were concentrated as required, aliquoted and flash-frozen in liquid nitrogen.

Ubiquitination assay. For in vitro ubiquitination assays, 5 µg of human Ub, 50 ng of E1 (mouse Uba1), 200 ng of E2 (mouse Ube2d2) and 500 ng of E3 (phosphorylated Nedd4-2¹⁸⁶⁻⁹⁷⁵) were incubated in 30 µl of the reaction mixture in a buffer containing 50 mM Tris pH 7.5, 2 mM ATP, 5 mM MgCl₂ and 2 mM DTT and incubated for 5, 10 and 15 min at 30 °C. The reactions were stopped by adding 5 × SDS-PAGE loading buffer (250 mM Tris pH 6.8, 50% glycerol, 500 mM DTT and 10% SDS) and incubating at 95 °C for 3 minutes to denature the samples. For reactions with 14-3-3η, Nedd4-2¹⁸⁶⁻⁹⁷⁵ was mixed with 14-3-3η in a 1:2 molar ratio and incubated for 30 minutes on ice before starting the reaction. In addition, 20 µl of reaction was separated by conventional SDS-PAGE on a 10% acrylamide gel and electro-blotted against a PVDF membrane in 20 mM Tris pH 7.5, 154 mM glycine and 10% methanol buffer overnight at 4 °C. Rabbit anti-Ub polyclonal antibody (Enzo) and anti-rabbit IgG, HRP-linked Antibody (Cell Signaling Technology) were used to visualize the transferred polyubiquitin chains. Chemiluminescence was induced by ECL and detected using Fusion Solo S (Vilber). The detected bands of E3-Ub were quantitated using the Image Lab software (Bio-Rad).

Fluorescence polarization assay. The FP assay was performed using a CLAR-Iostar microplate reader (BMG Labtech, Thermo Fisher Scientific, Waltham, MA, USA) on 384-well black low-volume flat-bottom plates (Corning, New York, USA) in a buffer containing 10 mM HEPES (pH 7.4), 150 mM NaCl, 0.1% (v/v) Tween 20 and 0.1% (w/v) BSA. Seven 14-3-3 protein isoforms at a starting concentration of 80 µM, followed by binary dilution series, were incubated for 1 h with 50 nM of FITC-labelled synthetic peptides FITC-PRSLpSSPTVT (pS342), FITC-ARSpTVTGGE (pT367) and FITC-LRScpSVTDVAV (pS448) where pS/pT denotes phosphoserine/phosphothreonine (Pepscan Presto BV). The excitation and emission wavelengths were 482 nm and 530 nm, respectively. The K_D values were determined as the mean of three independent measurements using GraphPad Prism version 8.0.1 for Windows, GraphPad Software, La Jolla California USA, www.graphpad.com.

Crystallization, data collection and structure determination. To crystallize the complex between 14-3-3γΔC (residues 1-234) and the synthetic peptides pep-S342 or pep-S342, 16 mg.mL⁻¹ 14-3-3γΔC was mixed with the Nedd4-2 synthetic peptides pep-S342 (LRScpSVTDVAV) or pep-S342 (PRSLpSSPTVT) at a 1:1.5 molar stoichiometry, in a buffer containing 20 mM HEPES (pH 7.0), 2 mM MgCl₂ and 2 mM TCEP. Crystals were grown from drops consisting of either 2 µl of the pep-S342:14-3-3γΔC complex and 2 µl of 100 mM HEPES (pH 7.5), 200 mM MgCl₂, 23% (v/v) PEG 400, and 2% hexafluoro-2-propanol or 2 µl of the pep-S448:14-3-3γΔC complex and 2 µl of 100 mM HEPES (pH 7.5), 200 mM MgCl₂, 16% (v/v) PEG 400, and 1% hexafluoro-2-propanol, respectively. Crystals were cryoprotected using 30% (v/v) PEG 400 and flash frozen in liquid nitrogen before data collection in oscillation mode at beamline 14.1 of the BESSY synchrotron.

To crystallize Nedd4-2³³⁵⁻⁴⁵⁵ in a complex with 14-3-3ηΔC, the mutant variant T367A was used to prevent sample heterogeneity. The 14-3-3ηΔC:Nedd4-2³³⁵⁻⁴⁵⁵T367A complex was mixed in a 1:2 molar stoichiometry and dialyzed overnight against 20 mM

Tris-HCl pH 7.5 and 1 mM TCEP buffer. The protein complex was concentrated to ~11 mg.mL⁻¹. Crystals were grown from drops consisting of 4 µl of the protein complex, 2 µl of Morphue C12 condition (composed of 0.03 M Sodium nitrate, 0.03 M Sodium phosphate dibasic, 0.03 M Ammonium sulfate, 0.1 M Bicine, 12.5% v/v MPD, 12.5% PEG 1000, 12.5% w/v PEG 3350) pH 7.5 and 0.6 µl of 30% w/v sucrose (Hampton Research Additive Screen). Crystals were flash frozen in liquid nitrogen without any additional cryoprotection before data collection in oscillation mode at the D8 Venture system (Bruker, MA, USA).

Diffraction datasets were processed using the packages XDS and XDSAPP^{60,61}. Crystal structures were solved by molecular replacement in MOLREP⁶², using the structures of the 14-3-3η (PDB ID: 2C63), 14-3-3γΔC:pepS139 (PDB ID: 6GKF) as search models and refined at a resolution of 1.8 Å (14-3-3γΔC:pepS342), 1.9 Å (14-3-3ηΔC 14-3-3γΔC:pep-S448) and 2.3 Å (14-3-3ηΔC:Nedd4-2³³⁵⁻⁴⁵⁵T367A), respectively, with the PHENIX package^{34,63}. The atomic coordinates and the structure factors of the complexes have been deposited in the RCSB PDB under accession codes GZBT, 6ZC9 and 7NMZ. All structural figures were prepared with PyMOL (<https://pymol.org/2/>).

Analytical ultracentrifugation (AUC) measurements. Sedimentation velocity (SV) experiments were performed using a ProteomLab™ XL-1, Beckman Coulter analytical ultracentrifuge⁶⁴. The samples were dialyzed against a buffer containing 20 mM Tris-HCl (pH 7.5), 150 mM NaCl, and 1 mM TCEP before analysis. The samples with the longer construct of Nedd4-2¹⁸⁶⁻⁹⁷⁵ were dialyzed against a buffer containing 50 mM Tris-HCl (pH 8.0), 500 mM NaCl, 1 mM TCEP and 0.01% (v/v) Tergitol NP-40 (Sigma). SV AUC experiments were conducted at various loading concentrations of 14-3-3η, Nedd4-2¹⁸⁶⁻⁹⁷⁵, Nedd4-2³³⁵⁻⁴⁵⁵ and its mutant variants in charcoal-filled Epon centerpieces with a 12-mm optical path length at 20 °C, and at 4000 or 46000 rpm rotor speed (An-50 Ti rotor, Beckman Coulter). The buffer density, viscosity, and partial specific volume of all proteins were estimated using the program SEDNTERP. All sedimentation profiles were collected with absorbance optics at 280 nm. The sedimentation coefficients *c*(*s*) distributions were calculated from raw data using the SEDFIT software package⁶⁵. The calculated distributions were integrated to establish the weight-average sedimentation coefficients corrected to 20 °C and the density of water, $s_{w(20, \rho)}$. The s_w values were plotted as a function of Nedd4-2³³⁵⁻⁴⁵⁵ or 14-3-3η concentration to construct s_w isotherms. The resulting isotherms were fitted with a A + B = AB model, as implemented in the SEDPHAT software package with previously known s_w values of each component. The parameters were verified, and the loading concentrations were corrected using global Lamm-equation modeling, also implemented in the SEDPHAT software⁶⁶.

Chemical Crosslinking combined with mass spectrometry. Both Nedd4-2¹⁸⁶⁻⁹⁷⁵ alone and in a complex with 14-3-3η were crosslinked with homobifunctional crosslinkers DSG and DSS in 1:1 (mol/mol) mixtures of non-deuterated and four-times-deuterated compounds (d0/d4). For the crosslinking reaction, the proteins were dialyzed in a buffer containing 20 mM HEPES (pH 7.5), 150 mM NaCl and 1 mM TCEP. In all samples, the protein concentration was 0.6 mg.mL⁻¹. Freshly prepared stock solutions of crosslinkers (10 mg.mL⁻¹ in DMSO) were added to proteins at a 50 × molar excess in a total reaction volume of 20 µl and incubated for 1 h at room temperature.

For quantitative studies, Nedd4-2¹⁸⁶⁻⁹⁷⁵ in the presence of 14-3-3η and Nedd4-2¹⁸⁶⁻⁹⁷⁵ alone were incubated with a 50-fold molar excess of light (12 C) and heavy (13 C) disuccinimidyl adipate (DSA; Creative Molecules). After a 30-min incubation at room temperature, Nedd4-2¹⁸⁶⁻⁹⁷⁵ in the presence of 14-3-3η labelled with 13 C and Nedd4-2¹⁸⁶⁻⁹⁷⁵ alone labelled with 12 C were mixed at a 1:1 ratio.

The proteins were reduced with 10 mM dithiothreitol, alkylated with 30 mM iodoacetamide, and digested overnight with trypsin at 37 °C. The peptides were injected into a Luna Omega 5µm Polar C18 100 Å 20 × 0.3 mm column (Phenomenex) and desalted at 20 µL/min for 5 min. Peptides were then separated by reversed-phase chromatography with a Luna Omega 3µm Polar C18 100 Å 150 × 0.3 mm column (Phenomenex) at 10 µL/min using a capillary UHPLC 1290 system (Agilent Technologies) with a gradient sequence of 1–10% for 1 min, 10–45% for 19 min, and 45–95% for 5 min of buffer solvent A (0.1% formic acid, 98% acetonitrile in water) in buffer solvent B (0.1% formic acid, 2% acetonitrile in water). The column was heated to 50 °C and directly connected to a 15 T solarix XR FT-ICR mass spectrometer (Bruker Daltonics, USA) operated in positive data dependent mode. StavroX software⁶⁷ was used to identify crosslinked peptides. Fixed carbamidomethylation of cysteines and variable methionine oxidation were set as modifications. The modification sites of DSG and DSS were N-termini, lysines, serines, threonines and tyrosines. The mass error threshold was set to 1 ppm, and all assigned fragments were manually curated. For quantitative studies, the Links software^{68,69} was used to identify crosslinked peptides. The nonoverlapping isotopes of peptides crosslinked with 12 C and 13 C DSA were used to calculate isotope ratios⁷⁰.

Small-angle X-ray scattering (SAXS). SAXS data were collected on the European Molecular Biology Laboratory (EMBL) P12 beamline, at the storage ring PETRA III (Deutsches Elektronen Synchrotron (DESY), Hamburg, Germany). The SEC-SAXS

measurements were conducted in a buffer containing 20 mM Tris-HCl (pH 7.5), 150 mM NaCl, 1 mM TCEP, 3% (w/v) glycerol using Superdex 200 Increase 5/150 GL column (GE Healthcare) at the flow rate 0.5 mL·min⁻¹ at 293.15 K.

The loading concentrations of the samples were 2.2 mg·mL⁻¹ for Nedd4-2¹⁸⁶⁻⁹⁷⁵, 2 mg·mL⁻¹ for 14-3-3 η and 8.9 mg·mL⁻¹ for the Nedd4-2¹⁸⁶⁻⁹⁷⁵:14-3-3 η complex (1:2 molar stoichiometry). The injection volume of the samples was 52 μ L. Elution profiles with the corresponding frames were processed using ATSAS 3.0.2 software CHROMIXS⁷¹. ATSAS software PRIMUS and GNOM were used to determine the excluded volume of the hydrated particle (V_p), the radius of gyration (R_g) and maximum particle dimension (D_{max})^{72,73}. The molecular mass (M_w) was determined using a methods described by Rambo et al.⁷⁴. Scattering profiles, $P(r)$ functions, normalized Kratky plots and Guinier approximations were visualized using GraphPad Prism version 8.0.1 for Windows (GraphPad Software, La Jolla California USA, www.graphpad.com). The program DAMMIF was used to calculate the *ab initio* molecular envelopes⁷⁵. For the complex, 10 surfaces were generated in slow mode and averaged using DAMAVER⁷⁶. The averaged surfaces were used as the final filtered model of the complex, which was superimposed to the structural model using the SUPCOMB program (EMBL, Hamburg, Germany)⁷⁷.

Structural modeling. The three-dimensional models of Nedd4-2¹⁸⁶⁻⁹⁷⁵ and the Nedd4-2¹⁸⁶⁻⁹⁷⁵:14-3-3 η complex were generated using CORAL. SAXS data and distance constraints derived from intramolecular crosslinks of Nedd alone (for model of Nedd4-2¹⁸⁶⁻⁹⁷⁵ alone), intermolecular crosslinks between 14-3-3 η and the Nedd4-2¹⁸⁶⁻⁹⁷⁵ and intramolecular crosslinks of the complexed Nedd4-2¹⁸⁶⁻⁹⁷⁵ (for model of the Nedd4-2¹⁸⁶⁻⁹⁷⁵:14-3-3 η complex) were used⁷⁸. The starting model of the complex was prepared using the crystal structures of 14-3-3 η (PDB ID: 2C63)⁷⁹ and 14-3-3 γ with the Nedd4-2 phosphopeptides pep-S342 and pep-S448 (PDB ID: 6ZBT and 6ZC9), as well as known solution structures of the WW1-3 (PDB ID: 1WR3, 1WR4, 1WR7) and HECT (PDB ID: 5HPK) domains⁸⁰. The unknown structure of the WW4 domain was generated using the SWISS-MODEL server (<https://swissmodel.expasy.org/>). Using the CORAL program, disordered loops missing in the crystal structures were modelled as interconnected dummy residue chains attached to the appropriate Ca atoms in rigid domains, but the linker length was limited to 5–100 residues. For this reason, the part of the Nedd4-2 region connecting the WW1 domain to the pSer³⁴² motif (residues Ser²³³, Phe²⁴⁹) was modeled as the α -helix based on secondary structure prediction by PSIPRED ([psipred@cs.ucl.ac.uk](http://psipred.cs.ucl.ac.uk/)). The best-scoring CORAL model was chosen according to the lowest χ^2 , and the distances were derived from intra- and intermolecular crosslinks.

Statistics and reproducibility. Results from the FP assay (Fig. 4) and immunoblot (Supplementary Fig. S1) are represented as means \pm SD from three replicates as indicated in the figure legend. Statistical analysis for the data from immunoblot were performed using Graph-Pad Prism 8.4. Student's *t*-test was used for comparison of relative changes of samples with and without 14-3-3 η at selected timepoints (ns, non-significant $P > 0.05$; *, $P < 0.05$).

Reporting summary. Further information on research design is available in the Nature Research Reporting Summary linked to this article.

Data availability

The authors declare that all data supporting the findings of this study are available within the article and its supplementary information file. Crystallography data have been deposited in the RCSB PDB with the accession codes: 6ZBT, 6ZC9 and 7NMZ. All source data underlying the graphs presented in the main and supplementary figures are made available in Supplementary Data 1.

Received: 21 April 2021; Accepted: 5 July 2021;

Published online: 22 July 2021

References

- Kumar, S. et al. cDNA cloning, expression analysis, and mapping of the mouse Nedd4 gene. *Genomics* **40**, 435–443 (1997).
- Kumar, S., Tomooka, Y. & Noda, M. Identification of a set of genes with developmentally down-regulated expression in the mouse brain. *Biochem Biophys. Res. Commun.* **185**, 1155–1161 (1992).
- Hansson, J. H. et al. Hypertension caused by a truncated epithelial sodium channel gamma subunit: genetic heterogeneity of Liddle syndrome. *Nat. Genet.* **11**, 76–82 (1995).
- Schild, L. et al. Identification of a PY motif in the epithelial Na channel subunits as a target sequence for mutations causing channel activation found in Liddle syndrome. *EMBO J.* **15**, 2381–2387 (1996).
- Goel, P., Manning, J. A. & Kumar, S. NEDD4-2 (NEDD4L): the ubiquitin ligase for multiple membrane proteins. *Gene* **557**, 1–10 (2015).
- Manning, J. A. & Kumar, S. Physiological functions of Nedd4-2: lessons from knockout mouse models. *Trends Biochem. Sci.* **43**, 635–647 (2018).
- Huang, X. & Dixit, V. M. Drugging the undruggables: exploring the ubiquitin system for drug development. *Cell Res.* **26**, 484–498 (2016).
- Harvey, K. F. & Kumar, S. Nedd4-like proteins: an emerging family of ubiquitin-protein ligases implicated in diverse cellular functions. *Trends Cell Biol.* **9**, 166–169 (1999).
- Andre, B. & Springael, J. Y. WWP, a new amino acid motif present in single or multiple copies in various proteins including dystrophin and the SH3-binding Yes-associated protein YAP65. *Biochem Biophys. Res Commun.* **205**, 1201–1205 (1994).
- Sudol, M. Structure and function of the WW domain. *Prog. Biophys. Mol. Biol.* **65**, 113–132 (1996).
- Rotin, D. & Kumar, S. Physiological functions of the HECT family of ubiquitin ligases. *Nat. Rev. Mol. Cell Biol.* **10**, 398–409 (2009).
- Maspero, E. et al. Structure of a ubiquitin-loaded HECT ligase reveals the molecular basis for catalytic priming. *Nat. Struct. Mol. Biol.* **20**, 696–701 (2013).
- Bruce, M. C. et al. Regulation of Nedd4-2 self-ubiquitination and stability by a PY motif located within its HECT-domain. *Biochem. J.* **415**, 155–163 (2008).
- Chen, S. Y. et al. Epithelial sodium channel regulated by aldosterone-induced protein sgk. *Proc. Natl Acad. Sci. USA* **96**, 2514–2519 (1999).
- Debonneville, C. et al. Phosphorylation of Nedd4-2 by Sgk1 regulates epithelial Na⁺ channel cell surface expression. *EMBO J.* **20**, 7052–7059 (2001).
- Snyder, P. M., Olson, D. R. & Thomas, B. C. Serum and glucocorticoid-regulated kinase modulates Nedd4-2-mediated inhibition of the epithelial Na⁺ channel. *J. Biol. Chem.* **277**, 5–8 (2002).
- Snyder, P. M., Olson, D. R., Kabra, R., Zhou, R. & Steines, J. C. cAMP and serum and glucocorticoid-inducible kinase (SGK) regulate the epithelial Na⁺ channel through convergent phosphorylation of Nedd4-2. *J. Biol. Chem.* **279**, 45753–45758 (2004).
- Lee, I. H., Dinudom, A., Sanchez-Perez, A., Kumar, S. & Cook, D. I. Akt mediates the effect of insulin on epithelial sodium channels by inhibiting Nedd4-2. *J. Biol. Chem.* **282**, 29866–29873 (2007).
- Edinger, R. S. et al. Functional regulation of the epithelial Na⁺ channel by IkappaB kinase-beta occurs via phosphorylation of the ubiquitin ligase Nedd4-2. *J. Biol. Chem.* **284**, 150–157 (2009).
- Bhalla, V. et al. Serum- and glucocorticoid-regulated kinase 1 regulates ubiquitin ligase neural precursor cell-expressed, developmentally down-regulated protein 4-2 by inducing interaction with 14-3-3. *Mol. Endocrinol.* **19**, 3073–3084 (2005).
- Ichimura, T. et al. 14-3-3 proteins modulate the expression of epithelial Na⁺ channels by phosphorylation-dependent interaction with Nedd4-2 ubiquitin ligase. *J. Biol. Chem.* **280**, 13187–13194 (2005).
- Nagaki, K. et al. 14-3-3 Mediates phosphorylation-dependent inhibition of the interaction between the ubiquitin E3 ligase Nedd4-2 and epithelial Na⁺ channels. *Biochemistry* **45**, 6733–6740 (2006).
- Chandran, S. et al. Neural precursor cell-expressed developmentally down-regulated protein 4-2 (Nedd4-2) regulation by 14-3-3 protein binding at canonical serum and glucocorticoid kinase 1 (SGK1) phosphorylation sites. *J. Biol. Chem.* **286**, 37830–37840 (2011).
- Obsil, T. & Obsilova, V. Structural basis of 14-3-3 protein functions. *Semin Cell Dev. Biol.* **22**, 663–672 (2011).
- Yaffe, M. B. et al. The structural basis for 14-3-3:phosphopeptide binding specificity. *Cell* **91**, 961–971 (1997).
- Liang, X., Peters, K. W., Butterworth, M. B. & Frizzell, R. A. 14-3-3 isoforms are induced by aldosterone and participate in its regulation of epithelial sodium channels. *J. Biol. Chem.* **281**, 16323–16332 (2006).
- Liang, X., Butterworth, M. B., Peters, K. W., Walker, W. H. & Frizzell, R. A. An obligatory heterodimer of 14-3-3beta and 14-3-3epsilon is required for aldosterone regulation of the epithelial sodium channel. *J. Biol. Chem.* **283**, 27418–27425 (2008).
- Johnson, C. et al. Bioinformatic and experimental survey of 14-3-3-binding sites. *Biochem. J.* **427**, 69–78 (2010).
- Ritinger, K. et al. Structural analysis of 14-3-3 phosphopeptide complexes identifies a dual role for the nuclear export signal of 14-3-3 in ligand binding. *Mol. Cell* **4**, 153–166 (1999).
- Yaffe, M. B. How do 14-3-3 proteins work?—Gatekeeper phosphorylation and the molecular anvil hypothesis. *FEBS Lett.* **513**, 53–57 (2002).
- Molzan, M., Weyand, M., Rose, R. & Ottmann, C. Structural insights of the MLF1/14-3-3 interaction. *FEBS J.* **279**, 563–571 (2012).
- Alblova, M. et al. Molecular basis of the 14-3-3 protein-dependent activation of yeast neutral trehalase Nth1. *Proc. Natl Acad. Sci. USA* **114**, E9811–E9820 (2017).

33. Kalabova, D. et al. 14-3-3 protein binding blocks the dimerization interface of caspase-2. *FEBS J.* **287**, 3494–3510 (2020).
34. Smidova, A. et al. 14-3-3 protein masks the nuclear localization sequence of caspase-2. *FEBS J.* **285**, 4196–4213 (2018).
35. Grimsey, N. J. et al. A tyrosine switch on NEDD4-2 E3 ligase transmits GPCR inflammatory signaling. *Cell Rep.* **24**, 3312–3323 e5 (2018).
36. Zhu, J. et al. Epilepsy-associated gene Nedd4-2 mediates neuronal activity and seizure susceptibility through AMPA receptors. *PLoS Genet.* **13**, e1006634 (2017).
37. Boucher, R. C., Stutts, M. J., Knowles, M. R., Cantley, L. & Gatzky, J. T. Na⁺ transport in cystic fibrosis respiratory epithelia. Abnormal basal rate and response to adenylate cyclase activation. *J. Clin. Invest.* **78**, 1245–1252 (1986).
38. Hummler, E. et al. Early death due to defective neonatal lung liquid clearance in alpha-ENaC-deficient mice. *Nat. Genet.* **12**, 325–328 (1996).
39. Lifton, R. P. Molecular genetics of human blood pressure variation. *Science* **272**, 676–680 (1996).
40. Snyder, P. M. et al. Mechanism by which Liddle's syndrome mutations increase activity of a human epithelial Na⁺ channel. *Cell* **83**, 969–978 (1995).
41. Kostecky, B., Saurin, A. T., Purkiss, A., Parker, P. J. & McDonald, N. Q. Recognition of an intra-chain tandem 14-3-3 binding site within PKCepsilon. *EMBO Rep.* **10**, 983–989 (2009).
42. Egleman, D. E. et al. Unbiased proteomic screening identifies a novel role for the E3 ubiquitin ligase Nedd4-2 in translational suppression during ER stress. *J. Neurochem.* **157**, 1809–1820 (2020).
43. Obsil, T., Ghirlando, R., Klein, D. C., Ganguly, S. & Dyda, F. Crystal structure of the 14-3-3zeta:serotonin N-acetyltransferase complex. a role for scaffolding in enzyme regulation. *Cell* **105**, 257–267 (2001).
44. Ganguly, S. et al. Role of a pineal cAMP-operated arylalkylamine N-acetyltransferase/14-3-3-binding switch in melatonin synthesis. *Proc. Natl Acad. Sci. USA* **98**, 8083–8088 (2001).
45. Kondo, Y. et al. Cryo-EM structure of a dimeric B-Raf:14-3-3 complex reveals asymmetry in the active sites of B-Raf kinases. *Science* **366**, 109–115 (2019).
46. Park, E. et al. Architecture of autoinhibited and active BRAF-MEK1-14-3-3 complexes. *Nature* **575**, 545–550 (2019).
47. Escobedo, A. et al. Structural basis of the activation and degradation mechanisms of the E3 ubiquitin ligase Nedd4L. *Structure* **22**, 1446–1457 (2014).
48. Fotia, A. B. et al. The role of individual Nedd4-2 (K14A0439) WW domains in binding and regulating epithelial sodium channels. *FASEB J.* **17**, 70–72 (2003).
49. Itani, O. A., Campbell, J. R., Herrero, J., Snyder, P. M. & Thomas, C. P. Alternate promoters and variable splicing lead to hNedd4-2 isoforms with a C2 domain and varying number of WW domains. *Am. J. Physiol. Ren. Physiol.* **285**, F916–929 (2003).
50. Harvey, K. F. et al. All three WW domains of murine Nedd4 are involved in the regulation of epithelial sodium channels by intracellular Na. *J. Biol. Chem.* **274**, 12525–12530 (1999).
51. Sato, S. et al. 14-3-3zeta is a novel regulator of parkin ubiquitin ligase. *Embo J.* **25**, 211–221 (2006).
52. Meek, S. E., Lane, W. S. & Pivnicka-Worms, H. Comprehensive proteomic analysis of interphase and mitotic 14-3-3-binding proteins. *J. Biol. Chem.* **279**, 32046–32054 (2004).
53. Pozuelo Rubio, M. et al. 14-3-3-affinity purification of over 200 human phosphoproteins reveals new links to regulation of cellular metabolism, proliferation and trafficking. *Biochem. J.* **379**, 395–408 (2004).
54. Jin, J. et al. Proteomic, functional, and domain-based analysis of in vivo 14-3-3 binding proteins involved in cytoskeletal regulation and cellular organization. *Curr. Biol.* **14**, 1436–1450 (2004).
55. Benzinger, A., Muster, N., Koch, H. B., Yates, J. R. 3rd & Hermeking, H. Targeted proteomic analysis of 14-3-3 sigma, a p53 effector commonly silenced in cancer. *Mol. Cell Proteom.* **4**, 785–795 (2005).
56. Tinti, M. et al. ANIA: ANnotation and Integrated Analysis of the 14-3-3 interactome. *Database (Oxford)* **2014**, bat085 (2014).
57. Stevers, L. M. et al. Modulators of 14-3-3 protein-protein interactions. *J. Med. Chem.* **61**, 3755–3778 (2018).
58. Obsilova, V. et al. 14-3-3zeta C-terminal stretch changes its conformation upon ligand binding and phosphorylation at Thr232. *J. Biol. Chem.* **279**, 4531–4540 (2004).
59. Itani, O. A., Stokes, J. B. & Thomas, C. P. Nedd4-2 isoforms differentially associate with ENaC and regulate its activity. *Am. J. Physiol. Ren. Physiol.* **289**, F334–46 (2005).
60. Kabsch, W. Xds. *Acta Crystallogr. Sect. D, Biol. Crystallogr.* **66**, 125–132 (2010).
61. Sparta, K. M., Heinemann, U., Mueller, U. & Weiss, M. S. XDSAPP2.0. *J. Appl. Crystallogr.* **49**, 1085–1092 (2016).
62. Vagin, A. & Teplyakov, A. MOLREP: an automated program for molecular replacement. *J. Appl. Crystallogr.* **30**, 1022–1025 (1997).
63. Adams, P. D. et al. PHENIX: a comprehensive Python-based system for macromolecular structure solution. *Acta Crystallogr. Sect. D. Biol. Crystallogr.* **66**, 213–221 (2010).
64. Kosek, D. et al. Biophysical and structural characterization of the thioredoxin-binding domain of protein kinase ASK1 and its interaction with reduced thioredoxin. *J. Biol. Chem.* **289**, 24463–24474 (2014).
65. Schuck, P. Size-distribution analysis of macromolecules by sedimentation velocity ultracentrifugation and lamm equation modeling. *Biophys. J.* **78**, 1606–1619 (2000).
66. Dam, J., Velikovskiy, C. A., Mariuzza, R. A., Urbanke, C. & Schuck, P. Sedimentation velocity analysis of heterogeneous protein-protein interactions: Lamm equation modeling and sedimentation coefficient distributions c(s). *Biophys. J.* **89**, 619–634 (2005).
67. Gotze, M. et al. StavroX—a software for analyzing crosslinked products in protein interaction studies. *J. Am. Soc. Mass Spectrom.* **23**, 76–87 (2012).
68. Young, M. M. et al. High throughput protein fold identification by using experimental constraints derived from intramolecular cross-links and mass spectrometry. *Proc. Natl Acad. Sci. USA* **97**, 5802–5806 (2000).
69. Kylarova, S., Psenakova, K., Herman, P., Obsilova, V. & Obsil, T. CaMKK2 kinase domain interacts with the autoinhibitory region through the N-terminal lobe including the RP insert. *Biochim Biophys. Acta Gen. Subj.* **1862**, 2304–2313 (2018).
70. Kukacka, Z., Rosulek, M., Strohal, M., Kavan, D. & Novak, P. Mapping protein structural changes by quantitative cross-linking. *Methods* **89**, 112–120 (2015).
71. Panjkovich, A. & Svergun, D. I. CHROMIXS: automatic and interactive analysis of chromatography-coupled small-angle X-ray scattering data. *Bioinformatics* **34**, 1944–1946 (2018).
72. Konarev, P. V., Volkov, V. V., Sokolova, A. V., Koch, M. H. J. & Svergun, D. I. PRIMUS: a Windows PC-based system for small-angle scattering data analysis. *J. Appl. Crystallogr.* **36**, 1277–1282 (2003).
73. Svergun, D. I. Determination of the regularization parameter in indirect-transform methods using perceptual criteria. *J. Appl. Crystallogr.* **25**, 495–503 (1992).
74. Rambo, R. P. & Tainer, J. A. Accurate assessment of mass, models and resolution by small-angle scattering. *Nature* **496**, 477–481 (2013).
75. Franke, D. & Svergun, D. I. DAMMIF, a program for rapid ab-initio shape determination in small-angle scattering. *J. Appl. Crystallogr.* **42**, 342–346 (2009).
76. Volkov, V. V. & Svergun, D. I. Uniqueness of ab initio shape determination in small-angle scattering. *J. Appl. Crystallogr.* **36**, 860–864 (2003).
77. Kozin, M. B. & Svergun, D. I. Automated matching of high- and low-resolution structural models. *J. Appl. Crystallogr.* **34**, 33–41 (2001).
78. Petoukhov, M. V. et al. New developments in the ATSAS program package for small-angle scattering data analysis. *J. Appl. Crystallogr.* **45**, 342–350 (2012).
79. Yang, X. et al. Structural basis for protein-protein interactions in the 14-3-3 protein family. *Proc. Natl Acad. Sci. USA* **103**, 17237–17242 (2006).
80. Zhang, W. et al. System-wide modulation of HECT E3 ligases with selective ubiquitin variant probes. *Mol. Cell* **62**, 121–136 (2016).
81. Maspero, E. et al. Structure of the HECT-ubiquitin complex and its role in ubiquitin chain elongation. *EMBO Rep.* **12**, 342–349 (2011).
82. Guinier, A. La diffraction des rayons X aux très petits angles: application à l'étude de phénomènes ultramicroscopiques. *Ann. Phys.* **11**, 161–237 (1939).

Acknowledgements

This study was funded by the Czech Science Foundation (V.O., grant number 20-00058S), the Grant Agency of Charles University (P.P. grant number 740119), the Czech Academy of Sciences (RVO:67985823 of the Institute of Physiology). We thank the Czech Infrastructure for Integrative Structural Biology (CIISB) for access to the CMS facilities at BIOCEV (project LM2015043 by MEYS) and MetaCentrum CESNET for the using of their computing clusters. We thank EMBL MX beamline 14.2 (BESSY, Berlin) and SAXS beamline P12 (Petra III DESY, Hamburg) for the allocated experimental beam time. We thank D. Kalabova, G. Kocarova and A. Smidova for technical assistance, P. Pompach and P. Vankova for their help with MS measurements and Carlos V. Melo for editing the article.

Author contributions

V.O. and T.O. conceived the study and provided scientific guidance. P.P. and R.J. prepared the recombinant proteins. P.P. performed F.P. assays, SAXS data processing and SAXS-based modeling and crystallized the 14-3-3zeta:Nedd4^{335–455} protein complex. P.P. performed the ubiquitination assay. O.P. performed SV-AUC and analyzed data. R.J. prepared samples for chemical crosslinking. V.O., P.P. and R.J. refined the crystal structures. V.O. and T.O. wrote the paper. All co-authors revised the manuscript.

Competing interests

The authors declare no competing interests.

Additional information

Supplementary information The online version contains supplementary material available at <https://doi.org/10.1038/s42003-021-02419-0>.

Correspondence and requests for materials should be addressed to T.O. or V.O.

Peer review information *Communications Biology* thanks the anonymous reviewers for their contribution to the peer review of this work. Primary Handling Editors: Min Zhuang and Eve Rogers. Peer reviewer reports are available.

Reprints and permission information is available at <http://www.nature.com/reprints>

Publisher's note Springer Nature remains neutral with regard to jurisdictional claims in published maps and institutional affiliations.



Open Access This article is licensed under a Creative Commons Attribution 4.0 International License, which permits use, sharing, adaptation, distribution and reproduction in any medium or format, as long as you give appropriate credit to the original author(s) and the source, provide a link to the Creative Commons license, and indicate if changes were made. The images or other third party material in this article are included in the article's Creative Commons license, unless indicated otherwise in a credit line to the material. If material is not included in the article's Creative Commons license and your intended use is not permitted by statutory regulation or exceeds the permitted use, you will need to obtain permission directly from the copyright holder. To view a copy of this license, visit <http://creativecommons.org/licenses/by/4.0/>.

© The Author(s) 2021

14-3-3-protein regulates Nedd4-2 by modulating interactions between HECT and WW domains

Pavel Pohl^{1,2}, Rohit Joshi^{1,3}, Olivia Petrvalska^{1,3}, Tomas Obsil^{1,3*} and Veronika Obsilova^{1*}

Affiliations

¹Department of Structural Biology of Signaling Proteins, Division BIOCEV, Institute of Physiology of the Czech Academy of Sciences, 252 50 Vestec, Czech Republic

²nd Faculty of Medicine, Charles University, V Uvalu 84, 15006 Prague, Czech Republic

³Department of Physical and Macromolecular Chemistry, Faculty of Science, Charles University, 128 43 Prague, Czech Republic

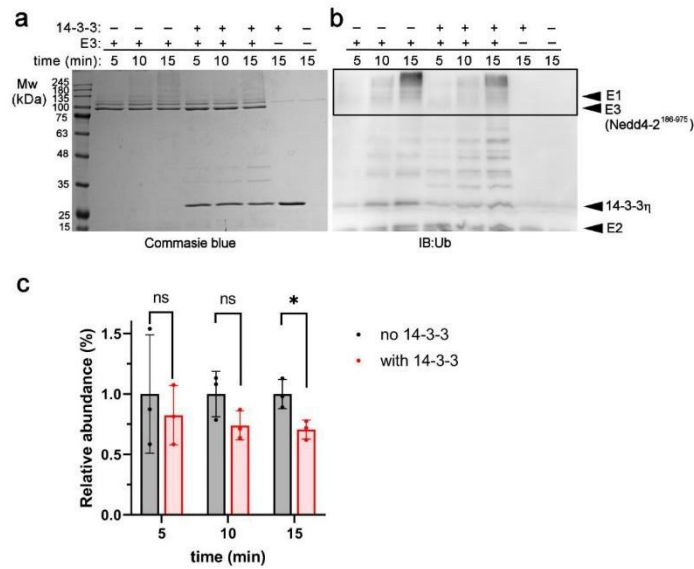
***Corresponding authors:** veronika.obsilova@fgu.cas.cz (V.O.); obsil@natur.cuni.cz (T.O.)

Supplementary Information (available in this document)

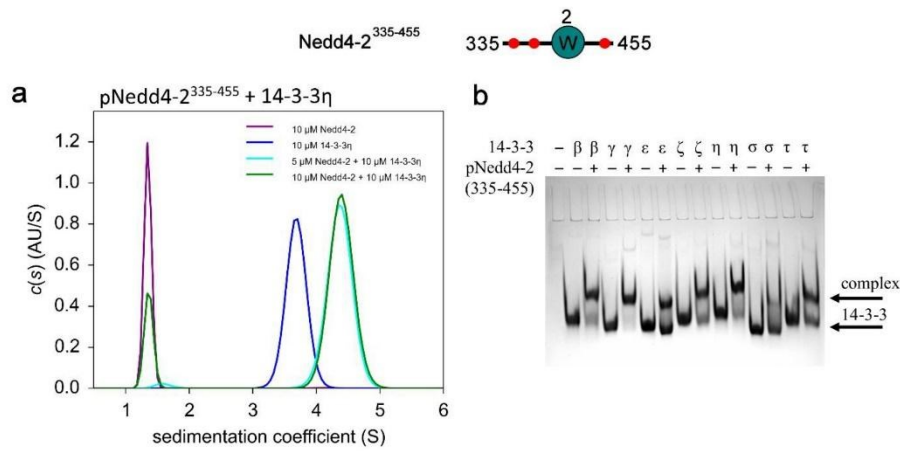
Supplementary Figures S1–S6

Supplementary Tables S1–S5

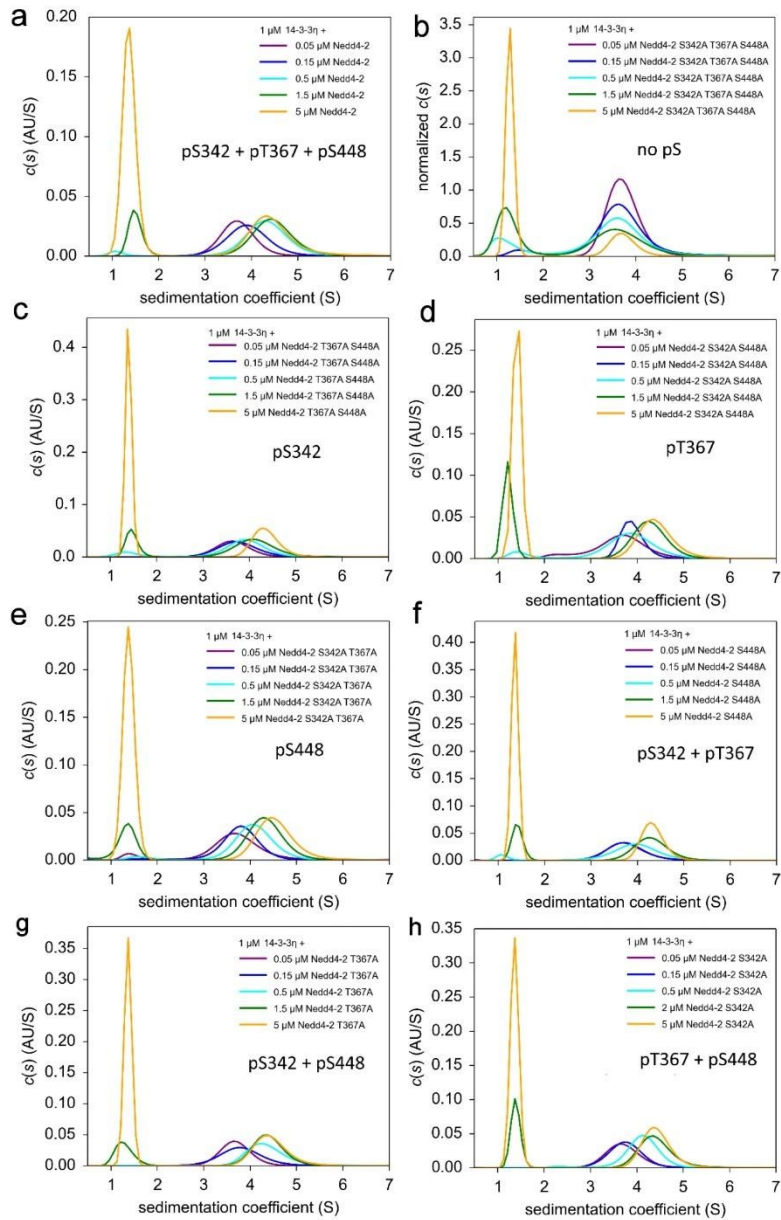
Supplementary References



Supplementary Fig. S1. 14-3-3 slows down the auto-ubiquitination of Nedd4-2¹⁸⁶⁻⁹⁷⁵. **a** Purity and integrity of the samples used in the Ub chain formation assay. The samples were resolved by 10% Tris/Glycine SDS-PAGE and stained with Coomassie G-250. **b** Ubiquitin (Ub) chain formation assay with and without 14-3-3 η and the representative immunoblot of Ub. Black rectangles denote the borders of the sample zones that were quantified. The presence of ubiquitinated Nedd4-2 in the quantified zones was confirmed by LC-MS analysis. **c** Relative abundances of ubiquitinated Nedd4-2¹⁸⁶⁻⁹⁷⁵ with and without 14-3-3 η based on the immunoblot of Ub. Error bars represent the standard deviation of three independent experiments. Results show the data distribution. Asterisks represent significant differences according to unpaired Student's t-tests comparing relative change between samples without and with 14-3-3 η at selected timepoints (ns, non-significant $P > 0.05$; *, $P < 0.05$).

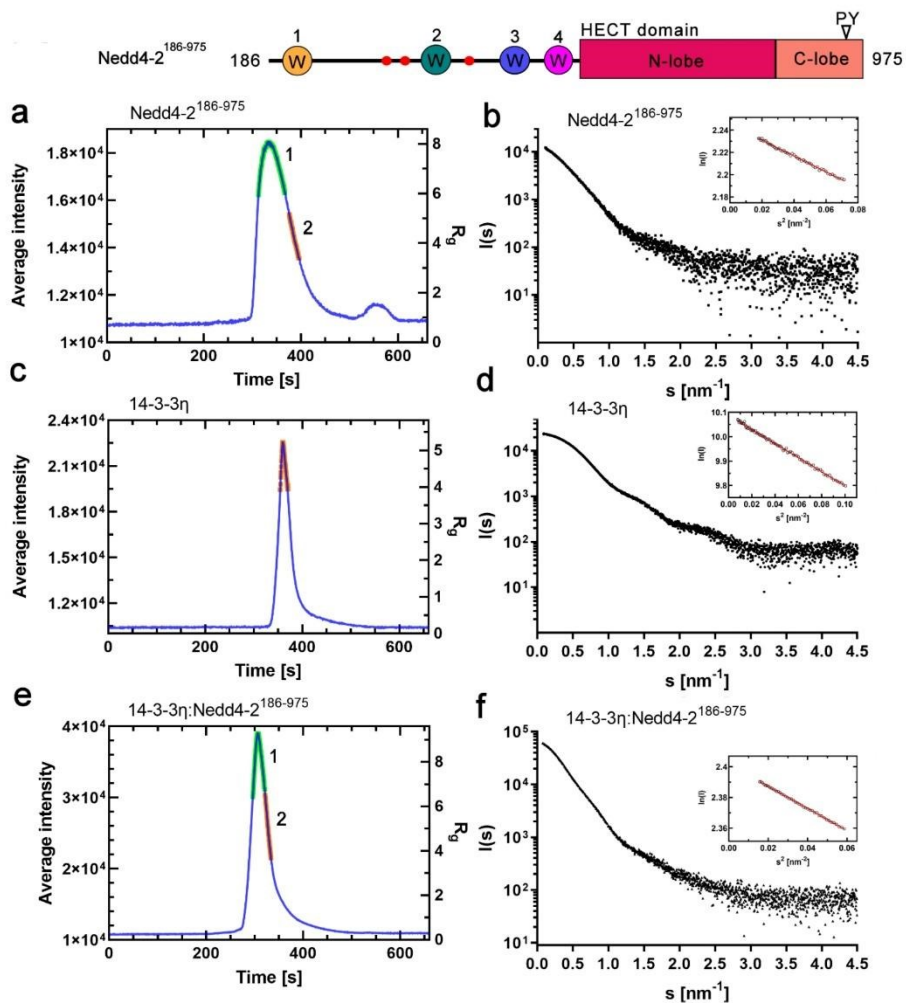


Supplementary Fig. S2. Characterization of the interaction between Nedd4-2³³⁵⁻⁴⁵⁵ and 14-3-3 in solution. **a** Continuous sedimentation coefficient distributions ($c(s)$) of 10 μM pNedd4-2³³⁵⁻⁴⁵⁵ alone (purple), 10 μM 14-3-3 η alone (blue), and the pNedd4-2³³⁵⁻⁴⁵⁵:14-3-3 η complex mixed at 1:2 (cyan) and 1:1 (green) molar ratios. The protein concentrations were 10 μM for 14-3-3 η and 5 μM or 10 μM for pNedd4-2³³⁵⁻⁴⁵⁵. **b** Isoform binding specificity of pNedd4-2³³⁵⁻⁴⁵⁵. Phosphorylated pNedd4-2³³⁵⁻⁴⁵⁵, 14-3-3 proteins and their complexes were separated by 12% TBE-PAGE to study the interaction of pNedd4-2³³⁵⁻⁴⁵⁵ with all seven human 14-3-3 isoforms (β , γ , ϵ , ζ , η , σ , and τ). The amounts of protein loaded on the native gel were 128 pmol of 14-3-3 and 64 pmol of pNedd4-2³³⁵⁻⁴⁵⁵.

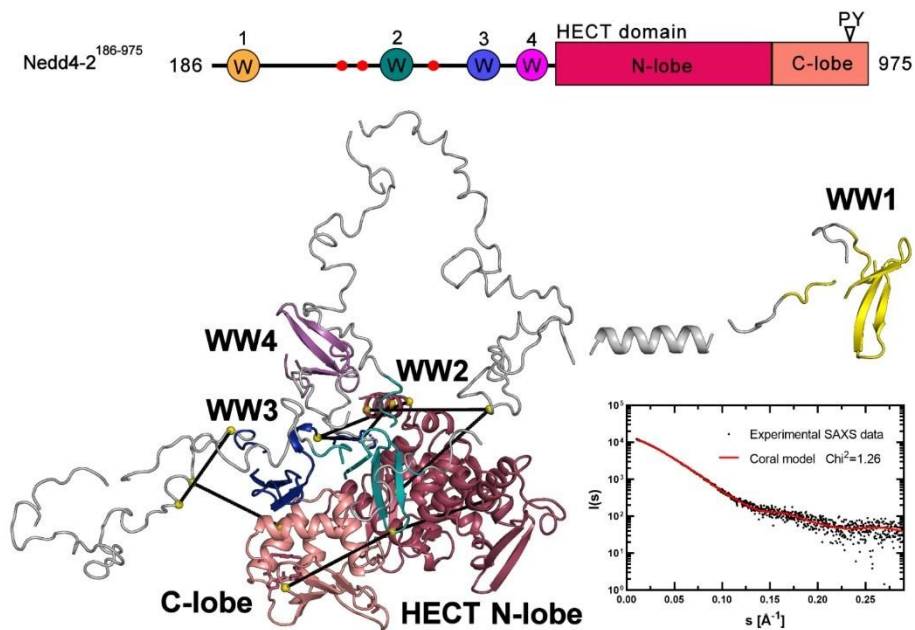


4

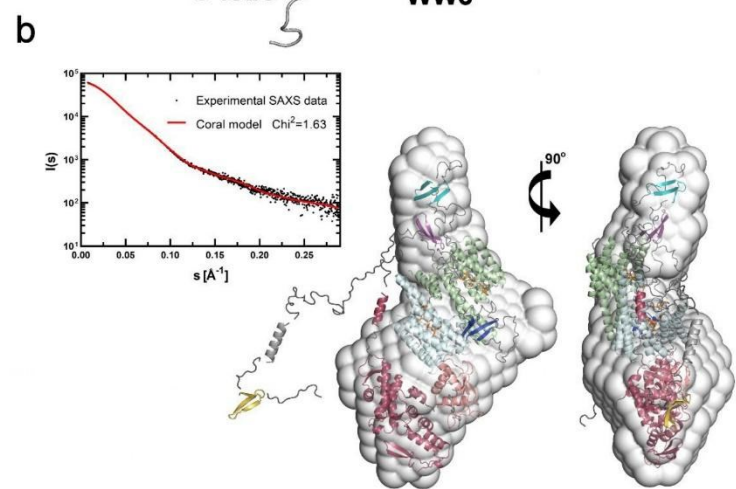
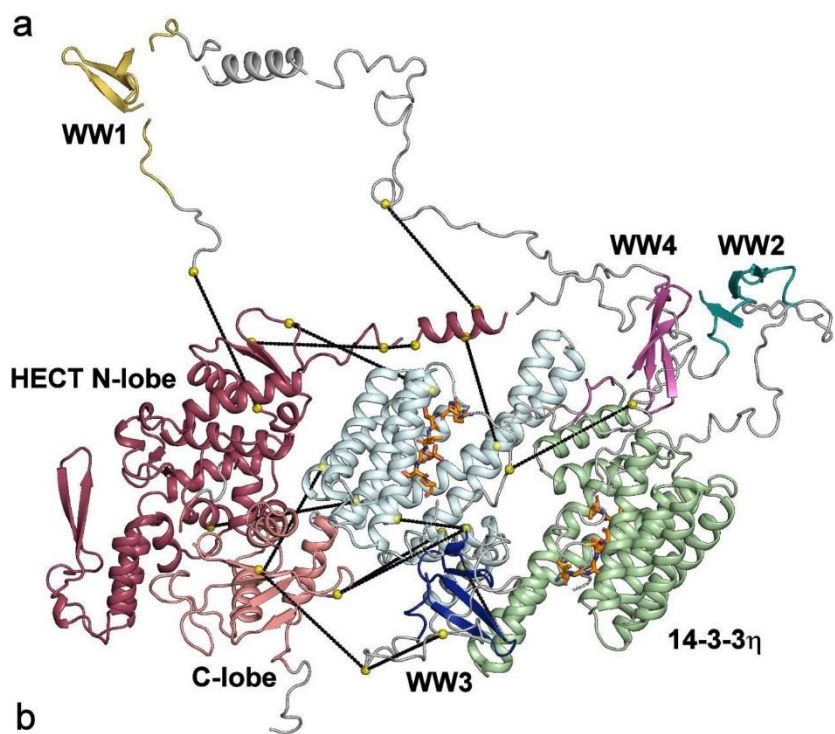
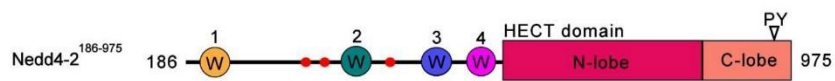
Supplementary Fig. S3. Sedimentation velocity analytical ultracentrifugation analysis of the pNedd4-2³³⁵⁻⁴⁵⁵:14-3-3 η complexes corresponding to Fig. 3. The c(s) distributions of mixtures of 1 μ M 14-3-3 η with 0.05–5 μ M pNedd4-2³³⁵⁻⁴⁵⁵ variants: **(a)** pS342 + pT367 + pS448, **(b)** no phosphorylation site, **(c)** pS342, **(d)** pT367, **(e)** pS448, **(f)** pS342 + pT367, **(g)** pS342 + pS448 and **(h)** pT367 + pS448.



Supplementary Fig. S4. SEC-SAXS data analysis. Elution profiles of average intensity as a function of elution time (blue line) of (a) Nedd4-2¹⁸⁶⁻⁹⁷⁵ alone, (c) 14-3-3η and (e) 14-3-3η:pNedd4-2¹⁸⁶⁻⁹⁷⁵ complex eluting from the in-line SEC connected to SAXS instrumentation are shown on the left. Red lines denote the regions with the selected frames for final analysis, green lines (1) denote regions not selected for analysis. (b,d,f) The corresponding scattering curves from SEC-SAXS experiment are shown on the right. Scattering intensity $I(s)$ is plotted in relation to the scattering vector s ($s = 4\pi\sin(\theta)/\lambda$, where 2θ is the scattering angle and λ is the wavelength). The insets are Guinier plots of low- q regions, with the red line showing linearity in $\ln(I)$ vs s^2 .



Supplementary Fig. S5: CORAL model of Nedd4-2¹⁸⁶⁻⁹⁷⁵ alone. Left, Best-scoring CORAL model of the Nedd4-2¹⁸⁶⁻⁹⁷⁵. HECT domain of Nedd4-2¹⁸⁶⁻⁹⁷⁵, N-lobe is shown in raspberry and C-lobe in salmon. WW1, WW2, WW3 and WW4 domains are shown in yellow, teal, blue and magenta, respectively. Flexible linkers between rigid bodies are shown in grey. C α atoms of crosslinked residues are represented as yellow spheres. Right, scattering curve calculated from the CORAL model of Nedd4-2¹⁸⁶⁻⁹⁷⁵ (red) compared with the experimental SAXS data (black dots)¹.



Supplementary Fig. S6: CORAL model of the pNedd4-2¹⁸⁶⁻⁹⁷⁵:14-3-3 η complex. **a** Best-scoring CORAL model of the Nedd4-2¹⁸⁶⁻⁹⁷⁵:14-3-3 η complex. The 14-3-3 η protomers are shown in pale green and pale cyan. In the HECT domain of Nedd4-2¹⁸⁶⁻⁹⁷⁵, the N-lobe is shown in raspberry and the C-lobe in salmon. WW1, WW2, WW3 and WW4 domains are shown in yellow, teal, blue and magenta, respectively. Structure of phosphorylated peptides in binding grooves solved by X-ray crystallography are represented as orange sticks, colored by elements (PDB ID: 6ZBT and 6ZC9, this work). Flexible linkers between rigid bodies are shown in grey. C α atoms of crosslinked residues are represented as yellow spheres. **b** Left, scattering curve calculated from the CORAL model of the Nedd4-2¹⁸⁶⁻⁹⁷⁵:14-3-3 η complex (red) compared with experimental SAXS data (black dots)¹. Right, averaged and filtered *ab initio* molecular envelope of the Nedd4-2¹⁸⁶⁻⁹⁷⁵:14-3-3 η complex (light grey envelope) calculated from the SAXS scattering curve using the program DAMMIF². The averaged and filtered molecular envelope (shown in light grey) was aligned with the CORAL model using the program SUPCOMB³.

Supplementary Tables:

Supplementary Table S1.

Intramolecular distance constraints of Nedd4-2¹⁸⁶⁻⁹⁷⁵ derived from the crosslinking experiments with DSG

#	Crosslinked peptides		Crosslinked residues		Observed mass	Error (ppm)
	Nedd4-2	Nedd4-2	Nedd4-2	Nedd4-2		
1.	472-506	472-506	Y485	T495	4071.97	0.4
2.	522-529	507-521	T522	K521	2827.38	0.05
3.	738-742	743-761	K742	T745	2923.34	0.05
4.	596-600	254-301	K598	T275	5748.77	0.38
5.	530-537	538-557	K531	K539	3329.71	-0.1
6.	395-398	254-301	K395	T275	5530.67	0.08
7.	573-580	564-572	T574	K572	2264.06	-0.5
8.	396-400	820-841	K398	K822	3188.70	-0.2
9.	657-665	648-656	Y660	S656	2183.06	0.14
10.	596-600	538-557	K600	S538	2981.50	0.11
11.	494-506	472-493	T495	S493	4089.98	0.75
12.	898-907	871-897	T903	K894	4558.36	-0.1
13.	716-725	726-737	K725	K737	2609.43	0.08
14.	396-400	908-938	K398	S932	4104.03	0.04

Nedd4-2 regions: WW1: 193-226, WW2: 385-418, WW3: 497-530, WW4: 548-581, HECT N-lobe: 595-857, HECT C-lobe: 858-974.

Supplementary Table S2

Intramolecular distance constraints of the Nedd4-2¹⁸⁶⁻⁹⁷⁵ complex with 14-3-3 η derived from the crosslinking experiments with DSG

Crosslink #	Crosslinked peptides		Crosslinked residues		Observed mass	Error (ppm)
	Nedd4-2	Nedd4-2	Nedd4-2	Nedd4-2		
1.	472-506 ^a	472-506	Y485	K493	4071.97	0.08
2.	522-529	507-521	T522	K521	2827.38	-0.3
3.	538-557	410-442	S538	S428	5911.9	0.44
4.	738-742	743-761	K742	T745	2923.34	-0.1
5.	607-617	607-617	K607	K609	1375.81	0.48
6.	596-600	254-301	K598	T275	5748.78	0.78
7.	573-580	564-572	T574	K572	2264.06	-0.4
8.	657-665	648-656	Y660	K656	2183.07	0.21
9.	494-506	472-493	K495	K493	4089.98	0.05
10.	716-725	726-737	K725	Y736	2609.43	-0.1
11.	946-958	959-975	Y951	K960	4663.17	0.18
12.	898-907	871-897	T903	K885	4558.36	-0.1
13.	530-537	908-938	K531	K935	4585.32	0.11

^aNedd

4-2 regions: WW1: 193-226, WW2: 385-418, WW3: 497-530, WW4: 548-581, HECT N-lobe: 595-857, HECT C-lobe: 858-974.

Supplementary Table S3

Quantitative intramolecular distance constraints of the pNedd4-2¹⁸⁶⁻⁹⁷⁵ complex with 14-3-3 η derived from the crosslinking experiments with 12C DSA/13C DSA.

Crosslink #	Crosslinked peptides		Crosslinked residues		Average ratio pNedd4-2/pNedd4-2:14-3-3 complex ^a	SD
	Nedd4-2	Nedd4-2	Nedd4-2	Nedd4-2		
1.	530-537	606-610	K531	K607	150	30
2.	610-617	618-634	K610	K621	60	10
3.	186-202	625-640	H186	K639	50	10
4.	472-493	865-885	K489	K870	70	10
5.	494-529	530-537	K521	K531	100	0
6.	472-493	871-895	K489	K885	130	10

^a Representation (%) of the individual crosslink isoform as a ratio between the abundance of 12C DSA (pNedd4-2¹⁸⁶⁻⁹⁷⁵) and 13C DSA (pNedd4-2¹⁸⁶⁻⁹⁷⁵:14-3-3 η).

Supplementary Table S4Intermolecular distance constraints of pNedd4-2¹⁸⁶⁻⁹⁷⁵ complex with 14-3-3 η derived from the crosslinking experiments

Crosslink #	Crosslinker	Crosslinked peptides		Crosslinked residues		Observed mass	Error (ppm)
		Nedd4-2	14-3-3 η	Nedd4-2	14-3-3		
1.	DSG	599-605	58-61	K600	S58	1553.75	0.23
2.	DSG	530-537	199-227	K531	K217	4451.23	0.05
3.	DSG	522-529	62-78	T522	K69	2827.38	0.87
4.	DSG	886-895	156-172	K894	K162	3185.64	-0.05
5.	DSG	737-742	111-123	K737	K120	2475.10	0.21
6.	DSG	918-935	21-49	K935	K28	5266.49	0.52
7.	DSS	648-656	143-154	K656	K143	2585.26	-0.73

Nedd4-2 regions: WW1: 193-226, WW2: 385-418, WW3: 497-530, WW4: 548-581, HECT N-lobe: 595-857, HECT C-lobe: 858-974.

Supplementary Table S5.

Oligonucleotide sequences for Nedd4-2¹⁸⁶⁻⁹⁷⁵ in pST39 and Nedd4-2³³⁵⁻⁴⁵⁵ in pRSFDuet-1.

Variant	Primer	DNA-Sequence (5'-3')
186-975	pST39-fw	AGTC TCTAGA AAT AAT TTT GTT TAA CTT TAA GAA GGA GAT ATA CAT ATG CAC CAA GAG GAA CTT CCT CC
186-975	pST39-rev	CCG CTG GTA CCC TAG TGG TGA TGA TGG TGA TGG CTG CTG TTA TCC ACC CCT TCA AAT CC
335-455	pHGT2_fw	TGCATGCCATGGGATCCTCAAGGTTGAGG
335-455	pHGT2_rev	GTTGTCCTTTGCGGCCGCTAAGATAAAGTTACTGTTGG
335-455	S342A-fw	GGTTGAGGTCATGCGCTGTCACCGACGCAG
335-455	S342A-rev	CTGCGTCGGTGACAGCGCATGACCTCAACC
335-455	T367A-fw	CGCGTTCATCAGCTGTCACGGGTGGTG
335-455	T367A-rev	CACCACCCGTGACAGCTGATGAACGCG
335-455	S448A-fw	GGCCTCGTAGCCTCGCCTCGCCAACAGTAAC
335-455	S448A-rev	GTTACTGTTGGCGAGGCGAGGCTACGAGGCC

Supplementary References

1. Petoukhov, M.V. et al. New developments in the ATSAS program package for small-angle scattering data analysis. *Journal of Applied Crystallography* **45**, 342-350 (2012).
2. Franke, D. & Svergun, D.I. DAMMIF, a program for rapid ab-initio shape determination in small-angle scattering. *Journal of Applied Crystallography* **42**, 342-346 (2009).
3. Kozin, M.B. & Svergun, D.I. Automated matching of high- and low-resolution structural models. *Journal of Applied Crystallography* **34**, 33-41 (2001).